machines



Special Issue Reprint

# Design and Experimental Activity of Testing Machines and Mechanical Test Rigs

Edited by
Ciro Santus and Massimiliano De Agostinis

mdpi.com/journal/machines

MDPI

# Design and Experimental Activity of Testing Machines and Mechanical Test Rigs

# Design and Experimental Activity of Testing Machines and Mechanical Test Rigs

Guest Editors

**Ciro Santus**
**Massimiliano De Agostinis**

MDPI

Basel • Beijing • Wuhan • Barcelona • Belgrade • Novi Sad • Cluj • Manchester

*Guest Editors*

Ciro Santus
Department of Civil and Industrial Engineering - DICI
University of Pisa
Pisa
Italy

Massimiliano De Agostinis
Department of Industrial Engineering
University of Bologna
Bologna
Italy

*Editorial Office*
MDPI AG
Grosspeteranlage 5
4052 Basel, Switzerland

This is a reprint of the Special Issue, published open access by the journal *Machines* (ISSN 2075-1702), freely accessible at: https://www.mdpi.com/journal/machines/special_issues/38ICZMA79F.

For citation purposes, cite each article independently as indicated on the article page online and as indicated below:

Lastname, A.A.; Lastname, B.B. Article Title. *Journal Name* **Year**, *Volume Number*, Page Range.

**ISBN 978-3-7258-8431-5 (Hbk)**
**ISBN 978-3-7258-8432-2 (PDF)**
**https://doi.org/10.3390/books978-3-7258-8432-2**

Cover image courtesy of Massimiliano De Agostinis

© 2026 by the authors. Articles in this reprint are Open Access and distributed under the Creative Commons Attribution (CC BY) license. The reprint as a whole is distributed by MDPI under the terms and conditions of the Creative Commons Attribution-NonCommercial-NoDerivs (CC BY-NC-ND) license (https://creativecommons.org/licenses/by-nc-nd/4.0/).

# Contents

**About the Editors** . . . . . **vii**

**Preface** . . . . . **ix**

**Zhenyi Yang, Jun Li and Guoyan Yu**
Influence of Piston Mass and Working Pressure on the Impact Performance of a Hydraulic Rock Drill Using the Stress Wave Method
Reprinted from: *Machines* **2023**, *11*, 987, https://doi.org/10.3390/machines11110987 . . . . . **1**

**Georg Ivanov, Thomas Burkhardt, Lars Penter and Steffen Ihlenfeldt**
New Method for Precise Measurement of Clamping Plate Deformations on Forming Presses
Reprinted from: *Machines* **2024**, *12*, 40, https://doi.org/10.3390/machines12010040 . . . . . **20**

**Dario Croccolo, Massimiliano De Agostinis, Stefano Fini, Mattia Mele, Giorgio Olmi and Chiara Scapecchi**
Design of Special Equipment for the Mechanical Testing of Runway Light Fixtures
Reprinted from: *Machines* **2024**, *12*, 41, https://doi.org/10.3390/machines12010041 . . . . . **48**

**Luca Vecchiato, Matteo Negri, Giulio Picci, Luca Viale, Giulio Zaltron, Stefano Giacometti and Giovanni Meneghetti**
Design and Development of a Brake Test Bench for Formula SAE Race Cars
Reprinted from: *Machines* **2024**, *12*, 135, https://doi.org/10.3390/machines12020135 . . . . . **62**

**Ciro Santus, Lorenzo Romanelli, Leonardo Bertini, Alessandro Burchianti and Tomoya Inoue**
Resonant Fatigue Tests on Polished Drill Pipe Specimens
Reprinted from: *Machines* **2024**, *12*, 314, https://doi.org/10.3390/machines12050314 . . . . . **79**

**Jiangong Du, Yuanying Qiu and Jing Li**
Research on Bolt Loosening Mechanism Under Sine-on-Random Coupling Vibration Excitation
Reprinted from: *Machines* **2025**, *13*, 80, https://doi.org/10.3390/machines13020080 . . . . . **98**

**Dequan Huang, Yan Li, Xingyuan Zheng and Gang Li**
Study on Dynamic Behaviors of Hypoid Gears Under Variable Tidal Current Energy Harvesting Conditions
Reprinted from: *Machines* **2025**, *13*, 178, https://doi.org/10.3390/machines13030178 . . . . . **125**

**Yougen Huang, Bin Li, Haohui Chen, Weigang Yang, Qianhao Xiao and Jun Wang**
Analysis of Performance and Noise on an Asymmetric Double-Suction Fan with Non-Uniformity Inlet Conditions
Reprinted from: *Machines* **2025**, *13*, 463, https://doi.org/10.3390/machines13060463 . . . . . **146**

**Zhinan Cao, Jie Feng, Shijun Xie, Qian Peng, Jiahui Chen, Cheng Wen and Jigang Huang**
Rapid Dismantling of Aluminum Stranded Conductors: An Automated Approach
Reprinted from: *Machines* **2025**, *13*, 608, https://doi.org/10.3390/machines13070608 . . . . . **168**

**Luigi Leopardi, Valerio Mangeruga, Matteo Giacopini, Marco Di Settimi and Roberto Rosi**
Development of a Test Rig for Detecting Fatigue Cracks in a Plastic Component of a Medical Device via Acoustic Signal Acquisitions
Reprinted from: *Machines* **2025**, *13*, 1118, https://doi.org/10.3390/machines13121118 . . . . . **186**

# About the Editors

**Ciro Santus**

Ciro Santus is a Full Professor at the University of Pisa, Dept. of Civil and Industrial Engineering—DICI in the sector IIND-03/A (former ING-IND/14)—Progettazione meccanica e costruzione di macchine. Prof. Ciro Santus teaches Fundamentals of Machine Design and Computational Methods for Structural Analysis in the Mechanical Engineering course of the University of Pisa. The research topics covered by Prof. Ciro Santus are as follows: Fatigue and fracture of metal components; Additive manufacturing technologies; Contact mechanics and fretting fatigue; Gear dynamics; gear tooth fatigue and rolling contact fatigue; Residual stress measurement with the hole-drilling method; Mechanical design of machine elements; Finite element modelling for structural applications; Experimental modal analysis of bladed wheels. Prof. Ciro Santus has published more than 90 papers, and his H-index is 26. Prof. Ciro Santus is also a member of the Quality Assurance Committee "Presidio della Qualità" of the University of Pisa; a Scientific Responsible of "Curriculum Meccanica" within the "Dottorato in Ingegneria Industriale", and an Editorial Board Member of *Machines* – MDPI.

**Massimiliano De Agostinis**

Massimiliano De Agostinis is Associate Professor of Mechanical Design and Machine Construction at the University of Bologna, Department of Industrial Engineering. He holds a PhD in Design and Development of Products and Industrial Processes from the University of Florence and a MEng in Mechanical Engineering from the University of Bologna. His main research interests span from joining technologies (bolted joints, adhesives) to design for additive manufacturing and the failure analysis of mechanical components. He teaches Mechanical Behaviour of Materials and Chassis & Body Design and Manufacturing at the School of Engineering of the University of Bologna. He has a track record of industrial research projects in collaboration with leading Italian and international industries. Since 2018, he has served on the board of the Doctorate School in Mechatronic Engineering and Mechanical Product Innovation of the University of Padova. He serves as an Associate Editor for *Proceedings of the Institution of Mechanical Engineers*—PartC, the *Journal of Mechanical Engineering Science*, and the ASME *Journal of Pressure Vessel Technology*. As of June 2026, he is responsible as the Head of CIRI MAM, Interdepartmental Center for Research, Advanced Mechanics and Materials of the University of Bologna. He is a founding member of Fast10 srl, a spinoff company of the University of Bologna, providing advanced solutions for threaded fastener applications.

# Preface

Many industrial sectors require highly specialized experimental setups capable of reproducing complex loading conditions such as fretting fatigue, dynamic vibrations, or full-scale operational scenarios. The contributions of this Special Issue focus on methodologies, design strategies, and implementation aspects related to the development of innovative mechanical testing facilities with special attention dedicated to mechanical design solutions, control architectures, instrumentation integration, and experimental validation procedures. The goal of this Special Issue is to promote knowledge sharing and stimulate the development of increasingly effective and innovative testing solutions within the mechanical engineering community.

**Ciro Santus and Massimiliano De Agostinis**
*Guest Editors*

machines

MDPI

*Article*

# Influence of Piston Mass and Working Pressure on the Impact Performance of a Hydraulic Rock Drill Using the Stress Wave Method

**Zhenyi Yang [1,2], Jun Li [1,2] and Guoyan Yu [1,3,*]**

[1] College of Mechanical Engineering, Guangdong Ocean University, Zhanjiang 524088, China; zhyiyang@gdou.edu.cn (Z.Y.); lij@gdou.edu.cn (J.L.)
[2] Guangdong Provincial Key Laboratory of Intelligent Equipment for South China Sea Marine Ranching, Guangdong Ocean University, Zhanjiang 524088, China
[3] Guangdong Provincial Marine Equipment and Manufacturing Engineering Technology Research Center, Zhanjiang 524088, China
* Correspondence: yugy@gdou.edu.cn

**Abstract:** To optimize and improve the impact performance of a hydraulic rock drill, it is helpful to test the stress waves of the drill and analyze the impact energy, impact frequency, and energy utilization rate. For this study, a stress wave test bench was designed and built, according to international standards, in order to study the impact process of a hydraulic rock drill under the working pressures of 18 MPa and 23 MPa. The impact energy, impact frequency, and energy utilization rate of two different hydraulic rock drill pistons in low, middle, and high gear were analyzed using a control variable method. The results demonstrate that the impact stress waves of the rock drill periodically occur in the drill rod, and then decay exponentially until they become close to zero. Moreover, the amplitude of the incident stress wave determines the rock-breaking ability of the drill. The impact energy of the short piston is greater than that of the long piston, with a maximum average value of 346.1 J; the impact frequency of the long piston is higher than that of the short piston, with a maximum average value of 62 Hz; and the energy utilization rate of the short piston is higher than that of the long piston, with a maximum average value of 56.92%, which is close to the theoretical ideal efficiency. Therefore, it can be concluded that the impact performance of a hydraulic rock drill can be effectively tested using the proposed horizontal bench, and that piston characteristics and the working pressure are the main factors affecting impact performance. Accordingly, when developing a hydraulic rock drill, it is advisable to select a shorter piston and a higher working pressure, thus allowing the drill to provide good impact performance.

**Keywords:** hydraulic rock drill; impact performance; stress wave

## 1. Introduction

The hydraulic rock drill is the external working mechanism of a rock drill jumbo and is the most important component for rock drilling [1]. It is widely used in mining, tunnel excavation, urban construction, and other engineering operations [2]. A hydraulic rock drill uses oil as its working medium, converting the pressure energy of the oil into the impact energy of the piston, and then transmits this energy through the drill rod into the rock in the form of a stress wave [3]. Previous research has generally focused on improving the impact performance and energy utilization of hydraulic rock drills.

Through experimentation, Jaho Seo et al. [4] established a hydraulic rock drill simulated calculation model. They analyzed the effect of working pressure on the impact performance of the rock drill, and concluded that the pressure was the main factor affecting the impact frequency and impact energy, which verified the reliability of the analysis model. Giuffrida et al. [5] carried out simulated calculations on the working process of a

hydraulic rock drill and found that the impact frequency of the rock drill increased with an increase in working pressure, while the impact efficiency was affected by the comprehensive effects of pressure, flow, and so on. Chang-heon Song et al. [6,7] used the Taguchi method to determine the main design parameters affecting the impact performance of rock drills. They concluded that the main factors affecting the impact force were the supply pressure in the impact system and the diameter of the impact piston rod. Hu et al. [8] established a dynamic simulation model of a hydraulic rock drill and tested two hydraulic rock drills: YYG138 and YYG150. The simulated results were consistent with their test results. Yang et al. [9] established a dynamic simulation model of a hydraulic impact system; analyzed the dynamic characteristics of the impact mechanism; obtained the piston chamber pressure, flow characteristic curve, and its impact on the impact performance; and optimized the working parameters of the impact system on the basis of an orthogonal test to improve the system's efficiency. Ji Hong et al. [10,11] established a dynamic model for the impact system of a hydraulic rock drill. Using state-space description theory and a linear system method, they deduced the existing range of piston vibrations in one impact period and analyzed the influence of the design parameters on impact performance. Laforgia et al. [12] established a detailed parametric simulation model to simulate the physical phenomena occurring during rock drill operation. The simulated results for pressure and frequency were consistent with the test. It was concluded that, when the actual input flow was used to replace its average value, the results of the simulation model did not change.

Research on the modeling and simulation of hydraulic rock drills has generally focused on the interactions between mechanisms of the hydraulic rock drill, the working process of the hydraulic impact system, and the influence of the component's design parameters on piston motion; however, detailed analyses of stress wave transmission during piston impact are not typically conducted.

Dutta et al. [13] established a basic equation describing the generation, transmission, and reflection of stress waves and compiled a calculation program. Using the finite difference method and the transmission–reflection relationship of stress waves, they calculated the stress wave generated by the impact hammer and drill rod. Wu [14] established a stress wave propagation and impact energy transmission analysis model for a hydraulic rock drill that accounted for the local deformation of the impact end of the piston rod joint. The results indicated that, when the local deformation was within the normal range, it had little impact on the energy transmission efficiency of the hydraulic rock drill. Nygrena et al. [15,16] studied the energy transmission of the incident wave through the elastic joint of a uniform rod, which maximized the energy transmission efficiency of the input and output rods under given, continuous incident wave conditions. They obtained the optimal junction point for different types of incident waves in order to determine the impedance characteristics and energy transmission efficiency of the optimal joint. Lundberg et al. [17] established the force–drilling relationship of the non-linear rock breaking process, using a three-dimensional elastic–plastic finite element model to simulate the impact hammer and rock. Under good drilling conditions, the rock's elastic response had a significant impact on the drilling efficiency and determined the pattern of drilling efficiency change. Chiang et al. [18] established a non-linear elastic rock–point interaction model for a down-the-hole drill. They corrected the calculation model using the error between the variable parameters obtained using a quasi-static tunneling test method and model analysis. Analyzing the stress–strain model, Kahraman et al. [19,20] found that the uniaxial compressive strength of rock properties, the Brazilian tensile strength, the point load strength, and the Schmidt value were the main parameters affecting the impact penetration rate. Assuming that driving speed depends on many factors (e.g., rock hardness, in-situ stress, and so on), Zhang et al. [21] analyzed the influence of impact force and torque on rock-drilling performance accounting for rocks with different properties. They proposed a drillability index evaluation model and rock classification rules suitable for the working parameters of the rock drill. Arffman et al. [22] studied the efficiency of a low-pressure impactor using a numerical simulation method. They investigated the

effect of turbulence velocity fluctuations on impactor performance by comparing the ratios between the simulated and experimental impactor efficiencies. Joo Young et al. [23,24] studied the hydraulic circuit and impact processes of a hydraulic rock drill, as well as the dynamic effect of rock hardness on impact performance. They found that the energy utilization rate of the rock drill decreased with an increase in hardness.

Studies on the working processes of hydraulic rock drills usually consider the rock drill as a whole power output unit, analyzing the stress wave propagation, energy transmission, and rock-breaking effect during rock drilling. Such research has not considered the effects of the characteristics of the piston performing the work, nor has it compared the applicability of multiple pistons with respect to one model. Research on the impact performance of hydraulic rock drills remains limited, as well as research on improving the energy utilization of rock drills.

For this study, a test method for the impact machines and tools specified in international standards [25,26] was used to determine a suitable piston for drilling, as well as to improve the impact performance of the hydraulic rock drill. A stress wave test bench was designed and built in order to test and analyze the transmission characteristics of the stress spectrum during the impact process of the hydraulic rock drill. Using the control variable method, the impact energy, impact frequency, and energy utilization rate of rock drills operating in three gears (i.e., low, middle, and high) were analyzed. This was achieved under the condition that the body size of the hydraulic rock drill had already been determined; that is, the stroke of the three gears was fixed, and two pistons of different sizes under working pressures of 18 MPa and 23 MPa were used.

## 2. Rock-Drilling Process

A hydraulic rock drill is usually composed of an impact system, a shank adapter rebound absorption system, a rotary system, and a head. When the rock drill is installed on the trolley in preparation for rock drilling, it also needs to be equipped with an auxiliary water supply, dust prevention, propulsion systems, and so on [2]. The operational process of the hydraulic rock drill comprises four functions: propulsion, impact, rotation, and flushing (see Figure 1).

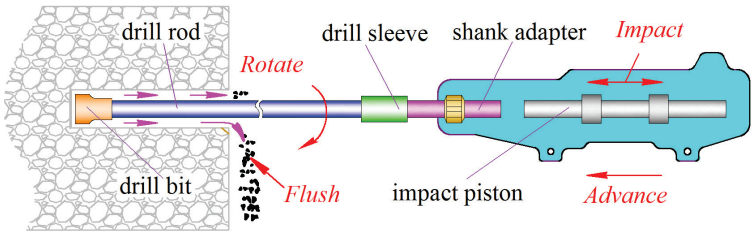



**Figure 1.** Working process of a hydraulic rock drill.

During the impact drilling process of a hydraulic rock drill, the hydraulic cylinder exerts a continuous pushing force on the rock drill: the drill rod bit is always in contact with the rock wall, ready to transmit the incident energy of the drill rod to the rock at any time to seamlessly drill the next blast hole. The impact system is the core component of the hydraulic rock drill. When the hydraulic pump supplies pressured oil to the rock drill, the pressure energy of the liquid is converted into the impact energy of the impact piston. The impact energy is then transmitted to the rock through the drill rod in the form of a stress wave, causing the rock to break. In the slewing function, the hydraulic motor outputs torque through the transmission gear to cause the drill bit to rotate to a new position after each impact, peeling off the cracked rock surface while waiting for the next impact. During drilling, the pressured water from the auxiliary water pump reaches the drill bit through the cleaning head and is sprayed out, thereby washing the rock debris out of the drill hole; washing is an essential function to improve drilling efficiency.

Hydraulic rock drills are often used in harsh construction environments, such as in mining and tunnelling operations. For this reason, testing and analysis of the impact process, impact energy, and impact frequency cannot be completed in an on-site manner.

## 3. Construction of Experimental Platform

### *3.1. Introduction to the Test Bench*

Due to the harsh working environment in which the hydraulic rock drill operates, the piston is enclosed within the body. Therefore, to measure the displacement and speed of the piston, some parts must be disassembled and may be damaged. For this reason, measurements cannot take place in real-time under actual working conditions, and performance testing can only be carried out under laboratory conditions. According to the provisions of international standards ISO/TS 17104-2006 and ISO2787-1984 [25,26], the impact performance of a rock drill should be tested using the stress wave method, which is a test method used for impact machinery and other products. The so-called 'stress wave method' refers to the method of directly testing the stress in the measuring rod to determine the impact energy. The advantages of this method include speed, accuracy, and a wide testing range.

An impact performance test system for a hydraulic rock drill was designed, according to the abovementioned international standards, by our research institute. The system is shown in Figure 2. The rock drill, drill rod, and energy absorption device to be tested were installed on the horizontal bench. Pressure sensors and flow meters were installed on the oil circuit of the hydraulic rock drill transmission system in order to measure the pressure and flow of the rock drill during operation. One end of the drill rod was connected to the shank adapter, while the other end was placed in the energy absorption device. Strain gauges were pasted on both sides of the drill rod, forming a measuring bridge to detect the stress wave signal in the drill rod; as such, the drill rod must be of a sufficient length to accurately capture the incident stress wave. The propulsion hydraulic cylinder was supplied by an independent hydraulic system. The propulsion cylinder exerts thrust on the mobile base, such that the shank adapter/drill rod is always in contact with the energy absorption device.

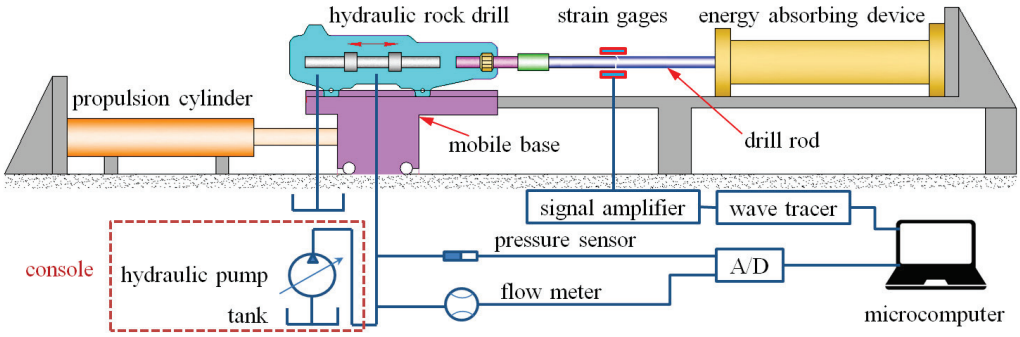



**Figure 2.** Impact performance test system for the rock drill.

The energy absorption device featured a circular tube structure constructed from 45 steel, possessing an elastic modulus of $2.06 \times 10^{11}$ Pa, a density of 7850 kg/m$^3$, and a Poisson's ratio of $\mu = 0.3$. The tail of the energy-absorbing circular tube was equipped with multiple layers of rubber pads, employing IIR rubber with an elastic modulus of $7.8 \times 10^6$ Pa, a density of 920 kg/m$^3$, and a Poisson's ratio of $\mu = 0.47$. One end of the drill rod was affixed to the rock drill, while the other end was inserted into the energy absorption device and linked to a series of disc-shaped friction plates. These friction plates were set at a specific inclination angle, with the spaces between them filled by an asphalt mixture characterized by an elastic modulus ranging from 1.2 to $1.4 \times 10^9$ Pa, a density of 1250 kg/m$^3$, and a Poisson's ratio of $\mu = 0.35$. The structural configuration is shown in Figure 3.

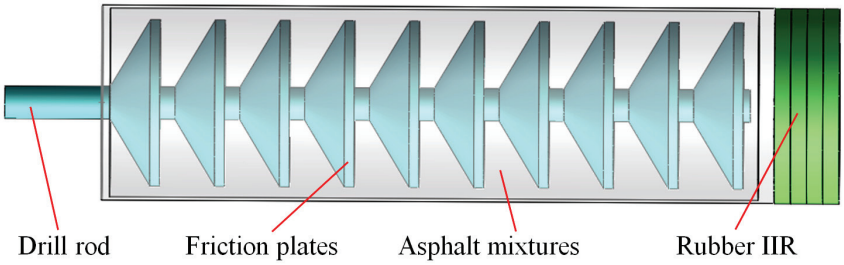



**Figure 3.** Energy absorption device.

For the experiment, we adopted a hydraulic rock drill with a working pressure of 18–25 MPa and working flow of 60–120 L/min developed by the author's team, as shown in Figure 4. The gear regulator is a cylindrical and rotatable component found on a hydraulic rock drill, featuring three grooves of varying lengths. As shown in Figure 5, there were four oil ports located below the gear regulator. The oil inlet, situated on the right side, connected to the hydraulic pump, while the remaining three outlets were linked to the piston chamber of the rock drill. The rotary gear regulator can open different oil passages, and the positioning of the oil port dictates the stroke of the rock drill piston. Consequently, the corresponding piston strokes were categorized into three gears: high (52 mm), medium (56 mm), and low (60 mm).

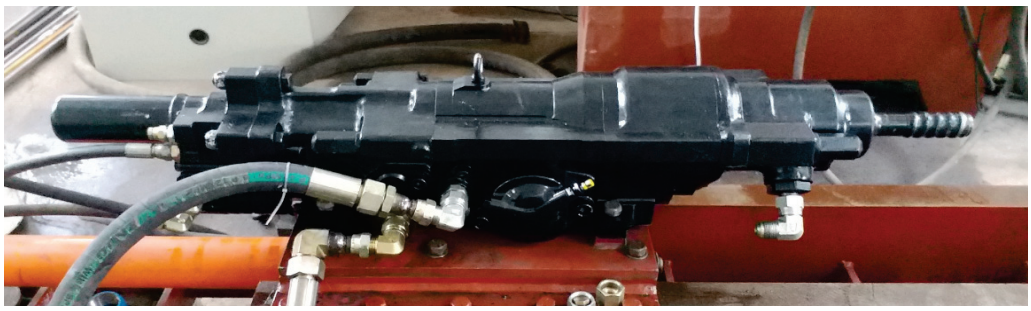


**Figure 4.** Hydraulic rock drill.

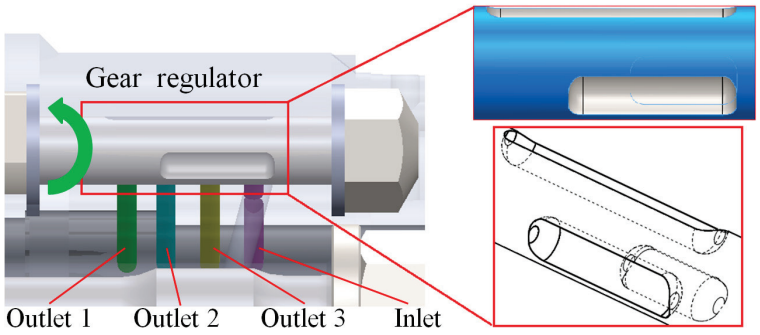



**Figure 5.** Gear regulator.

Once the size of the hydraulic rock drill body had been determined—that is, once the low, middle, and high gear strokes were fixed—two pistons of different sizes were designed for this model. As shown in Figure 6, the diameter, material, and production process of the two pistons were the same. Their stress spectrum, impact energy, impact frequency, and energy utilization ratio were tested and analyzed, and the change in impact performance of the hydraulic rock drills when the piston mass and piston driving conditions were changed was studied.



**Figure 6.** Hydraulic rock drill long and short pistons.

*3.2. Impact Energy Transfer Process*

The performance of drilling operations is influenced not only by the inherent characteristics of the rock drill but also by various factors, such as the properties of the rock material [27], the diameter of the drilling hole, the flushing of rock debris, the material properties of the drill, and structural parameters [21,28]. In this study, the drill rod and drill bit are considered to be an integrated system which is fully engaged in rock chiseling. The main focus is on the impact of the piston on the performance of the rock drill. Additionally, an energy absorption device was devised to investigate the impact performance of the rock drill. When the rock drill piston impacts the drill rod, the mass of the piston can be expressed as:

$$M_p = \rho A_h L = \frac{E}{c^2} \cdot \frac{A_R}{R} L = \frac{m_R}{c} \cdot \frac{L}{R} \tag{1}$$

where $\rho$ is the piston density, $A_h$ is the piston cross-section, $L$ is the piston length, $E$ is the elastic modulus, $c$ is the wave velocity, $R$ is the fluctuation inertia ratio of drill rod to piston, $A_R$ is the drill rod cross-section, and $m_R$ is the drill rod fluctuation inertia.

With the cross-sectional area and wave inertia of both the piston and the drill rod being equal, the stress wave exhibits an infinitely proportional decreasing order with a wavelength of $2L/c$ [29]. Consequently, the incident energy of the drill rod is:

$$\begin{aligned} E_i &= \tfrac{A_R c}{E} \textstyle\int_0^{2L/c} \sigma_R^2 dt = \tfrac{A_R c}{E} \cdot \tfrac{1}{4} \cdot \tfrac{E^2}{c^2} V_P^2 \cdot \tfrac{2L}{c} \\ &= m_R \cdot \tfrac{1}{4} \cdot V_P^2 \cdot \tfrac{2M_P R}{m_R} = \tfrac{1}{2} M_P V_P^2 \end{aligned} \tag{2}$$

This suggests that the incident energy equals the piston impact energy, resulting in the full energy being incident upon the drill rod.

Once the stress wave traverses through the energy absorption device, a significant portion of the energy is converted into frictional losses, with a smaller portion being reflected as energy. In accordance with international standards, an energy absorption exceeding 90% signifies the rationality and feasibility of the energy absorption device [25, 26]. The combination of friction plates and the asphalt mixture within the energy absorption device creates a series of lower friction coefficient points ($f_1, f_2 \ldots f_n$), which collectively fulfills the energy absorption requirements.

The energy absorption device takes the form of a multi-point series combination based on the principles of impact dynamics [30]. To further ascertain the optimal distribution of $f_n$ across multiple friction points, we assume the transmission energy coefficient $T_{En}$= $K(const)$, then $f = 1 - \sqrt[2n]{K}$, $R_{En} = \frac{1}{n}(1 - \sqrt{K})^2$. As the number of points increases, it becomes evident that the total reflected energy coefficient ($R_{En}$) rapidly diminishes. This phenomenon elucidates why the energy absorption device adopts an elongated tube structure, featuring multiple internal friction points arranged in series.

The conservation of energy can be expressed as, $T_E + R_E + F_E = 1$, where $T_E$ is the transmission energy coefficient, $R_E$ is the reflection energy coefficient, and $F_E$ is the friction energy coefficient. When the values are set to $K$ = 0.01, $n$ = 10, $f_{10}$ = 0.205, and $R_{En}$ = 0.081, the total reflected energy falls below 10% of the total energy, thereby complying with international standards [26]. Consequently, the energy absorption device is suitable for assessing the impact performance of rock drills. It is important to note that the total energy mentioned here refers to the incident energy, representing the impact energy imparted by the piston.

### *3.3. Experimental Calibration*

As the signal data in a test system can be affected by many factors, in order to ensure the accuracy of the test results it was first necessary to calibrate the equipment. The calibration work was carried out on a vertical test bench; in particular, the free-falling weight calibration method specified in the international standard [25] was used to calibrate the impact stress and impact energy of the test system, as shown in Figure 7. In the calibration system, the calibration tube was a seamless steel pipe which guided the falling of the drop hammer, where the areas of the end face of the drop hammer and the end face of the measuring rod were equal. A hammer-hanging mechanism was set on the calibration pipe rack, the drop hammer was lifted to a height of 2 m, and the equipment was then calibrated.

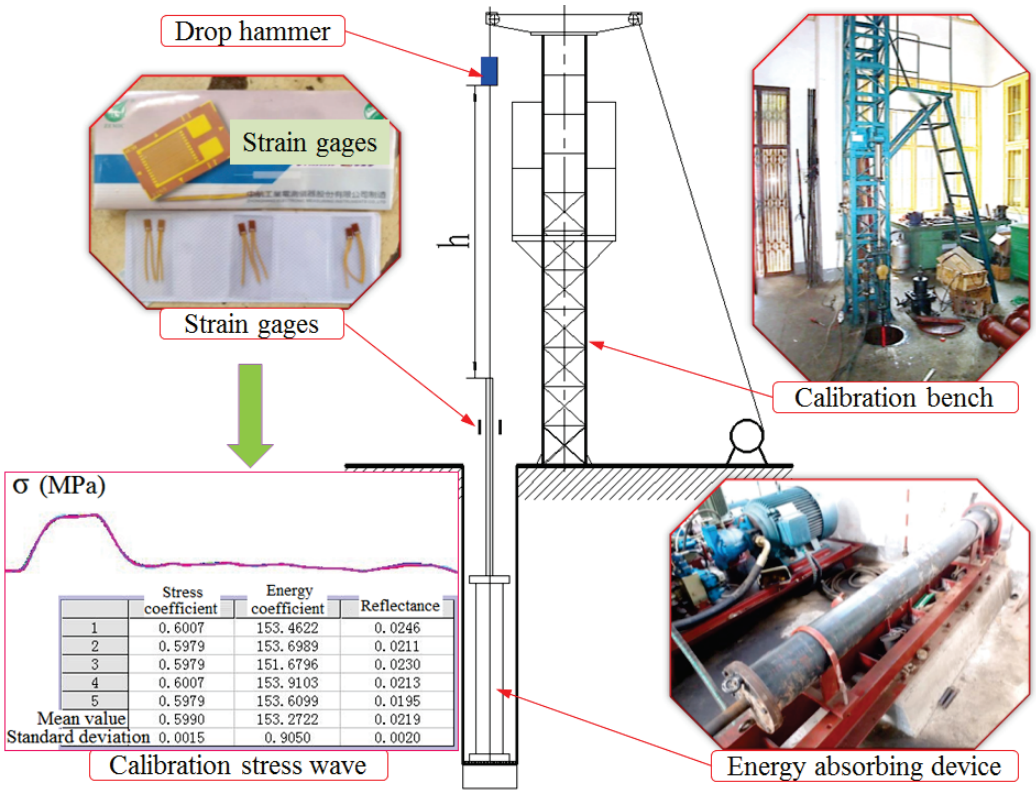



**Figure 7.** Calibration of rock drill test system.

At the start of calibration, the drop hammer was released, causing the drop hammer to fall freely along the wall of the calibration pipe and hit the drill rod, thus enabling calculation of the maximum stress produced by the measuring rod, $\sigma_{\max}$:

$$\sigma_{\max} = \varphi \frac{E}{C} V_p = \varphi \frac{E}{C} \sqrt{2gh} \tag{3}$$

where $E$ is the elastic modulus of the drill rod, $C$ is the wave velocity, $g$ is the acceleration due to gravity, $h$ is the height of the falling hammer, and $\varphi$ is the stress coefficient.

Indeed, the stress wave signal is of an analog nature, whereby analog signals exhibit continuous changes in both time and amplitude; whereas digital signals manifest as discrete entities in both time and amplitude. To convert analog signals into digital ones, the process of amplitude quantization is indispensable. Quantization is an integral component of the analog-to-digital (A/D) conversion process.

From the quantized value $n_{\max}$ of the wave peak point in the stress sampling, the stress calibration coefficient can be obtained as follows:

$$B_s = \frac{\sigma_{\max}}{n_{\max}} \tag{4}$$

According to the calibration coefficient, the maximum stress of the drill rod is $\sigma_{max} = B_s \cdot n_{max}$.

The impact energy of the drop hammer can be determined by integrating the quantized value of each sampling point of the stress wave, as follows:

$$E_p = \frac{AC}{E}\int \sigma^2 dt = \frac{AC}{E} B_s^2 \sum n^2 \Delta t = C_s S \tag{5}$$

where $A$ is the area of the drill-rod end face, $n$ is the quantized value of each sampling point in the stress wave, $C_S = \frac{AC}{E} B_s^2$ is the calibration coefficient of the impact energy, and $S = \sum n^2 \Delta t$ is the integral of the square of the quantized value in the stress wave.

Simultaneously, the same calibration method was used to calibrate the energy. From $mgh = \frac{AC}{E} B_E^2 S$, the stress calibration coefficient is

$$B_E = \sqrt{\frac{mgh \times E}{A \times C \times S}} \tag{6}$$

The calibration coefficient of energy can be obtained, by further derivation, as

$$C_E = \frac{mgh}{S} \tag{7}$$

Thus, the impact energy of the drop hammer can be determined as

$$E_P = C_E \cdot S \tag{8}$$

Under the same conditions, the results obtained by the two calibration methods detailed above were consistent. The stress wave curve obtained through calibration is shown in Figure 8. We determined the characteristic indices of the instrument and the measuring system, and eliminated system error as much as possible, thereby improving the accuracy of the measurement. The calibrated energy absorption device and measuring rod were lifted out of the calibration bench and installed on the horizontal bench. The impact performance of the hydraulic rock drill was then tested, and the stress, impact energy, and impact frequency of the drill rod were measured.

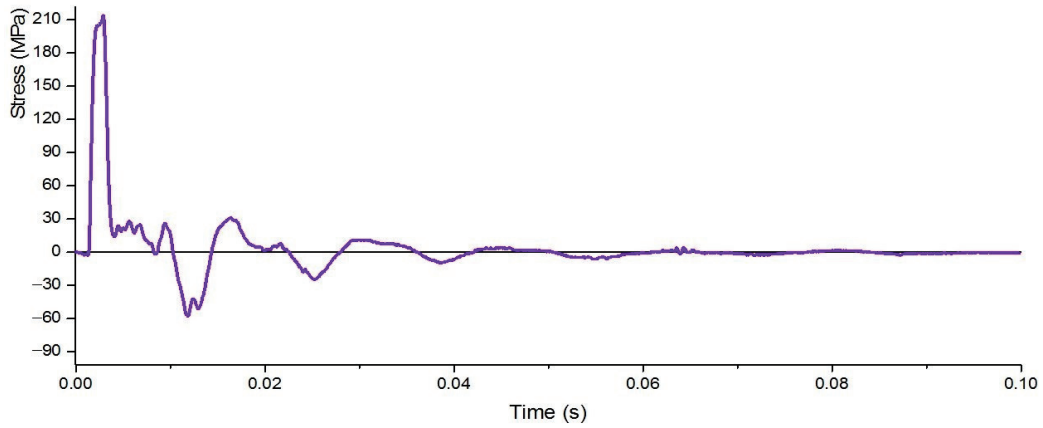



**Figure 8.** Calibrated stress wave curve.

## 4. Data Collection

### *4.1. Stress Spectrum*

During the hydraulic rock drill test, one end of the drill rod abutted the head of the hydraulic rock drill, while the other end was placed in the tubular energy absorption device. As such, the drill rod could not accurately obtain the incident stress spectrum of the piston, as shown in Figure 9. When the high-speed rock drill piston impacts the shank adapter, the impact energy of the piston is transmitted to the drill rod by the shank adapter and the extension sleeve through the impact, in the form of a stress wave. The stress wave generated in the drill rod causes the resistance of the resistance strain gauge to change. The consequent electrical signal is then amplified and sent to the waveform recorder to record the impact waveform data.

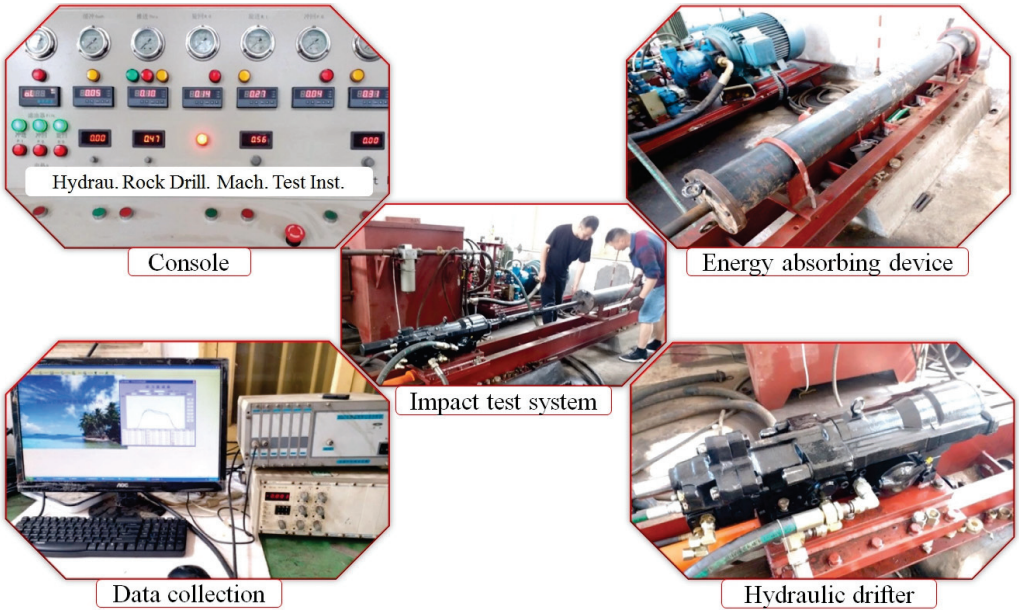



**Figure 9.** Test bench for hydraulic rock drill.

In Figure 10, the propagation process for a group of stress waveforms in the drill rod is depicted. Figure 10a shows the stress spectrum in the drill rod when the long piston is in the low gear under 18 MPa. The average impact frequency of the piston was 47.6 Hz and the average incident maximum stress was 216.4 J. As shown in Figure 10b, when the stress wave of the drill rod was transmitted to the energy absorption device—that is, when it was actually chiseled into the rock—the stress immediately and suddenly decreased. Each string of stress waves presented one or two reflections in the high-amplitude region, forming a low-amplitude region that attenuates exponentially. The high-amplitude stress determines the rock-breaking ability. As shown in Figure 10c, the incident stress gradually increased to the point where the attenuation was close to zero. The front part of the waveform had a limited period in which it increased, resulting in a certain slope, while the fall of the waveform also took a certain amount of time. The most desirable effect of percussive drilling is that as much energy is concentrated in the high-amplitude area as possible to break the rock, while less energy is required in the low-amplitude area. Each time the piston impacts the drill rod, the first incident stress waveform in the stress spectrum is the most important stress element in the rock-drilling process, and the single-impact energy can be obtained by integrating over this period of time. Therefore, the magnitude and duration of the incident stress peak determine the magnitude of the single-impact energy.

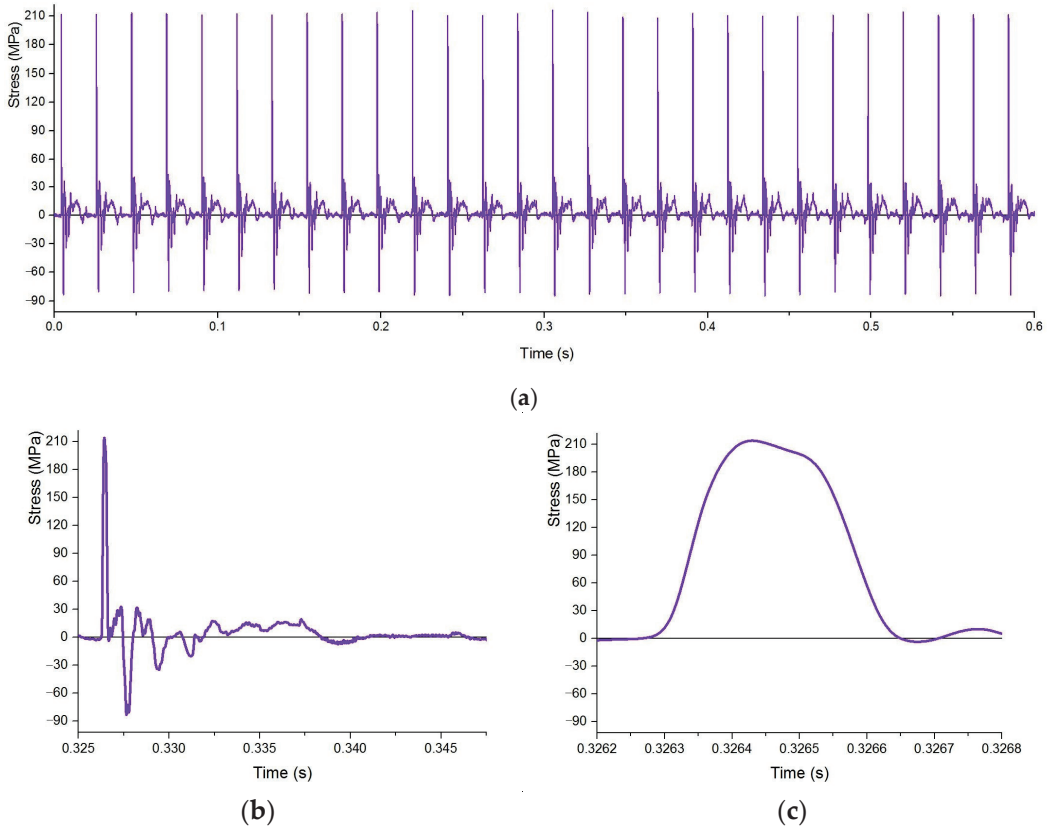



**Figure 10.** Stress wave of drill rod under 18 MPa long piston, low gear. (**a**) Impact stress spectrum; (**b**) transmitted stress wave; and (**c**) incident stress wave.

### *4.2. Impact Results*

The impact energy and impact frequency are key impact performance indicators of a hydraulic rock drill. For the hydraulic rock drill shown in Figure 4, two pistons with different characteristics (i.e., one long and the other short) were designed, as shown in Figure 6. The stress waves, impact energy, and impact frequencies of the hydraulic rock drill at three strokes—namely, high (52 mm), middle (56 mm), and low (60 mm) gear—were measured under the working pressures of 18 MPa and 23 MPa. Each sampled data point intercepted 25 consecutive impact cycles.

The output stress, impact energy, and impact frequency for the long piston under working pressures of 18 MPa and 23 MPa are shown in Figures 11–16.

The output stress, impact energy, and impact frequencies of the short piston under the working pressures of 18 MPa and 23 MPa were also measured, as shown in Figures 17–22.

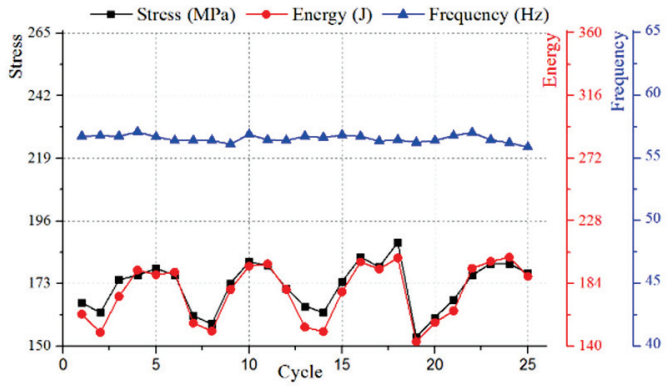



**Figure 11.** Long piston, high gear, 18 MPa.

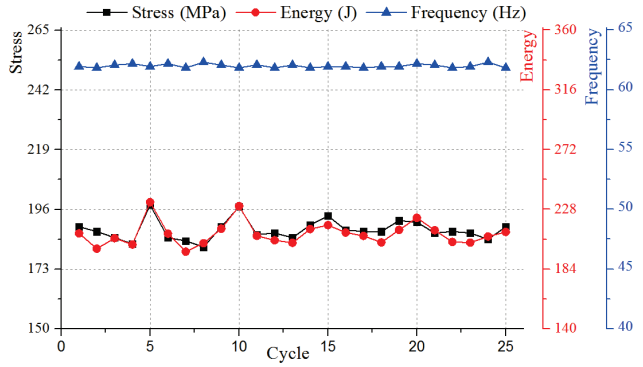



**Figure 12.** Long piston, high gear, 23 MPa.

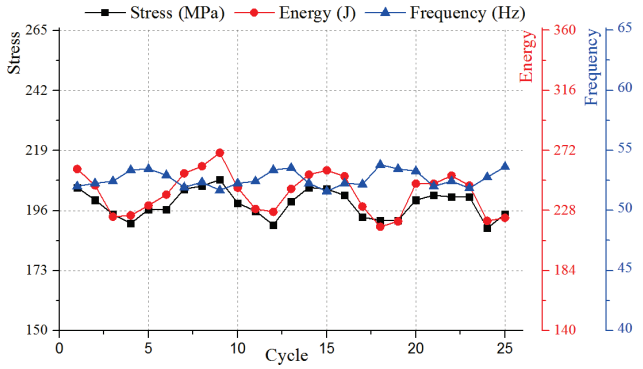



**Figure 13.** Long piston, middle gear, 18 MPa.

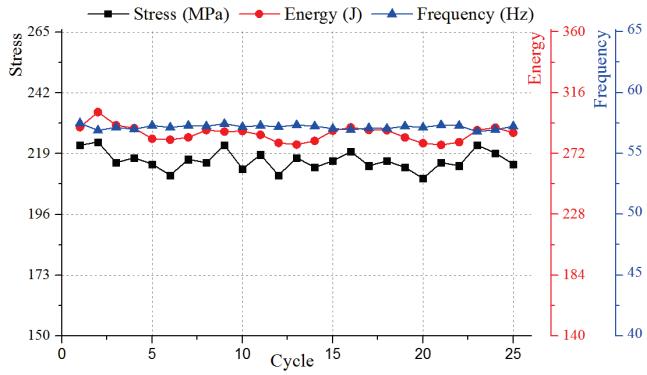



**Figure 14.** Long piston, middle gear, 23 MPa.

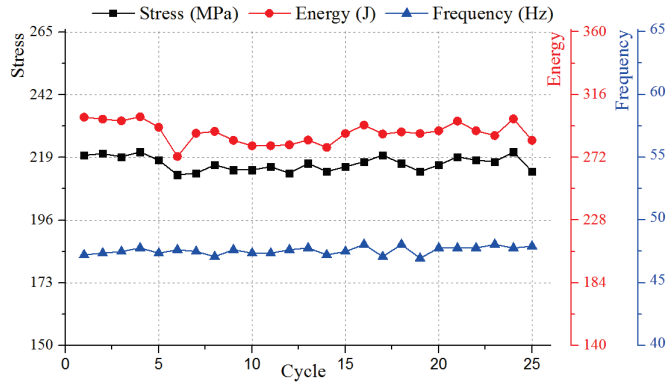



**Figure 15.** Long piston, low gear, 18 MPa.

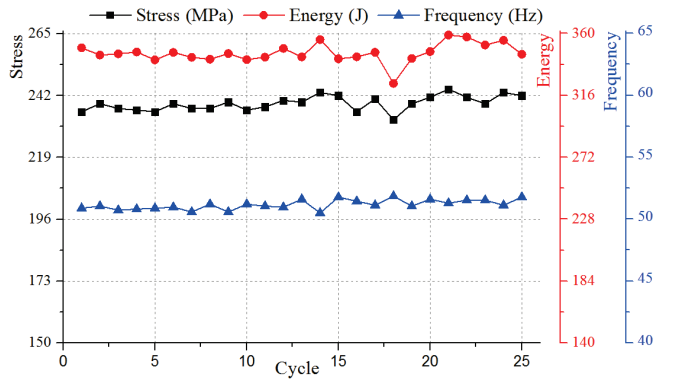



**Figure 16.** Long piston, low gear, 23 MPa.

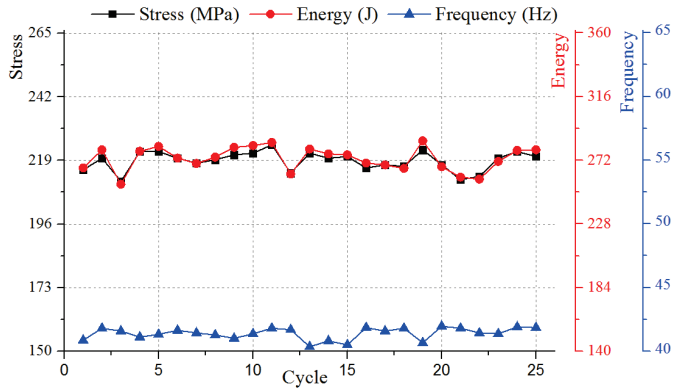



**Figure 17.** Short piston, low gear, 18 MPa.

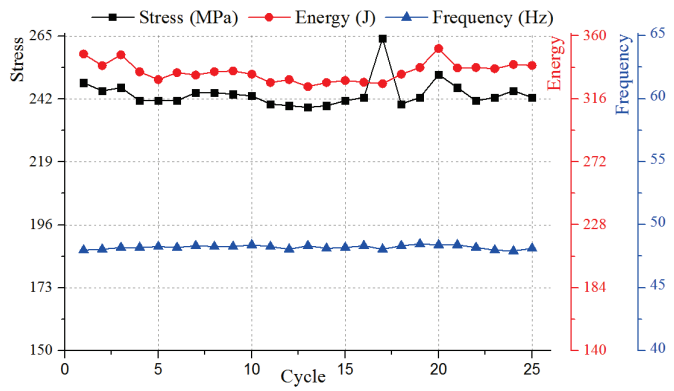



**Figure 18.** Short piston, low gear, 23 MPa.

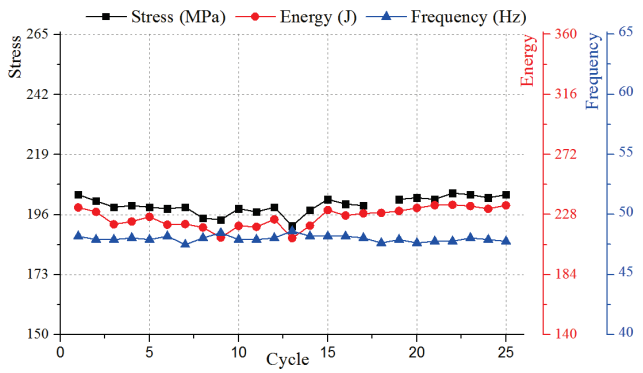



**Figure 19.** Short piston, middle gear, 18 MPa.

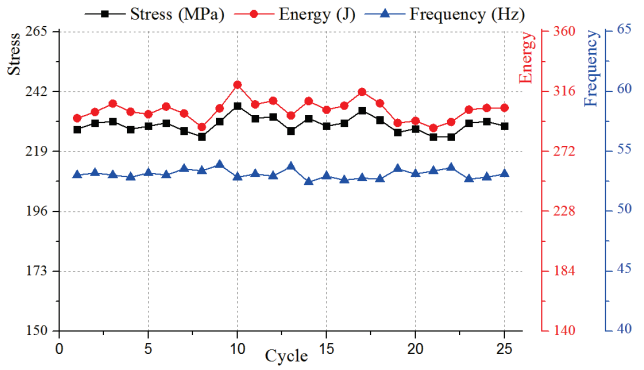



**Figure 20.** Short piston, middle gear, 23 MPa.

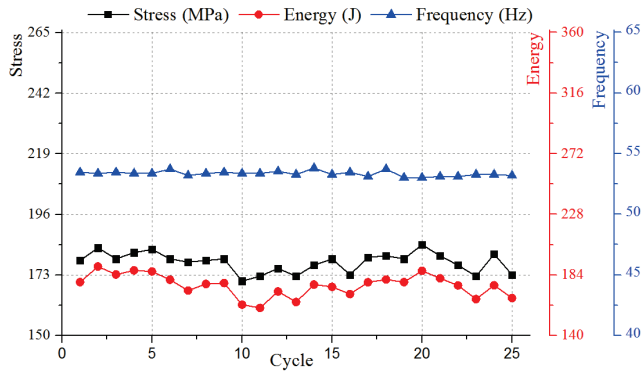



**Figure 21.** Short piston, high gear, 18 MPa.

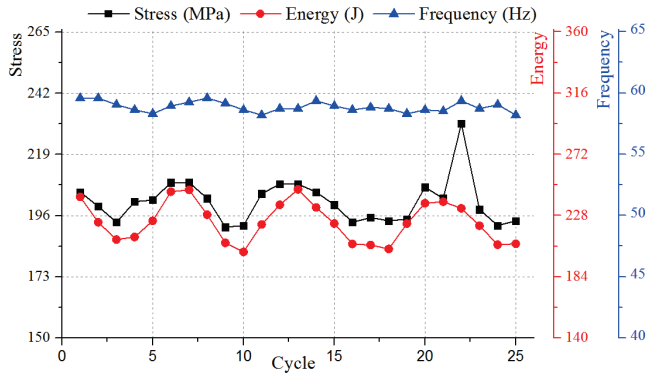



**Figure 22.** Short piston, high gear, 23 MPa.

Comparing the measurement results for the different rock drills in Figures 11–16 and Figures 17–22, for the same piston in the same gear, when the working pressure of the hydraulic rock drill increased, the impact energy and impact frequency of the piston also increased. In the same gear and at the same working pressure, the impact frequency decreased when the piston mass increased; however, the impact energy increased gradually and then decreased. In order to facilitate analysis of the main factors affecting the impact performance of the hydraulic rock drill, this performance was further analyzed according to the change in piston mass and driving conditions.

## 5. Impact Performance Analysis

### *5.1. Impact Performance When Piston Mass Changes*

As shown in Figure 23, for the long piston at 23 MPa and in the low gear, the impact energy was maintained at a high level (with an average of 346.11 J and a maximum of 358.95 J). At 18 MPa and in the high gear, the impact energy was maintained at a low level

(at an average value of 177.98 J and a minimum value of 143.22 J). In particular, the output impact energy fluctuated greatly. The impact frequency is shown in Figure 24. At 23 MPa and in the high gear, the impact frequency was maintained at a high state (with an average of 61.99 Hz and a maximum of 62.30 Hz). At 18 MPa and in the low gear, the impact frequency was maintained at a low state (at an average value of 47.56 Hz and a minimum value of 46.95 Hz).

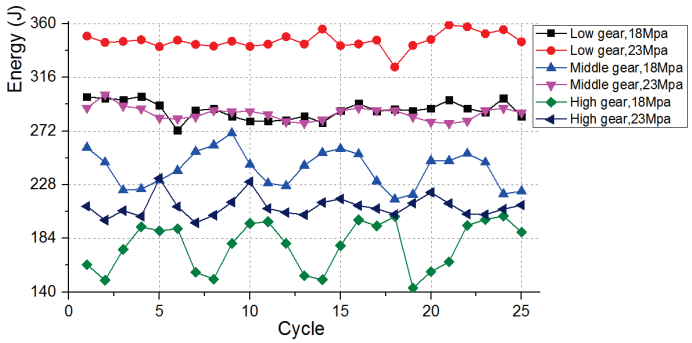



**Figure 23.** Impact energy of long piston.

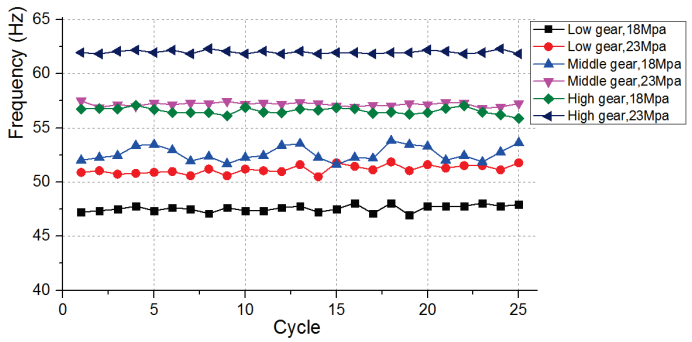



**Figure 24.** Impact frequency of long piston.

For the short piston, as shown in Figure 25, at 23 MPa and in the low gear, the impact energy was maintained at a high level (with an average of 334.97 J and a maximum of 351.19 J). At 18 MPa and in the high gear, the impact energy remained at a low state (at an average value of 176.38 J and a minimum value of 160.01 J). Again, the output impact energy fluctuated greatly. The impact frequency is shown in Figure 26. At 23 MPa and in the high gear, the impact frequency was maintained at a high state (with an average of 58.86 Hz and a maximum of 59.85 Hz). At 18 MPa and in the low gear, the impact frequency was maintained at a low state (at an average value of 41.39 Hz and a minimum value of 40.35 Hz).

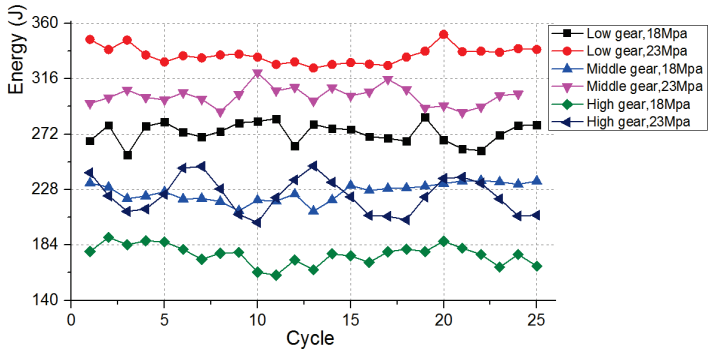



**Figure 25.** Impact energy of short piston.

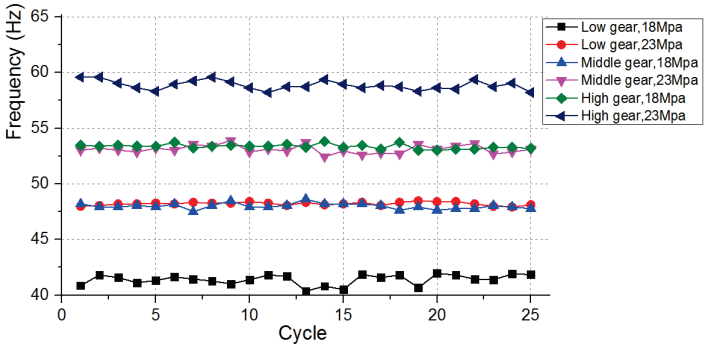



**Figure 26.** Impact frequency of short piston.

Therefore, in terms of impact frequency, that of the long piston was higher than that of the short piston when in the same gear. With an increase in piston mass, the reduction in piston stroke is greater than the reduction in acceleration [10,11], such that the time required for one piston cycle becomes smaller and the impact frequency increases. The impact energy of both pistons in the low gear was greater than that in the high gear; this is because the piston stroke in the low gear is long and the impact speed is high, which causes the impact energy to be high.

Comparing the two pistons of different mass, the impact energy of the long piston in the low gear was greater than that of the short piston in the low gear. This is due to the higher mass of the long piston, as piston mass was the main influencing factor. However, the impact energy of the short piston was greater than that of the long piston when in the high gear, as the piston speed was the main influencing factor in this case. Once the design parameters of the rock drill were fixed, the driving condition of the piston—namely, the working pressure—determined the impact speed.

### *5.2. Impact Performance When Working Pressure Changes*

Figure 27 shows the impact energy in the three gears for both the long and short pistons when the working pressure was 18 MPa. When the long piston was in the low gear, the impact energy always remained high (with an average value of 289.14 J and a maximum value of 300.13 J). When the short piston was in the high gear, the impact energy remained low (at an average value of 176.38 J), while the minimum value occurred when the long piston was in the high gear (with a minimum value of 143.22 J). The output impact energy fluctuated greatly. The impact frequency is shown in Figure 28: when the long piston was in the high gear, the impact frequency was maintained at a high state (with an average of 56.55 Hz and a maximum of 57.09 Hz). When the short piston was in the low gear, the impact frequency was maintained at a low state (at an average value of 41.39 Hz and a minimum value of 40.35 Hz).

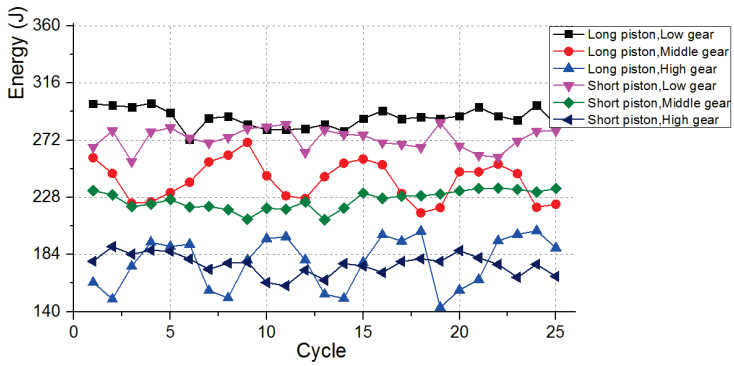



**Figure 27.** Impact energy at 18 MPa.

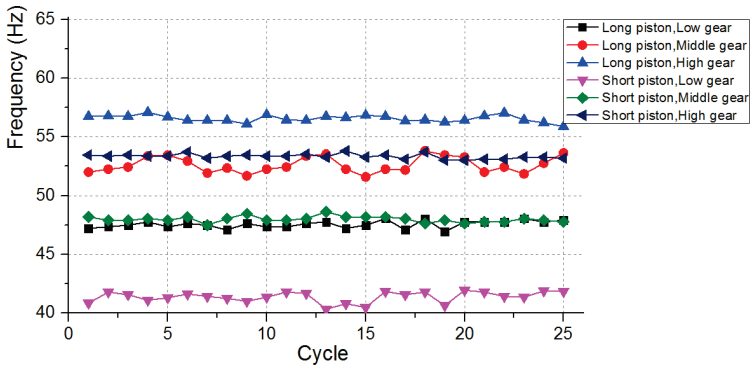



**Figure 28.** Impact frequency at 18 MPa.

Figure 29 shows the impact energy in the three gears, for both the long and short pistons, when the working pressure was 23 MPa. When the long piston was in the low gear, the impact energy always remained high (with an average of 346.11 J and a maximum value of 358.95 J). When the long piston was in the high gear, the impact energy remained at a low state (at an average value of 209.94 J and a minimum value of 196.83 J). Overall, the output impact energy presented a certain fluctuation. The impact frequency is shown in Figure 30. When the long piston was in the high gear, the impact frequency was maintained at a high state (with an average of 61.99 Hz and a maximum of 62.3 Hz). When the short piston was in the low gear, the impact frequency was maintained at a low state (at an average value of 48.21 Hz and a minimum value of 47.91 Hz).

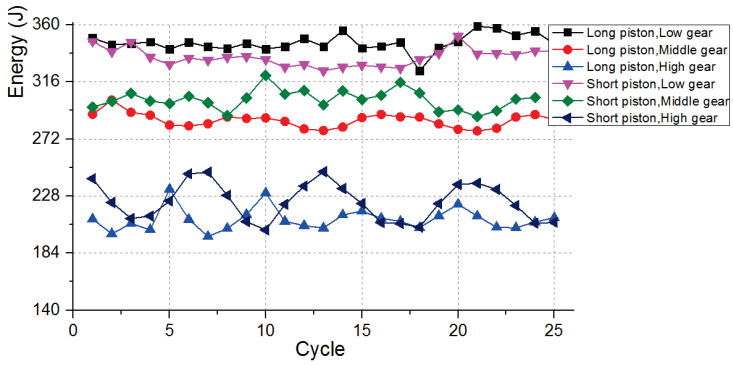



**Figure 29.** Impact energy at 23 MPa.

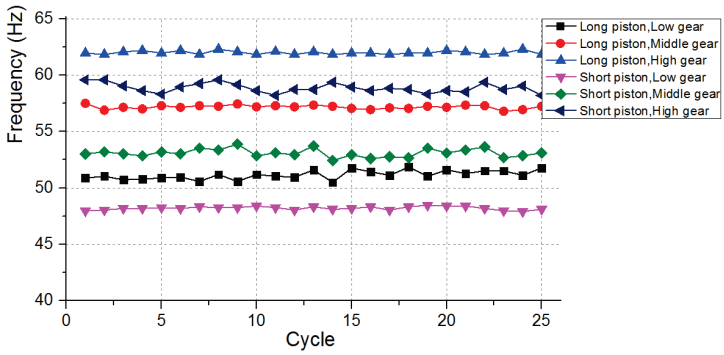



**Figure 30.** Impact frequency at 23 MPa.

Therefore, considering impact frequency and impact energy, when both pistons work in any gear, the impact frequency and impact energy at a working pressure of 23 MPa were greater than those at 18 MPa. As such, increasing the working pressure can improve the impact frequency and impact energy of a rock drill.

Comparing the working pressures of 18 MPa and 23 MPa, when the working pressure was 18 MPa, the impact energy of the long piston in the low and middle gears was greater than that of the short piston. In this case, the piston mass was the main factor affecting the impact energy. When the working pressure was 23 MPa, the impact energy of the short piston was greater than that of the long piston. In this case, the main factor affecting the impact energy was the working pressure of the driving piston. Therefore, when the working pressure of the liquid medium in the hydraulic rock drill is adjustable, it is advisable to select a piston with a smaller mass and a higher working pressure. The hydraulic rock drill can then achieve a high impact energy and frequency.

### *5.3. Energy Utilization Rate*

Analysis of the energy utilization rate is of great significance for the development of rock drills with good impact performance. The energy utilization rate of the hydraulic rock drill was obtained by combining the impact energy and impact frequency results for the drill. The impact power and energy utilization rates of the hydraulic rock drill are calculated as follows [31–33]:

$$P_i = 10^{-3} \cdot E \cdot f \tag{9}$$

$$\eta(\%) = \frac{60P_i}{\Delta pQ} \times 100 \tag{10}$$

where $P_i$ is the impact power, $E$ is the impact energy, $f$ is the impact frequency, $\Delta p$ is the difference between the inlet and outlet oil pressures, and $Q$ is the inlet oil flow. Table 1 provides a comparison of the obtained results.

**Table 1.** Comparison of results.

| Piston | Gear | Pressure (MPa) | Flow (L/min) | Average Stress (MPa) | Average Impact Energy (J) | Average Frequency (Hz) | Power (Kw) | Efficiency (%) |
|---|---|---|---|---|---|---|---|---|
| Long piston | low | 18 | 87.4 | 216.7 | 289.1 | 47.6 | 13.76 | 51.62 |
| | | 23 | 92.0 | 239.1 | 334.9 | 51.2 | 17.72 | 50.25 |
| | middle | 18 | 74.4 | 198.5 | 241.0 | 52.6 | 12.68 | 53.82 |
| | | 23 | 80.1 | 216.4 | 286.4 | 57.2 | 16.38 | 53.35 |
| | high | 18 | 66.2 | 172.1 | 178.0 | 56.6 | 9.90 | 49.85 |
| | | 23 | 70.8 | 188.1 | 209.9 | 62.0 | 13.01 | 47.94 |
| Short piston | low | 18 | 67.5 | 218.8 | 273.1 | 41.4 | 11.31 | 55.85 |
| | | 23 | 78.6 | 243.9 | 346.1 | 48.2 | 16.15 | 53.60 |
| | middle | 18 | 64.6 | 199.7 | 226.0 | 48.0 | 10.85 | 55.99 |
| | | 23 | 73.6 | 229.4 | 302.4 | 53.1 | 16.06 | 56.92 |
| | high | 18 | 55.7 | 177.9 | 176.4 | 53.4 | 9.44 | 56.49 |
| | | 23 | 61.6 | 201.2 | 223.4 | 58.9 | 13.16 | 55.73 |

Table 1 displays the energy utilization rates for the long and short pistons for the considered hydraulic rock drill at different working pressures. Different travel gears were analyzed, and it can be seen that the energy utilization rates in the short piston tests were above 53%, with the maximum value being 56.92%. According to the comparative literature, the hydraulic rock drill designed by Joo Young [23,24], with high pressure (210 bar) and large flow (120 L/min) parameters, obtained a sufficient drilling efficiency and impact force. Nygrena [15,16] concluded that the ideal energy utilization efficiency is close to 60% under very good drilling conditions, but could fall to less than 40% under poor drilling conditions. Our model rock drill, therefore, provides good impact performance. Although the impact power of the long piston was greater than that of the short piston, the energy utilization rate of the short piston was higher than that of the long piston. Therefore, when developing a hydraulic rock drill, a smaller-sized piston should be selected for a higher

working pressure. Our hydraulic rock drill obtained good results, in terms of impact energy, impact frequency, and energy utilization rate.

## 6. Conclusions

The stress wave test bench detailed in this paper can effectively test the impact process of a hydraulic rock drill. Our measurements showed that the stress wave is periodically incident in the drill rod and decays exponentially until it is close to zero; moreover, the amplitude of the incident stress wave determines the rock-breaking ability of the drill. In order to improve the impact performance of hydraulic rock drills, the impact energy, impact frequency, and energy utilization rates of two different pistons in the hydraulic rock drill at working pressures of 18 MPa and 23 MPa were analyzed using a control variable method. It was concluded that the piston characteristics and driving conditions are the main factors affecting the impact performance. In order to obtain a desirable impact performance, once the body size of the hydraulic rock drill has been determined and cannot be changed, it is advisable to develop a smaller-sized piston—taking into consideration the appropriate working pressure and gear for drilling—which will allow the final hydraulic rock drill to provide an optimal impact performance.

**Author Contributions:** Conceptualization, Z.Y.; methodology, G.Y.; investigation, J.L.; resources, Z.Y.; data curation, J.L.; writing—review and editing, Z.Y.; supervision, G.Y.; project administration, G.Y. All authors have read and agreed to the published version of the manuscript.

**Funding:** This research was funded by The Guangdong Marine Economic Development (six major marine industries) Special Project, grant number GDNRC [2021]42, Doctoral Research Start-up Project of Guangdong Ocean University, grant number 060302062103, and the Zhanjiang Key Laboratory of Modern Marine Fishery Equipment, grant number 2021A05023.

**Data Availability Statement:** Data sharing not applicable.

**Conflicts of Interest:** The authors declare no conflict of interest.

## References

1. Long, R.; Sun, S.; Lian, Z. Research on the hard-rock breaking mechanism of hydraulic drilling impact tunneling. *Math. Probl. Eng.* **2015**, *16*, 153648. [CrossRef]
2. Ma, W.; Geng, X.; Jia, C.; Gao, L.; Liu, Y.; Tian, X. Percussion characteristic analysis for hydraulic rock drill with no constant-pressurized chamber through numerical simulation and experiment. *Adv. Mech. Eng.* **2019**, *4*. [CrossRef]
3. Li, Y. Research on the matching of impact performance and collision coefficient of hydraulic rock drill. *Shock Vib.* **2021**, *2021*, 6651860. [CrossRef]
4. Seo, J.; Noh, D.K.; Lee, G.H.; Jang, J.S. A percussion performance analysis for rock-drill drifter through simulation modeling and experimental validation. *Int. J. Precis. Eng. Man.* **2016**, *17*, 163–170. [CrossRef]
5. Giuffrida, A.; Laforgia, D. Modelling and Simulation of a Hydraulic Breaker. *Int. J. Fluid Power* **2005**, *6*, 47–56. [CrossRef]
6. Song, C.; Chung, J.; Kim, J.H.; Oh, J.Y. Design optimization of a drifter using the taguchi method for efficient percussion drilling. *J. Mech. Sci. Technol.* **2017**, *31*, 1797–1803. [CrossRef]
7. Song, C.H.; Kwon, K.B.; Cho, M.G.; Oh, J.Y.; Shin, D.Y.; Cho, J.W. Development of lab-scale rock drill apparatus for testing performance of a drill bit. *Int. J. Precis. Eng. Man.* **2015**, *16*, 1405–1414. [CrossRef]
8. Hu, Q.; Yang, C.; Zheng, H.; Chen, M. Dynamic simulation and test research of impact performance of hydraulic rock drill with no constant-pressurized chamber. *Automat. Constr.* **2014**, *37*, 211–216. [CrossRef]
9. Yang, S.Y.; Ou, Y.B.; Guo, Y.; Wu, X.M. Analysis and optimization of the working parameters of the impact mechanism of hydraulic rock drill based on a numerical simulation. *Int. J. Precis. Eng. Man.* **2017**, *18*, 971–977. [CrossRef]
10. Yang, Z.Y.; Ji, H.; Li, Y.G. Analysis on the main design parameters influencing the impact efficiency of dual-chamber-controlled hydraulic drifter. *Int. J. Precis. Eng. Man.* **2018**, *19*, 1781–1791. [CrossRef]
11. Yang, Z.Y.; Ji, H.; Li, Y.G. Existence scope of only primary vibration within one impact period of a hydraulic drifter piston via point transformation. *J. Adv. Mech. Des. Syst.* **2018**, *12*, JAMDSM0123. [CrossRef]
12. Ficarella, A.; Giuffrida, A.; Laforgia, D. Numerical investigations on the working cycle of a hydraulic breaker: Off-design performance and influence of design parameters. *Int. J. Fluid Power* **2006**, *7*, 41–50. [CrossRef]
13. Dutta, P.K. The determination of stress wave forms produced by percussive drill pistons of various geometrical designs. *Int. J. Rock Mech. Min.* **1968**, *5*, 501–510. [CrossRef]
14. Changming, W. An analytical study of percussive energy transfer in hydraulic rock drills. *Min. Sci. Technol.* **1991**, *13*, 57–68. [CrossRef]

15. Nygren, T.; Andersson, L.E.; Lundberg, B. Optimization of elastic junctions with regard to transmission of wave energy. *Wave Motion* **2001**, *240*, 467–481. [CrossRef]
16. Nygren, T.; Andersson, L.E.; Lundberg, B. Synthesis of elastic junctions with wave transmission properties of a given junction. *Wave Motion* **1999**, *30*, 143–158. [CrossRef]
17. Lundberg, B.; Okrouhlik, M. Efficiency of a percussive rock drilling process with consideration of wave energy radiation into the rock. *Int. J. Impact. Eng.* **2006**, *32*, 1573–1583. [CrossRef]
18. Chiang, L.E.; Elas, D.A. Modeling impact in down-the-hole rock drilling. *Int. J. Rock Mech. Min.* **2000**, *37*, 599–613. [CrossRef]
19. Kahraman, S.A.İ.R.; Bilgin, N.; Feridunoglu, C. Dominant rock properties affecting the penetration rate of percussive drills. *Int. J. Rock Mech. Min.* **2003**, *40*, 711–723. [CrossRef]
20. Li, X.; Rupert, G.; Summers, D.A.; Santi, P.; Liu, D. Analysis of impact hammer rebound to estimate rock drill ability. *Rock Mech. Rock Eng.* **2000**, *33*, 1–13. [CrossRef]
21. Zhang, K.; Hou, R.; Zhang, G.; Zhang, G.; Zhang, H. Rock drillability assessment and lithology classification based on the operating parameters of a drifter: Case study in a coal mine in China. *Rock Mech. Rock Eng.* **2016**, *49*, 329–334. [CrossRef]
22. Arffman, A.; Marjamäki, M.; Keskinen, J. Simulation of low pressure impactor collection efficiency curves. *J. Aerosol Sci.* **2011**, *42*, 329–340. [CrossRef]
23. Oh, J.Y.; Lee, G.H.; Kang, H.S.; Song, C.S. Modeling and performance analysis of rock drill drifters for rock stiffness. *Int. J. Precis. Eng. Man.* **2012**, *13*, 2187–2193. [CrossRef]
24. Oh, J.Y.; Song, C.H.; Kim, D.J.; Kim, J.G.; Park, J.Y.; Cho, J.W. Numerical investigation of performance of hydraulic percussion drifter. *Int. J. Precis. Eng. Man.* **2016**, *17*, 879–885. [CrossRef]
25. *DD ISO/TS 17104-2006*; Rotary Tool for Threaded Fasteners-Hydraulic Impulse Tools-Performance Test Method. ISO: Geneva, Switzerland, 2006.
26. *DD ISO 2787-1984*; Rotary and Percussive Pneumatic Tools-Performance Tests. ISO: Geneva, Switzerland, 1984.
27. Babitsky, V. Dynamics should be sexy. In *On the Waves of a Pulsating World*, 1st ed.; Gruzenberg, A., Ed.; Springer: Cham, Switzerland, 2019; pp. 119–123.
28. Sun, F.; Chen, L.; Li, Y.; Wang, Z.; Xiao, B.; Chen, Z. Fidelity performance of coring bits during drilling and cutting in deep extreme environments. *Appl. Sci.* **2023**, *13*, 8173. [CrossRef]
29. Zhao, T.W. Wave theory analysis of impact drilling process. In *Dynamics of Percussive Drilling*; Qing, Q.Y., Ed.; Metallurgical Industry Press: Beijing, China, 1996; pp. 99–116.
30. Zhao, T.W. Testing the impact performance of rock drill. In *Dynamics of Percussive Drilling*; Qing, Q.Y., Ed.; Metallurgical Industry Press: Beijing, China, 1996; pp. 203–213.
31. Song, H.; Shi, H.; Li, G. Numerical simulation of the energy transfer efficiency and rock damage in axial-torsional coupled percussive drilling. *J. Petrol. Sci. Eng.* **2021**, *196*, 107675. [CrossRef]
32. Song, H.; Shi, H.; Chen, Z.; Li, G.; Chen, H. Numerical study on impact energy transfer and rock damage mechanism in percussive drilling based on high temperature hard rocks. *Geothermics* **2021**, *96*, 102215. [CrossRef]
33. Hashiba, K.; Fukui, K.; Liang, Y.Z.; Koizumi, M.; Matsuda, T. Force-penetration curves of a button bit generated during impact penetration into rock. *Int. J. Impact Eng.* **2015**, *85*, 45–56. [CrossRef]


**Disclaimer/Publisher's Note:** The statements, opinions and data contained in all publications are solely those of the individual author(s) and contributor(s) and not of MDPI and/or the editor(s). MDPI and/or the editor(s) disclaim responsibility for any injury to people or property resulting from any ideas, methods, instructions or products referred to in the content.

machines

MDPI

*Article*

# New Method for Precise Measurement of Clamping Plate Deformations on Forming Presses

**Georg Ivanov [1], Thomas Burkhardt [1], Lars Penter [2] and Steffen Ihlenfeldt [2,*]**

[1] ICM—Institute for Mechanical and Plant Engineering Chemnitz e.V., Otto-Schmerbach-Straße 19, 09117 Chemnitz, Germany; g.ivanov@icm-chemnitz.de (G.I.); t.burkhardt@icm-chemnitz.de (T.B.)
[2] Machine Tool Development and Adaptive Controls, Institute of Mechatronic Engineering, TUD Dresden University of Technology, Helmholtzstraße 7a, 01069 Dresden, Germany; lars.penter@tu-dresden.de
* Correspondence: steffen.ihlenfeldt@tu-dresden.de

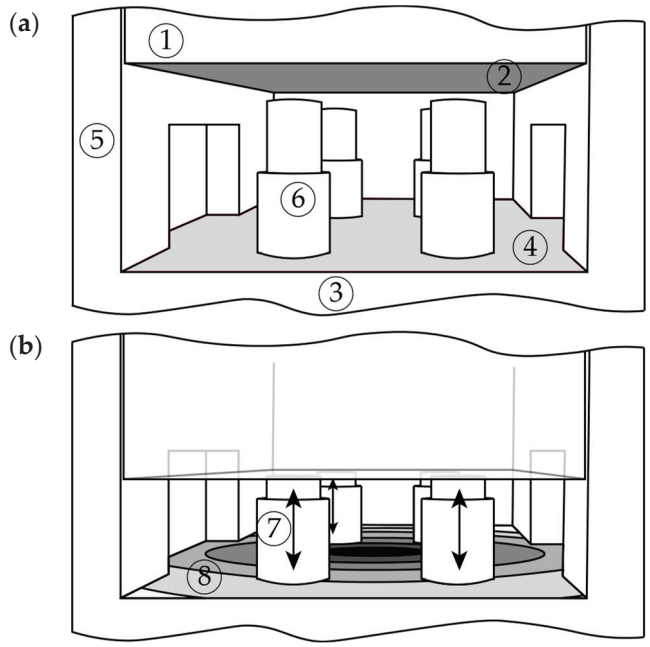
**Abstract:** The deformation of press bolster plates under load can significantly impact the quality of manufactured workpieces. Consequently, press manufacturers are usually obliged to provide the metric proof of the permissible deformation values during the press commissioning process. Unfortunately, the existing measurement methods for determining bolster plate deformations present flaws in the measurement accuracy, the application flexibility, the metrological effort, and other aspects. These issues have been addressed through the development of a new measurement method using multiple inclination profiles on the surface of the measured object. Based on the difference in the inclination between the unloaded and loaded states, the method approximates the inclination surface and calculates the deformation of the measured object through integration. The measurement method was first used for commissioning tests of forming presses. A comparison with the results obtained with a measurement frame equipped with high-resolution measurement probes demonstrates an accuracy of the new method of less than 20 µm.

**Keywords:** deformation measurement; local inclination; machine tool; press commissioning; press clamping plates

## 1. Introduction

The experimental characterization of machine tools plays an increasingly important role in quality assurance, process design, and predictive maintenance. This article focuses on the experimental determination of static deformations in machine tools using the example of forming presses. A novel measurement method is presented for determining deformations and deflections in machine tool assemblies based on locally measured inclination signals. In this paper, it is initially demonstrated that this method achieves a similar or even higher measurement accuracy compared to previous methods, with the potential for increased application flexibility, reduced metrological effort, and other positive effects.

In the case of deformation measurements, particularly in forming presses, the determination of bolster plate deformations under load is usually of primary interest. Figure 1 depicts a schematic representation of a press working area and a loading device consisting of multiple load cylinders. In Figure 1a, the press is shown in an unloaded state. Figure 1b illustrates the ram in the bottom dead center (BDC), with both the bolster plate and the ram plate subjected to a loading force applied by the load cylinders. Both plates deform due to this loading force.




1. press ram; 2. ram plate; 3. press bolster; 4. bolster plate; 5. press frame; 6. load device; 7. load device under pressure; 8. deformed bolster plate under load.

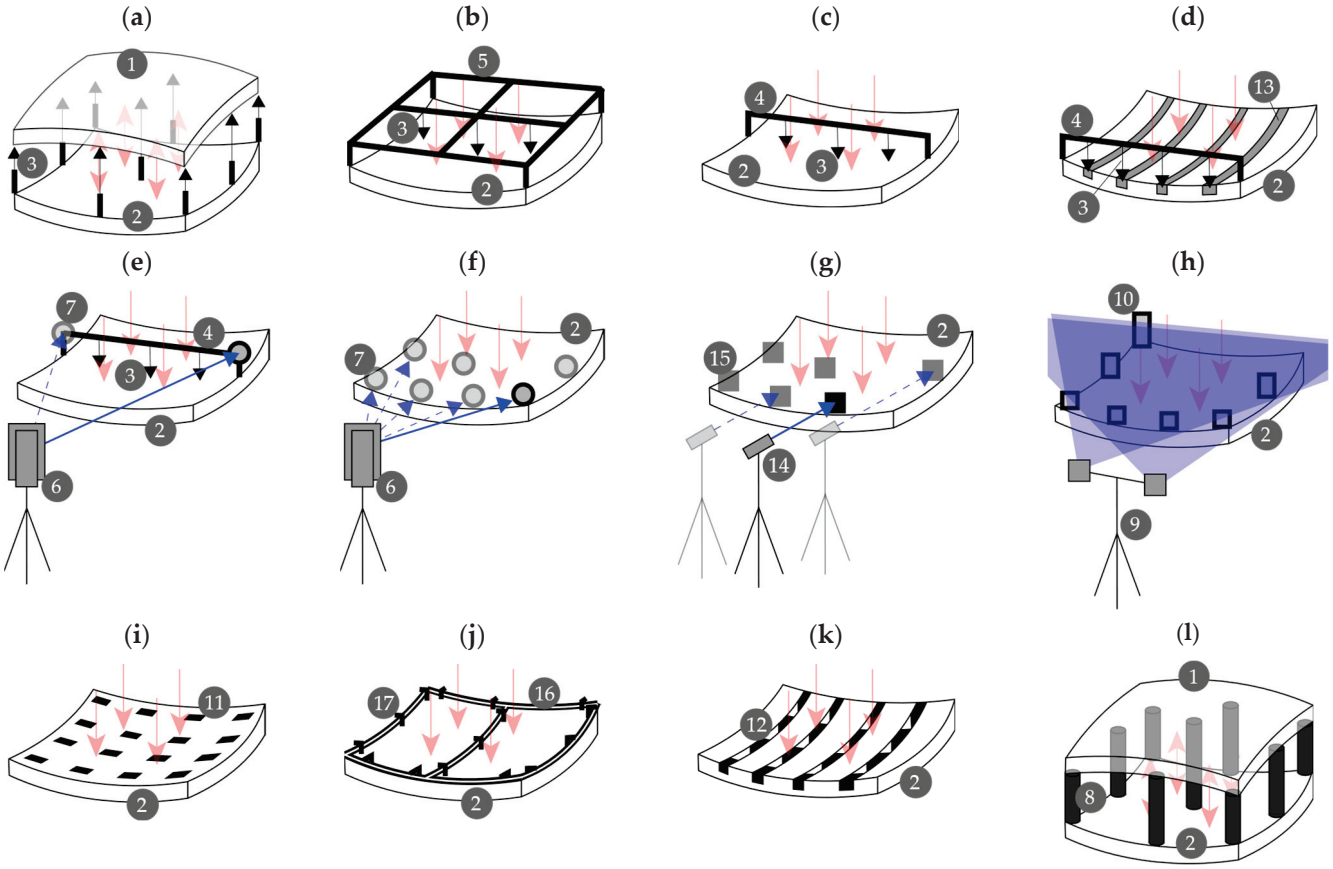
**Figure 1.** Press workspace with load device: (**a**) press workspace without load and press ram in upper position; and (**b**) press under load with ram in bottom dead center (BDC) and deformed bolster plates.

One simple measurement method to capture these deformations involves placing displacement sensors (e.g., dial gauges) on freestanding measurement stands within the press working space, as described in [1,2]—see Figure 2a. However, this approach has several disadvantages. Firstly, it only allows for the measurement of overall deformations of the table and ram bolster plates without the ability to assign deformation values to one of the two bolster plates. Secondly, the method introduces measurement errors caused by the inclination of the freestanding sensors due to the deflection of the table and the ram bolster plates, resulting in angular errors.

These problems have been addressed by using measuring frames [3–7] or measuring bars [8–10] equipped with displacement sensors. However, the measurement frames (Figure 2b) and bars (Figure 2c) have disadvantages such as low flexibility, a high setup effort, and their mounting points do not align with the corners of the press table in most cases, even in modular systems. As a result, the setups experience displacement in the z direction due to a bolster plate deformation, which distorts the measurement. Tehel addresses the issue of support point displacement during bolster plate deformations by employing an additional laser tracker measurement at the support locations of a measurement bar [8]—see Figure 2e. The method appears labor-intensive since the laser tracker can only measure the displacement of a single target at a time. The accuracy may be compromised due to a lack of synchronization between the measurement techniques (i.e., the measuring bars and laser tracker). Moreover, support structures like measurement frames and bars have a tendency toward oscillation during the dynamic load introduction, making reliable and accurate data analysis challenging—see, for example, the measurement results in [4,11].

Struck also uses measuring bars, which are mounted in the T-slots of the bolster plate and which use eddy current sensors to measure the change in distance of the measuring bar from the T-slot base at various points in the T-slots [6]. Struck also performs a second measurement to determine the self-displacement of the measuring bars as the table deforms. To do this, he uses additional measuring bars at 90° to the T-slots, located in the corners of the bolster plate (Figure 2d). Based on this arrangement, the displacements of the T-slot bars are measured at their outer edges using precision probes. This method seems labor-intensive to implement. The self-displacement of the additional measurement bars cannot be securely ruled out, as their support points may not necessarily be in the table corners

when the table dimensions vary. Another disadvantage is the considerable effort required for the material-specific calibration of each eddy current sensor to the corresponding measurement object (i.e., the bolster plate).




1. Ram plate; 2. bolster plate; 3. displacement sensor; 4. measuring bar; 5. measuring frame; 6. laser tracker; 7. target; 8. compression specimen; 9. stereo camera; 10. marker; 11. strain gauge; 12. T-slot sensor; 13. T-slot measuring bar; 14. laser; 15. PSD sensor; 16. measuring bar with optical fiber Bragg sensor; 17. clamping element.

**Figure 2.** State of the art measuring methods for detecting clamping plate deformation in presses (red arrows represent load force). (**a**) Freestanding sensors; (**b**) measuring frame with displacement sensors; (**c**) measuring bar with displacement sensors; (**d**) T-slot measuring bar with eddy current sensors and additional measuring bar; (**e**) measuring bar with displacement sensors and additional laser tracker measurement; (**f**) laser tracker with targets; (**g**) laser—PSD combination; (**h**) stereo camera with markers; (**i**) strain gauges on clamping plate; (**j**) measuring bar with strain gauges or optic fiber sensor; (**k**) T-slot sensors; (**l**) compression specimens.

Optical measurement methods with external references, based on laser trackers [12–15] (Figure 2f), laser–PSD combinations [16] (Figure 2g), or stereo camera systems [9,11,17–24] (Figure 2h), have also been used for the determination of bolster plate deformations.

Laser trackers capture the movements of measurement targets mounted on the press clamping plate. By design, these systems only capture the motion of a single target per measurement. In deformation measurements with many targets, a larger number of individual measurements must be conducted, requiring a separate ram stroke with the machine for each. Laser PSD (Position Sensitive Detector) applications also rely on a laser positioned in front of the machine, but the displacement measurement of the individual measurement points is carried out by PSD sensors positioned inside the machine (alternatively, CCD sensors or similar can be used). Again, multiple unsynchronized individual measurements must be performed in this case as well.

For the evaluation of stereo camera recordings, various methods are employed, including stereoscopy [11,18,19,22–24] and the Digital Image Correlation (DIC) method [9,20,21]. The DIC method is becoming an increasingly important measurement method for deformation measurements. A comprehensive overview of DIC methods for capturing surface deformations up to 2018 is provided in [25]. Some recent contributions can be found in [23–31]. Due to the restricted visibility of the press working area, identifying the deformation measurement directly on the clamping plates' surface is not feasible. Therefore, reflective markers must be used in both methods, distributed across the clamping plate. The displacement measurement of the markers, unlike with the laser tracker and laser PSD applications, is synchronized for all markers. However, Pilthammar indicates that, for a sufficiently accurate image evaluation using the DIC method, several individual measurements have to be performed, with each measurement capturing the deformation of a quarter of the clamping plate [9]. A resolution of the deformation measurement of only 0.1 mm was achieved. Müller utilized classical stereoscopy for image evaluation and reported similarly low resolutions for the deformation measurement using a single stereo camera system (0.2 mm) [18]. Further improvement in accuracy was achieved through the use of two synchronized stereo cameras. Salfeld specifies a measurement accuracy of 25 µm for this setup [32]. However, these approaches have the disadvantages of a high setup effort and high acquisition costs, with the base version of a suitable stereo camera system costing around EUR 70,000 and a suitable laser tracker costing at least EUR 100,000. Overall, optical measurement methods with external references are not optimal for determining bolster plate deformations on forming presses.

Another optical measurement method is based on optical fiber sensors integrated into specially designed measurement beams [9,33]—see Figure 2j. The beams are securely connected to the clamping plate through specially designed clamping elements, allowing them to follow its deformation under load. While Pilthammar provides good correlation coefficients for a comparison with the stereo camera measurements (based on the DIC method) in his latest publication, the resolution of the DIC approach is only stated as 0.1 mm. Therefore, the measurement accuracy of the new method is not yet precisely known and must be assumed to be 0.1 mm.

Another indirect measurement method is based on strain measurements and the calculation of deformations using an analytical deformation model. The strain measurements can be performed either directly on the measurement object (Figure 2i) [18] or on a measurement beam firmly connected to the clamping plate [9]—see Figure 2j. The method only provides coarse measurement results in the range of 0.15 mm [9]. Furthermore, it is unclear how the decision is made regarding which polynomial degree is assigned to the underlying polynomial model to represent the real deformation. From conversations with press manufacturers, another basic method is known, which involves placing compression specimens within the working area (Figure 2l). Upon plastic deformation of the specimens by the machine, they are individually measured, and the height changes are used to calculate the overall deformation. Disadvantages include the limitation of only measuring overall deformations, a high inaccuracy due to the elastic springback of the compression specimens and their support structure, and a significant time expenditure.

Other approaches for the in-process measurement of bolster plate deformations are based on strain gauge- and piezo-based sensors for the measurement of width changes of T-slots under load [12,34,35] (Figure 2k), as well as novel clamping systems for forming tools [36,37] where the deformation of the clamping devices themselves is used to infer the bolster plate deformation. However, the calculation of absolute deformation values from the measurement data of both systems can currently only be achieved through prior calibration measurements using established measurement methods.

The main disadvantages of previous measurement methods for capturing clamping plate deformations in forming presses can be summarized as follows:

- Accuracy: low resolution/coarse results;
- Flexibility: inflexibility for varying machine dimensions;

- Effectivity: only overall deformations; limited visibility of the clamping plate;
- Effort: time-consuming setup, many measurements, and calibration measurement;
- Costs: expensive equipment; execution only by highly qualified staff.

Figure 3 shows an evaluation of the previously used measurement methods based on the criteria mentioned above. The evaluation is based on our own professional judgment and is to be understood qualitatively. It becomes evident that existing measurement methods are not suitable in all aspects for the specific requirements in capturing clamping plate deformations in forming presses. This article addresses these limitations by introducing a new measurement approach based on local inclination measurements. As Figure 3 illustrates, the authors succeed in improving the experimental measurement of clamping plate deformations in all aspects. In comparison to previous measurement techniques, the new measurement method combines high accuracy with high efficiency in capturing separate deformations on the bolster and ram plate, as well as maximum flexibility for various workspace dimensions. The method offers straightforward handling, and the required metrological equipment is comparatively affordable. Potential users include press manufacturers, forming tool manufacturers, and press operators.

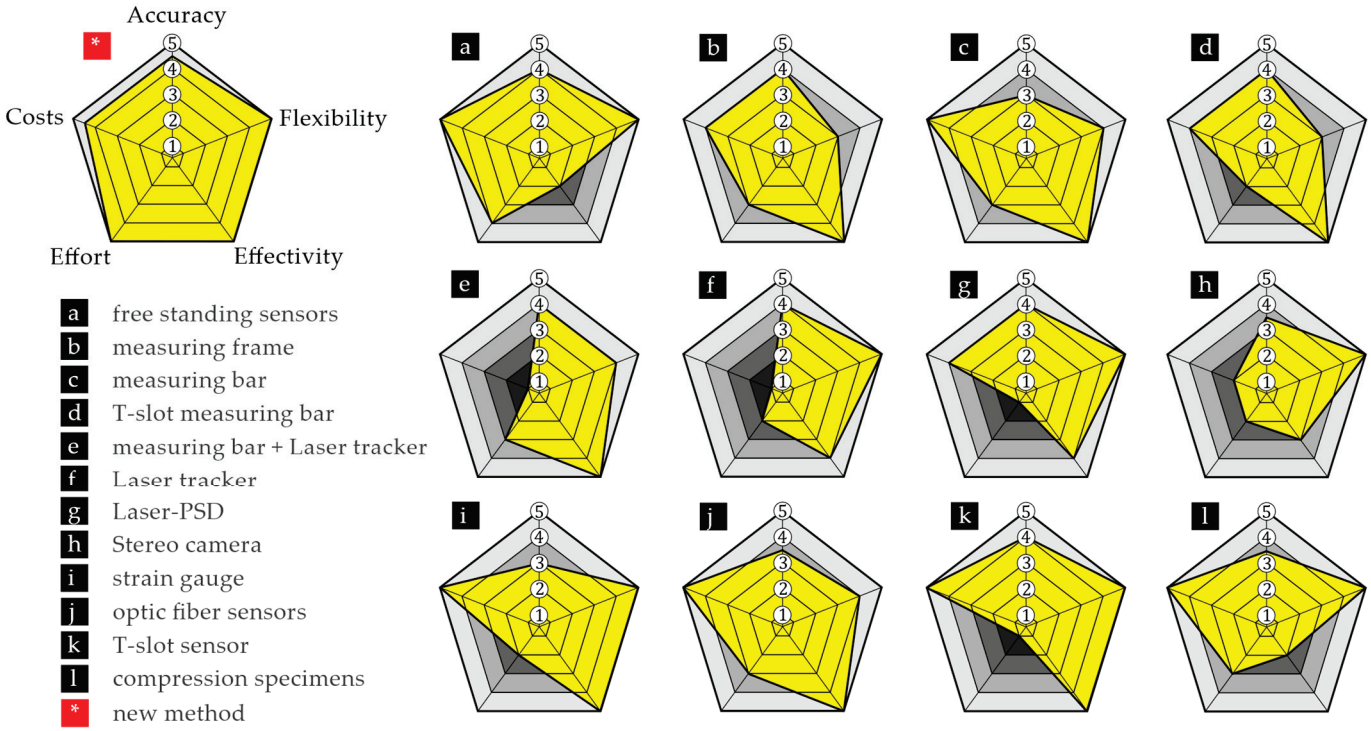



**Figure 3.** Evaluation of previous measurement methods for capturing clamping plate deformations. Rating legend: 1—insufficient, 2—sufficient, 3—satisfactory, 4—good, 5—very good.

Most existing contributions on inclination-based deformation measurements primarily deal with the analysis and monitoring of structures such as buildings or geotechnical systems and do not specifically address the experimental analysis of machine tools. Furthermore, none of the previous studies anticipate the results presented here from a methodological perspective. Some representative contributions can be found in [38–42].

## 2. Development and Testing of an Inclination-Based Deformation Measuring Method

The following work is organized in two parts: a theoretical investigation followed by an experimental validation. Initially, a method to determine two-dimensional deformations on a 2D bending beam is considered, examining the effects of the measurement point number and positioning. Subsequently, the method was expanded to measure three-dimensional deformations and to conduct theoretical functional testing. To experimentally

validate the three-dimensional measurement method, measurements are first performed on a test object in a laboratory setting. Subsequently, comparative measurements are conducted using a measurement framework and precision probes to authenticate the results. In the second stage of validation, the deformation of the bolster plate is recorded on an industrial machine during press commissioning at a press manufacturer. Again, comparative measurements are conducted using a measurement frame equipped with several precision probes.

### *2.1. Development and Theoretical Testing*

#### 2.1.1. Approach for Two-Dimensional Measurements

This measurement method is based on inclination sensors arranged on a measurement object—see Figure 4. The approach uses two inclination values at each x position of the measurement object, in both its unloaded (1) and loaded state (2)—see Equation (1). The difference in inclination between the unloaded state $\alpha_{unload}(x)$ and the loaded state $\alpha_{load}(x)$ of the measurement object is then calculated to $\alpha(x)$ and plotted against $x$ (3). A Matlab® internal spline fitting function is then used to approximate the overall trend of the inclination differences (4).

$$\alpha(x) = \alpha_{unload}(x) - \alpha_{load}(x) \tag{1}$$

$$z(x) = \int \alpha_{Approx}(x)\, dx \tag{2}$$

Finally, the numerical integration of the approximation function $\alpha_{Approx}(x)$ along the length of the measurement object results in the deformation curve of the measurement object under load $z(x)$ (5)—see Equation (2).

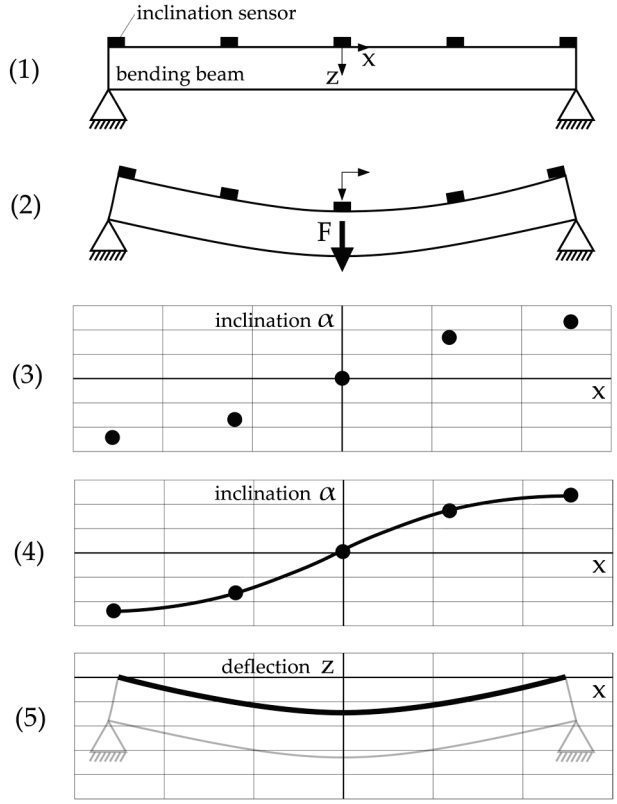



**Figure 4.** Approach for two-dimensional inclination-based deformation measurement: (**1**) unloaded object; (**2**) fully loaded object; (**3**) inclination differences between unloaded and loaded states; (**4**) approximation of inclination values; (**5**) numerical integration of inclination approximation.

2.1.2. Theoretical Analysis of the Example of a Two-Dimensional Bending Beam

The measurement method was first subjected to a basic theoretical functional test on the 2D bending beam. The aim of this first investigation was, on the one hand, to provide a simple theoretical proof of function for the inclination-based measurement method. On the other hand, the sensitivity of the measurement result to the number of measurement points and the positioning of the measurement points should be fundamentally analyzed. Figure 5 shows the boundary conditions used in this analysis.

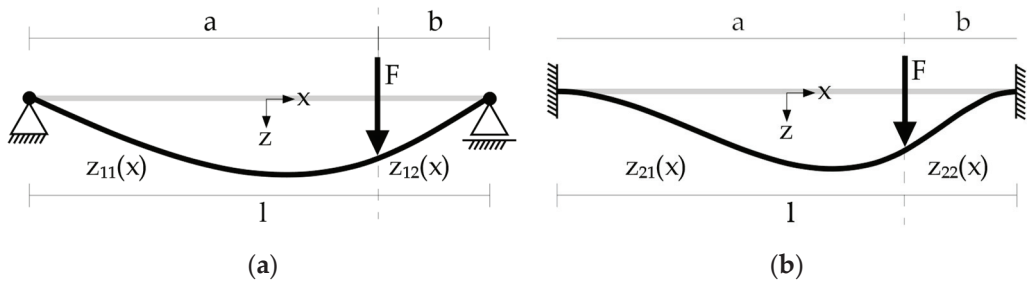



**Figure 5.** Parameters and boundary conditions on the 2D bending beam for different support conditions (a and b represent the distances from the bearing points to the point of force application) (**a**) both sides with loose bearings; and (**b**) both sides with fixed clamping.

Two bending curve approaches were considered: a bending curve with support on both sides with loose bearings (beam (a), Equations (3) and (4)), and a bending curve with support on both sides with fixed clamping (beam (b), Equations (5) and (6)). $z_{11}(x)$ and $z_{21}(x)$ represent the deformations of the bending beams from their left end to the position of the applied load force, while $z_{12}(x)$ and $z_{22}(x)$ represent the deformations from the load position to the right end of the beam.

Here, $l$ is the length of the bending beam, $a$ is the distance of the applied load force from the left end of the beam, and $b$ is the difference between the beam length $l$ and the distance $a$.

$$z_{11}(x) = \frac{b}{6 \cdot l} \cdot \left( l^2 \cdot x - b^2 \cdot x - x^3 \right), -\frac{l}{2} \leq x < 0 \tag{3}$$

$$z_{12}(x) = \frac{b}{6 \cdot l} \cdot \left( \frac{l}{b} \cdot (x-a)^3 + \left( l^2 - b^2 \right) \cdot x - x^3 \right), \; 0 \leq x \leq \frac{l}{2} \tag{4}$$

$$z_{21}(x) = \frac{b^2}{6 \cdot (a+b)^3} \cdot (3 \cdot a \cdot (a+b) - x \cdot (3 \cdot a + b)) \cdot x^2, -\frac{l}{2} \leq x < 0 \tag{5}$$

$$z_{22}(x) = \frac{a^2}{6 \cdot (a+b)^3} (a \cdot (a+b) - x \cdot (3 \cdot b + a)) \cdot (a+b-x)^2, \; 0 \leq x \leq \frac{l}{2} \tag{6}$$

The results of the theoretical preliminary investigations in the 2D space are shown in Figures 5 and 6. Starting from the theoretical Equations (1)–(4), the bending curve profiles were first calculated for both support situations. The accuracy of the measurement methods presented is theoretically independent of the length and the maximum deflection of the bending beam. Therefore, the values for load force F, elasticity modulus E, and moment of inertia Iy were set to 1, and the bending curve profiles were normalized for this initial qualitative investigation. The derivation of the equations yields the inclination curves over the bending curve length—see Equation (7).

$$\alpha_{ij}(x) = \frac{d}{dx} z_{ij}(x) \tag{7}$$

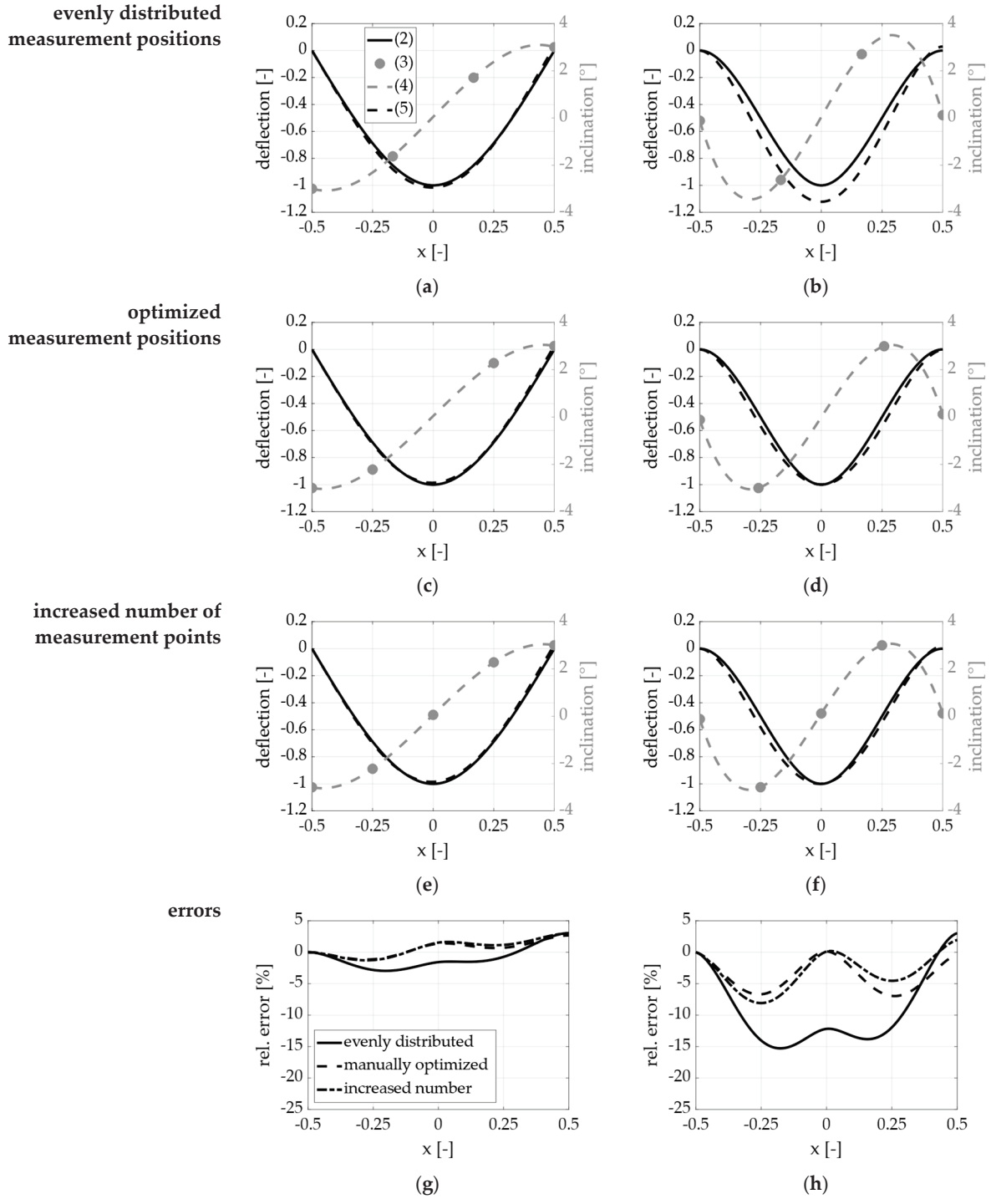



**Figure 6.** Results of theoretical investigations on the 2D bending beam under central loading: (**a**) evenly distributed measurement positions—beam a; (**b**) evenly distributed measurement positions—beam b; (**c**) manually optimized measurement positions—beam a; (**d**) manually optimized measurement positions—beam b; (**e**) increased number of measurement points—beam a; (**f**) increased number of measurement points—beam b; (**g**) relative error curves—beam a; and (**h**) relative error curves—beam b.

Now, the task was to reconstruct the original bending curve out of just a few local inclination values at different *x* positions. The theoretical inclination measurements can be calculated from the derivative equations at predefined x values (the theoretical measurement positions)—see Figure 6. Then the inclination curves were approximated from these

local inclination values and their associated positions using a MATLAB® internal spline interpolation function. Finally, the calculation of the bending line curve was achieved through a numerical integration of the resulting inclination approximation. The legends in Figures 6a and 7a are to be applied to Figures 6b–f and 7b–f, and they represent the steps from Figure 4.

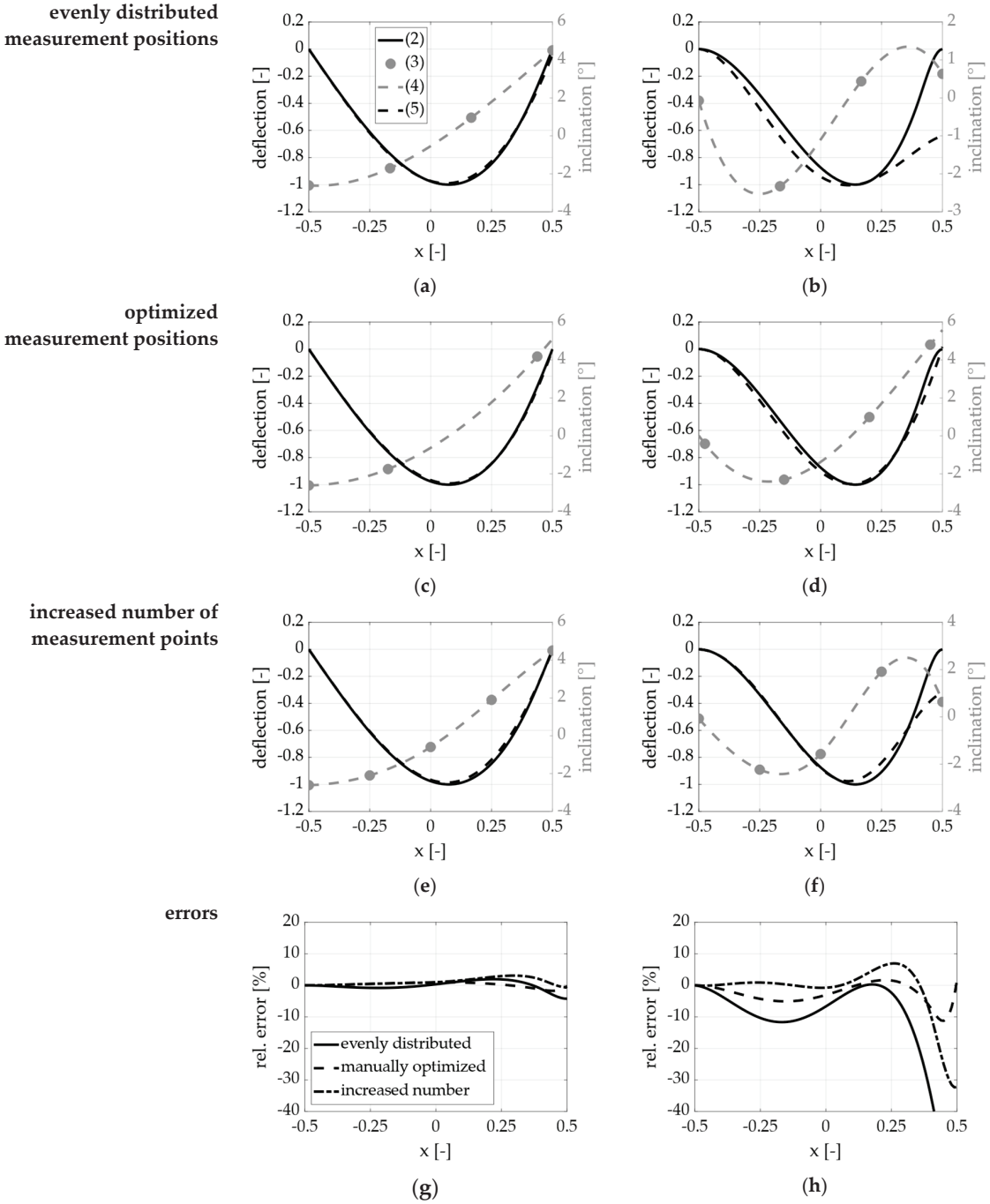



**Figure 7.** Results of theoretical investigations on the 2D bending beam with 90% off-centric loading: (**a**) evenly distributed measurement positions—beam a; (**b**) evenly distributed measurement positions—beam b; (**c**) manually optimized measurement positions—beam a; (**d**) manually optimized measurement positions—beam b; (**e**) increased number of measurement points—beam a; (**f**) increased number of measurement points—beam b; (**g**) relative error curves—beam a; and (**h**) relative error curves—beam b.

It turns out that for a simple 2D bending line with both sides loosely supported, the original deformation profile of the bending beam can already be reconstructed based on just four inclination values evenly distributed over the length of the beam—see Figure 6a. The maximum error is already below 3% with only four theoretical measurement points in relation to the maximum deformation—see Figure 6g. For the slightly more complex deformation profile of the beam with both sides firmly clamped, significantly larger errors arise with such a small number of measurement points—see Figure 6b,h. However, a simple manual optimization of the theoretical measurement positions already shows a significant improvement of the theoretical measurement result—see Figure 6d,h.

The manual optimization involved a systematic trial of various theoretical measurement positions. Alternatively, the number of measurement points can be increased to enhance the measurement accuracy—see Figure 6e–h. Figure 7 shows, following the same approach as described above, the results of an investigation of an off-centric load application on the 2D bending beam.

Here too, a manual optimization of the theoretical measurement positions leads to a significant improvement in the theoretical measurement results, compared to an even distribution of the measurement points—Figure 7c,d,g,h. With loose support on both sides (beam a), an increase in accuracy can be achieved by optimizing the measuring points, even by reducing the number of measuring points from four to three. A bending beam with loose support on both sides can be represented with a measurement error of less than 5% using three theoretical inclination measurements. For a bending beam with fixed support on both sides, a measurement error of about 10% is obtained with five manually optimized measurement positions. The theoretical measurement error generally decreases with an increasing number of measurement points—Figure 7e–h. For the even distribution of measurement points, Equation (8) was applied. Here, $l$ represents the length of the bending beam, $n$ is the number of measurement points, and $x_{pos}(i)$ denotes the calculated theoretical measurement positions.

$$x_{pos}(i) = \frac{l}{(n-1)} \cdot (i-1) - \frac{l}{2},\ 1 \leq i \leq n \tag{8}$$

The investigation shows the theoretical functionality of determining deformations based on local inclinations and reveals the dependence of the measurement result on the number and positioning of individual measurement points. This will be further examined later in this work.

#### 2.1.3. Approach for Three-Dimensional Measurements

The basic approach described above needs to be extended from a two-dimensional deformation measurement to a 3D space, which is the basis for deformation measurements of clamping plates of machine tools.

Figure 8 shows the basic approach. The load-induced local inclinations are determined at several measurement positions distributed on the measurement object (the bending plate), with inclinations being recorded in both the x and y directions (1). The inclination differences between the unloaded and loaded states are calculated following Equation (1). From the calculated inclination differences (2), two inclination surfaces are calculated, representing all measured inclinations in the x direction and the y direction, respectively (3). For this purpose, a MATLAB® internal interpolation function is used (the thin plate spline interpolation—TPS).

The two approximated inclination surfaces (3) are numerically integrated separately. This results in an integration surface from the inclination approximation in the x direction $z^*_{integ-x}(x_i, y_i)$ and an integration surface from the inclination approximation in the y direction $z^*_{integ-y}(x_i, y_i)$ (Figure 8; (4) above and below, respectively)—see Equations (9)

and (10). Therefore, $alpha_x(x_i, y_i)$ represents the approximated inclination surface in the x direction and $alpha_y(x_i, y_i)$ the inclination surface in the y direction.

$$z^*_{integ-x}(x_i, y_i) = \int alpha_x(x_i, y_i)\, dx \tag{9}$$

$$z^*_{integ-y}(x_i, y_i) = \int alpha_y(x_i, y_i)\, dy \tag{10}$$

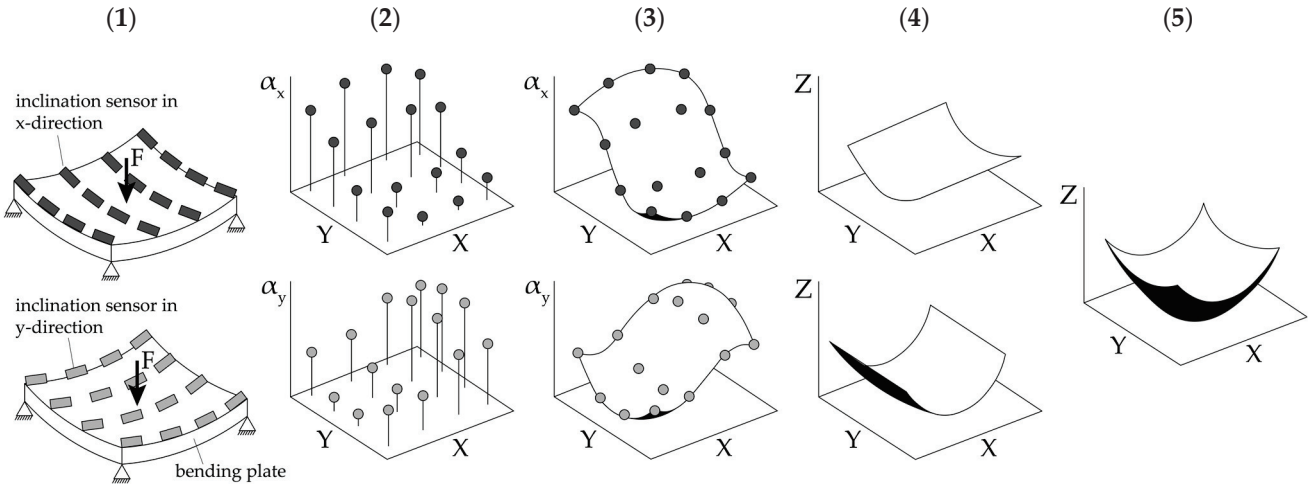



**Figure 8.** Approach for the three-dimensional inclination-based deformation measurement: (**1**) measurements on loaded object; (**2**) inclination differences in the x and y directions; (**3**) approximation of inclination values; (**4**) numerical integration; (**5**) calculation of measurement result.

Based on these two integration surfaces, the final deformation surface (5) of the measurement object is calculated. Therefore, the initial displacements of the $x$-integration surface $z^*_{integ-x}(x_i, y_i)$ at the minimum $y$-value and the initial displacements of the y-integration surface $z^*_{integ-y}(x_i, y_i)$ at the minimum $x$-value are extracted. The $x$-initial displacements are then subtracted from the $y$-integration surface, and the y-initial displacements are subtracted from the x-integration surface over the full range of values—see Equations (11) and (12). Therefore, $z_{integ-x}(x_i, y_i)$ and $z_{integ-y}(x_i, y_i)$ represent the two integration surfaces in the $x$ and $y$ directions, corrected for edge deformations.

$$z_{integ-x}(x_i, y_i) = z^*_{integ-x}(x_i, y_i) - z^*_{integ-y}(x_{min}, y_i) \tag{11}$$

$$z_{integ-y}(x_i, y_i) = z^*_{integ-y}(x_i, y_i) - z^*_{integ-x}(x_i, y_{min}) \tag{12}$$

The background for this procedure is that there is no information available about the initial displacement of the inclination sensors at the edge of the bending plate at the minimum $y$-value for the inclination measurements in the $x$ direction. The same applies to the inclination measurements in the $y$ direction at the press table edge at the minimum $x$-value. The initial deformations of the two integration surfaces at the press table edges are integrated into the calculation of the deformation profile by the method described above. The final deformation surface $z_{meas}(x_i, y_i)$ is ultimately calculated as the arithmetic mean of the two resulting integration surfaces according to Equation (13)—Figure 8 (5).

$$z_{meas}(x_i, y_i) = \frac{z_{integ-x}(x_i, y_i) + z_{integ-y}(x_i, y_i)}{2} \tag{13}$$

2.1.4. Theoretical Analysis of the Example of Three-Dimensional Deformation Data

The previous methods were subsequently extended to a 3D space. The aim of this second investigation is, again, to provide a theoretical proof of function for the extended

measurement method for 3D deformations. The functionality was initially tested on the existing published measurement results from the dissertation by Roth [4]—see Figure 9.

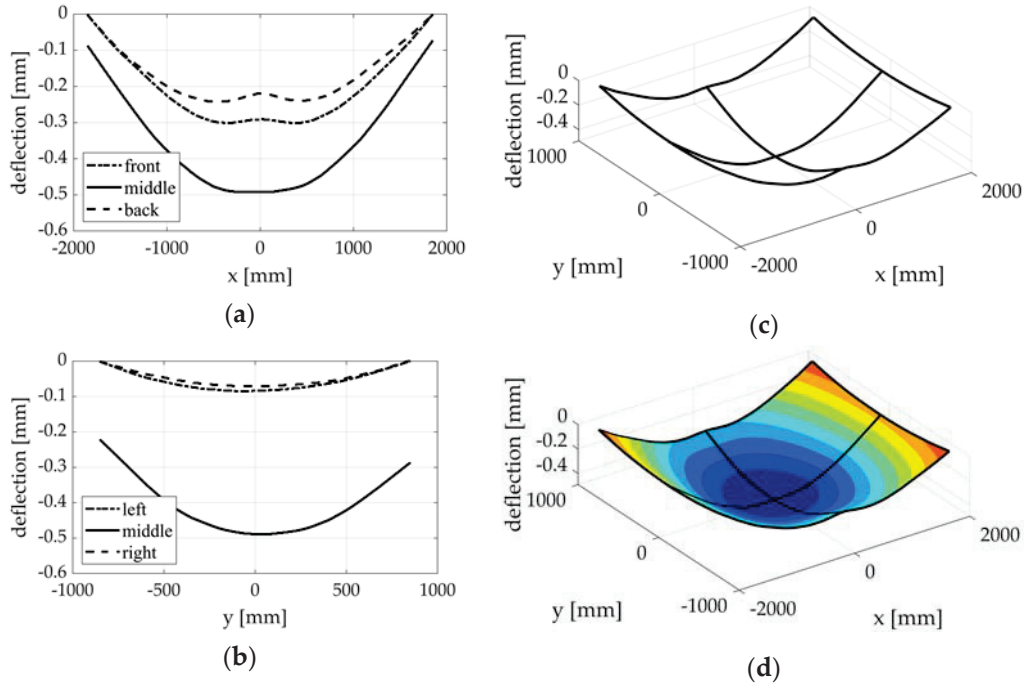



**Figure 9.** Digitization of measurement value curves of press bolster plate deformations from [4], test machine A: (**a**) measurement values of the bolster plate deformation parallel to the x axis; (**b**) measurement values of the bolster plate deformation parallel to the y axis; (**c**) digitization of the measurement values and transfer into the 3D space; (**d**) and approximation to a 3D surface.

The measurement data from Roth [4] contain the measured deformation profiles of press bolster plates of large-scale car body presses. For this purpose, the given measurement profiles were digitized using a self-developed MATLAB® image analysis function. The procedure applied is shown in Figure 8. Two measurement data diagrams belonging to one test machine (Figure 9a,b) were digitized and then transferred to the 3D space (Figure 9c). The generated 3D grid was then used to approximate a theoretical deformation surface of the bolster plate (Figure 9d).

To investigate the developed measurement method on the previously generated 3D fit of the bolster plate deformations from [4], the inclination values of the deformation surface at previously defined theoretical measurement positions must be extracted. The inclinations at the respective measurement points are calculated from the slope of a linear function, which intersects the virtual deformation surface just before and just after the respective measurement position in the $x$ or the $y$ direction (secant). With this approach, the inclination of the deformation surface in the $x$ and the $y$ directions is calculated at each defined theoretical measurement point—see Equations (14) and (15). The two inclination values calculated from the 3D fit are to be understood as virtual inclination measurements $\alpha_x(x_{pos}, y_{pos})$ and $\alpha_y(x_{pos}, y_{pos})$ at the virtual measuring positions given by $x_{pos}$ and $y_{pos}$. $x_{contact}$ represents the distance from the specified measurement position in both positive and negative directions where the secant intersects the virtual deformation surface. From the two z-coordinates of the virtual deformation surface and the distance of the intersection points determined in this way, the inclinations in the $x$ and $y$ directions at the specified measurement positions can be approximated.

$$\alpha_x(x_{pos}, y_{pos}) = \frac{z_{approx}(x_{pos} + x_{contact}, y_{pos}) - z_{approx}(x_{pos} - x_{contact}, y_{pos})}{(x_{pos} + x_{contact}) - (x_{pos} - x_{contact})} \quad (14)$$

$$\alpha_y(x_{pos}, y_{pos}) = \frac{z_{approx}(x_{pos}, y_{pos} + y_{contact}) - z_{approx}(x_{pos}, y_{pos} + y_{contact})}{(y_{pos} + y_{contact}) - (y_{pos} - y_{contact})} \quad (15)$$

From the inclination values of the different measuring positions, the procedure in Section 2.1.3 is applied to calculate the two inclination surfaces (Figure 10a,b) and the two integration surfaces (Figure 10c,d).

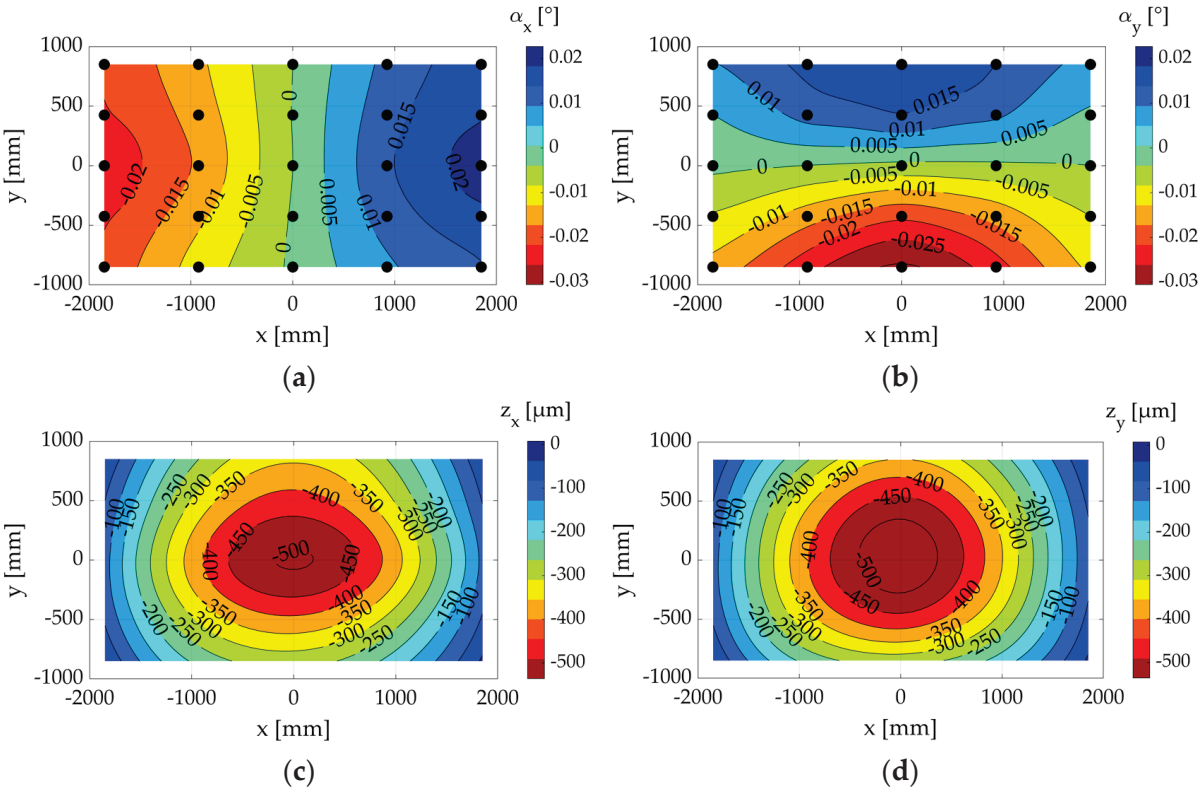



**Figure 10.** Results of the theoretical investigations on measurements from [4]: (**a**) inclination approximation in the x direction; (**b**) inclination approximation in the y direction; (**c**) integration surface of the inclination approximation in the x direction after subtracting the initial y-deformations; and (**d**) integration surface of the inclination approximation in the y direction after subtracting the initial x-deformations.

Figure 11b shows the theoretical measurement result for 25 evenly distributed theoretical inclination measurement positions on the 3D fit of the bolster plate (the digitized table deformation surface of test machine A in [4]). Figure 11a, in comparison, shows the original deformation surface calculated from the measurement data of [4]. Figure 11c shows the absolute and Figure 11d the relative error image of these two surfaces.

$$dz_{rel}(x_i, y_i) = \frac{z_{approx}(x_i, y_i) - z_{meas}(x_i, y_i)}{\max(abs(z_{approx}))} \cdot 100 \quad (16)$$

The calculation of the relative error image $dz_{rel}(x_i, y_i)$ refers to the maximum value of the virtual deformation $z_{approx}(x_i, y_i)$ in its center and is calculated according to Equation (16). $z_{meas}(x_i, y_i)$ is the virtual measurement result according to Equation (13). With the use of 25 evenly distributed measurement positions, errors below 4% could be achieved in large areas of the measurement object using the developed measurement method. Slightly larger errors of up to 10% result in small areas at the upper and lower edge.

For the even distribution of the measurement points on a given surface, various rectangular and triangular grids are calculated. The calculation of rectangular grids is based on a consideration of the given number of measurement points as the least common

multiple of the number of measurement points in the $x$ direction and the number of measurement points in the $y$ direction. Different combinations of values are computed, and, from the valid pairs of values for the specified number of measurement points, the one with the smallest difference in spacing between the measurement points in the $x$ direction and the measurement points in the $y$ direction is selected. If no meaningful value pair can be found by calculating a uniform rectangular grid, the calculation proceeds to generate a triangular grid. The calculation is initially based on generating different rectangular grids. The triangular grid is created by defining an additional measurement point in the center of each rectangle. A valid triangular grid is achieved when the specified number of measurement points can be completely divided among the specific triangular grids. The calculation is carried out iteratively.

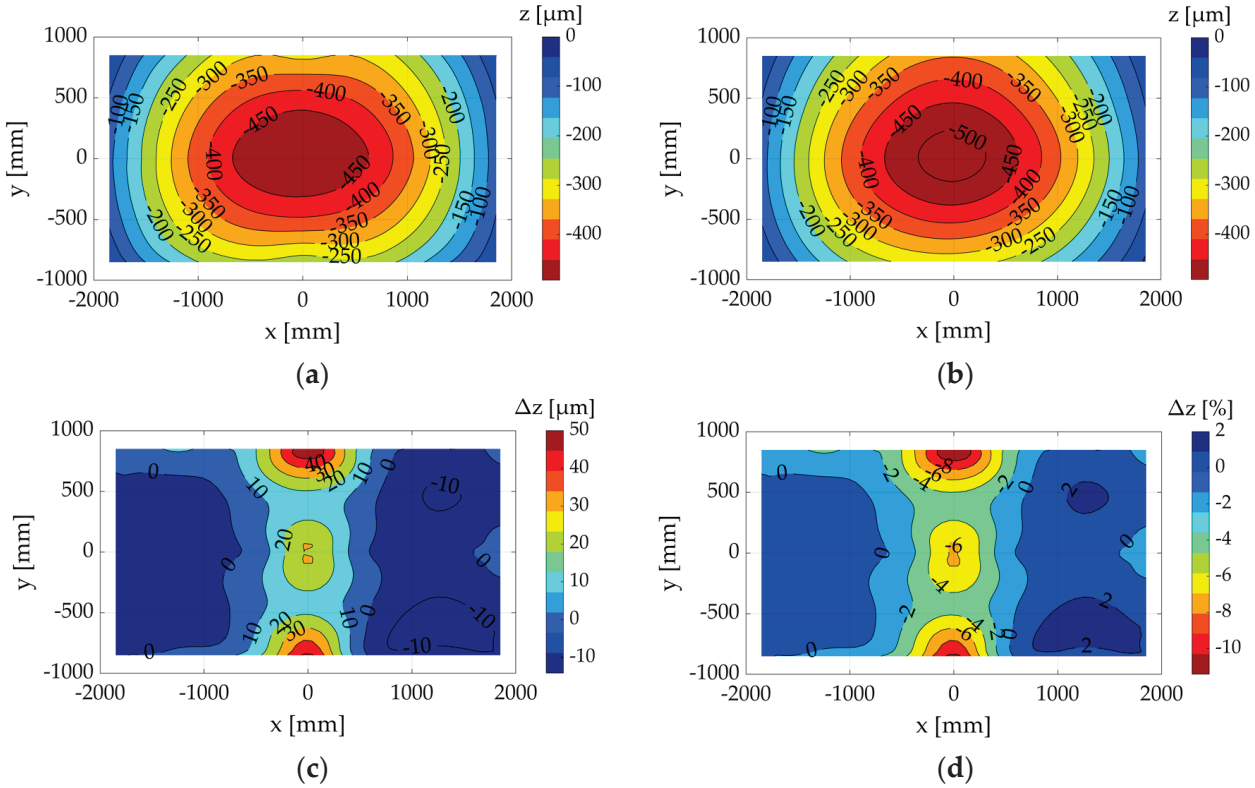



**Figure 11.** Theoretical investigation results of measurements from [4]: (**a**) 3D deformation surface of test machine A based on measurement results; (**b**) theoretical measurement result of virtual inclination-based deformation measurement; (**c**) theoretical measurement error in µm; and (**d**) theoretical measurement error in %.

### 2.1.5. Sensitivity Analysis of the Theoretical Measurement Point Quantity and Position

Analogous to the investigations on the 2D bending beam, the sensitivity of the measurement result to the number of measurement points and their positioning was analyzed. The aim was to answer the following two questions:

1. How many evenly distributed measurement points are theoretically necessary for measurement errors $\leq 10\%$ of the maximum deformation? See Figure 12.
2. Can a theoretical improvement in the measurement results be achieved by manually optimizing the measurement positions? See Figure 13.

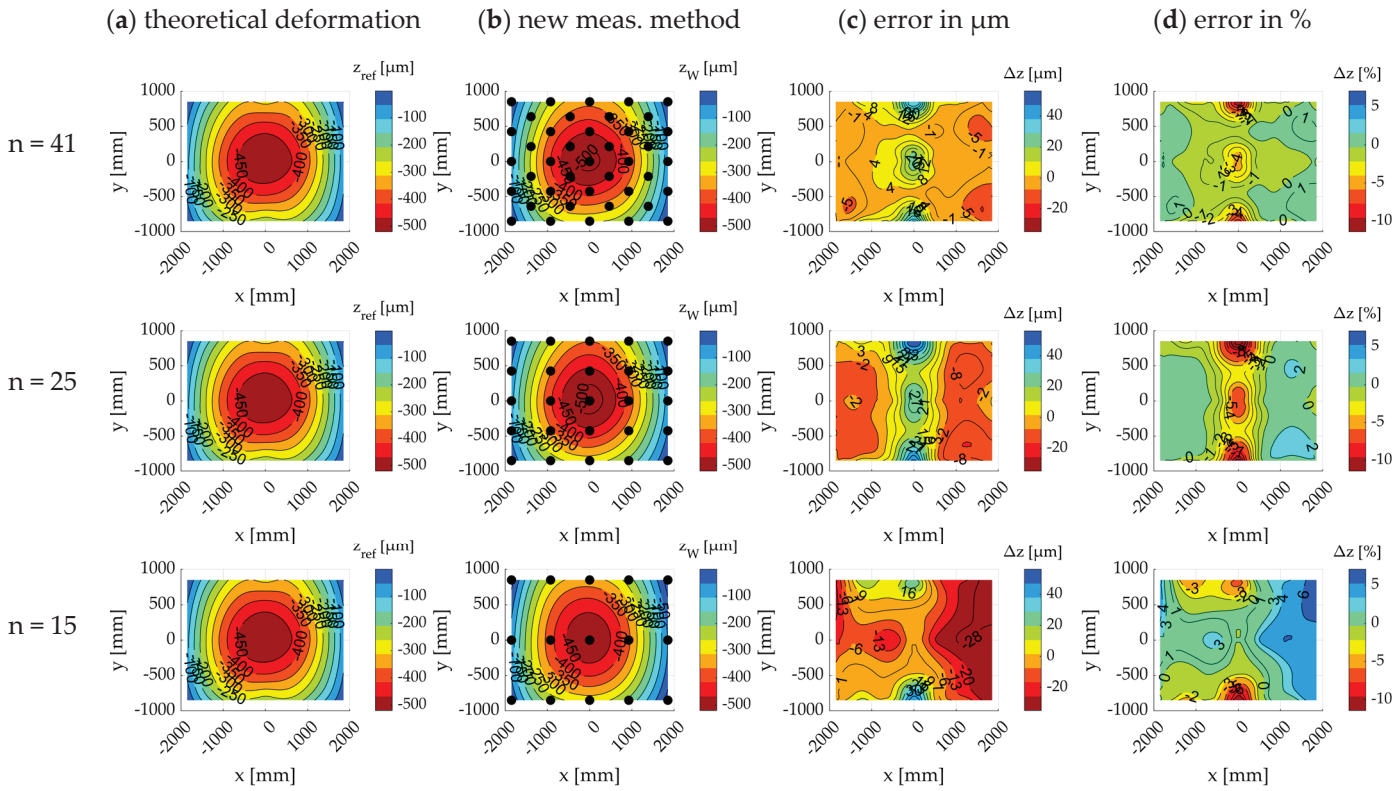



**Figure 12.** Sensitivity analysis of the number of evenly distributed measurement points for the calculated theoretical deformation of the bolster plate of test machine A in [4].

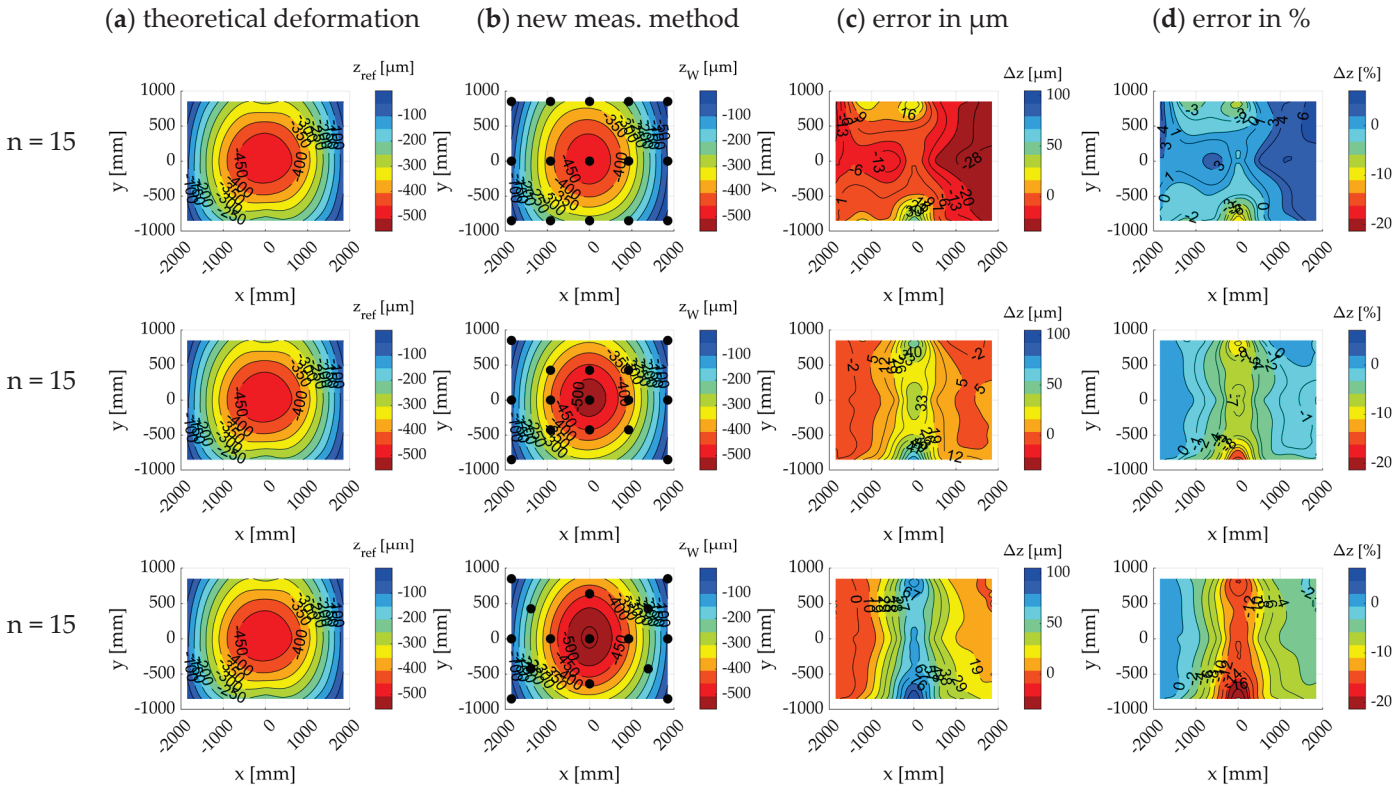



**Figure 13.** Sensitivity analysis of the measurement positions for the calculated theoretical deformation of the bolster plate of test machine A in [4].

Figure 12 shows a sensitivity analysis of the number of measurement points on the theoretical measurement object explained in Section 2.1.3. The measurement positions are evenly distributed. As anticipated and identical to the results on the 2D bending beam, the measurement error magnifies as the number of measurement points decreases.

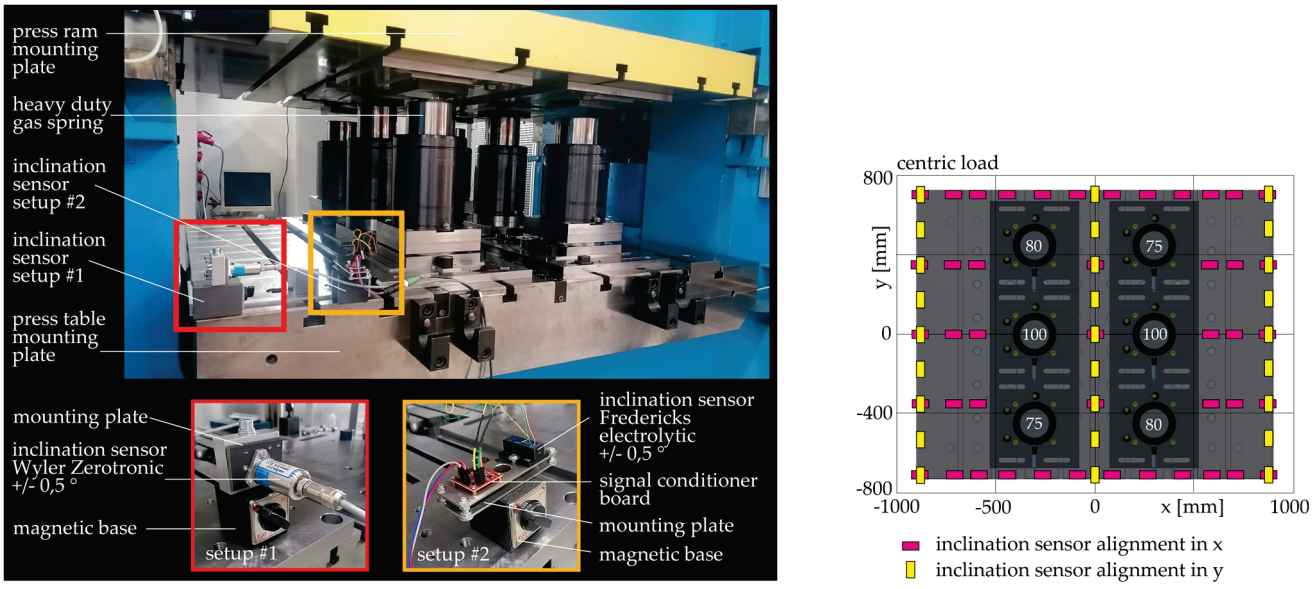
The theoretical outcomes reveal that the measurement error stays under 7% over vast regions, even when the number of measurement points is cut to 15. It is only in small peripheral areas that the measurement error reaches a maximum of 10%.

Figure 13 shows the results for an even distribution of the measuring points and two freely chosen modifications of the measuring point positions for 15 measurement points. The theoretical measurement error increases when compared to an even distribution. In contrast to choosing the optimal measurement point positions on the 2D bending beam, there are significantly more degrees of freedom available in a 3D space. Improving the theoretical measurement accuracy by manually optimizing the measurement point positions is no longer straightforward in the 3D space.

## *2.2. Experimental Verification of Deformation Measurement of Press Bolster Plates*

### 2.2.1. Basic Experimental Testing under Laboratory Conditions

As part of the experimental tests, the basic functionality of the presented measurement method was first tested. Figure 14 shows the test setup on a test object at TU Dresden. The load was introduced via a gas spring assembly consisting of six staggered heavy-duty gas springs (Figure 14a). The testing was initially carried out with a manual selection of evenly distributed inclination measurement points in the $x$ and $y$ directions (Figure 14b).




(**a**) (**b**)

**Figure 14.** Measurement setup for inclination-based deformation measurements on the bolster plate of the test object: (**a**) gas spring loading setup and used inclination sensor setups; and (**b**) applied measurement positions for inclination measurements in the x and y directions.

The inclination measurements were carried out in duplicate for each measurement point with each inclination sensor setup: using an expensive capacitive sensor (Wyler Zerotronic) and a comparatively cheap electrolytic sensor (Fredericks). The necessary angular resolution of the sensors depended on the dimensions of the bolster plate and the amount of deformation. Through an examination of the measurement data presented in the literature concerning deformations of bolster plates (see [1,4,6,7,11,43]), the theoretically necessary angular resolutions could be computed by employing a basic bending beam

model. These resolutions fell within the range of 0.0003 to 0.0005 degrees, aligning closely with the specifications of the two sensors utilized.

At each measurement point, the inclination curves were recorded in the $x$ and the $y$ directions (see Figure 14b). The measurement started with an unloaded machine and therefore an un-deformed bolster plate. Subsequently, the press ram was moved down to the bottom dead center (BDC) during the measurement, compressing the gas pressure springs to their maximum force. After a short hold of the ram in the BDC, the return stroke and the unloading of the machine took place, followed by the end of the inclination measurement. The described procedure was carried out for 45 measurement points evenly distributed on the press table. Figure 15 illustrates the procedure for processing the measurement data. The raw data for each measurement point (Figure 15a) were first smoothed using a moving average filter and converted into an inclination angle value using the calibration curve of the sensor. The minimum value (the unloaded measurement object; red points) and the maximum value (the fully loaded measurement object; blue points) were then extracted from each smoothed data curve and assigned to the respective measurement position (Figure 15b).

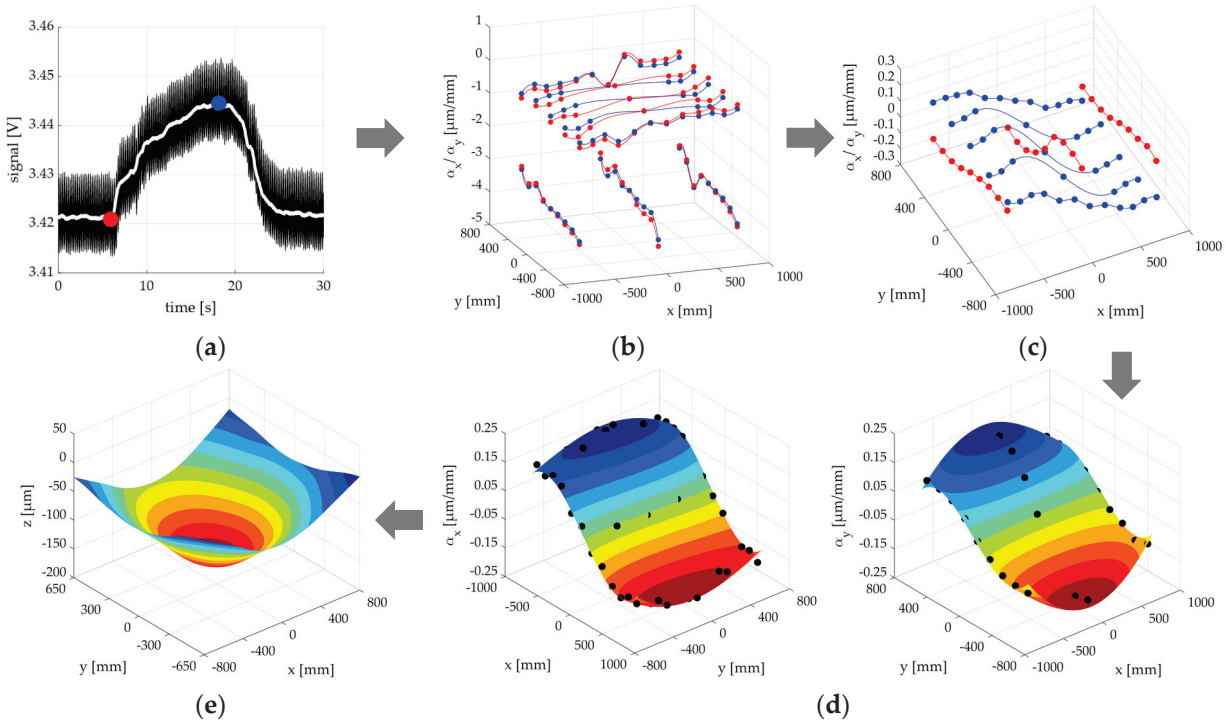
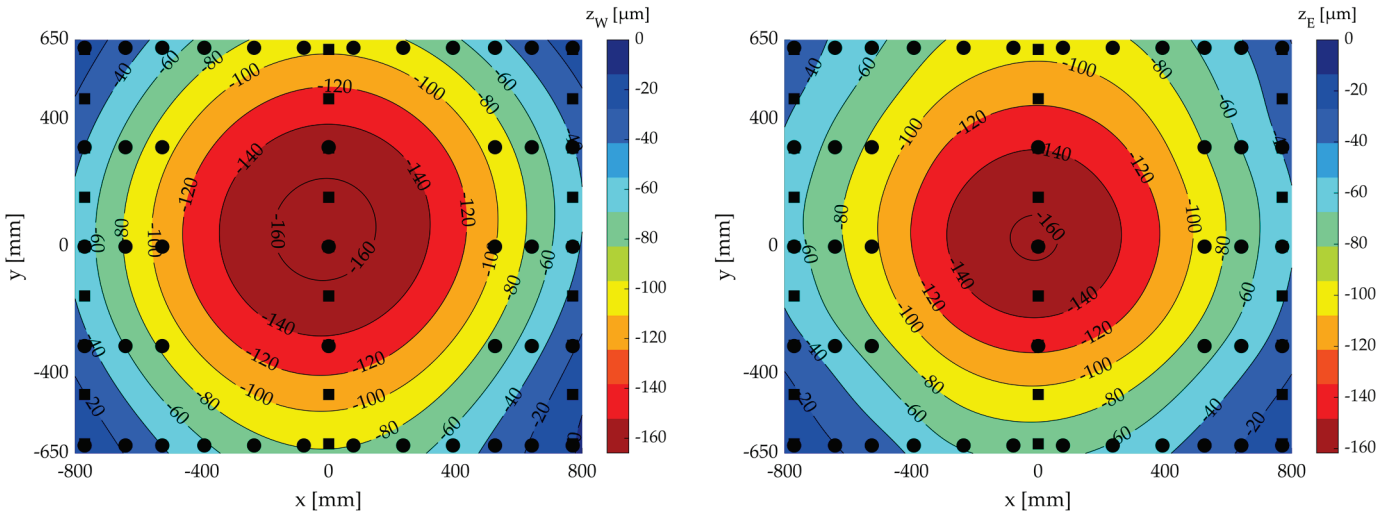



**Figure 15.** Approach for the measurement data analysis: (**a**) raw measurement data and moving average filter (red—unloaded state, blue—loaded state); (**b**) extracted minimum and maximum inclination values (red—unloaded state, blue—loaded state); (**c**) calculated inclination differences between loaded and unloaded states (red—y direction, blue —x direction); (**d**) calculated inclination approximations in x and y directions (dots represent measurement points); and (**e**) final deformation image of the measured object (the measurement result).

The inclination differences were then calculated (Figure 15c), from which the two inclination approximations in the x and y directions were calculated (Figure 15d) using the equations given in Section 2.1.3. This yielded the final deformation image of the measurement object (Figure 15e). Figure 16 shows the two measurement results:

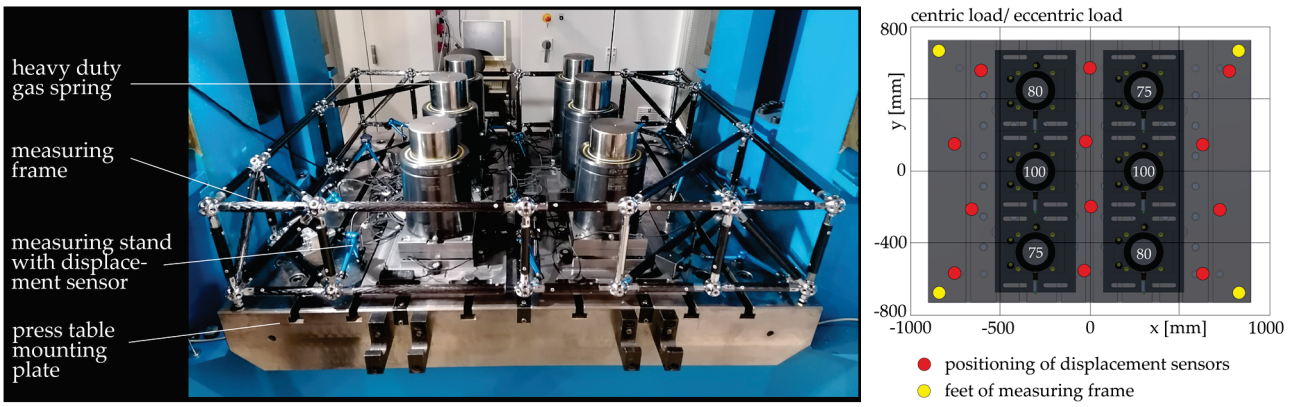



(**a**) (**b**)

**Figure 16.** Measurement results of the developed measurement method under central load application on the test object: (**a**) Wyler Zerotronic inclination sensor, evenly distributed measurement points that were manually selected; and (**b**) Fredericks electrolyte sensor, evenly distributed measurement points that were manually selected.

Figure 16a shows the two measurement results for a centrally loaded machine and evenly distributed measurement points, using the Wyler Zerotronic 3 sensor and the Fredericks electrolyte sensor (Figure 16b). It is evident that using significantly cheaper electrolyte sensors can yield nearly the same measurement results.

To validate the developed measurement method, a comparison measurement was carried out using a proven measurement procedure (see Figure 17). The measurement of the bolster plate deformation was carried out using 12 high-resolution measurement probes, which were mounted on a carbon fiber measurement frame using measurement stands. The four support points of the measurement frame were placed in the corner areas of the bolster plate to ensure a minimal measurement error due to external table deformations.




(**a**) (**b**)

**Figure 17.** Measurement setup for conducting a comparative measurement on the bolster plate of the test object: (**a**) gas spring setup and measurement frame equipped with high-resolution measurement probes; and (**b**) positions of the measurement probes and support points (numbers 75, 80, 100 represent the stroke lengths of the gas springs).

The measurement data analysis was initially carried out analogously to Figure 15a. The deformation at the respective measurement points was directly calculated from the

extracted minimum and maximum values as well as the respective sensor positions (Figure 17b). In addition, four further virtual measurement points were added to the support points of the measurement frame and integrated into the analysis with a deformation of 0 µm. A continuous deformation image (Figure 18) was then calculated from the resulting 16 measurement points using the MATLAB® internal TPS function.

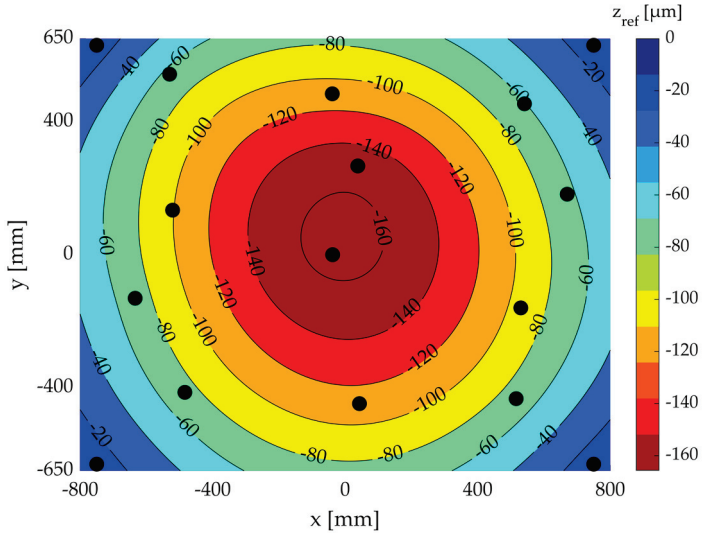



**Figure 18.** Measurement result of the comparison measurement of the bolster plate deformation of the test object under central load application.

By extrapolating the deformation image beyond the support points of the measurement frame, the table deformation in the outer regions of the bolster plate (outside the measurement frame) could ultimately also be taken into account. For the extrapolation, the support points of the measuring frame were added as virtual measurement points, and their displacement was set to z = 0 µm. Subsequently, a surface approximation was calculated from the totality of all measurement points. For this purpose, a Matlab® internal fitting function (thin plate smoothing spline—TPS) was used, allowing an extrapolation beyond the originally contained range of values in the measurements. Figure 19 shows the measurement results for the central load introduction. The support points of the measuring frame are located in the corners of the bolster plate in Figure 18 (see also Figure 17b). Figure 19 depicts the calculated absolute and relative error maps of the measurement results on the test object.

The absolute error maps represent the difference between the inclination sensor-based deformation measurement and the performed direct comparative measurement. In order to provide a better assessment of the accuracy of the developed measurement method, relative error images were also calculated. A direct consideration of the relative deviations, where the percentage deviations between the two measurements are calculated with the spatial resolution, is not appropriate here. The reason is that the relative error increases disproportionately at very small deformation values in the peripheral areas of the bolster plate. This would not provide a sensibly evaluable error pattern. Therefore, the relative error images were calculated from the absolute error images in such a way that the relative values refer to the maximum deformation of the reference measurement in the center of the bolster plate. A comparison of the measurement accuracies generated by the two different types of inclination sensors reveals that both sensors provide deformation results within the same range of accuracy. When using the Wyler Zerotronic 3 sensor, the absolute errors range from −19 to +13 µm, corresponding to a relative accuracy of −8 to +11%. When using the Fredericks electrolytic sensor, the absolute errors range from −13 to +18 µm, which corresponds to relative errors of −11 to +8%.

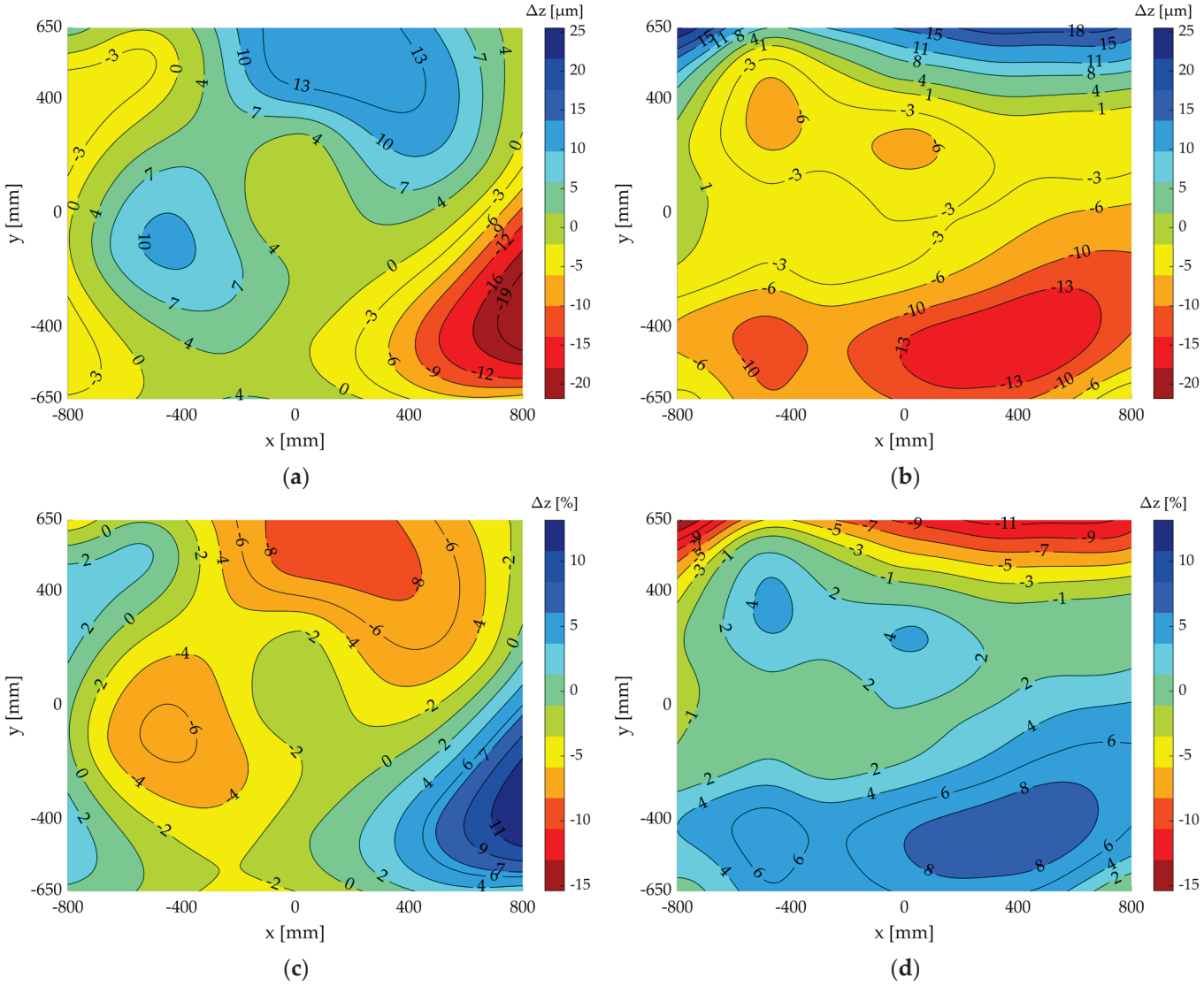
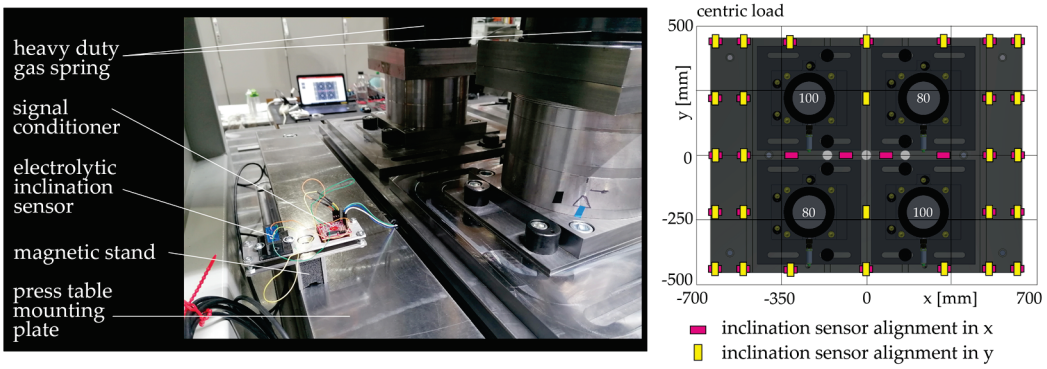


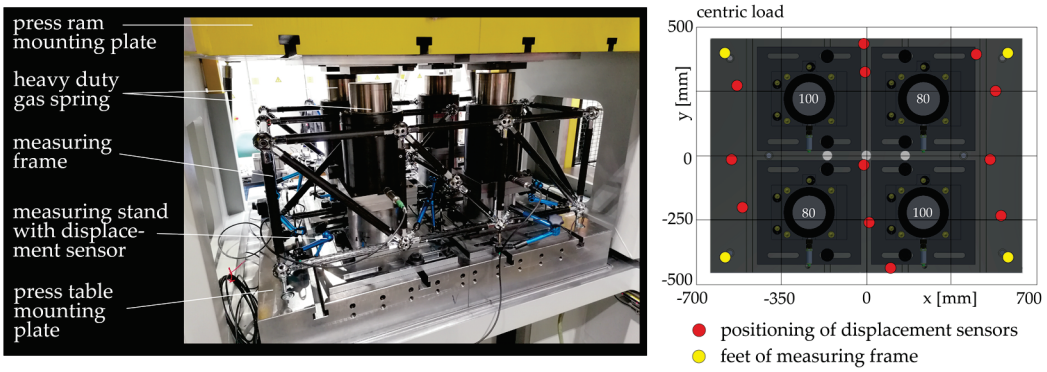

**Figure 19.** Comparison of the measurement results using the novel measurement method, with the results of the comparative measurement on the test object: (**a**) error in µm with the Wyler Zerotronic 3 sensor; (**b**) error in µm with the electrolytic sensor; (**c**) error in % with the Wyler Zerotronic 3 sensor; and (**d**) error in % with the electrolytic sensor.

### 2.2.2. Testing as Part of a Press Commissioning at a Press Manufacturer

This section extends the basic testing of the newly developed inclination-based method using measurements under real conditions and a comparison with the proven displacement-based method on the same machine. For this purpose, the commissioning of a particularly precise servo spindle press at a press manufacturer was used—this is the test machine in the following. Figure 20 shows the applied test setups. The load was applied to the machine using a two-stage gas spring arrangement consisting of four gas springs of up to 1200 kN nominal force. The crosswise arrangement of springs with the same stroke length created a central load.




(**a**)




(**b**)

**Figure 20.** Experimental setups for the determination of bolster plate deformations during a press commissioning test on the test machine (numbers 80, 100 represent the stroke lengths of the gas springs): (**a**) gas spring loading setup for central load force introduction and simplified inclination sensor setup; measurement points for inclination-based deformation measurement at evenly distributed positions; and (**b**) gas spring setup and measurement frame with 12 measurement probes for comparative measurement; measurement probe positions and support points for comparative measurement.

Good results were achieved in the laboratory test (Section 2.2.1) with the significantly cheaper electrolytic inclination sensor, so that only the electrolytic inclination sensor setup was used in the tests carried out here. According to the method described above, several inclination measurements in the x and y directions were carried out distributed on the bolster plate. Since only one prototypical inclination sensor setup was available, a separate load stroke was carried out with the machine for each measurement and an inclination profile was recorded from the unloaded to the fully loaded bolster plate.

In addition to the developed measurement method (Figure 20a), a second measurement using a measurement frame with 12 high-resolution measurement probes was applied, as described in Section 2.2.1 (Figure 20b). Due to the slightly inwardly shifted support points, the measurement frame shifts downward during load application. This measurement error is approximately compensated for by extrapolating the deformation surface generated from the measurement points to the edges of the bolster plate. Figure 21a,b show the measurement results obtained from the two applied measurement methods.

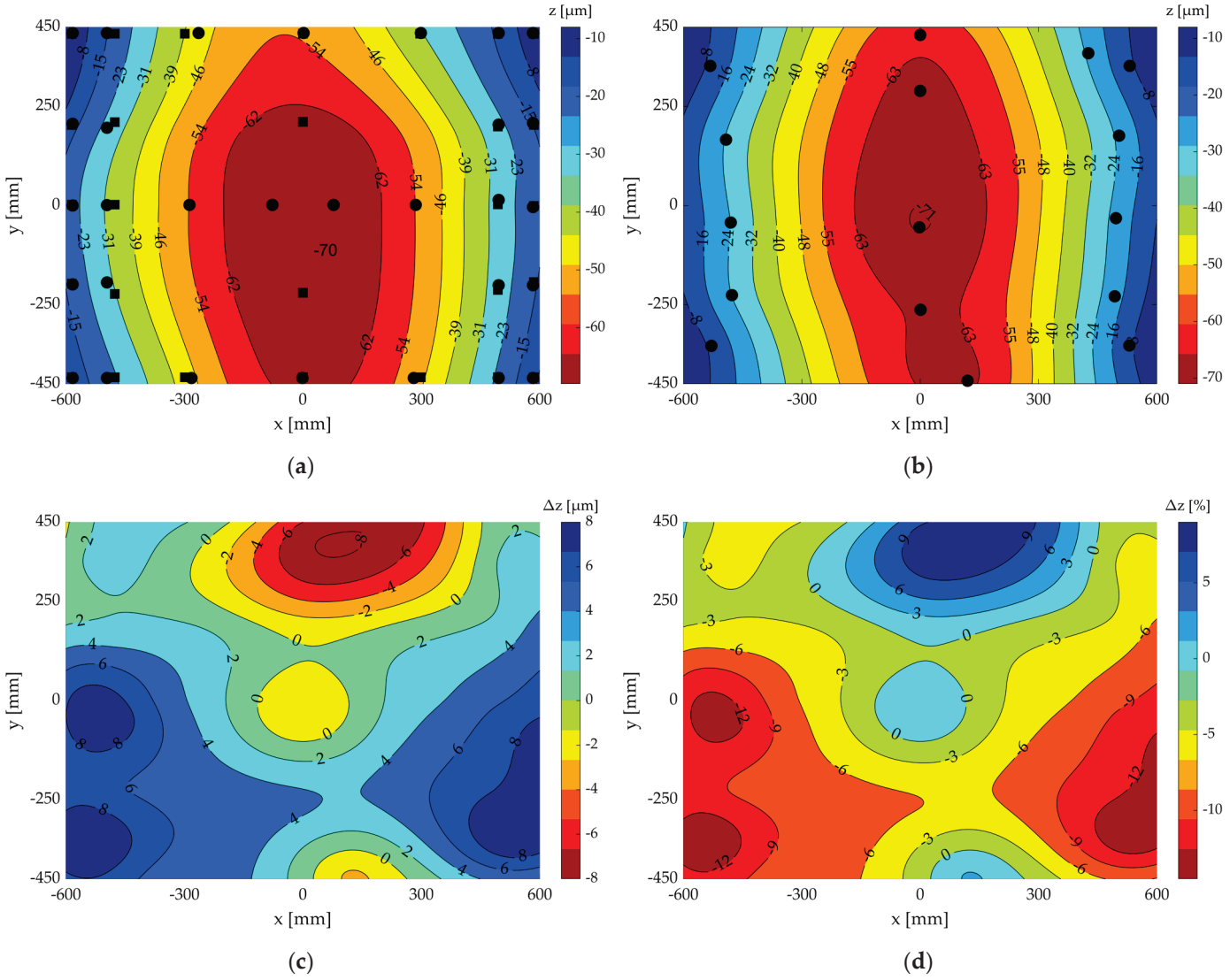



**Figure 21.** Measurement results of the deformation measurements conducted on the test machine and a comparison with the results of the comparative measurement: (**a**) measurement results obtained using the developed measurement method with evenly distributed manual measurement positions; (**b**) measurement results of the comparative measurement; (**c**) error in µm with the Fredericks electrolytic sensor; and (**d**) error in % with the Fredericks electrolytic sensor.

Figure 21c,d illustrate the measurement accuracies of the measurements conducted on the high-precision servo press. The measurements were performed using a cost-effective electrolytic inclination sensor. The achieved measurement accuracies range from −8 to +8 µm, corresponding to relative measurement accuracies of −11 to +6% relative to the maximum bolster plate deformation. The new measurement method yields comparable results to the established method in real conditions, indicating its effectiveness.

## 3. Discussion

Based on the findings from the theoretical investigations from Sections 2.1.2 and 2.1.5, the sensitivity of the measurement results to the number of measurement points and the position of the individual measurements was investigated.

### *3.1. Sensitivity Analysis of Measurement Point Quantity*

For this purpose, the individual measurement point readings were excluded from the calculation of the deformation images. Figure 22 shows the results of the developed

measurement method for the evaluation of 45, 25, and 10 of the originally recorded measurement points on the test object, as well as the respective deviations from the comparison measurement. Figure 23, in analogy, presents the evaluation of 32, 20 and 14 of the measurement points recorded on the investigated test machine.

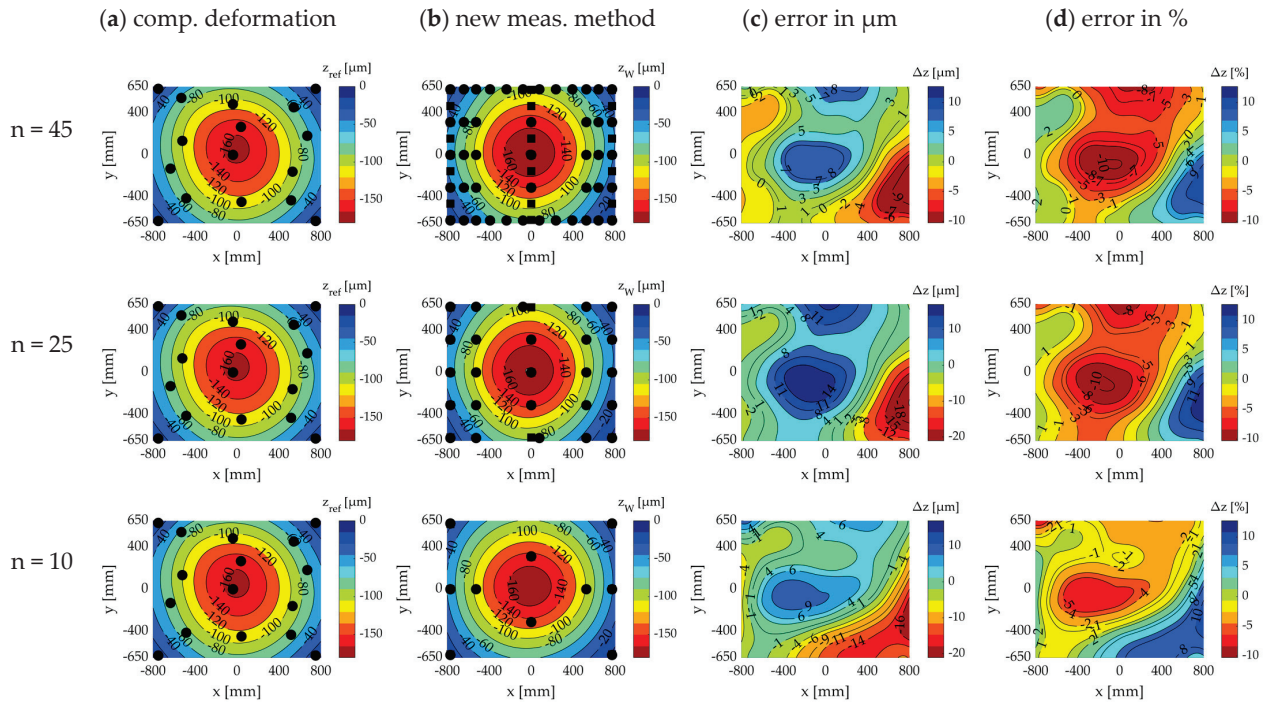



**Figure 22.** Sensitivity analysis of the number of measurement points for the bolster plate deformation measurement on the test object.

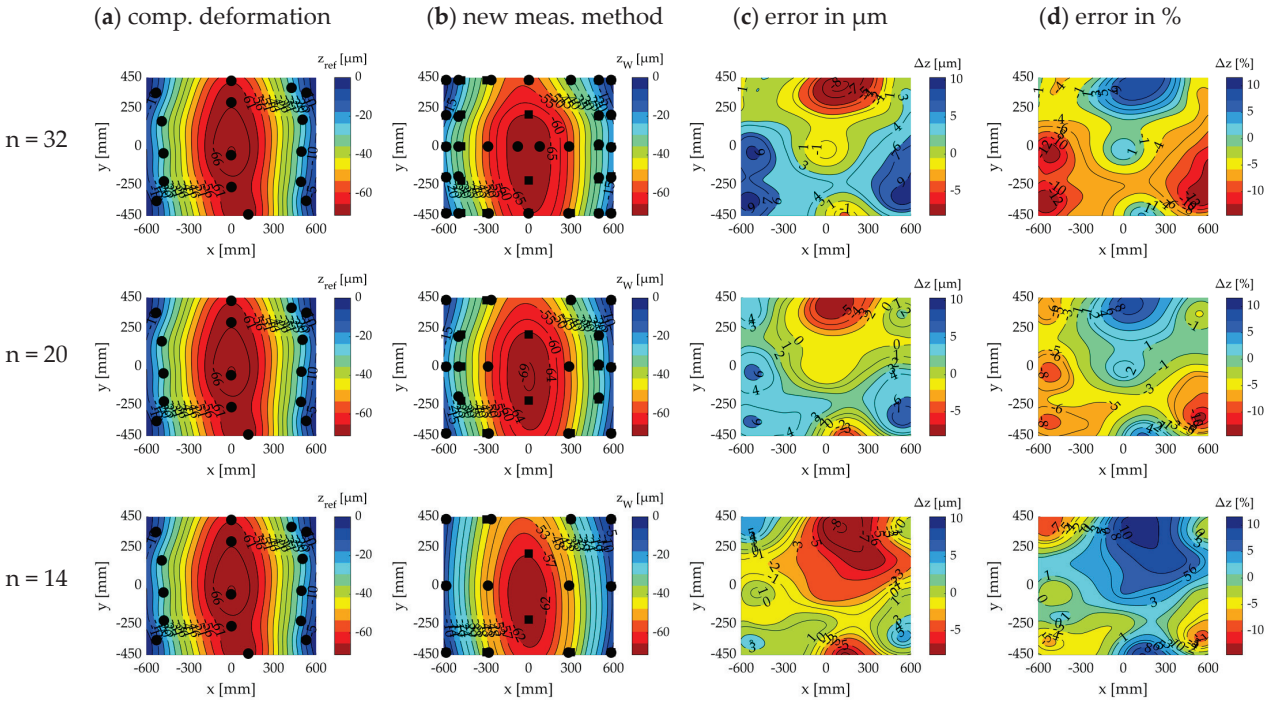



**Figure 23.** Sensitivity analysis of the number of measurement points for the bolster plate deformation measurement on the test machine.

The calculated error images between the comparison measurement and the novel measurement method show that there is only a slight dependency of the measurement result on the number of measurement points. Even when evaluating only 10 measurement points (on the test object), the deviations compared to the comparison measurements are only slightly larger than when evaluating all recorded measurement points. For the test object the maximum errors range between 18 µm and 21 µm (11–14.5%). However, the deciding factor for this is the position of the measurement points on the object being measured. While there is a nearly even distribution of measurement points with 45 or 25 points on the test object (Figure 22), with 10 measurement points there is already a large degree of discretion in choosing the positions for the local inclination measurements on the test object.

Similarly, for the test machine, a reduction in the measurement points leads to only a slight increase in measurement inaccuracy—see Figure 23. For the test machine the maximum errors range between 8 µm and 10 µm (11–13%). Here too, however, the influence of the individual measurement positions on the calculated measurement result increases as the number of measurement points decreases. If an even distribution of a sufficient number of measurement points is not possible, it is especially important to capture the local inclinations where, as expected, high inclination values occur during deformation. In the example measurements of the bolster plate deformations with a centric load, the measurement points shown here are primarily located on the coordinate axes of the press coordinate system and in the bolster plate corners.

### *3.2. Sensitivity Analysis of Measurement Point Position*

Figure 24 shows that for a small number of measuring points there can be a high sensitivity of the measuring accuracy at the individual measurement positions. The maximum absolute and relative errors on the test object vary between 19 and 46 µm (11.5–27.5%) when using nine measuring points. In the case of the test machine with 10 measuring points, a variation in the maximum measurement error of just 21–24 µm (29–33%) is observed, which suggests a much lower sensitivity. The different positioning variants of the measuring points in Figures 24 and 25 were freely chosen from the available measurement data.

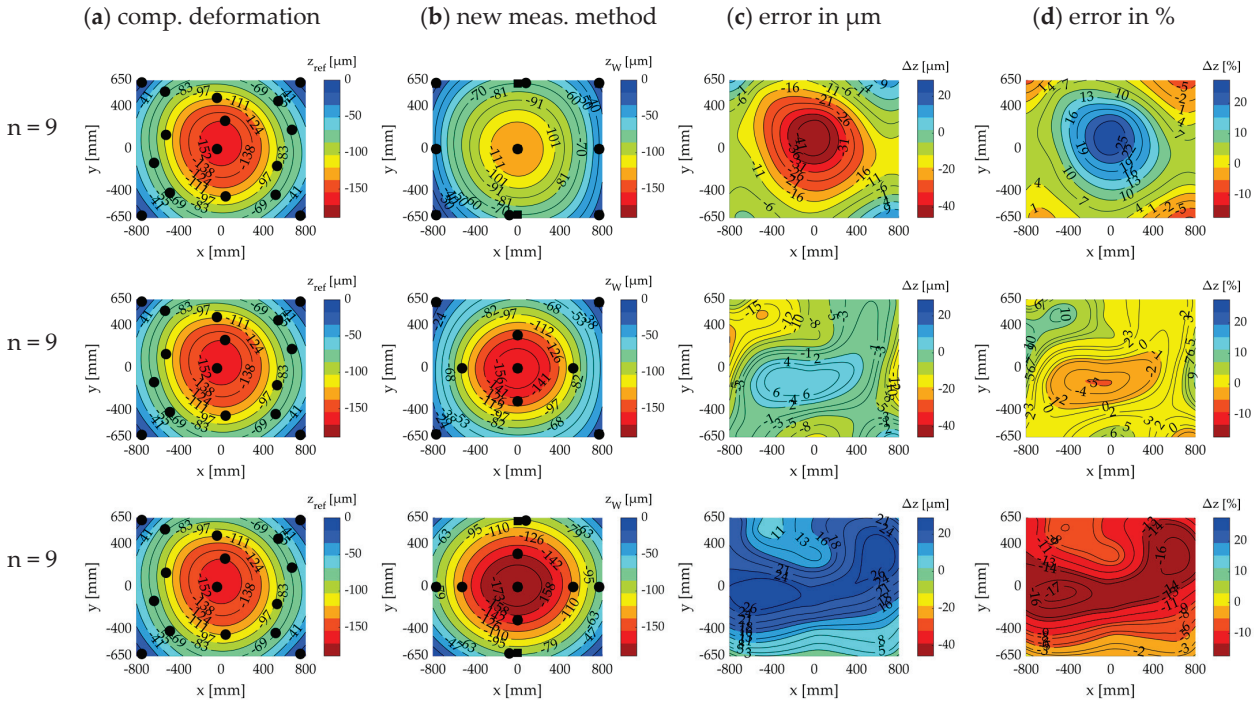



**Figure 24.** Sensitivity analysis of the positions of measurement points for the bolster plate deformation measurement on the test object.

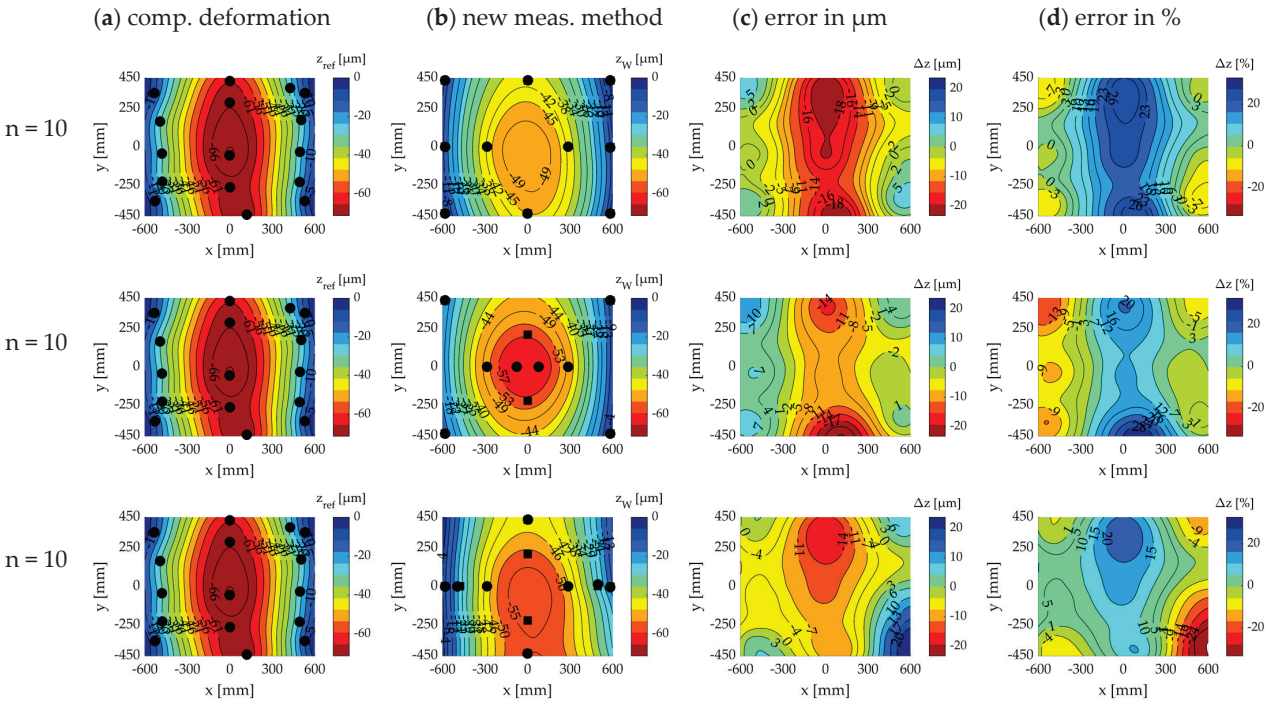



**Figure 25.** Sensitivity analysis of the positions of measurement points for the bolster plate deformation measurement on the test machine.

### *3.3. Error Considerations of the Conducted Measurements*

The presented measurement results were obtained under the influence of several potential sources of error, which are briefly addressed below. Simplified inclination sensor setups were used in the studies to capture the inclination signals on the bolster plates under investigation. Only one sensor per sensor type was available for the fundamental studies performed, requiring a large number of individual measurements that were not synchronized in time for each series of measurements. The inclination measurements and the probe measurements of the comparative measurement were conducted on separate days for both machines. In summary, the following potential sources of error can be identified:

- Deviations in the load application between the inclination-based deformation measurement and the comparative measurement due to temperature differences in the gas pressure springs and minimal leakage at the spring valves;
- Deviations in the load application due to control deviations in the force or stroke controls of the test object and the machine;
- Inaccuracies in the manual evaluation of the non-synchronized raw measurement data of the individual inclination measurements;
- Inaccuracies in the manual alignment of the sensor setups on the bolster plates;
- Angular errors due to deviations from perpendicularity during the setup of the sensors on the simplified sensor setups;
- Angular errors due to deviations from perpendicularity during the alignment of the sensor setups on the bolster plates of the test machines;
- Temperature drifts of the inclination sensors during the recording of a measurement series (lasting several hours);
- Minimal adjustment of the sensor alignment on the recording plates of the simplified sensor setups;
- Insufficient holding time at maximum load at BDC.

It can be assumed that by reducing the potential sources of errors, the measurement results would be even more precise. One essential measure for this is the synchronized

measurement of all measurement points involved in a deformation measurement, as well as the precise and stable installation of the sensors in the measurement modules.

## 4. Conclusions

This paper presents a novel measurement method for the 3D deformation measurement on machine tools based on local inclination measurements. Its functionality was demonstrated for the deformation measurements on press bolster plates within an accuracy range of <20 µm. For the measurement of static bolster plate deformations, the presented method offers significant advantages over existing methods. These include a high application efficiency, a high level of application flexibility, and comparatively low acquisition costs compared to laser trackers or stereo camera systems, as well as measurement frames with high-precision measurement probes. In addition to pure deformation measurements, the presented method and the corresponding measurement system also allow displacement measurements, e.g., to determine ram tilting due to eccentric load application. Further investigations will be carried out.

It was experimentally proven that, starting from 20 local inclination measurement points, central bolster plate deformations can be reliably detected. As the number of measurement points decreases, the influence of the measurement positions on the measurement result increases. Future work will therefore focus on methods for a model-based optimization of the measurement positions.

It is also expected that a further improvement in the measurement accuracy can be achieved by using time-synchronized measurement modules. The development of such a measurement system is currently in progress at ICM e.V. The measurement system will consist of 25 measurement modules and is intended to enable a simple and time-saving yet precise determination of the deformations and deflections in forming presses under load. A patent application for the presented measurement method and the developed measurement system has already been filed by ICM.

At present, it is not possible to carry out dynamic measurements during continuous cycling of the press or to introduce dynamic loads at this stage of the system development. Nonetheless, it is feasible to extend the fundamental approach to dynamic measurements with the aid of appropriate sensors. This is also planned for future research.

## 5. Patents

Patent application under the patent number 10 2023 115 430.3.

**Author Contributions:** Conceptualization; software; validation; formal analysis; data curation; writing—original draft preparation; visualization; project administration; and funding acquisition, G.I.; methodology, G.I. and T.B.; investigation, G.I.; writing—review and editing, L.P. and S.I.; supervision, G.I. and L.P.; All authors have read and agreed to the published version of the manuscript.

**Funding:** This research was funded by the Federal Ministry for Economic Affairs and Climate Action (BMWi), grant number 49MF200106, and the APC was funded by ICM—Institute for Mechanical and Plant Engineering Chemnitz e.V.

**Data Availability Statement:** The data presented in this study are available on request from the corresponding author. The data are not publicly available due to agreements between the machine owners and ICM—Institute for Mechanical and Plant Engineering Chemnitz e.V.

**Acknowledgments:** Special thanks go to the Chair of Machine Tool Development and Adaptive Control at TU Dresden and H&T ProduktionsTechnologie GmbH.

**Conflicts of Interest:** The authors declare no conflict of interest.

## Abbreviations/Nomenclature

| Term | Explanation |
|---|---|
| bolster plate | clamping plate for tool fixture in forming presses |
| press commissioning | setup and initiation process, including testing and making the press operational |
| press ram | movable part of a press that applies pressure to the material being processed |
| press table | flat surface or platform on a press where the material or workpiece is positioned and processed |
| press working space/area | area between the table and the ram of a forming press |
| T-slot | groove in press table or ram for tool fixation |
| BDC | Bottom Dead Center |
| DIC | Digital Image Correlation |
| ICM | ICM—Institut Chemnitzer Maschinen- und Anlagenbau e.V. |
| PSD | Position Sensitive Detector |
| TPS | Thin plate smoothing spline |
| 2D | Two dimensional |
| 3D | Three dimensional |

## References


1. Behrens, B.-A.; Werbs, M.; Brecher, C.; Hork, M. *Entwicklung und Erweiterung Standardisierter Messverfahren zur Statischen und Dynamischen Pressenvermessung*; EFB-Forschungsbericht: Hanover, Germany, 2006; p. 250.
2. Behrens, B.-A.; Brecher, C.; Hork, M.; Werbs, M. New standardized procedure for the measurement of the static and dynamic properties of forming machines. *Prod. Eng. Res. Dev.* **2007**, *1*, 31–36. [CrossRef]
3. Abbasi, F.; Sarasua, A.; Trinidad, J.; Otegi, N.; Saenz de Argandoña, E.; Galdos, L. Substitutive Press-Bolster and Press-Ram Models for the Virtual Estimation of Stamping-Tool Cambering. *Materials* **2022**, *15*, 279. [CrossRef]
4. Roth, T. Ermittlung von Kennwerten von Einfachwirkenden Umformmaschinen für die Zustandsorientierte Instandhaltung und die Qualifizierung des Werkzeugentstehungsprozesses. Ph.D. Thesis, Chemnitz University of Technology, Chemnitz, Germany, 2015.
5. Struck, R. Berücksichtigung von Werkzeug- und Pressenelastizitäten in der Umformsimulation zur verbesserten Vorhersage des Pressenkraftbedarfes. *VDI-Berichte* **2008**, *2031*, 185–199.
6. Struck, R. Bestimmung der Minimal Notwendigen Pressenkraft zur Herstellung von Karosseriestrukturbauteilen im Automobilbau. Ph.D. Thesis, Leibniz University Hannover, Hannover, Germany, 2010.
7. Wagener, H.-W.; Weikert, J. Messung der Tisch- und Stößeldurchbiegung an Torgestellpressen. *Blech Rohre Profile* **1997**, *5*, 46–52.
8. Tehel, R.; Päßler, T.; Kurth, R.; Nagel, M.; Reichert, W.; Ihlenfeldt, S. Virtual Tryout: Case Study on Simulation-Based Design and Die Spotting of Forming Tools. *Eng. Proc.* **2022**, *26*, 9. [CrossRef]
9. Pilthammar, J.; Skåre, T.; Galdos, L.; Fröjdh, K.; Ottosson, P.; Wiklund, D.; Carlholmer, J.; Sigvant, M.; Ohlsson, M.; Sáenz de Argandoña, E.; et al. New press deflection measuring methods for the creation of substitutive models for efficient die cambering. *IOP Conf. Ser. Mater. Sci. Eng.* **2021**, *1157*, 012076. [CrossRef]
10. Wiedenmann, X. Dynamische Prozesse in Pressen erkennen—Der digitale Fingerabdruck. In Proceedings of the Conference Mehr Effizienz im Presswerk 2023, Würzburg, Germany, 15 June 2023.
11. Zgoll, F. Methodik zur Maschinenoptimalen Werkzeugeinarbeitung Durch Virtuelle Kompensation der Werkzeug- und Pressendurchbiegung. Ph.D. Thesis, Technical University of Munich, Munich, Germany, 2021.
12. Kurth, R.; Bergmann, M.; Tehel, R.; Dix, M.; Putz, M. Cognitive clamping geometries for monitoring elastic deformation in forming machines and processes. *CIRP Ann.* **2021**, *70*, 235–238. [CrossRef]
13. Schapp, L.O. Gekoppelte Simulation von Maschine und Prozess in der Massivumformung. Ph.D. Thesis, RWTH Aachen University, Aachen, Germany, 2008.
14. Tehel, R.; Päßler, T.; Mihm, M. Modeling elastic behavior of forming machine components to reduce tool manufacturing time. *Procedia Manuf.* **2019**, *27*, 177–184. [CrossRef]
15. Tehel, R.; Päßler, T.; Bergmann, M. Effective FE models for simulating the elasto-mechanical characteristics of forming machines. *Int. J. Adv. Manuf. Technol.* **2020**, *58*, 9–12, 588. [CrossRef]
16. Wagener, H.-W.; Wiedner, M. Analyse des statischen und dynamischen Genauigkeitsverhaltens einer 5000 kN-Vierpunkt-Exzenterpresse mit Hilfe der Lasermesstechnik. *UTF Sci.* **2001**, *1*, 9–14.
17. GOM Gesellschaft für Optische Messtechnik. Application Note: 3D Motion Analysis—Optical Measuring Technology for Dynamic Analysis of Press Machines. Available online: https://mailassets.gom.com/user_upload/industries/forming_machine_EN.pdf (accessed on 30 December 2023).
18. Müller, P. Analyse Elastischer Wechselwirkungen an Servo-Spindelpressen. Ph.D. Thesis, Chemnitz University of Technology, Chemnitz, Germany, 2018.

19. Müller, P.; Kriechenbauer, S.; Drossel, W.-G. Experimental analysis of the elastic boundary conditions of press machines for modelling the deep-drawing process. *Int. J. Adv. Manuf. Technol.* **2019**, *101*, 579–592. [CrossRef]
20. Pilthammar, J.; Sigvant, M.; Hansson, M.; Pálsson, E.; Rutgersson, W. Characterizing the Elastic Behaviour of a Press Table through Topology Optimization. *J. Phys. Conf. Ser.* **2017**, *896*, 12068. [CrossRef]
21. Pilthammar, J. Elastic Press and Die Deformations in Sheet Metal Forming Simulations. Ph.D. Thesis, Blekinge Institute of Technology, Karlskrona, Germany, 2017.
22. Zgoll, F.; Götze, T.; Volk, W. Building a substitute model of a bolster based on experimentally determined deflection. *J. Phys. Conf. Ser.* **2017**, *896*, 012044. [CrossRef]
23. Zgoll, F.; Götze, T.; Volk, W. Influence of the elastic behaviour of a moving bolster on the active surface of a punch: A numerical investigation. In Proceedings of the Forming Technology Forum 2017, Enschede, The Netherlands, 12–13 October 2017.
24. Zgoll, F.; Kuruva, S.; Götze1, T.; Volk, W. Virtual die spotting: Compensation of elastic behavior of forming presses. *IOP Conf. Ser. Mater. Sci. Eng.* **2019**, *651*, 012021. [CrossRef]
25. Pan, B. Digital image correlation for surface deformation measurement: Historical developments, recent advances and future goals. *Meas. Sci. Technol.* **2018**, *29*, 082001. [CrossRef]
26. Amirpour, M.; Bickerton, S.; Calius, E.; Das, R.; Mace, B. Numerical and experimental study on deformation of 3D-printed polymeric functionally graded plates: 3D-Digital Image Correlation approach. *Compos. Struct.* **2019**, *211*, 481–489. [CrossRef]
27. Almazán-Lázaro, A.-J.; López-Alba, E.; Rubio-García, L.; Díaz-Garrido, F.-A. Indentation Measurement in Thin Plates under Bending Using 3D Digital Image Correlation. *Appl. Sci.* **2021**, *11*, 2706. [CrossRef]
28. Pupurs, A.; Loukil, M.; Varna, J. Digital Image Correlation (DIC) Validation of Engineering Approaches for Bending Stiffness Determination of Damaged Laminates. *Appl. Compos. Mater.* **2022**, *29*, 1937–1958. [CrossRef]
29. Xu, W.; Li, J.; Zhang, B.; Yang, L. A new approach to reduce springback in sheet metal bending using digital image correlation. *Int. J. Mater. Res.* **2019**, *110*, 726–733. [CrossRef]
30. Gothivarekar, S.; Coppieters, S.; Van de Velde, A.; Debruyne, D. Advanced FE model validation of cold-forming process using DIC: Air bending of high strength steel. *Int. J. Mater. Form.* **2020**, *13*, 409–421. [CrossRef]
31. Sun, W.; Xu, Z.; Li, X.; Chen, Z.; Tang, X. Three-Dimensional Shape and Deformation Measurements Based on Fringe Projection Profilometry and Fluorescent Digital Image Correlation via a 3 Charge Coupled Device Camera. *Sensors* **2023**, *23*, 6663. [CrossRef] [PubMed]
32. Salfeld, V. Experimentelle und numerische Untersuchungen zur Verlagerung des Pressenstößels infolge einer Horizontalkraft. Ph.D. Thesis, Leibniz University Hannover, Hannover, Germany, 2015.
33. Ottosson, P.; Pilthammar, J.; Wiklund, D.; Skåre, T.; Sigvant, M. Substitutive models of press deflections for efficient numerical die cambering. *IOP Conf. Ser. Mater. Sci. Eng.* **2023**, *1284*, 012060. [CrossRef]
34. Kurth, R.; Alaluss, M.; Wagner, M.; Tehel, R.; Riemer, M.; Ihlenfeldt, S. Process Monitoring using Digital Twin-Based Sensors integrated in Tool Clamping Surfaces. *IOP Conf. Ser. Mater. Sci. Eng.* **2023**, *1284*, 012016. [CrossRef]
35. Alaluss, M.; Kurth, R.; Tehel, R.; Wagner, M.; Wagner, N.; Ihlenfeldt, S. Potential of Tool Clamping Surfaces in Forming Machines for Cognitive Production. *J. Mach. Eng.* **2022**, *22*, 116–131. [CrossRef]
36. Kurth, R.; Tehel, R.; Päßler, T.; Putz, M.; Wehmeyer, K.; Kraft, C.; Schwarze, H. Forming 4.0: Smart machine components applied as a hybrid plain bearing and a tool clamping system. *Procedia Manuf.* **2019**, *27*, 65–71. [CrossRef]
37. Tehel, R. *Smart Machine Components. Fundamental Part of Cognitive Forming Machines. 21*; Werkzeugmasch.-Fachsemin: Dresden, Germany, 2019. [CrossRef]
38. Gao, N.H.; Zhao, M.; Li, S.Z. Displacement Monitoring Method Based on Inclination Measurement. *Adv. Mater. Res.* **2011**, *368–373*, 2280–2285.
39. Guidi, V.; Mazzolari, A.; Salvador, D.; Carnera, A. Silicon crystal for channelling of negatively charged particles. *J. Phys. D Appl. Phys.* **2009**, *42*, 182005. [CrossRef]
40. Hou, X.; Yang, X.; Huang, Q. Using Inclinometers to Measure Bridge Deflection. *J. Bridge Eng.* **2005**, *10*, 564–569. [CrossRef]
41. Sousa, H.; Cavadas, F.; Henriques, A.; Bento, J.; Figueiras, J. Bridge deflection evaluation using strain and rotation measurements. *Smart Struct. Syst.* **2013**, *11*, 365–386. [CrossRef]
42. Yu, H.; Chen, X.; Ren, M.; Yin, L.; Wu, Q.; Zhan, J.; Liu, Q. A coupled bend-twist deformation monitoring method based on inclination measurement and rational cubic spline fitting. *Mech. Syst. Signal Process.* **2021**, *147*, 107084. [CrossRef]
43. Roskam, R. In-Prozess-Überwachung von Pressen der Blechverarbeitung. Ph.D. Thesis, Leibniz University Hannover, Hannover, Germany, 1999.


**Disclaimer/Publisher's Note:** The statements, opinions and data contained in all publications are solely those of the individual author(s) and contributor(s) and not of MDPI and/or the editor(s). MDPI and/or the editor(s) disclaim responsibility for any injury to people or property resulting from any ideas, methods, instructions or products referred to in the content.

machines

MDPI

*Article*

# Design of Special Equipment for the Mechanical Testing of Runway Light Fixtures

**Dario Croccolo, Massimiliano De Agostinis *, Stefano Fini, Mattia Mele, Giorgio Olmi and Chiara Scapecchi**

Department of Industrial Engineering, University of Bologna, 40136 Bologna, Italy; dario.croccolo@unibo.it (D.C.); stefano.fini@unibo.it (S.F.); mattia.mele@unibo.it (M.M.); giorgio.olmi@unibo.it (G.O.); chiara.scapecchi@unibo.it (C.S.)

* Correspondence: m.deagostinis@unibo.it; Tel.: +39-051-209334

**Abstract:** Runway lights are essential components of the airstrip. However, there is currently no international standard that outlines methods for the testing of runway light fixtures. In this study, a novel testing method is developed to simulate the forces exerted on the lights during landing. The testing equipment is specifically designed to be easily mounted on a standard hydraulic press commonly used for tensile tests. This system allows for the regulation of the normal force between the aircraft tire and the fixture of the runway lighting system. To minimize load fluctuations during part sliding, Belleville washers are employed. The overall compliance of the system is validated through finite element analysis. Tests carried out by means of the proposed testing equipment allow the effective description of the variations in load at different positions during sliding. The system presented in this paper can be used to investigate the effects of landing on various combinations of cap design and tire material.

**Keywords:** runway light fixture; testing method; landing gear; customized test; aircraft

## 1. Introduction

Runway edge lighting is used to outline the edges of runways during periods of darkness or in restricted visibility conditions [1,2]. The functionality of these lights holds paramount significance in ensuring the safety of flight operations [3]. Research in this domain has predominantly focused on monitoring the optical efficacy of these lighting systems to ascertain the attainment of adequate visibility [4,5]. Nevertheless, ensuring the proper functionality of the lighting system necessitates the assurance of the structural resilience of these lights. The lights are protected by aluminium caps (fixtures) that are required to withstand the possible impacts with aircraft wheels, especially during landing, where the highest applied forces are achieved. Notably, there remains an absence of studies addressing the determination or assessment of such protective structures. Presently, there are no established standards providing guidance for the design or testing of this specific fixture. Moreover, no previous studies have addressed this issue by proposing methodologies to evaluate the performance of runway light fixtures on a laboratory scale. The objective of this study is to fill this void by introducing a test method and equipment capable of replicating the loading conditions experienced by the fixture during landings. The proposed test method outlined in this research aims to serve as a benchmark for future investigations in this field.

To design the equipment, relevant standards and technical documentations have been taken into account. The shear load, responsible for the deformation of caps' edges, has been assessed by comparing four standards regarding the landing of specific plane models (the Airbus A380 [6] and the Boeing 777 [7]), one regarding specifications for runway and taxiway light fixtures [8] and one regarding specifications for large planes in general [9]. In particular, ref. [8] has been used to determine the shear load for the elastic model,

whereas [6,7,9] have been used to determine the shear load for the elastic–plastic model. An intermediate value of deceleration between the one from [7] and the one from [9] was considered ($3 \times a_z$), whereas the maximum plane weight at landing (MLW) was taken from [6], as the A380 has a higher MLW than the Boeing 777.

Section 2 details the design of the testing equipment. Specifically, an experimental test bench has been designed and manufactured to be able to run experimental campaigns on these light fixtures. The conceptual scheme of this test is discussed in Section 2.1. The ad hoc designed apparatus allows for the accommodation of the test piece on a standard Instron 1275 500 kN universal testing machine and the application of (i) a normal force to the planar upper surface of the light fixture by means of a series of bolts and of an interchangeable rubber pad and of a (ii) tangential motion to the planar upper surface of the light fixture in order to adequately simulate the impact between the wheel and the fixture itself. The design of the architecture is presented in Section 2.2, while Section 2.3 provides an insight into the clamping system used to generate the normal force on the rubber pad.

FEA models have been developed, applying the retrieved shear loads, in order to determine the entity of the deformation in a worst-case scenario. These calculations are presented in Section 2.4.

Section 2.5 focuses on the design of the connection to the universal testing machine. Finally, Section 2.6 covers the handling and operation of the equipment.

The applications of the proposed testing equipment to actual fixtures and tires are outlined in Section 3 to illustrate the effectiveness of the proposed solution in measuring contact forces. Ultimately, conclusions regarding the current work are drawn in Section 4.

Issues of novelty arise from the lack of studies both in the scientific and in the technical literature dealing with the development of similar devices. The developed testing rig can be used not only for FEA validation purposes, but also for experimental tests aimed at assessing the safety of the light fixtures. The originality of the performed non-trivial design task arises also from the lack of specific standards providing recommendations or reference schemes for the execution of lab tests aimed at assessing the structural response of the light fixtures under their normal duty cycle.

## 2. Design of the Equipment

### *2.1. Conceptual Scheme of the Test*

For the scope of these tests, the landing gear tire is substituted by a cylindrical rubber pad of 200 mm diameter, fabricated from the same elastomeric material. Considering that the objective of the test is to replicate the contact experienced during landing, the rubber pad must be pushed against the light fixture with a specific normal force denoted as $F_N$. Equation (1) may be used to estimate the value of $F_N$.

$$F_N = \frac{m_a \mathrm{g}}{N_g} \tag{1}$$

where $m_a$ is the mass of the airplane, g is the acceleration of gravity and $N_g$ is the number of landing gear tires. Table 1 reports the values calculated for an Airbus A380 and a Boeing 777, the acceleration of gravity being $\mathrm{g} = 9.81\ \mathrm{m/s^2}$.

**Table 1.** Calculation of the normal force $F_N$ in two aircraft.

| Aircraft | $m_a$ (ton) | $N_g$ | $F_N$ (kN) | Reference (%) |
|---|---|---|---|---|
| A380 | 386 | 16 | 237 | [6] |
| Boeing 777 | 296 | 18 | 161 | [7] |

In Figure 1a, a schematic illustrates the gear making contact with the fixture during landing. Here, the load $F_N$ presses the gear against the fixture as it moves forward, resulting

in the generation of a tangential force $F_T$ due to the friction between the tire and the fixture. To examine the loading conditions that arise when the tire component moves on the runway lighting fixture, the testing system must facilitate the sliding motion of the rubber pad with respect to the cap, as illustrated in Figure 1b.

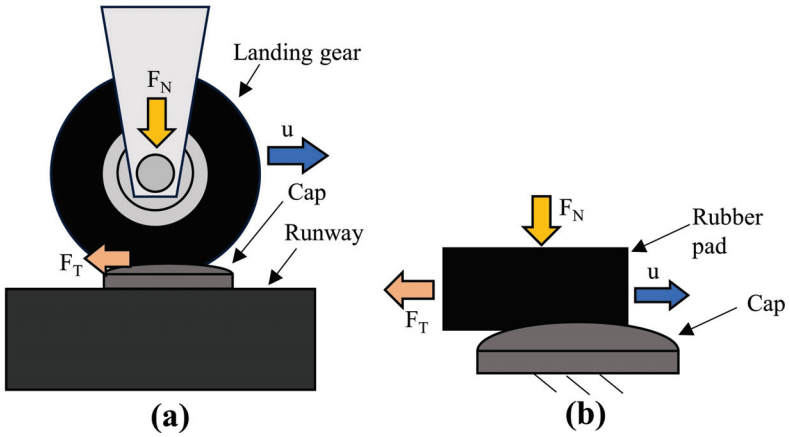



**Figure 1.** (**a**) Schematic representation of the tire touching the fixture during landing and (**b**) conceptual scheme of the test.

The controlled parameter of the test is the displacement, denoted as $u$, in the direction of sliding. Additionally, the testing system should enable the measurement of the tangential force $F_T$ resulting from the friction between the rubber pad and the cap.

The testing apparatus was designed to be adaptable to a standard universal testing machine equipped with a load cell, which is commonly utilized for tensile testing purposes. Specifically, a INSTRON 1275, load capacity 500 kN, by Instron®, Norwood, MA, USA, was used.

### *2.2. Architecture of the Equipment*

An assembly drawing of the testing system developed for these experiments is shown in Figure 2.

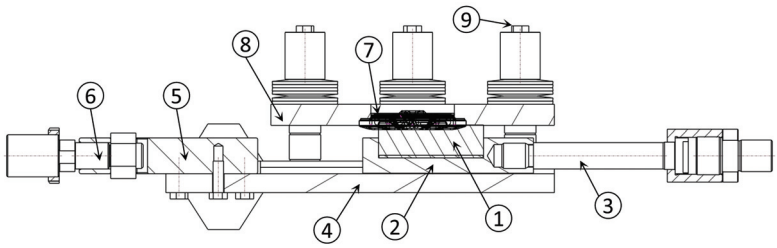



**Figure 2.** Assembly of the testing equipment.

The rubber pad, labeled as (1) in Figure 2, is mounted on a support (2) that is connected to the piston of the hydraulic press through an adapter (3). The pad support is linked to a base plate (4) via rails, allowing relative sliding between these two elements along the piston axis. The base plate is then connected to the fixed crossbeam of the press. As shown in Figure 2, an intermediate block (5) is bolted to the base plate and connected to the machine using a second adapter (6). This configuration enables the alignment of the two adapters, i.e., the forces, along the axis of the hydraulic press. The linear variable differential transducer (LVDT) of the press is used to measure the movement u of the pad, while the load cell measures the tangential force $F_t$. All the components mentioned thus far, except for the elastic pad, are made of S355JR steel.

The runway light fixture under testing (7) is mounted on a S355JR counterplate (8). This counterplate is pressed against the base plate (4) by six bolts (9). The normal force Fn can

be adjusted by varying the tightening torque of these bolts [10]. However, it is important to note that the high elasticity of the rubber pad, combined with the variable height of the cap, may result in significant variations in the preload of the bolts. To monitor fluctuations in the normal force $F_N$, four strain gauges, L2A-06-125LW-350 (Micro Measurements, Raleigh, NC, USA), arranged in a full bridge configuration (two longitudinal and two transverse), were applied to each of the two specular central columns of the system, as shown in Figure 3.

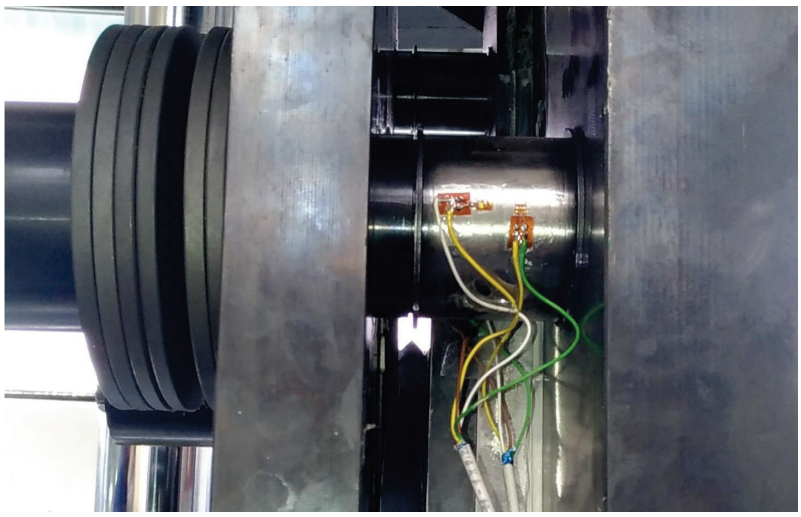
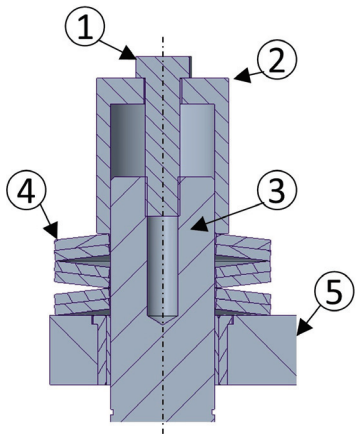


**Figure 3.** Picture of the strain gauges applied on the central columns.

A custom software program running in the LabVIEW 2020 (National Instruments, Austin, TX, USA) environment and sampling through a NI cDAQ 9184 carrier equipped with a bridge module NI 9237 was used to acquire the signal from these gauges and synchronize it with those from the LVDT and load cell. The analog inputs from the machine were sampled by means of an NI 9219 module, plugged into the same carrier. Further details regarding the dimensioning of the clamping system are presented in Section 2.3.

### *2.3. Design of the Clamping System*

Figure 4 depicts a detailed view of the clamping system.




| | |
|---|---|
| 1 | Bolt |
| 2 | Cap |
| 3 | Column |
| 4 | Bellevile washer (×6) |
| 5 | Counterplate |

**Figure 4.** Detail of the clamping screw.

As illustrated in Figure 4, the screw is tightened on a central column, which transfers the load to the base plate (not shown in Figure 4). To this end, 6 screws, M20X60 grade 10.9, were used. According to ISO 898-1 [11], these screws have a proof load equal to 203 kN. Therefore, the maximum value of Fn before yielding is 1218 kN, i.e., more than 5 times the maximum estimated value in Table 1.

The stiffness $K_b$ of each screw can be approximately calculated as in Equation (2):

$$K_b = \frac{E\,A_t}{L_0} \tag{2}$$

where $E$ is the elastic modulus of the material, $A_t$ is the nominal stress area and $L_0$ is the free length of the screw. Assuming $E = 205{,}000$ MPa, and with $L_0 = 32$ mm and $A_t = 245$ mm$^2$ [11], it can be found that $K_b = 1.57 \times 10^6 \frac{\text{N}}{\text{mm}}$. As there are six parallel screws, the total stiffness is $6K_b$.

Fluctuations in $F_N$ resulting from the elastic deformations of the pad, previously discussed in Section 2.2, can lead to a sudden variation in preload, which may in turn lead to the inconsistent application of the normal force (thus, the shear force) to the fixture along the stroke. To prevent this issue, a set of Belleville washers is employed against the counterplate. As depicted in Figure 4, the screw underhead region makes contact with a cap, which in turn compresses six Belleville washers against the counterplate.

The Belleville washers have an external diameter $D_e = 125$ mm, an internal diameter $d_i = 61$ mm, a thickness $t = 6$ mm and a free height $h_0 = 3.6$ mm. The stiffness is determined using the elastic modulus $E = 210$ GPa. The stiffness of an individual washer can be calculated using Equation (3), with $C2'$ and $C2''$ defined as in Equation (4) and Equation (5), respectively [12], where $\alpha = D_e/d_i$:

$$K_{1w}(\delta) = \frac{E\delta}{(1-\nu^2)R^2}[C_2'(h-\delta)(h-\frac{\delta}{2})t + C_2''t^3] \tag{3}$$

$$C_2' = \pi(\frac{\alpha+1}{\alpha-1} - \frac{2}{ln(\alpha)})(\frac{\alpha}{\alpha-1})^2 \tag{4}$$

$$C_2'' = \frac{\pi}{6}ln(\alpha)(\frac{\alpha}{\alpha-1})^2 \tag{5}$$

The arrangement of the washers consists of three pairs of washers (i.e., parallel-connected), working in series. This configuration will be named 2P-2P-2P in the following. Given that each of the six columns is equipped with a similar set of washers, the final spring arrangement is as depicted in Figure 5.

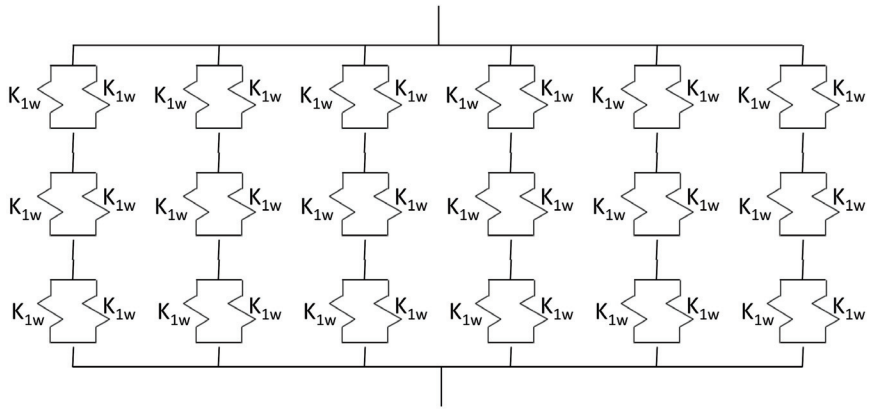



**Figure 5.** Scheme of the washers' configuration.

Consequently, the overall equivalent stiffness is equal to $K_eq = 4K_{w1}$.

Figure 6 illustrates the displacement ($\delta$) versus force ($F$) plot for the Belleville washers.

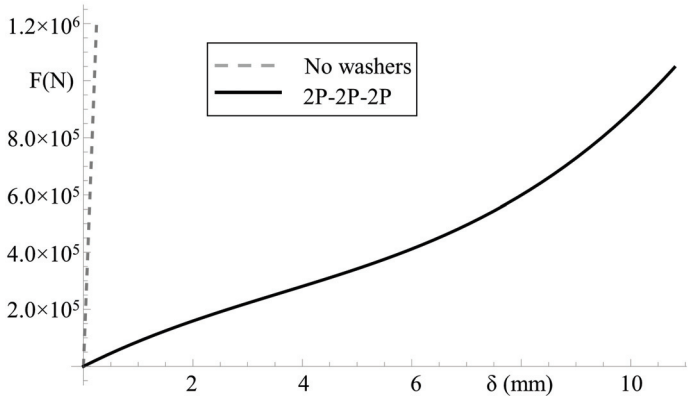



**Figure 6.** Displacement ($\delta$) versus force ($F$) plot for the set of Belleville washers.

As observed in Figure 6, this configuration effectively reduces the variation in axial load on the pad–fixture contact in the event of slight thickness variations thereof. Specifically, a nominal force of 240 kN corresponds to a displacement of 3.31 mm for the washers. Deviations of ±20% from this displacement value result in corresponding variations of ±16% in the contact force.

It is interesting to highlight that the adoption of Belleville washers allows for the easy adaptation of the stiffness of the system to the loads used for testing. For example, assuming that all six washers are used, the following alternative configurations can be obtained:

- Six washers in parallel (6P);
- Three washers in parallel with the other three washers in parallel (3P-3P);
- Two pairs of washers in parallel and two single washers, working in series (2P-2P-P-P);
- One pair of washers in parallel and three single washers, working in series (2P-P-P-P-P);
- Six washers in series (P-P-P-P-P-P).

Figure 7 compares the force versus displacement curves of the different configurations, including the one presented above.

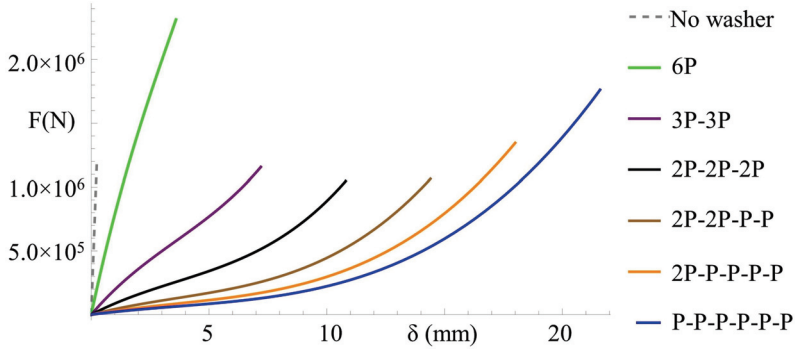



**Figure 7.** Displacement ($\delta$) versus force ($F$) plot for different configurations of Belleville washers.

By observing Figure 7, it can be seen that a broad range of properties can be achieved by simply changing the orientation of the washers.

### *2.4. Numerical Assessment of Stiffness*

To validate the stiffness of the testing system, a finite element analysis (FEA) was conducted. The objective of this analysis was to estimate the maximum displacement of the plate and counterplate following the tightening of the screws. For safety purposes, the calculation incorporated a preload of 203 kN on each bolted connection, corresponding to the force at which the screws yield. The model employed for the calculation is illustrated in Figure 8.

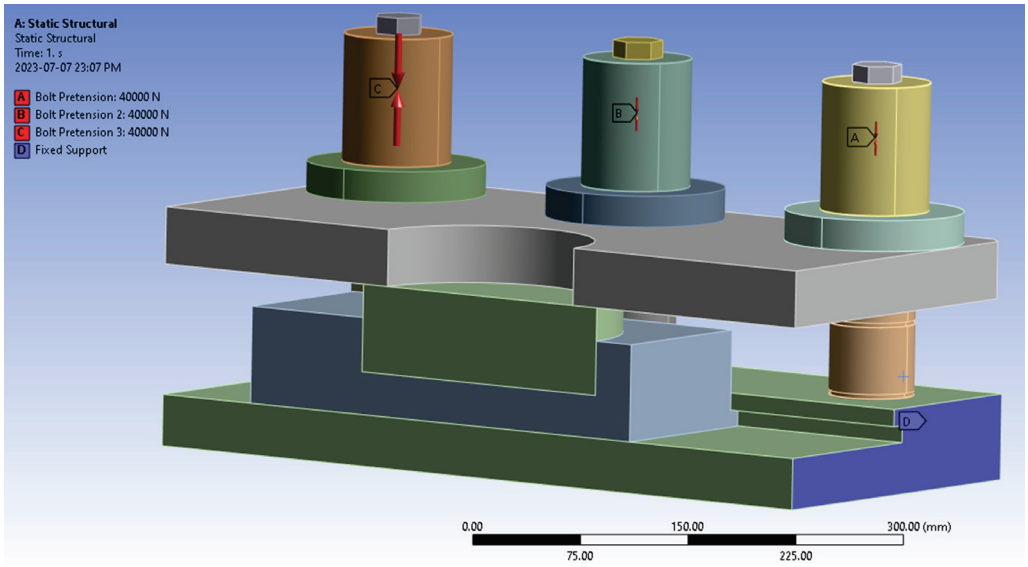



**Figure 8.** Finite element model used for the stiffness verification.

The model was simplified for the analysis, which was run by Ansys R.17.2. Firstly, extraneous details such as centering holes were eliminated from the 3D model. Additionally, since the Belleville washers were fully compressed under the investigated load, they were substituted with an annular element having a height of 21.6 mm, which was six times the thickness of a single washer. The rubber pad was treated as a rigid element made of steel that comes into contact with the counterplate at the location of the cap ring. The connections between the equipment and the testing machine were disregarded as they had a minimal influence on the analysis. Finally, the simulation took advantage of the equipment's symmetry to reduce the computational effort.

The mesh used for simulation, which is shown in Figure 9, comprised 351,189 nodes and 147,511 elements. Second-order hexahedral and tetrahedal elements were used.

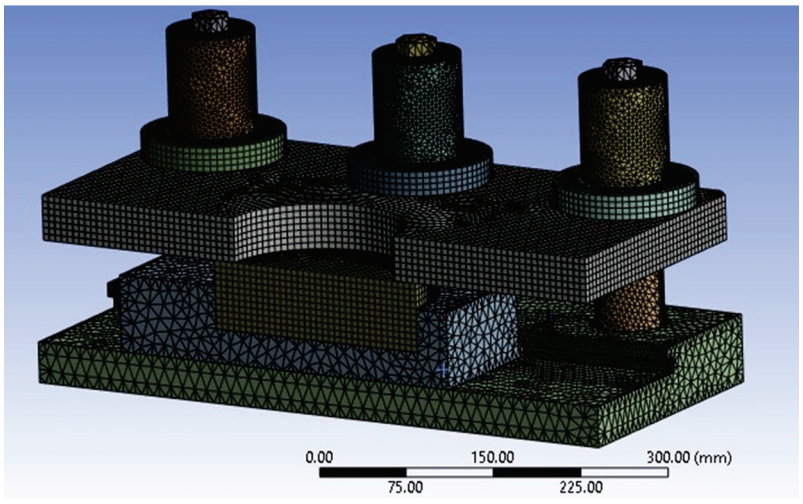



**Figure 9.** Mesh of the assembly used for the finite element analysis.

Contacts among the elements of the system were assumed to be fixed in the case of planar mating surfaces and frictionless in the case of cylindrical coupling. CONTA174-TARGE170 elements were used in the contact regions.

For the purposes of the calculation, the system was assumed to be fixed on one side of the blue-colored base plate shown in Figure 8. The bolt pretension tool was employed to apply the axial force to the bolts, which were modeled by means of solid bodies and meshed

with tetrahedral elements. The contact element in the underhead region was bonded for the sake of simplicity.

The simulation results, indicating the overall displacement of the two plates, are presented in Figure 10.

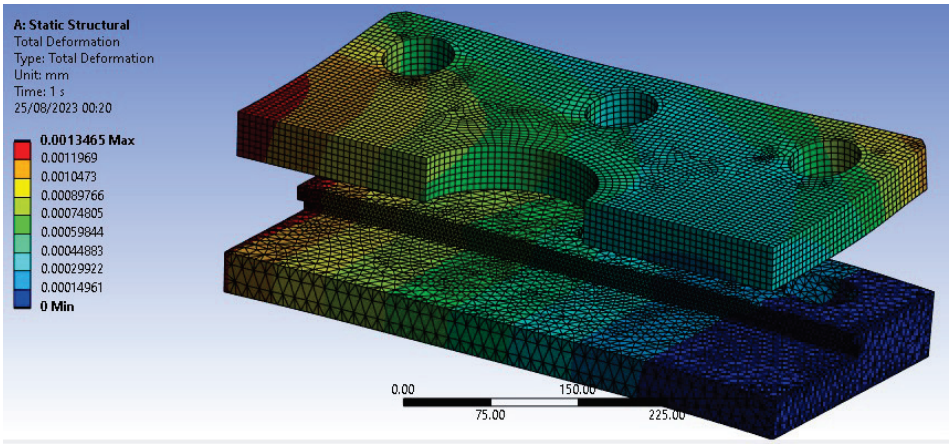



**Figure 10.** Results of the FEA in terms of total displacement on the plates (scale 2100×).

The maximum displacement observed on both plates was found to be slightly below 1.5 µm, which is considered negligible for this particular application. This negligible displacement aligns with the discussion in Section 2.3, where the clamping system's design aims to maintain the load as constant as possible during the deformation of the rubber pad. For instance, in a realistic configuration employing a 2P-2P-2P arrangement of washers and a nominal normal load $F_N = 180$ kN, referring to the characteristic curve shown in Figure 6, at $\delta = 2.322$, the value of $F_N$ measures 180.03 kN. Deviations of $\pm 15$ µm on $\delta$ result in a fluctuation of $\pm 0.09$ kN, representing an error of $\pm 0.05\%$ on $F_N$. Moreover, it is essential to note that the calculated value of 1.5 µm considers the maximum admissible preload on each bolt, significantly higher than the actual load used for testing.

### *2.5. Design of the Connection to the Testing Machine*

As described in Section 2.2, the base plate is connected to an intermediate block, which in turn is solid with the adapter. The connection between the base plate and the block is achieved by means of 5 screws M20x60 grade 10.9, placed as shown in Figure 11.

To design this connection, an estimation of the tangential force $F_t$, namely the measured variable, was needed. This estimation was made considering the tangential force acting on the tire during braking. In more detail, the design landing stop acceleration according to [9] is $a_z = 3.1$ m/s$^2$. As an A380 has $N_w = 16$ braking wheels, the tangential force $F_z^*$ on each tire can be estimated as in Equation (6):

$$F_T = \frac{m_a\, a_z}{N_w} = 75 \text{ kN} \tag{6}$$

The clamp exerted by the bolts must be sufficient to avoid the sliding between the mating surfaces. The load $R_T$ that each screw must apply to this end can be calculated as in Equation (7):

$$R_t = \frac{F_T}{n\,\mu} \tag{7}$$

where $n = 5$ is the number of screws, and $\mu$ is the coefficient of friction. The latter is assumed to be $\mu = 0.15$ in the case of non-lubricated steel on steel surfaces [13]. Under this hypothesis, each screw must ensure a 93.3 kN clamping force.

As the two plates are not aligned, a bending moment $M_f$ arises in the region of the bolts. The modulus of this bending moment is calculated as in Equation (8):

$$M_f = F_T(\frac{t_1}{2} + \frac{t_1}{2}) \tag{8}$$

where $t_1$ and $t_2$ are the thickness of the base plate and intermediate block, respectively. According to the dimensions shown in Figure 11, it is $M_f = 3900$ Nm.

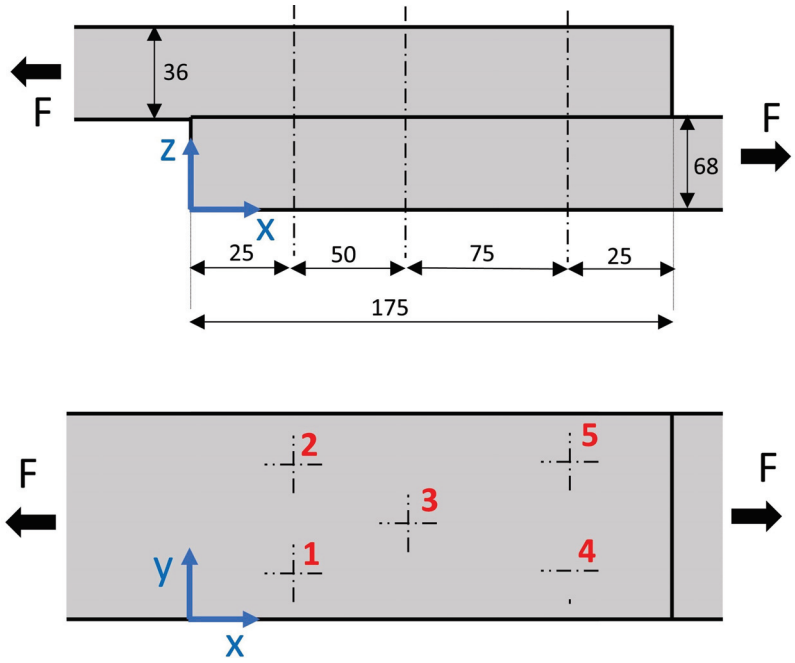



**Figure 11.** Schematic representations of the screws connecting the base plate to the intermediate block (parts 4 and 5, respectively, in Figure 2). All the dimensions are in mm.

As all the screws have the same size, their centroid coordinate along the X-axis can be calculated as in Equation (9):

$$x_G = \frac{\sum_1^5 x_i}{5} \tag{9}$$

where $x_i$ is the x-coordinate of the generic screw. It can be found that $x_G = 85$ mm. The additional preload $R_{N,j}$ to be applied on the generic $j$-th screw in order to balance the momentum is given in Equation (10):

$$R_{n,j} = M_f \frac{|x_j - x_G|}{\sum_1^5 (x_i - x_G)^2} \tag{10}$$

It can be found that the most critical elements are the screws numbered 4 and 5 in the scheme of Figure 11, whose additional preload is $R_{n,4} = R_{n,5} = 16{,}095$ N. Indicating as $F_i$ the preload on the screw, the safety factor $SF$ can be calculated as in Equation (11):

$$SF = \frac{F_i}{R_{n,4} + R_t} \tag{11}$$

As discussed in Section 2.3, the proof load of M20 10.9 equal to 203 kN. Assuming an utilization factor equal to 0.8, it can be found $SF = 1.4$.

### *2.6. Handling and Operation of the Testing System*

For testing purposes, the rubber pad is mounted on the plate, while the cap is positioned on the counterplate. The system is subsequently closed, as illustrated in Figure 2, using six screws.

The total weight of the testing system is approximately 360 kg. Therefore, the assembly and installation of the equipment require the use of a forklift. The supports highlighted in Figure 12 are specifically designed to accommodate the forklift truck's fork, enabling the convenient and safe handling of the equipment.

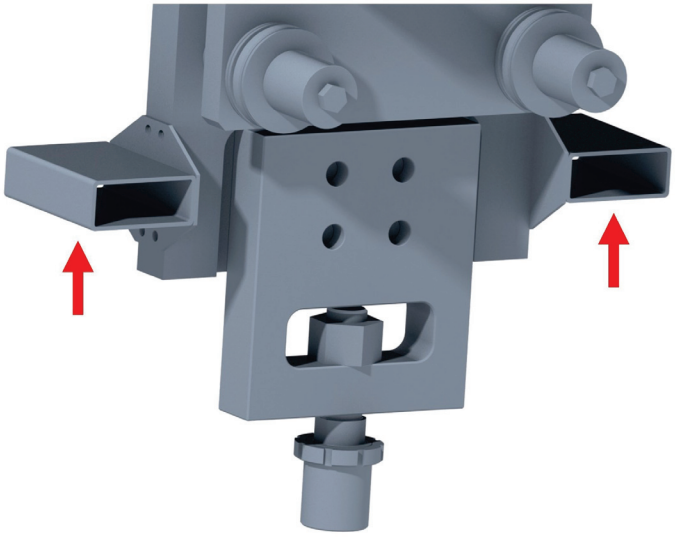


**Figure 12.** Supports for handling of the testing equipment by means of a forklift.

The testing equipment is lifted into the testing area using the forklift, and the machine is connected to the two adapters (labeled as 3 and 6 in Figure 2). The testing system installed on the Instron press is shown in Figure 13.

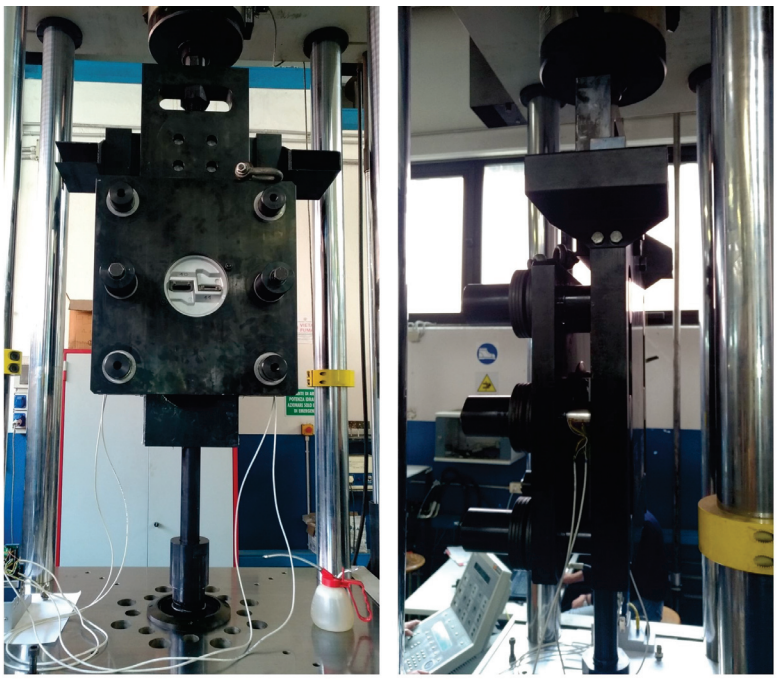


**Figure 13.** Testing equipment assembled on the Instron hydraulic press.

After assembling the system, the six bolts are tightened to achieve the desired value of the normal load ($F_N$) as indicated by the strain gauges. Subsequently, the test begins by lowering the piston of the testing machine until the pad completely disengages from the cap. Following this, the piston movement is reversed, applying compression to induce the pad to slide in the opposite direction.

After testing a configuration, loosening the six screws allows the adjustment of the counterplate, enabling the replacement of the rubber pad and fixture without the need to remove the entire equipment from the testing machine. This feature significantly saves time, especially when conducting multiple tests.

## 3. Results and Discussion of Experimental Tests

The equipment was used to test an innovative design of runway light fixtures in combination with different tire materials. The tests were conducted at a speed of 1 mm/s, with a 30-s delay before the backward movement. Given that the diameter of the tested fixtures was 200 mm, the entire test duration amounted to 5 min and 30 s.

A representative diagram of the force measured during the test is shown in Figure 14.

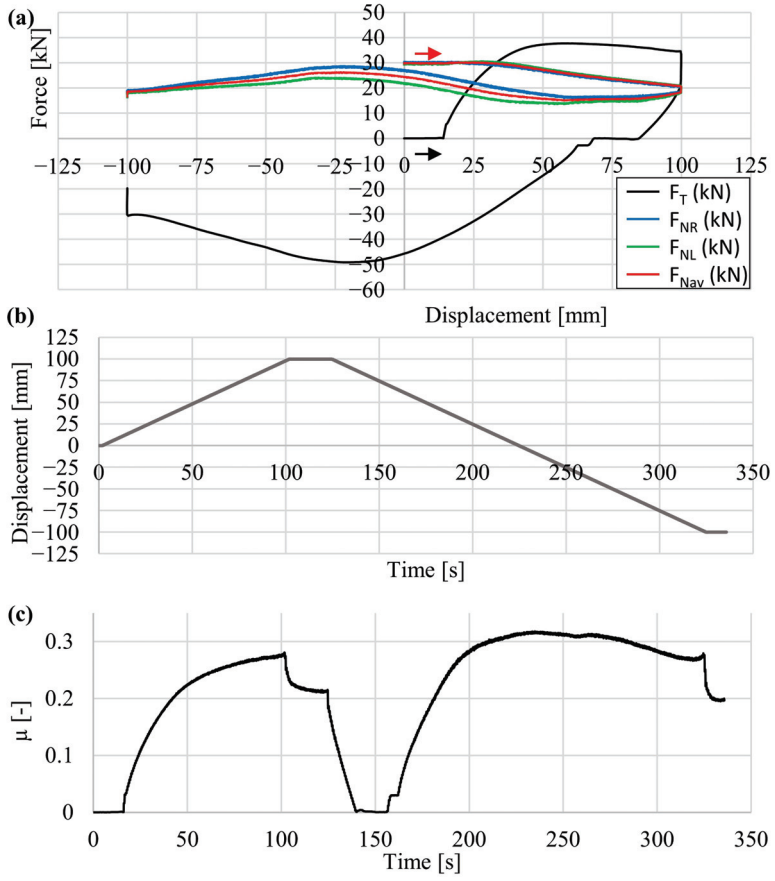



**Figure 14.** Plot of (**a**) tangential and normal forces versus displacement, (**b**) Displacement versus time and (**c**) apparent coefficient of friction versus time (initial normal force $F_N = 180$ kN).

Figure 14 shows several values, expressed as functions of the displacement $u$, namely (i) the tangential force measured by the load cell ($F_T$), (ii) the normal load on the left and right columns ($F_{NL}$ and $F_{NR}$, respectively) read by the strain gauges and (iii) their average value ($F_{Nav}$). The plots should be read in the direction indicated by the arrows to observe the evolution of forces during the test. For clarity, the displacement versus time plot of the test is reported in the bottom part of Figure 14. The zero displacement position corresponds to the configuration in which the rubber pad is coaxial to the cap.

By observing the plot of $F_T$, it is possible to distinguish different phases.

In the first interval, the tangential load remains almost constant while the displacement increases. During this phase, the elastomer of the pad is prestressed by shear stress. Once the elastic deformation of the pad is completed, $F_T$ rapidly increases to a maximum value and then slightly decreases. This region corresponds to the sliding of the pad on the first half of the cap.

Once the value of $u$ reaches 100 mm (roughly half the diameter of the light fixture), the motion of the system is inverted, i.e., a compression force is applied by the press on the testing equipment. In this phase, force $F_T$ decreases to 0 as the compression of the rubber pad is released. Then, there is a phase of null tangential load similar to that observed at the beginning of the test, during which the pad is deformed. Finally, the absolute value of the tangential load increases to a peak around $u = 0$ mm and then decreases, moving to $u = -100$ mm. This finding is consistent with the shape of the light fixture, whose maximum thickness is in the central region.

By observing the trend of normal forces, it can be seen that the initial force on each column was set to 30 kN, i.e., the nominal value of $F_N$ for this test was 180 kN. During the first sliding, the normal force slightly decreases while the pad moves away from the central point. This can be attributed to the reduction of the compression force on the pad due to the lower height of the cap. The decrease in normal force at $u = 100$ mm is approximately 38% of the nominal value.

In the second run, the normal force increases to a maximum corresponding to that of $F_T$; it then decreases while approaching $u = -100$ mm. It is worth mentioning that the peak reached in this phase is 12% lower than the initial value. This indicates the occurrence of several phenomena, among which are (i) embedding of the elastomeric pad in the receptacle of the sliding carriage, (ii) wear/abrasion of the elastomeric component on the contact side and (iii) self-adjustment of the loose parts of the apparatus.

Figure 14 reports also the apparent coefficient of friction $\mu$, calculated as in Equation (12):

$$\mu = \frac{F_T}{6F_{Nav}} \tag{12}$$

The calculation in Equation (12) is an estimation based on the hypothesis that the plate is perfectly rigid, i.e., all the Belleville washers undergo the same displacement. It can be observed that the coefficient of friction increases during the second run. This is consistent with the wear of the elastomeric pad on the contact side.

For the sake of comparison, Figure 15 shows the plots of tests carried out with an initial value of $F_N$ equal to 100 kN.

By comparing Figure 14 and Figure 15, it can be observed that the percent reductions in $F_N$ are more relevant in the second case. Specifically, the reduction in $F_N$ at the end of the first sliding is equal to 58% of the initial value, while the difference between the initial value and the second peak is equal to 24%. This finding suggests that the normal load applied by the system is more stable at higher values. This result is consistent with the characteristics of the elastic system presented in Section 2.3 and shown in Figure 6.

It is crucial to note that due to the lack of alternative equipment designed for this specific type of testing, the comparison of these results with any existing primary data is currently not possible.

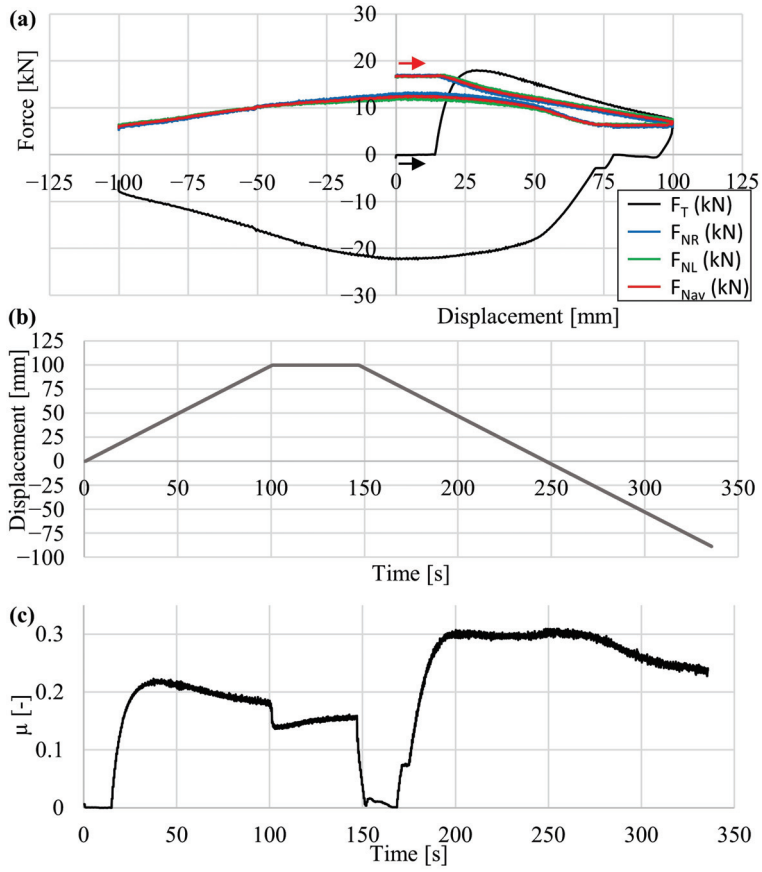



**Figure 15.** Plot of (**a**) tangential and normal forces versus displacement, (**b**) Displacement versus time and (**c**) appearent coefficient of fricion versus time (initial normal force $F_N = 100$ kN).

## 4. Conclusions

The research detailed in this paper outlines the development and construction of an innovative piece of equipment specifically designed to evaluate the interaction between tires and runway light fixtures during landing sequences. The finalized design exhibits ease of manufacturability while ensuring exceptional stiffness during testing, substantiated through finite element analysis (FEA). The use of Belleville washers enables the seamless reconfiguration of the system to accommodate the varying normal loads required for the tests.

Significantly, this equipment does not necessitate specialized actuation, as it is tailored for use with a universal testing machine. This feature broadens its accessibility, offering numerous research centers and companies the opportunity to conduct analyses on runway light fixtures. Furthermore, the design's incorporation of forklift supports simplifies the handling of the testing equipment.

Preliminary tests have evidenced the efficacy of this equipment in measuring the tangential force exerted on the runway fixture. Notably, the utilization of washers contributes to minimizing the force fluctuations attributable to fixture shapes.

The collective merits outlined above position the testing equipment elucidated in this paper as a notable advancement in experimental methodologies for the assessment of runway lighting.

**Author Contributions:** Conceptualization, M.D.A. and S.F.; methodology, M.D.A., S.F. and D.C.; validation, M.D.A., G.O., M.M. and C.S.; formal analysis, G.O.; investigation, D.C., M.D.A., S.F., M.M., G.O. and C.S.; data curation, G.O.; writing—original draft preparation, M.M. and C.S.; writing—review and editing, M.M., C.S. and M.D.A.; supervision, D.C. and M.D.A.; project administration, M.D.A. and S.F.; funding acquisition, M.D.A., S.F. and D.C. All authors have read and agreed to the published version of the manuscript.

**Funding:** The research on the equipment described in this paper has been partially funded by OCEM Airfield Technology, Energy Technology srl.

**Data Availability Statement:** Additional information can be requested from the authors.

**Acknowledgments:** The authors would like to thank Matteo Mazzotti at OCEM Airfield Technology, Energy Technology srl, Bologna (IT) for supporting this project.

**Conflicts of Interest:** The authors declare no conflicts of interest.

## References

1. Granado, J.; Chávez, J.; Torralba, A.; Oria, A.C. Modeling airfield ground lighting systems for narrowband power-line communications. *IEEE Trans. Power Deliv.* **2010**, *25*, 2399–2405. [CrossRef]
2. Sudjoko, R.I.; Hartono; Hariyadi, S.; Suwito. Design and Simulation of Airfield Lighting System Using 8 Luminaire in Airfield Lighting Laboratory at Politeknik Penerbangan Surabaya. *J. Phys. Conf. Ser.* **2021**, *1845*, 012034. [CrossRef]
3. Chlebek, J. Runway lighting systems as a key tool to extend operational capabilities of VFR airports. *Transp. Res. Procedia* **2019**, *43*, 236–242. [CrossRef]
4. McMenemy, K.; Niblock, J.; Peng, J.X. Monitoring the Performance of Aerodome Ground Lighting. *Int. Airpt. Rev.* **2008**, *12*, 60–64.
5. Sitompul, D.S.D.; Surya, F.E.; Suhandi, F.P.; Zakaria, H. Runway Edge Light Photometry by Vertical Scanning Method Using Drone Mounted Photodiode Array. In Proceedings of the International Conference on Electrical Engineering and Informatics, Bandung, Indonesia, 9–10 July 2019; pp. 301–305. [CrossRef]
6. Hebborn, A. *A380 Landing Gear and Systems—The Feet of the Plane*; Airbus: Hamburg, Germany, 2008.
7. Commercial, B. *777-200/300 Airplane Characteristics for Airport Planning*; Boeing Co.: Seattle, WA, USA, 1998.
8. Administration, F.A. *Advisory Circular AC150/5345-42H*; Technical Report; Federal Aviation Administration, U.S. Department of Transportation: Washington, DC, USA, 2015.
9. EASA. *Certification Specifications for Large Aeroplanes*; Cs-25; EASA: Cologne, Germany, 2005; p. 750.
10. Croccolo, D.; De Agostinis, M.; Fini, S.; Mele, M.; Olmi, G. Effect of different underhead shot-peening and lubrication conditions on high-strength screws undergoing multiple tightenings. *Tribol. Int.* **2023**, *188*, 108874. [CrossRef]
11. *ISO 898-1: 2013*; Mechanical Properties of Fasteners Made of Carbon Steel and Alloy Steel. Part 1: Bolts, Screws and Studs with Specified Property Classes—Coarse Thread and Fine Pitch Thread. Technical Report; ISO: Geneva, Switzerland, 2013.
12. Wahl, A. *Mechanical Springs*, 2nd ed.; Mc GrawHill Book Company: Berlin, Germany, 1964.
13. Niemann, G.; Winter, H.; Hohn, B.R. *Maschinenelemente Bd I*; Springer: Berlin, Germany, 2005.

**Disclaimer/Publisher's Note:** The statements, opinions and data contained in all publications are solely those of the individual author(s) and contributor(s) and not of MDPI and/or the editor(s). MDPI and/or the editor(s) disclaim responsibility for any injury to people or property resulting from any ideas, methods, instructions or products referred to in the content.

machines

MDPI

*Article*

# Design and Development of a Brake Test Bench for Formula SAE Race Cars

**Luca Vecchiato [1], Matteo Negri [1], Giulio Picci [1], Luca Viale [1], Giulio Zaltron [1], Stefano Giacometti [2] and Giovanni Meneghetti [1,*]**

[1] Department of Industrial Engineering, University of Padova, via Venezia, 1, 35131 Padova, Padova, Italy; luca.vecchiato@unipd.it (L.V.)
[2] OZ Racing S.p.A., via Monte Bianco, 10, 35018 San Martino di Lupari, Padova, Italy
* Correspondence: giovanni.meneghetti@unipd.it; Tel.: +39-049-8276751; Fax: +39-049-8276785

**Abstract:** The optimization of the brake systems is crucial for vehicle performance and safety of Formula SAE (FSAE) race cars. This study introduces a specialized brake test bench designed to enhance the understanding and testing of these systems. The bench integrates a rotating mechanical system mounting a brake disc-caliper group, which is driven by an electric motor, a pneumatic brake pedal assembly to simulate real braking conditions, and a comprehensive array of sensors that facilitate the measurement of critical parameters, such as rotation speed, braking torque, oil pressure, and disc temperature. Its structure, sensor integration, and control electronics are fully described, demonstrating the capability to replicate on-track scenarios in a controlled environment. The results underscore the utility of the bench in providing precise and consistent testing conditions essential for analyzing the efficiency, durability, and safety of the braking systems of FSAE race cars.

**Keywords:** brake system; FSAE; mechanical testing; electrical actuation; pneumatic actuation

## 1. Introduction

Formula SAE® is a series of competitions in which different teams of university undergraduate and graduate students compete to design, construct, test, and promote a race car prototype that adheres to stringent regulations [1] and mimics real-world racing standards. The present work underscores the importance of the brake system in these high-performance vehicles [2–5], which are subject to intense engineering scrutiny and competitive performance. Traditional design and testing methods fall short, particularly since the brake system can typically only be evaluated after the entire vehicle is assembled, leading to potential issues being discovered too late in the development process [6].

Over the years, the need to overcome these limitations has suggested the adoption of laboratory brake testing devices, which are superior in efficiency and control to vehicle testing, as they involve fewer variables and reduced testing and engineering resources [7]. Numerous test systems have been proposed and adopted in the automotive sector (but also in other sectors, for example, railways [8–10]), each distinguished by the test procedures, experimental setups, and samples they adopt [11]. Generally, testing machines can be categorized into three main types based on whether the experimental tests are conducted using a pin-on-disc (or block-on-ring) configuration [12–16], a brake dynamometer (also called inertia dynamometer) [17,18], or a roller chassis bench (also called chassis dynamometer) [6,19]. Clear and useful overviews of the main testing systems, along with a concise history of the development of automotive brake test systems, are available in [20,21].

Despite the wide range of dynamometers already available, the need for designing and building a dynamometer dedicated to FSAE cars is two-fold. The first and most important concern is the size of the machines. For an FSAE car's brake system, commercial dynamometers are generally quite oversized since they are designed for road vehicles. To clarify this point, consider that standard cars are designed to last hundreds of thousands of

kilometers and to travel at cruising speeds of up to 130 km/h or even more. As a result, the smallest commercial inertia dynamometers are designed to test brake systems with maximum rotational speeds of up to about 300 rad/s, simulate inertias ranging from tens to thousands of kg·m$^2$, apply braking torques in the order of 2000–5000 Nm, and supply the brake line with pressures even higher than 200 bar. It will be shown in the following section that these values are out of scale compared to those of a FSAE car, which are quite lighter and typically meant to cover at most a few thousand kilometers with a maximum speed of about 90 km/h. The second reason, more trivial, is identified in the cost of the machinery, which clearly follows the size of the machine.

Nevertheless, besides the size or the costs of the selected setup, another reason justifying the need for developing a brake test bench dedicated exclusively to FSAE cars concerns the operating mode of the bench and the adopted test protocols. Noteworthily, considerable effort has been invested in creating guidelines to minimize variability and enhance the correlation between dynamometer and vehicle test results. Indeed, factors like the measuring system (dynamometer and test setup) and the methodology (laboratory procedures, data gathering, and reporting), along with variations in the friction pair (both within and across production batches of friction materials and rotors), significantly affect the consistency and range of the brake parameters measured during a specific test (or sequence of tests), e.g., the friction coefficient [7,22]. This aspect, as well as the need to homologate mass-produced braking systems with increasingly larger volumes, has made it progressively necessary to define appropriate standardized test protocols to perform repeatable measurements at very low time and cost [7,11,20,22]. As a result, numerous standards (e.g., [23–29]) have been established, each marked by rigorous testing protocols that define a sequence of braking runs, regulated by pressure or deceleration, across various conditions (including braking and release speeds, pressure or deceleration levels, and brake temperature).

While the use of standards provides a benchmark for repeatable and objective assessments and ensures a standardized level of safety and quality, on the other hand, it may prove inadequate or even restrictive for racing, which often demands customized and generally higher performance and specifications compared to standard vehicles. In fact, racing components are designed to maximize performance in a specific track or test (e.g., brake test, autocross, or endurance for FSAE cars [1]), often sacrificing cost-effectiveness, durability, and other features (which are essential in standard vehicles).

Consequently, there is a need to develop equipment and testing protocols specific to the sector that consider the unique requirements and allow for the study of the braking system's performance in light of its real operating conditions.

There are some examples in the literature of brake test benches specifically designed and built for FSAE cars. For instance, the authors in [2] proposed an experimental setup that mimics the entire braking system of the car, including the pedal assembly. However, it is limited to tests of the pedal assembly and the pipeline since it has a stationary brake disc. Other authors have developed dynamic systems dedicated to FSAE vehicles by adapting a commercial dynamometer [30] or creating a new dynamometer from scratch [3]. However, the proposed systems are limited to braking at constant speed and pressure or according to standard test protocols and regulations [3,30].

In other words, as far as the authors know, there are no dynamometers for FSAE vehicles in the literature that accurately reproduce the entire braking system of the car under real operating conditions. Accordingly, this work sets out to overcome these challenges by creating a brake test bench that allows for earlier and more detailed testing of the brake system for FSAE cars. More in detail, the present contribution describes a comprehensive study on the design, development, and testing of a brake test bench tailored for Formula SAE race cars and conceived to replicate the real-world conditions the car's braking system would undergo during races. The proposed brake test bench can faithfully replicate both the entire braking system (from disc, pad, and caliper to tubing, pump, and pedal assembly) and the real operating conditions experienced in the track. This enables the testing and

comparison of different brake disc-caliper combinations and friction pairs under non-standard operating conditions, such as those derived from actual track data. It can also allow for the study of the brake system's thermal regime under realistic operational loads, making it possible to compare and validate analytical/numerical models (as undertaken, for example, in [30] for a simple load history). Eventually, it permits evaluating and verifying the structural durability and fatigue strength of new non-commercial engineering solutions for the braking system, studying fading behavior and wear mechanisms, or investigating the differences in pedal feedback under various loading conditions.

In what follows, a detailed examination will be given of the brake test bench's concept, followed by an in-depth analysis of the main components and electronic control system. Eventually, attention will be directed towards replicating the on-track conditions on the test bench, focusing particularly on the velocity profile and the brake disc temperature profile.

## 2. The Brake Test Bench: Concept and Overview

The brake test bench is a complex assembly of mechanical and electronic systems, including moving mechanical components, a pneumatic actuation system, a powered electrical line, and a sensor network connected to a single electronic control system running LabView code. A schematic and essential representation of the brake test bench is shown in Figure 1, while some images of the actual bench are provided in Figure 2.

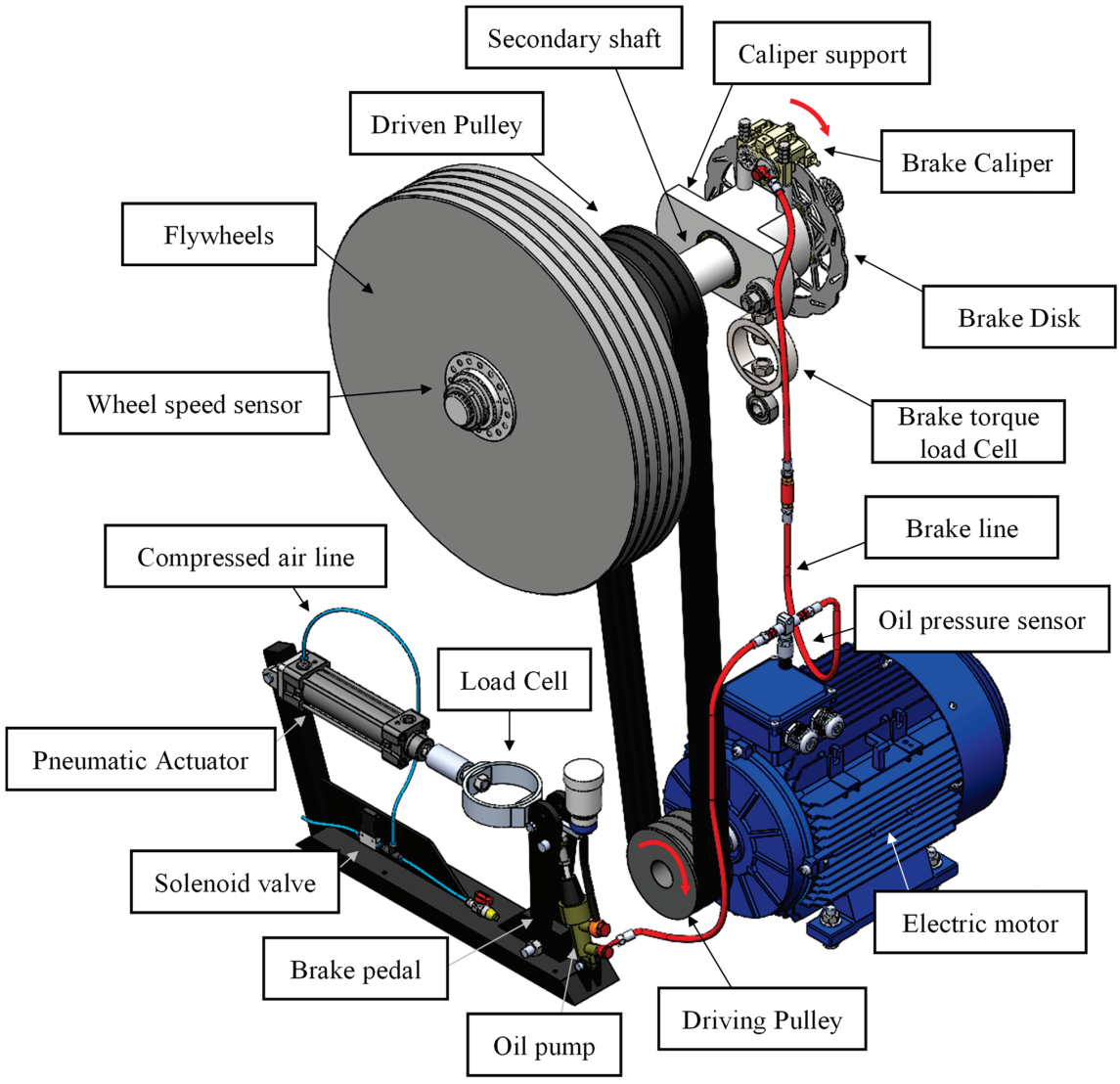



**Figure 1.** Layout of the brake test bench.

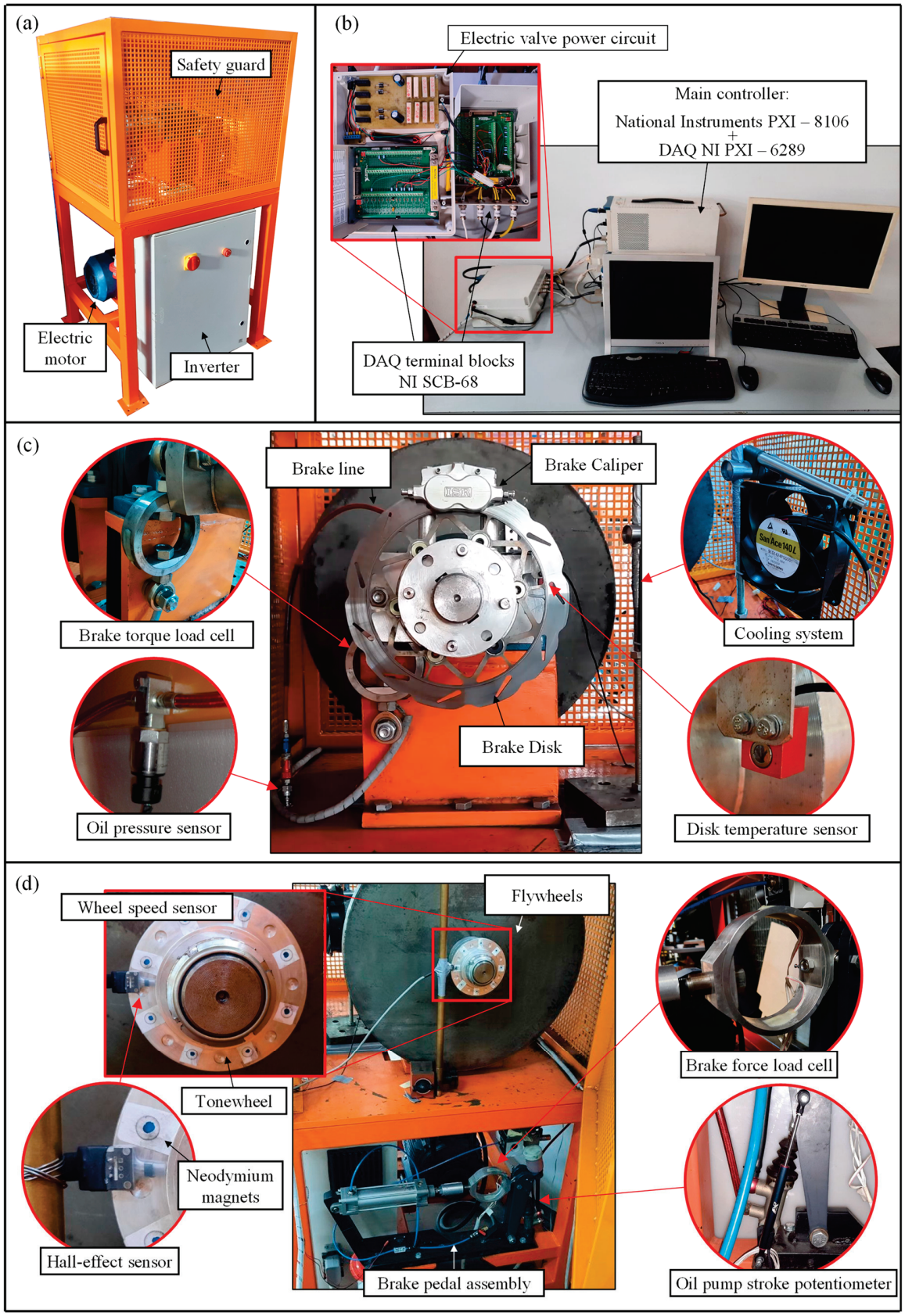



**Figure 2.** The brake test bench with indications of each component and sensor along with their location: (**a**) view from outside of the test rig; (**b**) view of the control electronics and of the workstation; (**c**) view from the left side; and (**d**) from the right side of the bench.

The operating principle of the brake test bench is very straightforward: a brake disc is installed and allowed to float on a rotating shaft, which is accelerated by an electric motor and decelerated by a brake caliper attached to the bench's frame (Figure 1). In more detail, the system consists of a steel tubular structure (Figure 2a) to which the rotating shaft is attached via two ball bearings. Its rotation is permitted by a belt drive system powered by a three-phase asynchronous electric motor (Figure 1), which is controlled by a dedicated electronic control system (Figure 2b). The bench is equipped with a series of flywheels (in varying numbers as needed) that accumulate kinetic energy to be dissipated during the braking phase, simulating the vehicle's inertia. As mentioned, this braking is made possible by the presence of the brake caliper (Figure 2c), which is connected to the frame and operated by a braking system with a pedal and brake pump similar to that of a real vehicle (Figure 2d).

The concept of the main components of the bench, such as the flywheel mass and electric motor, was aimed at replicating the most severe braking conditions encountered in the car, i.e., in the case of the highest initial speed and deceleration. Accordingly, the first step was to assess the maximum kinetic energy stored by the individual front wheel group, as this is the most stressed due to load transfer:

$$E_{\mathrm{K,F},max} = \frac{1}{2} m_{\mathrm{F},max} v_{max}^2 \tag{1}$$

where $m_{\mathrm{F},max}$ is the maximum value of the car's mass that is transferred to each front wheel group during braking, and $v_{max}$ is the maximum speed of the car. Assuming a flat track, a symmetric car, and symmetry of loads in the pitch plane (perfectly straight accelerations and braking), an effective estimate of $m_{\mathrm{F},max}$ can be made using the model shown in Figure 3.

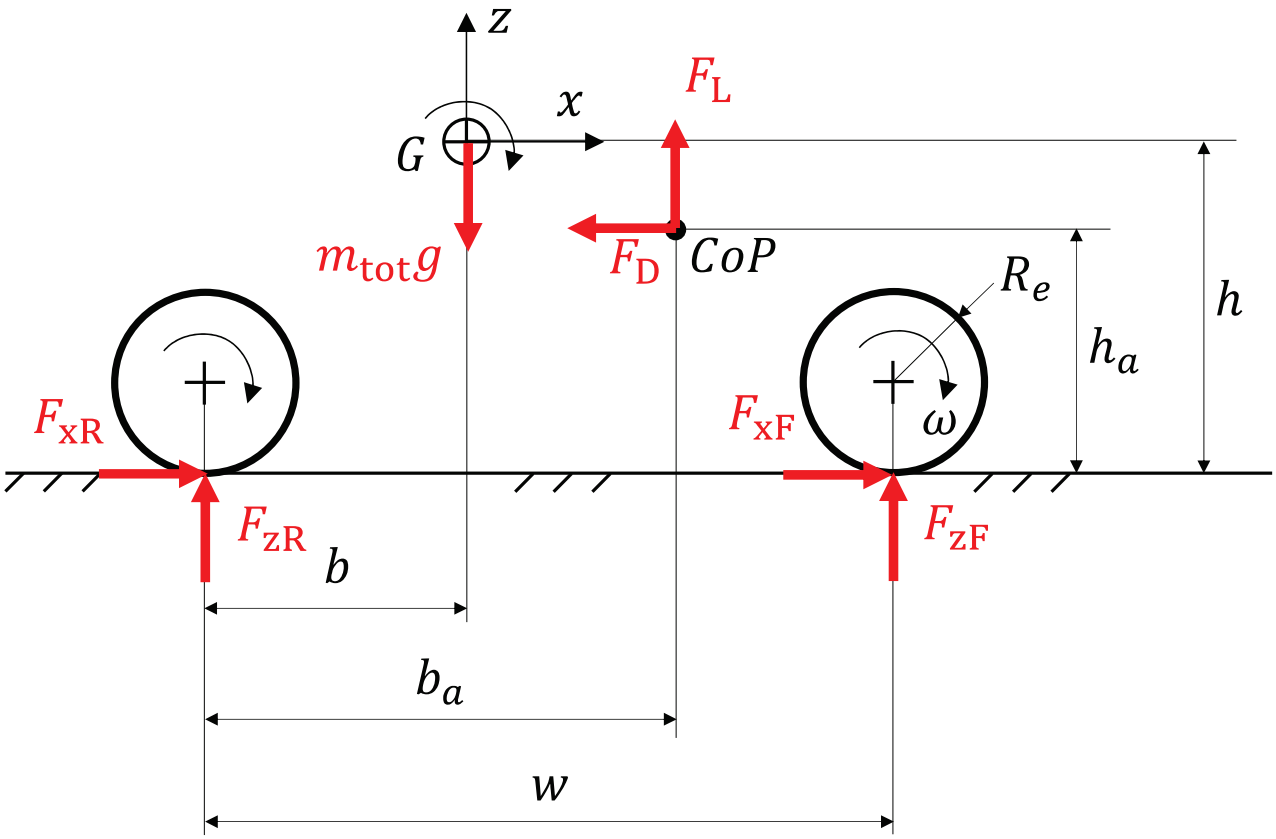



**Figure 3.** Schematic model of the FSAE car in the pitch plane.

In this model, the vehicle and driver are represented by a point mass $m_{\text{tot}}$ at the overall center of mass $G$. This is located at a distance $b$ and a height $h$ from the rear wheel contact point, while the center of pressure, i.e., the point of application of the resultant aerodynamic lift and drag forces, is at the coordinates ($b_a$,$h_a$). The wheelbase of the vehicle is $w$. The external forces acting on the vehicle are the drag force $F_{\text{D}}$, the lift force $F_{\text{L}}$, the weight $m_{\text{tot}} \cdot g$ and the forces exchanged by the tires with the ground in the pitch plane, i.e., $F_{\text{xR}}$, $F_{\text{zR}}$, $F_{\text{xF,}}$ and $F_{\text{zF}}$ (the latter, given the symmetry of the problem, are twice the force exchanged by each of the tires with the ground).

With reference to the schematic in Figure 3, the following motion equations can be written [31]:

$$\begin{cases} F_{\text{xR}} + F_{\text{xF}} - F_{\text{D}} = m_{\text{tot}} \ddot{x}_{\text{G}} \\ F_{\text{zR}} + F_{\text{zF}} - m_{\text{tot}} g + F_{\text{L}} = 0 \\ bF_{\text{zR}} - (w-b)F_{\text{zF}} - h(F_{\text{xR}} + F_{\text{xF}}) + (h-h_a)F_{\text{D}} - (b_a - b)F_{\text{L}} = I_{\text{F}} \ddot{\theta}_{\text{F}} + I_{\text{R}} \ddot{\theta}_{\text{R}} \pm I_e \ddot{\theta}_e \end{cases} \tag{2}$$

where $\ddot{x}_G$ is the longitudinal acceleration of the vehicle; $I_{\text{F}}$, $I_{\text{R}}$, and $I_{\text{e}}$ are the moment of inertia of the front axle, the rear axle, and the set of rotating parts belonging to the engine reduced to the transmission shaft, respectively, while $\ddot{\theta}_{\text{F}}$, $\ddot{\theta}_{\text{R}}$, and $\ddot{\theta}_e$ are their respective angular accelerations. After rearranging the first two equations and substituting them into the third, it is possible to explicitly calculate the value of the force $F_{\text{zF}}$ as follows:

$$F_{\text{zF}} = m_{\text{tot}}\, g \frac{b}{w} - m_{\text{tot}} \ddot{x}_{\text{G}} \frac{h}{w} - F_{\text{D}} \frac{h_a}{w} - F_{\text{L}} \frac{b_a}{w} - \frac{I_{\text{F}}}{w} \ddot{\theta}_{\text{F}} - \frac{I_{\text{R}}}{w} \ddot{\theta}_{\text{R}} \mp \frac{I_e}{w} \ddot{\theta}_e \tag{3}$$

wherein the first term is related to the static distribution of mass, while the others are responsible for load transfer and are non-zero only when the vehicle is in motion. More specifically, the second is an inertial term, the third and fourth are aerodynamic contributions, while the last three terms are related to the inertia of the rotating systems of the front axle, rear axle, and engine group reduced to the shaft. Regarding the latter, it's important to note that its sign depends on the rotation direction of the engine, which can be either co-rotating (+) or counter-rotating (−). If we initially ignore both the aerodynamic contributions and those related to the rotating parts, the relationship simplifies to:

$$F_{\text{zF}} = m_{\text{tot}} \cdot g \cdot \left( \frac{b}{w} - \frac{h}{w} \cdot \frac{\ddot{x}_{\text{G}}}{g} \right) \tag{4}$$

Therefore, the portion of the car's mass that is transferred to each front wheel group is half of the ratio between the force $F_{\text{zF}}$ and the acceleration of gravity $g$:

$$m_{\text{F}} = \frac{1}{2} \cdot m_{\text{tot}} \cdot \left( \frac{b}{w} - \frac{h}{w} \cdot \frac{\ddot{x}_{\text{G}}}{g} \right) \tag{5}$$

Observing Equation (5), it's easy to see that the maximum value of vertical force on each front wheel group occurs at maximum deceleration ($\ddot{x}_G \equiv \ddot{x}_{G,min}$). Then, having known the total mass of the vehicle $m_{\text{tot}}$ = 293 kg, along with the wheelbase $w$ = 1535 mm, the distance $b$ = 752 mm, and the height $h$ = 345 mm, telemetric data of a FSAE car was analyzed (see Figure 4) to accurately choose the values of maximum speed and deceleration (to be used in the calculation of kinetic energy, Equation (1)). In particular, Figure 4a shows that the profile of the car's longitudinal speed during a race has a maximum value $v_{max} = 25$ m/s. Figure 4b, instead, shows the so-called g-g map, i.e., a map of the vehicle's longitudinal acceleration versus the lateral one (both normalized to the acceleration of gravity $g$ = 9.81 m/s$^2$). The latter allows us to identify a maximum deceleration of $\ddot{x}_{\text{G},min} = -1.5$ g, which results in $m_{\text{F},max} = 121$ kg (~0.4·$m_{\text{tot}}$) and $E_{\text{K,F},max} = 34.7$ kJ.

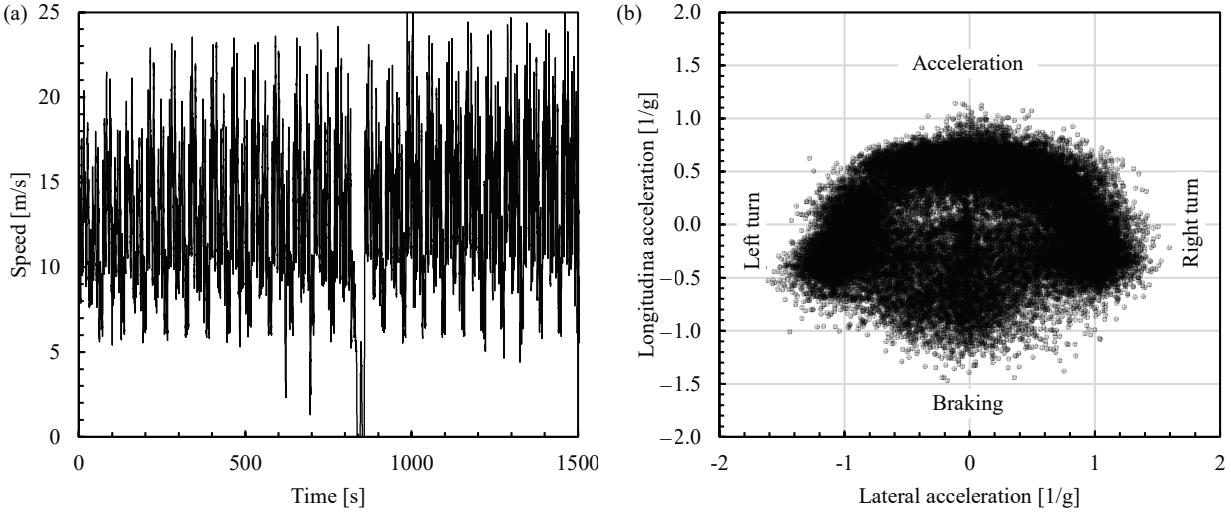



**Figure 4.** Typical track data of a FSAE car: (**a**) vehicle's longitudinal speed profile and (**b**) map of the vehicle's longitudinal and lateral acceleration normalized to the acceleration of gravity.

The choice of the right motor size has been made by ensuring it delivers enough power to accelerate the flywheel in the same way as the car accelerates the wheel assembly under real operational conditions. An initial estimate has been made through a straightforward energy balance equation. Essentially, if friction and other forms of energy loss are ignored, the electric motor's power to accelerate the flywheels from a standstill to their top speed is the following:

$$P_{\mathrm{m}} = \frac{\Delta E_{\mathrm{K}}}{\Delta t} = \frac{E_{\mathrm{K},max}}{\Delta t} \tag{6}$$

where $\Delta t$ represents the time required to accelerate a stationary car up to 25 m/s. Thanks to Figure 4b, an average longitudinal acceleration of $\ddot{x}_{\mathrm{G},max} = +0.6$ g, which results in $\Delta t = v_{max}/\ddot{x}_{\mathrm{G},max} = 4.2$ s, has been estimated. Once inserted into Equation (6), a motor power requirement of $P_{\mathrm{m}}$ = 9 kW has been found.

The second crucial parameter for selecting the motor is the rotation speed. As shown in Figure 1, the brake assembly is installed on a rotating shaft whose speed is related to the car's maximum speed by the following relationship:

$$\omega_{max} = v_{max}/R_e \tag{7}$$

thanks to which a value of $\omega_{max} = 106.4$ rad/s (two or three times smaller than the maximum speed of a commercial dynamometer), with $R_e = 235$ mm being the front wheel's effective rolling radius. Accordingly, the bench features a three-phase asynchronous ELVEM T2H-132M4 electric motor with four poles supplied at 380 V, with a nominal power of 9.2 kW and a nominal rotation speed of 1455 rpm, i.e., 152.4 rad/s. Then, the belt drive system connecting the electric motor to the main shaft has been sized to ensure the maximum shaft rotation speed is 105.8 rad/s, with the transmission ratio between the driven and driving pulleys being $\tau$ = 125 mm/180 mm = 0.694.

Finally, an estimate of the magnitude of the flywheel mass's moment of inertia $I^*$ to replicate the car's kinetic energy has been made using the following relationship:

$$E_{\mathrm{K},max} = \frac{1}{2} \cdot I^* \cdot \omega_{max}^2 \tag{8}$$

from which $I^* = 2E_{\mathrm{K},max}\omega_{max}^2 \sim 6.7$ kg·m$^2$ has been estimated, this value being the same as the smallest of commercial dynamometers and at least tens or even hundreds of times smaller than their average inertia.

The brake system of the bench can be properly sized by knowing two fundamental parameters of the car: the maximum brake torque and brake line pressure. The maximum braking torque has been estimated by referring to the locked brake configuration, i.e., when the tire is the pure longitudinal slip. Referring to Figure 3, the incipient slip of the front tire is obtained when the maximum applied braking torque equals the moment generated by the maximum longitudinal force between the tire and the ground at the contact point $F_{\mathrm{xF},max}$:

$$M_{\mathrm{b},max} = \mu_{\mathrm{x}} \cdot m_{\mathrm{F},max} \cdot g \cdot R_e \tag{9}$$

where $M_{\mathrm{b},max}$ is the maximum brake torque and $\mu_x \approx 1.7$ is the static longitudinal friction coefficient between tires and (dry) asphalt. For the considered test bench, a maximum braking torque $M_{\mathrm{b},max} \approx 500$ Nm was obtained, and a slightly higher value (600 Nm) was adopted to size the entire system. Interestingly, the required brake torque is much smaller than that of a commercial dynamometer. A similar conclusion can be drawn with respect to the maximum brake line pressure $p_{max}$ since it ranges from 30 to 50 bar, while it is in the order of 200 bar for commercial dynamometers.

## 3. Sensors and Control Electronics

The system is equipped with several sensors that allow for precise measurement of the shaft's rotation speed, the brake line pressure, the disc temperature, the pedal travel, the pedal force, and the braking torque.

Specifically, disc temperature is measured using a Texys INFKL-800 infrared sensor, which is installed on the brake caliper support (Figure 2c), in the same position it has on the FSAE car. Pedal travel is measured using an Aviorace DIA9.5-50 linear potentiometer installed next to the oil pump so as to mimic the exact pedal travel during the braking phase (Figure 2d). The pedal force is measured by means of a custom bending ring-type strain gage load cell (where four strain gauges are bonded to an aluminum ring and connected in a full Wheatstone bridge configuration) that allows to measure tension-compression axial forces up to $\pm$750 N (Figure 2d).

Finally, the most important sensor is that used to measure the braking torque. It consists of a single-axis load cell placed between the brake caliper support and the bench frame (see Figure 5). It must be noted that the brake caliper support is connected to the rotating shaft through two slightly loose ball bearings (Figure 5a), which allow it to rotate and float relative to the shaft. However, the rotary movement of the caliper support is inhibited by the load cell, since it is fixed to the frame with a known offset from the shaft's axis (95 mm, as shown in Figure 5b). More specifically, the adopted load cell is a bending ring-type strain gage load cell that is designed to work in compression (see Figure 5b) and enables measurement of tension-compression axial forces up to $\pm$7 kN (this value being chosen to read the maximum brake torque, i.e., 600 Nm/0.095 m).

The mechanical system and sensor network are fully interfaced and integrated into an electronic control system based on National Instruments PXI (Figure 2b). Specifically, it consists of a NI PXI-8106 controller with an Intel Core 2 Duo processor running Windows XP as the operating system and is housed in an NI PXI-1052 chassis. Signal generation for bench control and data acquisition is made possible thanks to the NI PXI-6289 M Series multifunction I/O Data Acquisition (DAQ) device, a system equipped with various analog and digital inputs/outputs and two counters. The physical connection of various bench components and sensors to the DAQ is achieved through a dedicated NI SCB-68 terminal block. The system also includes an NI SCXI 1520 module with an SCXI-1314 terminal block, allowing the strain gage to measure the two load cells. The comprehensive management of all sensors and components is enabled by custom LabView code specifically developed for the system.

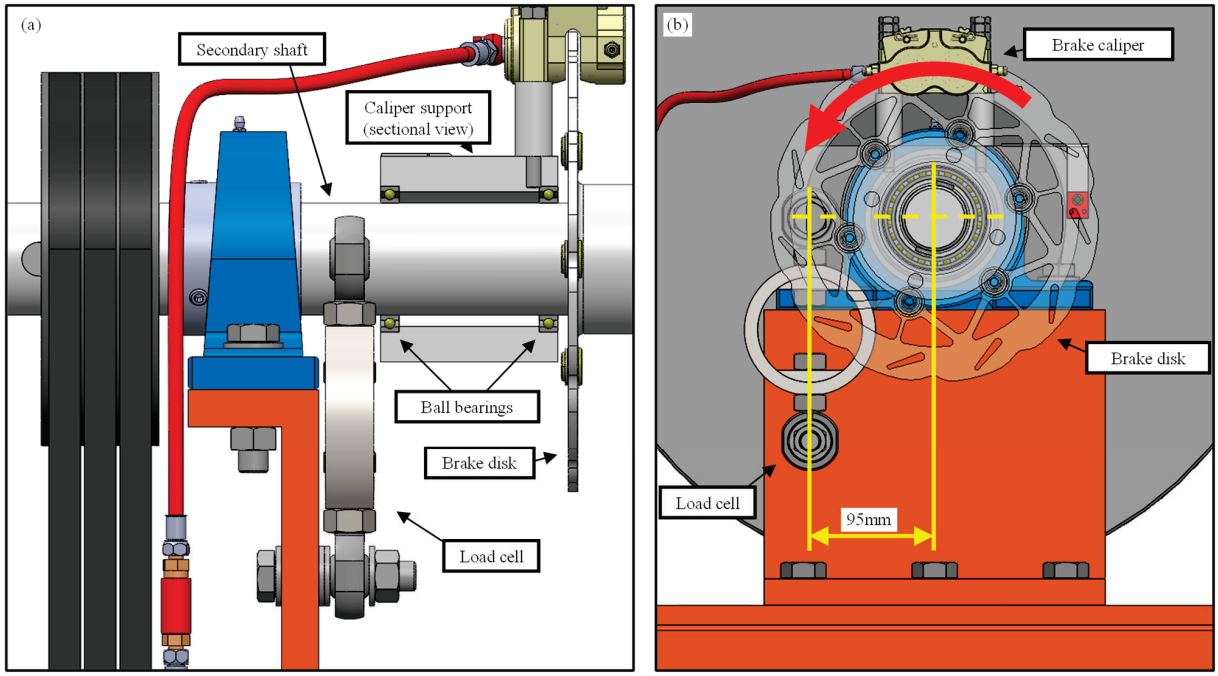



**Figure 5.** Working principle of the brake torque sensor: (**a**) side view of the bench with highlighted offset between the load cell and the axis of the secondary shaft, and (**b**) sectional view of the caliper support showing the ball bearing allowing its rotation.

## 4. Rotation Speed

Previously, it was noted that the bench has been designed to simulate braking from an initial velocity equal to the vehicle's maximum speed. Nevertheless, this operational mode does not encompass the full spectrum of testing conditions to which an actual braking system may be subjected. For this reason, the bench is equipped with a commercial three-phase inverter, the ABB ACS355-03E-23A1-4, with a nominal power of 11 kW and an output current of 23.1 A. It allows the variation of the motor's rotation speed by simply increasing or decreasing the stator field frequency that powers the motor. The power circuit of the inverter consists of a rectifier, which converts the incoming three-phase AC into a DC signal; a bank of capacitors in the intermediate circuit, necessary to stabilize the voltage output from the rectifier; and an actual inverter capable of transforming the DC current from the intermediate circuit into AC at the desired frequency. In particular, the installed inverter allows the user to define a variable motor supply frequency (and thus its rotation speed) different from the nominal one by means of an analog input voltage from 0 V to 10 V proportional to the desired frequency.

The rotation speed of the secondary shaft is then controlled in a closed loop with a speed sensor placed at one end of the shaft (Figure 2d). This device is characterized by a passive digital Hall-effect sensor A3144, fixed to the frame, and by a magnetic tone wheel, attached to the rotating shaft. The tone wheel houses a series of neodymium magnets, evenly spaced around the circumference, which alter the local magnetic field when passing near the Hall effect sensor and switch its logic level from 0 V to 5 V. Eventually, the rotation speed measurement is made possible by connecting the Hall effect sensor to a counter of the PXI-6289 DAQ and by using the appropriate LabView code.

## 5. Braking System

The braking system consists of a brake disc-caliper system that can be easily replaced and adapted to test various types of braking systems, e.g., different brake caliper or pad compounds. The braking force is generated by a dedicated pedal assembly that has been designed to simulate braking conditions similar to those of a Formula SAE car (Figure 6): the

brake line is supplied by an AP Racing CP7855 brake pump (bore 14 mm), mounted through rod-ends on a pedal assembly that simulates the vehicle's kinematics (Figure 6a). The pedal is moved by a pneumatic circuit (Figure 6b) that powers a CAMOZZI 60M1L040A0075 single-acting pneumatic actuator (bore 40 mm, stroke 75 mm). The actuator is equipped with an internal spring located in front of the piston, ensuring its return to the neutral position by simply venting the air inside the cylinder into the atmosphere after the braking phase is completed. Like the brake pump, two hinges are used to connect the actuator to the frame, allowing for purely axial loading. The maximum compressed air supply pressure is set to 6 bar; this value is maintained constant by a pressure regulator valve located immediately downstream of the connection to the supply line (Figure 6).

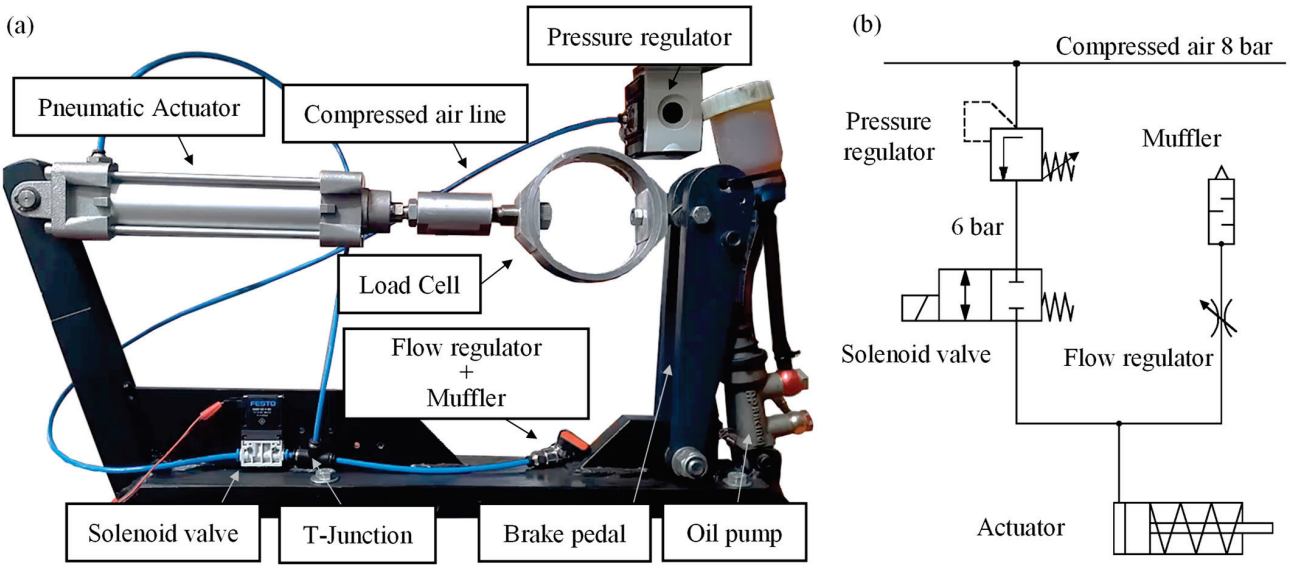



**Figure 6.** Brake pedal assembly: (**a**) overview of the complete assembly, and (**b**) schematic diagram of the pneumatic circuit.

The air exiting the pressure regulator passes through a normally closed, monostable 2/2 solenoid valve with pneumatic return and electronic activation (FESTO MHJ9-QS-4-MF). Downstream from the solenoid valve, there is a 'T' junction: one outlet of the junction directs air to the pneumatic piston, while the other outlet is connected to a ball valve acting as a flow regulator, downstream of which a muffler is mounted to vent the pressurized air into the atmosphere. The flow regulator induces a significant pressure drop; therefore, upon opening the solenoid valve, most of the air will flow into the pneumatic cylinder, with only a portion venting directly into the atmosphere. By adjusting the flow regulator's opening, the maximum pressure achievable inside the cylinder is regulated. In the current configuration, the flow regulator has been set so as to reach a maximum pressure within the braking circuit of approximately 60 bar.

The solenoid valves require a variable current over time to properly operate. Specifically, they open only after a current spike of at least 1.6–1.8 A lasting about 0.5 ms. Once opened, a much lower current value (~0.4 A) is sufficient to keep the solenoid valve open, reducing power consumption and limiting Joule heating to acceptable levels during operation. The circuit enabling this mode of powering the solenoid valve is schematically represented in Figure 7.

The electrovalve, represented as the series of an inductor ($L$) and a resistor ($R_e = 4\ \Omega$), is connected in series with the parallel of a resistor ($R_p = 54\ \Omega$) and a capacitor ($C = 1000\ \mu F$) (see Figure 7). The circuit's terminals are then connected to a DC voltage generator ($V_{cc} = 24$ V) and a main switch that allows to supply or not the solenoid valve circuit. To better understand how it works, consider two different instants of time: in the first one, the circuit is initially open with both the inductor and capacitor discharged and then is

closed and supplied at $V_{cc}$. Otherwise, the second instant corresponds to the steady-state condition, where the circuit is supplied at $V_{cc}$ and both the inductor and capacitor are fully charged.

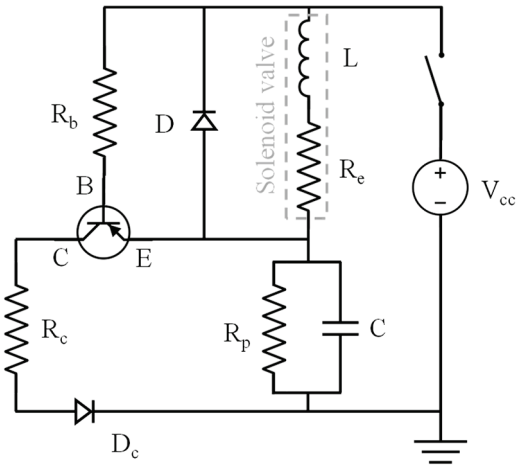



**Figure 7.** Schematic diagram of the electronic power circuit of the solenoid valve.

In the first case, the capacitor acts as a short circuit, allowing for a high initial current flow through the electrovalve, its magnitude being approximately $I_{peak} = V_{cc}/R_e = 6$ A. This high current value equals the peak current required to open the solenoid valve. Noteworthily, the description here discussed is a simplified representation of the actual circuit behavior, which includes additional non-linearity related to the inductor's charge, not considered here. A moment later, the capacitor starts to charge, causing a parallel current (initially zero) through resistor $R_p$. In the steady state, the charged capacitor acts as an open switch, and the inductor acts as a short circuit. Therefore, the system simplifies to the series of two resistors $R_e + R_p = 58\ \Omega$ supplied with a current $I = V_{cc}/(R_e + R_p) = 0.41$ A. This current value, lower than the previous one due to increased circuit resistance, keeps the electrovalve open, dissipating less power and generating less heat.

Another crucial feature of the circuit is the presence of a freewheel diode (also known as a flyback diode and denoted as D in Figure 7). This diode is connected across the inductor to eliminate flyback, which is a sudden spike voltage observed across an inductive load when its supply current is abruptly interrupted. This diode also minimizes the circuit discharge times (with a time constant $\tau_L = L/R_e$) and, consequently, the switching times of the electrovalve (it opens and closes faster). Then, the other components of the circuit in Figure 7 are necessary to prevent the capacitor discharge phase ($\tau_C = R_p \cdot C$) from slowing down the system. This includes a PNP transistor TIP34C whose base is connected to the $+V_{cc}$ supply, the emitter to the positive terminal of the capacitor, and the collector to the negative one. When the whole circuit is powered, the base-emitter junction is reverse-biased, and the transistor is turned off. Conversely, when the circuit is open, the transistor is turned on, and a current flow is allowed between the emitter and collector. This creates a circuit where the capacitor (charged) powers two resistors in parallel ($R_p$ and $R_c$). However, since $R_c = 2.5\ \Omega << R_p = 54\ \Omega$, the overall resistance of the circuit is $R_{tot} \sim R_c = 2.5\ \Omega$, so the new time constant of the capacitor discharge circuit can be roughly estimated as $\tau_c' = R_c \cdot C \ll R_p \cdot C$, allowing for a much faster discharge of the circuit and, therefore, a higher switching frequency for the electrovalve.

Now that the power section of the circuit has been clarified, it is worth noting that the main switch of the system, which allows for interrupting the connection of the circuit to the 24 V power supply, is accomplished through a digital-type switch generated by the main controller. Specifically, the control signal generated by the controller comes to the power electrical circuit through a photo-coupler TPL523, a small device that enables communication between two electrical systems while electrically isolating them

thanks to a light signal generated by an emitting diode and detected by a receiving diode. Once suitably conditioned and amplified, this signal allows the system to work correctly and prevents potential overcurrent and overvoltage in the power circuit from damaging the controller.

Finally, to continuously vary the compressed air flow into the cylinder, the electrovalve's opening is modulated with a PWM (pulse width modulation) signal, i.e., by means of a square wave having a set frequency (50 Hz) and variable duty cycle. In the "high" logic state, the electrovalve is powered with the maximum supply voltage ($V_{cc}$ = 24 V) and fully opens, while in the "low" logic state, it is not powered and remains closed, blocking the flow of compressed air to the actuator.

The control signal is generated through the second digital counter of the DAQ PXI-6289 and is managed by the NI controller with the appropriate LabView code. In particular, the system is controlled by a PID controller that automatically adjusts the duty cycle to maintain the desired braking force. The closed-loop control is based on the signal from a piezoelectric membrane oil pressure transducer (Aviorace SP100-M10 × 1) located on the brake line (see Figure 2c).

## 6. Testing

### *6.1. Operating Modes*

The test bench offers various testing modes through different possible test protocols:

1. *Manual*. This program allows the operator to choose and vary the rotation speed and brake system pressure in real-time within the allowable maximum values (0–90 km/h, 0–60 bar).
2. *Constant Speed and Pressure Tests*. The system can maintain a constant rotation speed of the shaft and brake system pressure (in this case, the installed motor power, i.e., 9.2 kW, which sets upper limits on usable pressure and speed).
3. *Brake Ramps at Constant Speed and Set Pressure*. In this case, the motor accelerates the brake disc to reach a predetermined target speed within a set time, which is maintained for a certain duration before turning off the motor and starting a braking phase at constant pressure. After the braking phase, it waits for a preset time interval and repeats the same experiment for a number of cycles chosen by the operator.
4. *Track Data Reproduction*. This method allows the motor to simulate inertia and the bench to reproduce any operational condition, particularly those recorded by telemetry from a Formula SAE (FSAE) car during races.

### *6.2. Speed Profile*

Focusing on the last-mentioned operating mode, i.e., that one allowing to replicate on-track conditions on the test bench, the operator inputs to the controller a .csv file containing 4 columns of data corresponding to time (in seconds), oil pressure (in bar), brake disc temperature (in °C), and vehicle speed (in km/h). Then, the system reads the .csv file and automatically replicates the entered speed, oil pressure, and disc temperature profiles. However, given the input speed profile, the actual profile replicated at the bench is a function of the installed flywheel mass. In more detail, the maximum inertia of the bench has been sized with respect to the most severe braking conditions, which never happened during a race. For the same braking force, excessive flywheel inertia results in lower deceleration compared to the input one (and vice versa, since if the flywheel inertia is too small, the motor has not enough power to replicate the wanted speed profile). In other words, there exists an optimum value of the flywheel inertia that allows for the proper reproduction of the input speed profile on the test bench.

To find its value, preliminary tests can be performed by discretely varying the flywheel mass, i.e., by removing one flywheel at a time between runs, and by comparing the speed profile obtained for each configuration. The optimal number of flywheels is the one that minimizes the difference between the input speed profile and that of the bench. An example is shown in Figure 8, where the input speed and pressure profiles are depicted in black

and red, respectively. The same figure shows the same quantities as replicated by the test bench. In particular, the grey line represents the pressure profile generated by the brake pedal assembly, while the other colored lines represent the bench's speed profiles with a different number of flywheels. Specifically, a total of 6 flywheels (five of type A and one of type B having polar moments of inertia equal to 1.401 kg·m$^2$ and 0.272 kg·m$^2$, respectively) have been used in different combinations. In the specific case considered, the optimal one consists of two type A flywheels and one flywheel of type B, the difference between the input speed profile and the applied one being minimized during deceleration phases (compare the black and purple lines in Figure 8). The same figure shows that a different total number of flywheels obviously results in a higher difference between input and measured speed profiles (compare the orange, yellow, green, and blue lines with the black one in Figure 8), with the deceleration being less than the desired one the greater the number of flywheels, and vice versa.

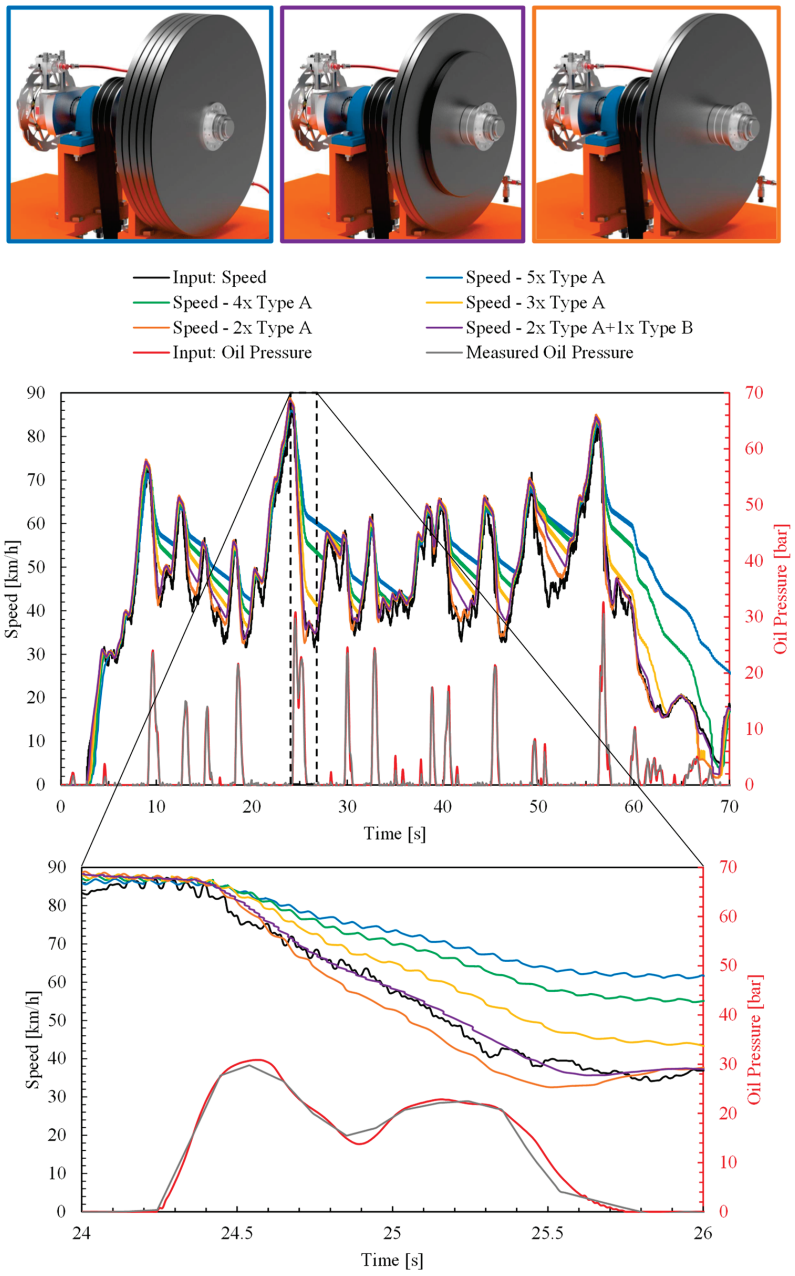



**Figure 8.** Comparison between the speed profiles of a FSAE car and those effectively replicated by the brake test bench. Different colors refer to different runs having different flywheel inertia installed.

*6.3. Cooling System*

Another key aspect of the test bench is the cooling system, which can be turned off, run continuously at maximum flow, or operated variably to ensure faithful reproduction of a temperature profile given as an input to the main controller. In more detail, the cooling system mimics the vehicle's cooling conditions and consists of a SAN ACE 140 L-9LG1424P5G001 fan that directs airflow directly onto the brake disc and caliper, as illustrated in Figure 9.

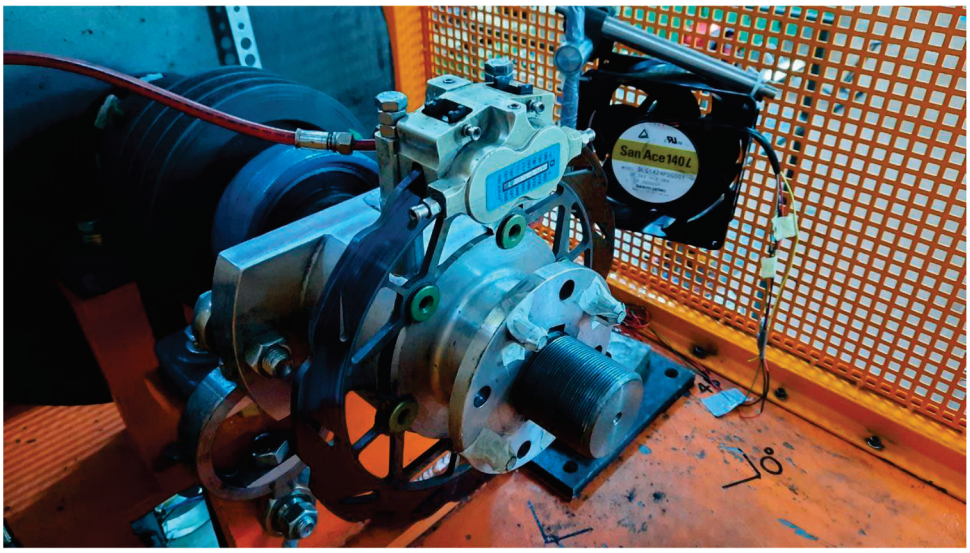



**Figure 9.** View of the cooling system and its position with respect to the brake disc.

It is well known that temperature is a parameter that has a huge influence on the brake system performance [7,22,30,32], so the need for implementing a cooling system becomes evident when observing the difference between the red temperature profile and the black one in Figure 10. It is noticeable that the temperature profile reproduced on the bench without the fan (no fan—red line in Figure 10) differs significantly from the one originating on the track (black line in Figure 10), showing differences of up to approximately 120/130 °C. Noteworthily, as observed in [7,22,32], the effect of cooling air direction relative to the brake and its distance from the rotor has a relatively low influence on the test results, suggesting the possibility of positioning the cooling system without the need to faithfully replicate the operational conditions of the car, where the airflows can assume complex and difficult-to-reproduce patterns.

Accordingly, the selection of the ventilation system was made through various experimental tests, which not only helped to choose the proper fan but also identified that variations of the airflow incidence within 0° and 45° relative to the disc have a limited influence on the thermal exchange, although its magnitude is slightly higher when positioning the fan at 45°. The same preliminary tests also confirmed that running the fan at a constant maximum speed during the test could result in excessive heat removal, causing the system to be overcooled compared to the required temperature profile.

For this reason, the cooling system is supplied with variable voltage to modulate the fan's rotation speed (ranging from 2300 to 7500 rpm) and, consequently, adjust the airflow. To achieve this, the fan is powered by a continuous voltage of variable magnitude generated using a PWM signal. Modulation is made possible through closed-loop control based on the input temperature profile, which automatically increases the rotation speed when the temperature difference between the bench and the target value is detected and decreases it in the opposite case. In this way, the bench can accurately track the target temperature profile, with their difference being maintained within ±15 °C, as shown in Figure 10.

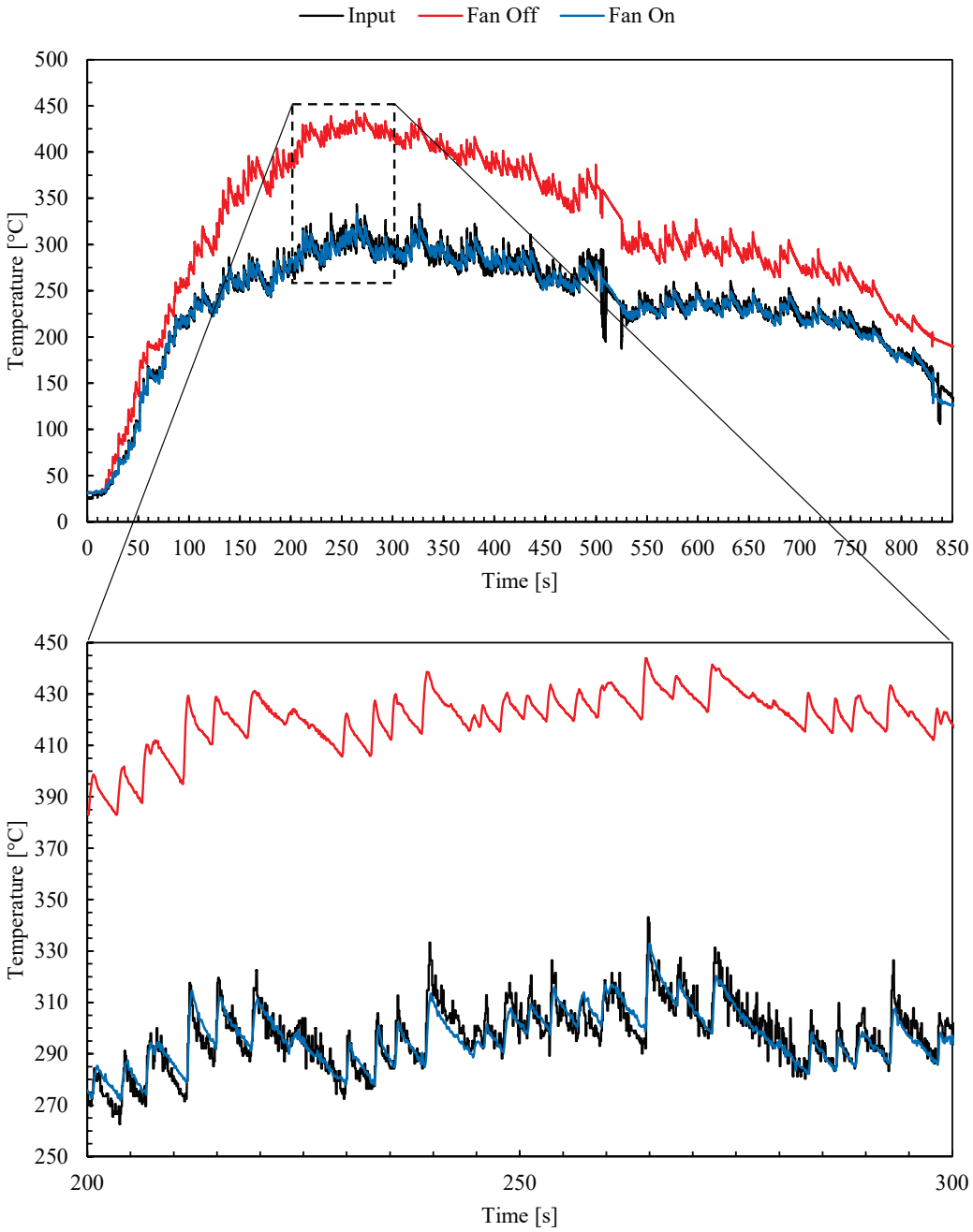



**Figure 10.** Comparison between the brake disc temperature profile of a FSAE and those obtained at the brake test bench running or not the cooling system.

## 7. Conclusions

This study presented the design and development of a brake test bench tailored for Formula SAE (FSAE) race cars. The bench incorporates a rotating shaft system, pneumatic brake pedal simulation, and an array of sensors to evaluate various brake disc-caliper combinations and pad materials. The system's design enables the measurement of critical parameters such as rotation speed, braking torque, oil pressure, and disk temperature, providing a comprehensive overview of brake performance under different conditions. The research detailed the bench's structure, the selection and integration of sensors, and the control electronics, highlighting its capability to simulate on-track braking scenarios in a controlled environment. The findings demonstrate the bench's utility in offering precise and repeatable testing conditions, which are crucial for analyzing the efficiency, durability,

and safety of braking systems in FSAE race cars. While the paper primarily focuses on the bench's conceptualization, construction, and initial testing, the results lay a solid groundwork for subsequent, more in-depth studies and optimizations of FSAE braking systems. The approach and methodologies employed offer a valuable reference for similar future endeavors aiming at enhancing performance and safety in automotive engineering.

**Author Contributions:** Conceptualization, L.V. (Luca Vecchiato) and G.M.; methodology, L.V. (Luca Vecchiato), M.N., G.P., L.V. (Luca Viale), G.Z., S.G. and G.M.; software, L.V. (Luca Vecchiato), M.N., G.P., L.V. (Luca Viale) and G.Z.; validation, L.V. (Luca Vecchiato), M.N., G.P., L.V. (Luca Viale) and G.Z.; formal analysis, L.V. (Luca Vecchiato), M.N., G.P., L.V. (Luca Viale) and G.Z.; investigation, L.V. (Luca Vecchiato), M.N., G.P., L.V. (Luca Viale) and G.Z.; resources, S.G. and G.M.; data curation, L.V. (Luca Vecchiato), M.N., G.P., L.V. (Luca Viale) and G.Z.; writing—original draft preparation, L.V. (Luca Vecchiato); writing—review and editing, L.V. (Luca Vecchiato) and G.M.; visualization, L.V. (Luca Vecchiato) and G.M.; supervision, G.M.; project administration, G.M.; All authors have read and agreed to the published version of the manuscript.

**Funding:** This research received no external funding.

**Data Availability Statement:** Data are available upon request.

**Conflicts of Interest:** The authors declare no conflict of interest.

## References

1. SAE International. *Formula SAE Rules 2024*; SAE International: Warrendale, PA, USA, 2023.
2. da Silva, P.H.M.; Idehara, S.J. *Characterization of the Brake System of a Formula SAE Vehicle, 2018-36-0148, SAE Technical Paper*; SAE International: Warrendale, PA, USA, 2018. [CrossRef]
3. Carvalho, D.F.T.; Melo, C.A.P. *Simulation Model and Testing of a Formula SAE Brake System, 2021-36-0430, SAE Technical Paper*; SAE International: Warrendale, PA, USA, 2021. [CrossRef]
4. Gupta, E.; Bora, D.K.S.; Rammohan, A. Design and analysis of brake system for FSAE race car. *Eng. Res. Express* **2022**, *4*, 25039. [CrossRef]
5. Mahajan, P.; Gupta, D.; Chawla, V.K. Design and analysis of brake disc assembly for an FSAE vehicle. *Mater. Today Proc.* **2021**, *47*, 3407–3412. [CrossRef]
6. Liao, Z.C.; Bai, X.X.F.; Li, Y.; Deng, X.C.; Sun, J. Design, modeling, and verification of a test bench for braking simulation of 1/4 vehicle. *Proc. Inst. Mech. Eng. Part D J. Automob. Eng.* **2020**, *234*, 1425–1441. [CrossRef]
7. Grochowicz, J.; Wollenweber, K.-H.; Agudelo, C.; Abendroth, H. *Brake Dynamometer Test Variability—Analysis of Root Causes, SAE Technical Paper*; SAE International: Warrendale, PA, USA, 2010. [CrossRef]
8. Sawczuk, W.; Cañás, A.M.R.; Ulbrich, D.; Kowalczyk, J. Modeling the Average and Instantaneous Friction Coefficient of a Disc Brake on the Basis of Bench Tests. *Materials* **2021**, *14*, 4766. [CrossRef] [PubMed]
9. Kurčík, P.; Gerlici, J.; Lack, T.; Suchánek, A.; Harušinec, J. Innovative solution for test equipment for the experimental investigation of friction properties of brake components of brake systems. *Transp. Res. Procedia* **2019**, *40*, 759–766. [CrossRef]
10. Zhong, W.; Zhang, X.; Wang, Z.; Zhang, X.; Yan, Q. The braking performance of pads for high-speed train with rigid and flexible structure on a full-scale flywheel brake dynamometer. *Tribol. Int.* **2023**, *179*, 108143. [CrossRef]
11. Grochowicz, J.; Agudelo, C.; Li, S.; Abendroth, H.; Wollenweber, K.-H.; Reich, A. Influence of Test Procedure on Friction Behavior and its Repeatability in Dynamometer Brake Performance Testing. *SAE Int. J. Passeng. Cars—Mech. Syst.* **2014**, *7*, 1345–1360. [CrossRef]
12. Wahlström, J.; Söderberg, A.; Olander, L.; Jansson, A.; Olofsson, U. A pin-on-disc simulation of airborne wear particles from disc brakes. *Wear* **2010**, *268*, 763–769. [CrossRef]
13. Singireddy, V.R.; Jogineedi, R.; Kancharla, S.K.; Farokhzadeh, K.; Filip, P. On scaled-down bench testing to accelerate the development of novel friction brake materials. *Tribol. Int.* **2022**, *174*, 107754. [CrossRef]
14. Kshirsagar, M.P.; Khairnar, H.P. Comparison of the theoretical and experimental coefficient of friction for the brake disc-brake pad system. *Tribol. Mater.* **2023**, *2*, 78–87. [CrossRef]
15. Tonolini, P.; Montesano, L.; Pola, A.; Landriani, E.; Gelfi, M. The effect of laser-cladding on the wear behavior of gray cast iron brake disc. *Procedia Struct. Integr.* **2021**, *33*, 1152–1161. [CrossRef]
16. Thompson, J.K.; Marks, A.; Rhode, D. *Inertia Simulation in Brake Dynamometer Testing, 2002-01-2601, SAE Technical Paper*; SAE International: Warrendale, PA, USA, 2002.
17. Schmitt, O.; Duncan, T. Method for Extracting Full Spectrum of Friction Materials Performance (Fingerprinting) using the SAE J2681. *SAE Trans.* **2004**, *113*, 1170–1176.
18. Perricone, G.; Wahlström, J.; Olofsson, U. Towards a test stand for standardized measurements of the brake emissions. *Proc. Inst. Mech. Eng. Part D J. Automob. Eng.* **2016**, *230*, 1521–1528. [CrossRef]

19. Horn, M.; Zehetner, J. A Brake-Testbench for Research and Education. In Proceedings of the 2007 IEEE International Conference on Control Applications, Singapore, 1–3 October 2007; pp. 444–448. [CrossRef]
20. Zimmer, D. *ATE Friction Test Machine and Other Methods of Lining Screening, SAE Technical Paper*; SAE International: Warrendale, PA, USA, 1982. [CrossRef]
21. Feo, M.L.; Torre, M.; Tratzi, P.; Battistelli, F.; Tomassetti, L.; Petracchini, F.; Guerriero, E.; Paolini, V. Laboratory and on-road testing for brake wear particle emissions: A review. *Environ. Sci. Pollut. Res.* **2023**, *30*, 100282–100300. [CrossRef] [PubMed]
22. Grochowicz, J.; Agudelo, C.; Reich, A.; Wollenweber, K.-H.; Abendroth, H. Brake Dynamometer Test Variability Part 2- Description of the Influencing Factors. *SAE Int. J. Passeng. Cars—Mech. Syst.* **2011**, *4*, 1394–1421. [CrossRef]
23. *ISO 26867:2009*; Road Vehicles: Brake Lining Friction Materials—Friction Behaviour Assessment for Automotive Brake Systems. ISO: Geneva Switzerland, 2009.
24. *ECE R90-02*; Uniform Provisions Concerning the Approval of Replacement Brake Lining Assemblies, Drum Brake Linings and Discs and Drums for Power-Driven Vehicles and Their Trailers. Economic Commission for Europe: Geneva, Switzerland, 2018.
25. *J2522_202312*; Inertia Dynamometer Disc and Drum Brake Effectiveness Test Procedure. SAE International: Warrendale, PA, USA, 2023.
26. *J2784_202101*; FMVSS Inertia Dynamometer Test Procedure for Vehicles Below 4540 kg GVWR. SAE International: Warrendale, PA, USA, 2021.
27. *JASO C406:2019*; Passenger Car—Braking Device—Dynamometer Test Procedures. Japanese Automotive Standards Organization: Tokyo, Japan, 2019.
28. *VDA 285-1*; Scheibenbremsbeläge—Qualitätssicherung. Verband der Automobilindustrie: Berlin, Germany, 1996. (In German)
29. *J661_202110*; Brake Lining Quality Test Procedure. SAE International: Warrendale, PA, USA, 2021.
30. Ferranti, B.; da Costa Santos, A.H.; dos Santos Júnior, A.A. *Theoretical and Experimental Thermal Analysis of Brake Discs for Formula SAE Racing Vehicles, SAE Technical Paper*; SAE International: Warrendale, PA, USA, 2008. [CrossRef]
31. Limebeer, D.J.N.; Massaro, M. *Dynamics and Optimal Control of Road Vehicles*; Oxford University Press: Oxford, UK, 2018.
32. Limpert, R. *Brake Design and Safety*; SAE International: Warrendale, PA, USA, 2011.


**Disclaimer/Publisher's Note:** The statements, opinions and data contained in all publications are solely those of the individual author(s) and contributor(s) and not of MDPI and/or the editor(s). MDPI and/or the editor(s) disclaim responsibility for any injury to people or property resulting from any ideas, methods, instructions or products referred to in the content.

machines

MDPI

*Article*

# Resonant Fatigue Tests on Polished Drill Pipe Specimens

**Ciro Santus [1], Lorenzo Romanelli [1,*], Leonardo Bertini [1], Alessandro Burchianti [2] and Tomoya Inoue [3]**

[1] Department of Civil and Industrial Engineering—DICI, University of Pisa, Largo Lucio Lazzarino 1, 56122 Pisa, Italy; ciro.santus@unipi.it (C.S.)
[2] ACTA Srl, Via della Villana 154, 57016 Rosignano Solvay, Italy
[3] Engineering Department, JAMSTEC—Japan Agency for Marine-Earth Science and Technology, Yokosuka 238-8550, Japan
* Correspondence: lorenzo.romanelli@phd.unipi.it

**Abstract:** In this study, the fatigue strength of polished drill pipe specimens was investigated and compared with previous test results of corroded and not-corroded pipes. The resonant fatigue test rig, which was designed and implemented by the University of Pisa, is initially presented by providing a detailed description of the set-up of the machine, the calibration of the strain gauges, the control system, and the correct identification of the vibrational node locations. A polishing rig was also designed and put into operation to remove the corrosion pits from the outer surface of almost the entire length of the drill pipe specimens. After the fatigue tests with the resonant rig, and the observation of the fatigue fracture of the specimens, a few samples were extracted from different zones (corroded and not corroded) of the failed drill pipe specimens. This allowed for investigations to be carried out using a scanning electronic microscope. The obtained results were analyzed using the Murakami model, and a discussion is presented about the effect of the corrosion pits on the fatigue strength.

**Keywords:** resonant fatigue test rig; drill pipe specimens; polished pipes; corrosion pits; scanning electronic mycroscope; Murakami model

## 1. Introduction

At present, the employment of drill strings for oil and gas extraction [1,2] and in various scientific investigations, for example, to reach deep sub-seafloor sediments [3–5], is widespread. The dimensions of drill strings are defined by the American Petroleum Institute (API) standard [6], and these long tubular elements are mainly composed of drill pipes. These latter feature two mating parts, the pin and the box tool joints, which are connected by a threaded connection. Both the pin and the box are then composed of three parts: the connection zone, the upset region and the pipe body. The upset region provides a link between the connection zone and the pipe body, which has a classical cylindrical tubular section, and can also smooth the stress concentration during the transition from the connection zone to the pipe body. As highlighted in Refs. [7–11], the fatigue strength of drill pipes is a widespread topic among researchers, and in Ref. [12] several factors that could trigger the initiation of cracks are highlighted, such as the stress concentration at the upset region and at the threaded connection zone and the effect of the corrosion pits.

Several investigations have been carried out by researchers in recent years regarding the stress concentration effect provided by the threaded connection in the drill pipe. In Ref. [13] an elastic–plastic finite element (FE) model was set up to investigate the effect of tensile compression and bending loads on a conical threaded connection obtained by downscaling, maintaining the same stress concentration factor, the real conical threaded connection of the API standards. A 2D axisymmetrical model was built for the tensile compression case, while a complete 3D model was employed for the bending loading case. The maximum stress concentration effect was found at the root of the last engaged thread

of the pin (LET) or at the root of the first engaged thread of the box (FET). Alternatively, given the high computational cost of the employed FE model, a purely elastic closed-form expression was proposed to easily compute the stress distribution at the threaded zone. Similar analyses of the threaded connection zone were developed in other research, as in Refs. [14–20]. In addition to the numerical investigations, researchers proposed optimized geometrical solutions to reduce the stress concentration effects in the connection zone. For example, in Ref. [21], FE and experimental analyses found that the maximum value of the stress was located at the FET of the pin, so FE analyses were performed to optimize the taper of the pin thread to reduce the stress concentration factor.

Numerical investigations were also performed regarding the upset area, as in Ref. [22], where FE analyses of this part of the drill pipe were carried out to analyze the effects of the wall thickness and the length of the upset transition area on the stress concentration factor. Finally, an optimized geometrical solution of the upset area, with respect to the classical API standard, was proposed to reduce the stress concentration factor, and it moves the maximum stress value from the vanishing area of the internal upset taper to the external wall. Other solutions to reduce the stress concentration effect at the upset area can be found in the literature, as in Ref. [23]. As concerns the analysis of the upset region, another scientific topic of interest is the erosion of the drilling fluid on the internal upset area, as investigated in Ref. [24]. In this latter piece of research, computational fluid dynamics simulations were performed to obtain the values of the pressure and the shear stress at the interface between the fluid and the upset.

Finally, corrosion pits can have detrimental effects on the fatigue strength of drill pipes [25]. In Ref. [26], the inner diameters of the drill pipe connections were coated with a Nichel plating, and the drilling fluid had an erosive action on the protective Nichel plating, which consequently fell off. After that, the oxygen content in the drilling fluid underwent corrosive reactions with the steel matrix of the inner diameter by forming corrosion pits in which the cracks started. The quantitative effects of these latter chemical reactions were analyzed by the authors with a 3D FE model, where the stress concentration of the corrosion pits was estimated. In addition to the oxygen, even the $H_2S$, which typically comes from the decomposition of sulfonated drilling fluid or from the environment where the drill pipe is used [27], can have a detrimental effect on the fatigue strength of drill pipe steel, as shown in Ref. [28]. In this latter, the effect of $H_2S$ on specimens made of V150 steel, which is gaining considerable attention with respect to classical drilling steel due to its high strength and low cost, was investigated. The authors proposed a fatigue test machine, which allowed them to perform fatigue tests in an environment permeated by $H_2S$, and the obtained results clearly showed that the fatigue strength of the V150 steel was weaker when tested in an environment with $H_2S$ with respect to the same tests carried out in air. In these cases, the hydrogen can act in two ways: with an electrochemical reaction between the steel and $H_2S$ or by diffusing into the metal lattice, causing hydrogen embrittlement. Similar studies about the corrosive effect of oxygen and $H_2S$ on the fatigue strength of drill pipe steel were performed in other research, as in Refs. [29–36] for G105, S135, and V150 steels. There are also other chemical elements that can have detrimental corrosive effects on the fatigue strength of drill pipes, such as Si, Cl, Al, and Ca, as highlighted in Refs. [12,37,38]. Considering the strong effect of corrosion on drill pipes' strength, several techniques have been adopted by researchers over the years to prevent this phenomenon: in Ref. [39], the authors suggested that the steel of the drill pipes should undergo heat treatment to reduce the band structure segregation and they also suggested using drill pipes with a double shoulder instead of those with a single shoulder. This latter was investigated by the authors in high-salt and polysulfonate mud environments, and they observed that a liquid vortex channel can occur at the end-face clearance area of the single shoulder, and this can enrich the drill pipe steel with chloride ions, which can trigger the corrosion phenomenon. Some researchers suggested moving from the use of steel to the use of aluminium alloy for the drill pipes, as in Refs. [40–42], where it was suggested that aluminium alloys, such as, for example, the superficially treated 2024 aluminium alloy, could be valid alternatives to steel

due to their specific strength, their lightness compared to steel, and for their resistance to corrosion. In some situations, titanium alloys have also been promoted as good alternatives to steel for drill pipes in horizontal wells [43].

Another challenging aspect of drill pipes is performing fatigue tests on full-scale specimens with less energy and in a reasonable time. Quasi-static fatigue tests can be employed to characterize the fatigue strength of drill pipes, and in Ref. [44], the authors developed an apparatus for classical rotating bending tests. The design of the proposed test rig was inspired by the classical rotating bending test for laboratory-scale specimens. Quasi-static fatigue test rigs for drill pipes were also proposed in other research, as in Refs. [45,46]. As highlighted in Ref. [47], fatigue strength analyses of complex structures under complex loadings in a high-cycle fatigue regime could take a large amount of time and have high energy costs; thus, resonant fatigue test rigs appear as valid alternatives. The resonant fatigue test rig used in this research was first presented by the authors in Ref. [48], showing two kinds of resonant fatigue test rigs. The first one is suitable for testing short connection regions, for example, drill collars [49], and it includes two couples of counter-rotating eccentric masses, which rotate at the same angular velocity but with different phases. The structure operates at a frequency near to (but lower than) the first natural frequency of the system and the specimens undergo an in-plane alternating bending moment. The second proposed test rig is suitable for longer connection specimens, for example, drill pipes, and it includes two fixed masses at both ends and one rotating eccentric mass at one end. The bending moment provided by the eccentric mass is small in modulus, but the rotating eccentric mass is spun at a slightly lower frequency than the first natural frequency of the structure. It is important to note that the two latter resonant test rigs are able to reproduce fully alternating loadings ($R = -1$), and thus with a null value of the mean stress. The resonant fatigue test rig for long tubular structures was utilized by the authors of this research in previous studies, as in Refs. [50,51], and in subsequent years, some changes were proposed to improve the performance of the tests. This test rig is similar to other testing machines, as shown in Refs. [52,53]. The principle of the resonant fatigue test rig was that it could be used not only for drill pipe specimens but also for other components. In Ref. [54], a resonant test rig was proposed to investigate the fatigue behaviour of full-scale railway rails using counter-rotating eccentric masses and springs to apply a mean stress to the tested specimens, thus obtaining a not fully alternating load. Some other examples of fatigue resonant test rigs were proposed to test other components in the field of mechanical and civil engineering, for example, crankshafts in Ref. [47], cylindrical specimens made of concrete or rolled plates made of S355 structural steel in Ref. [55], high-strength, self-compacting concrete in Ref. [56], marine risers with flange joints in Ref. [57], and casing joints of offshore architectures in Ref. [58]. Recently, resonant test rigs have been also used to investigate the structural behaviour of components in the field of the renewable energies, as in Ref. [59] for wind turbine blades, in Ref. [60] for the rotor blades of the wind turbines, and in Ref. [61] to study the bolt force relaxation in wind towers.

Given the corrosive effect of the marine environment, the drill pipe specimens generally present several corrosion pits, as highlighted in Ref. [62]. In order to investigate the possibility of reusing older and corroded drill pipe specimens, in this research, a novel investigation into the fatigue strength of drill pipe specimens after a polishing operation at the external surface was carried out. A bench to polish corroded drill pipe specimens (not connection) made of S150 and S140 steels was then proposed, and the resonant fatigue test rig developed by the University of Pisa in collaboration with ACTA Srl was employed to perform fatigue tests at alternating imposed stresses. Several aspects of the resonant test rig are emphasized here, such as the strain gauges' calibration, the research on the correct node locations, and the control system that regulates the test rig during the tests. Some small samples were then extracted from the failed drill pipe specimens, and they were analyzed via scanning electron microscope (SEM) to better understand where the crack initiations were located and the impact of the corrosion pits on the fatigue strength. The effect of the

observed corrosion pits on the fatigue strength was then quantified with the Murakami model, and a final discussion is presented.

## 2. Theoretical Background

In this research, the Murakami model was employed to quantify the impact of the corrosion pits on the fatigue strength. In Ref. [63], Murakami proposed Equation (1) for a plain specimen under a uniform remote tensile stress ($\sigma_0$), to quantify the mode I threshold stress intensity factor, and Equation (2) for the stress intensity factor. In this latter equation, the coefficient 0.65 is valid for the surface defects. The term $\sqrt{area}$ in Equations (1) and (2) indicates the square root of the projected area of the various defects and inclusions on the plane perpendicular to the axial loading, as shown in Figure 1. Both Equations (1) and (2) are only defined for symmetrical loadings ($R = -1$), and by combining these two equations, paying attention to the units of measurement, as shown in [63], Equation (3) can then be obtained. According to this equation, the fatigue limit ($\sigma_w$) linearly depends on the Vickers hardness ($H_V$) of the material with the two constants 1.43 and 120. The constant 1.43 can change depending on the location of the defects, and this value is valid for surface defects, while 1.41 and 1.56 are valid for defects in contact with the surface and internal defects, respectively. The main concept of this model is that the fatigue limit also depends on the term $\sqrt{area}$. Murakami [63,64] also developed an expression to make an equivalence between the surface roughness and the term $\sqrt{area}$ to capture the impact of the surface roughness on the fatigue strength. When the Murakami formula is employed to analyze not-symmetrical loadings, a corrective multiplicative factor can be added to account for the mean stress [63], and this latter can, for example, be inspired by the well-known Smith Watson and Topper fatigue model [65–67]. In principle, in the current study, the Murakami formula could not be applied given that the drill pipe specimens were tested at an imposed alternating stress, which did not correspond to the fatigue limit. However, Equation (3) can be still considered a valid indicator to quantify the impact of the corrosion pits on the fatigue strength, which allows for comparisons between the pipe specimens and the samples extracted from the pipes.

$$\Delta K_{th} = 3.3 \times 10^{-3}(H_V + 120)\left(\sqrt{area}\right)^{1/3} \quad (1)$$

$$\Delta K_I = 0.65\Delta\sigma_0\sqrt{\pi\sqrt{area}} \quad (2)$$

$$\sigma_w = \frac{1.43(H_V + 120)}{(\sqrt{area})^{1/6}} \quad (3)$$

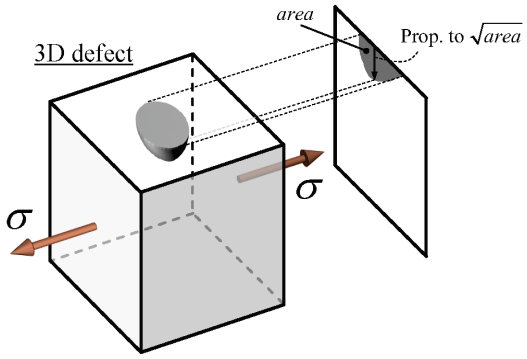



**Figure 1.** Graphical introduction of the term $\sqrt{area}$ according to the Murakami model.

## 3. Materials and Methods

### *3.1. Description of the Resonant Test Rig and the Tested Specimens*

The resonant fatigue test rig was designed by the University of Pisa in collaboration with ACTA Srl and is shown in Figure 2. Figure 2a represents the CAD design of the entire test rig, while Figure 2b provides a real and almost complete overview of the test rig with the various components. Two fixed masses were added to reduce the first natural frequency of the tubular structure and the two supports were placed at the two corresponding nodes; thus, they were only able to balance the weight of the drill pipe specimens. Figure 2c shows the rotating eccentric mass at one end, driven by an asynchronous electric motor, that rotates at a frequency close to (actually slightly lower than) the first natural frequency of the tubular structure. This generates a rotating bending moment on the drill pipe specimen, which does not rotate instead. The electric motor is linked to the rotating eccentric mass by a homokinetic joint for angular and displacement misalignments. In Figure 2d, the two lasers employed to measure the horizontal and vertical displacements at a specific location are shown, and their role is further clarified below.

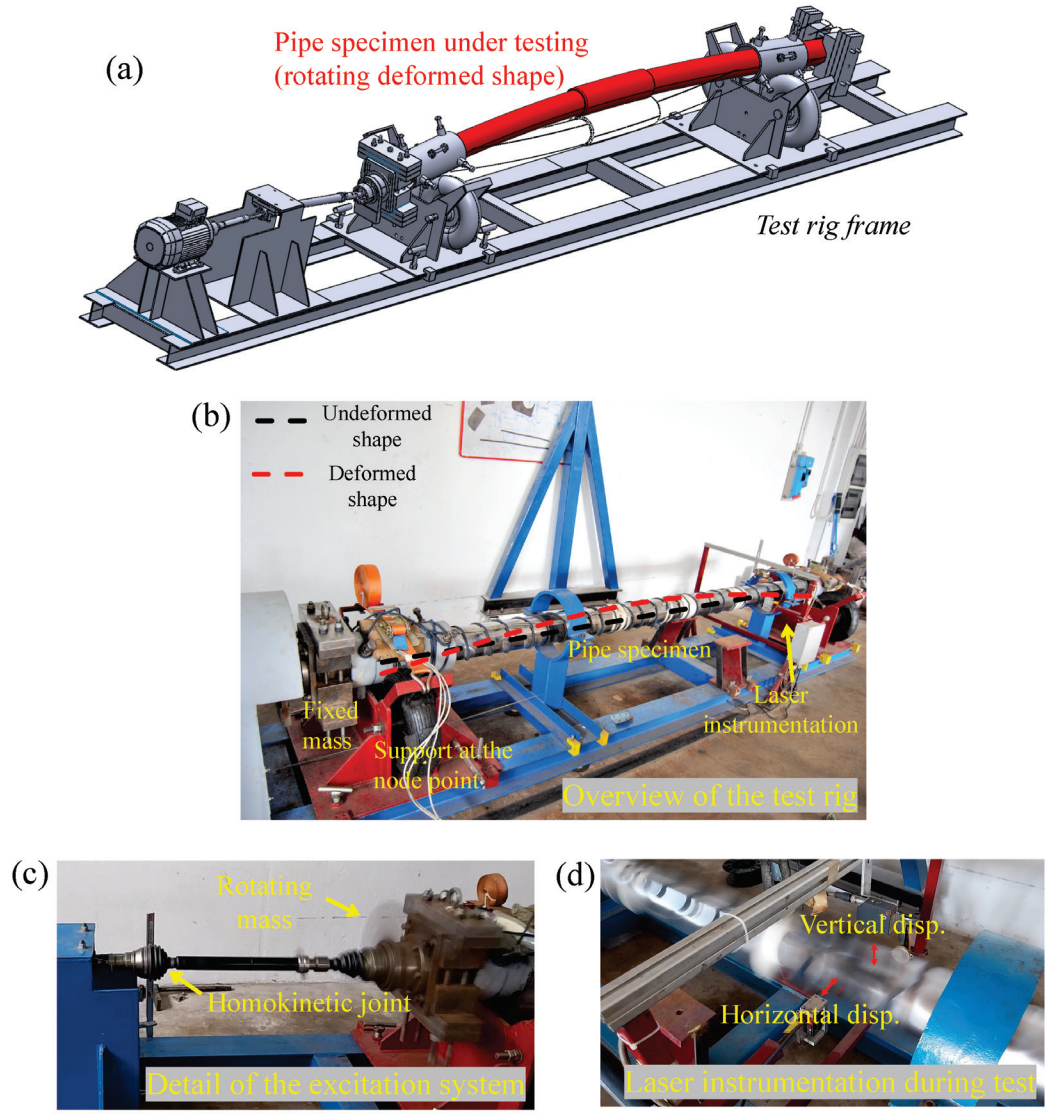



**Figure 2.** (**a**) CAD model of the test rig, (**b**) overview of the resonant fatigue test rig, (**c**) rotating mass during tests and (**d**) lasers to measure the horizontal and vertical displacements at a specific location.

The tested geometries are presented in Figure 3, and they are just two kinds of drill pipe specimen without a connection. Drill pipe specimen 1 was made of steel grade

S150, which provides a yield strength equal to $S_Y = 150$ ksi ($S_Y = 1034$ MPa) or greater, while drill pipe specimen 2 was made of steel grade S140 with a yield strength equal to $S_Y = 140$ ksi ($S_Y = 965$ MPa) or greater. Both pipe specimen 1 and the pipe specimen 2 presented an external diameter equal to $D_{ext} = 139.7$ mm, while pipe specimen 1 presented a thickness of approximately 12.9 mm and pipe specimen 2 presented a thickness of approximately 10.5 mm. As shown in Figure 3a,b, strain gauges 1, 2 and 3 (SG_1, SG_2 and SG_3) were attached to three locations of the specimens to correctly monitor the applied alternating stress, and the imposed alternating stress during the tests was $\sigma_{a,ref} = 270$ MPa in correspondence of the SG_2. This latter aspect will be clarified below. The gluing of the strain gauges to the specimens has received attention as they could fail during the tests, and, as shown in Figure 3a, a covering foil of soft material was used to avoid large vibrations during the tests.

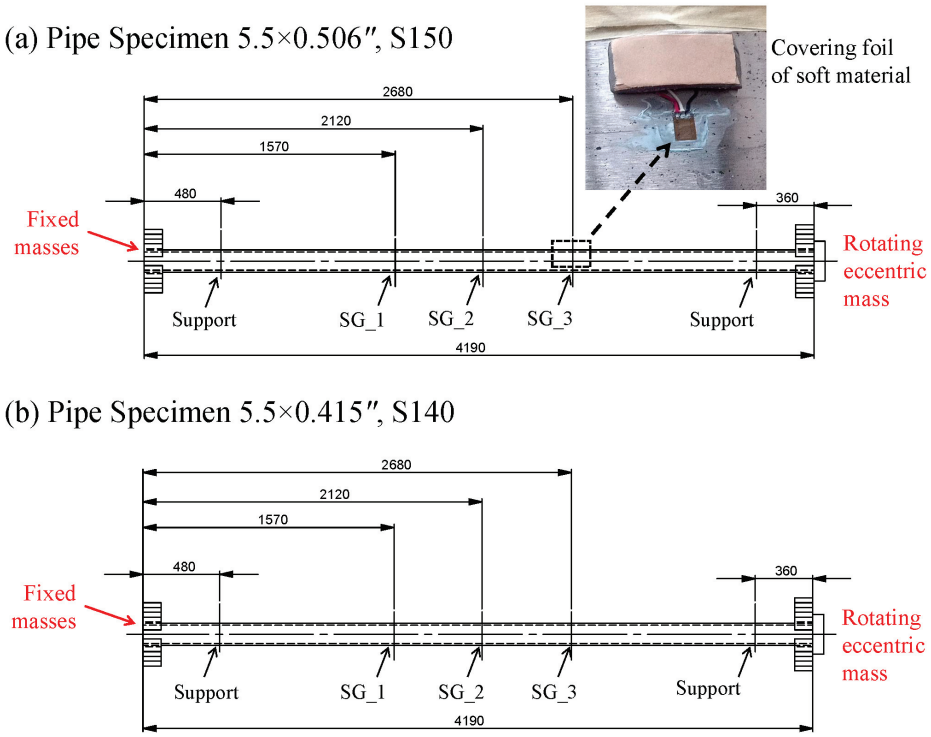



**Figure 3.** (**a**) Drill pipe specimen 1, 5.5 × 0.506″ and (**b**) drill pipe specimen 2, 5.5 × 0.415″.

FE simulations of the pure modal and the harmonic response were implemented to obtain the first natural frequency of the structure, the correct locations of the nodes, and the evaluation of the expected stress at the strain gauge locations. Although the two structural steels of the drill pipe specimens were different, the slight differences in the material properties were negligible. Therefore, in all the performed FE analyses, the Young's modulus of the material was set equal to $E = 205{,}000$ MPa, the Poisson's ratio was set equal to $\nu = 0.3$, and the volumetric density was set equal to $\rho = 7860$ Kg/m$^3$. Given that the tests were not performed at exactly the first natural frequency of the structure, where the internal and external dissipations can play significant roles, structural damping was not considered in the FE simulations. The FE modal analysis of the entire structure was useful to obtain the value of the first natural frequency of the tubular structure and the node locations, as shown in Figure 4a. The eccentric rotating mass is represented in the FE model by an additional cylindrical mass at one end, which includes the eccentric rotating mass and the the bearings between the eccentric rotating mass and the pipe specimen. Given that the pure modal analysis is an eigenvalues problem, the displacement is defined at least of one constant, and the graphic shown in Figure 4a was obtained by imposing the stress in the correspondence of the SG_2 equal to $\sigma_{a,ref} = 270$ MPa. Given that, during

the tests, there was a pulsating load, FE models of the harmonic response of the tubular structure were implemented to better investigate the structural behaviour, as shown in Figure 4b. The FE model of the harmonic response was implemented by applying a rotating force at the location of the rotating eccentric mass. This latter force had two components: the horizontal one was equal to $F_H = m\omega^2 R\cos(\omega t)$, while the vertical one was equal to $F_V = m\omega^2 R\sin(\omega t)$. In the two expressions of the applied rotating force, $m$ and $\omega$ are the mass and the angular velocity of the rotating eccentric mass, respectively, while $R$ is the radius of the circumference described by the rotating eccentric mass. The FE simulations of the harmonic response allowed to obtain the rotating frequency to have an alternating stress equal to $\sigma_{a,ref} = 270$ MPa at the location of the SG_2. The obtained value of the frequency from the FE simulation of the harmonic response was near to (lower than) the value of the first natural frequency of the structure extracted from the modal analysis. In addition to this, it was found that the location of the node near the load application point changed appreciably with respect to that obtained from the modal analysis, as shown in Figure 4b. The support of the test rig near the eccentric rotating mass was then moved to the location obtained from the FE analysis of the harmonic response. This latter aspect was of fundamental importance to avoid the presence of spurious external forces during the fatigue tests, and the two supports were then only employed to balance the weight of the drill pipe specimen. Several other FE simulations of the harmonic response were performed to calculate the frequency, which allowed for different and lower values of the alternating stress to be obtained at the SG_2. The differences between the first natural frequency obtained from the modal analysis and those obtained from the harmonic response analyses became higher by lowering the imposed alternating stress. In addition to this, even the discrepancies between the location of the node near the load application point obtained from the modal analysis and the corresponding locations extracted from the harmonic response analyses became higher by lowering the imposed alternating stress, as highlighted in Figure 4b.

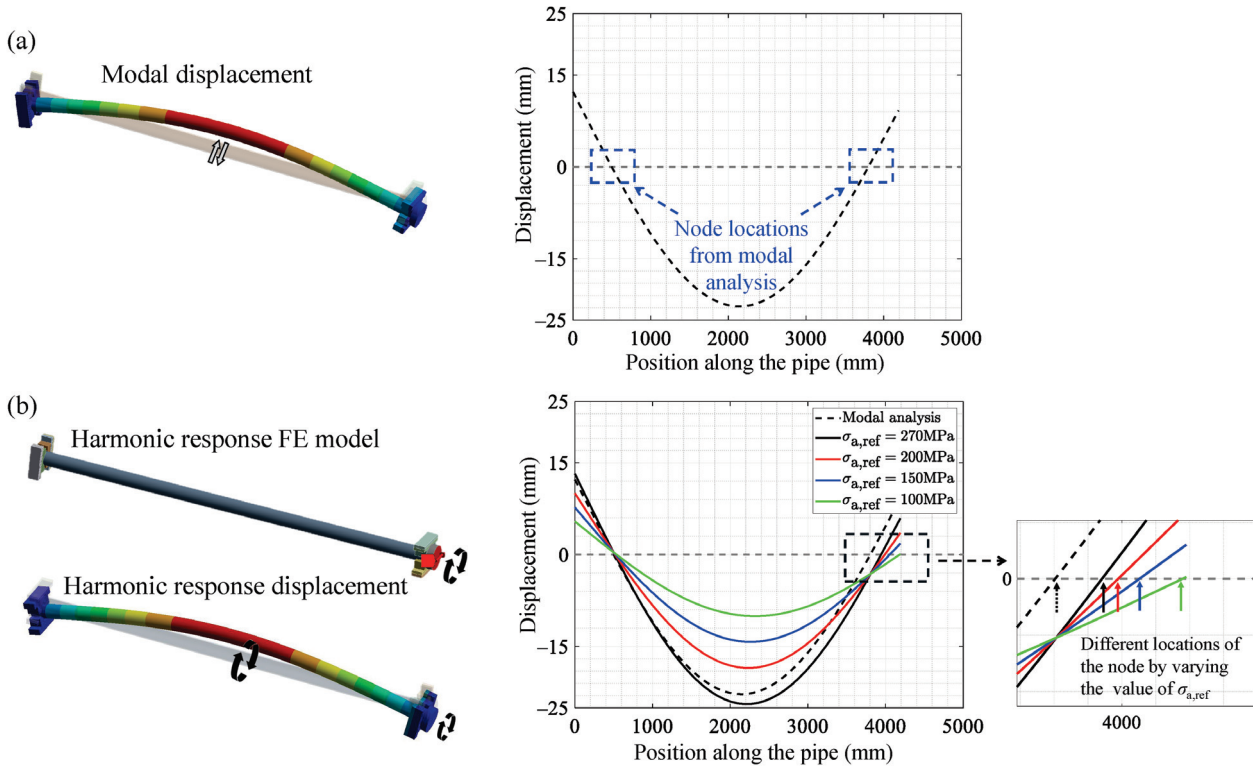



**Figure 4.** (**a**) Modal displacement at the first natural frequency of the pipe specimen and (**b**) displacements obtained with the harmonic response analysis by varying the imposed frequency and, in turn, the alternating stress amplitude.

*3.2. Strain Gauges and Lasers Calibrations*

The use of the strain gauges during the tests was of fundamental importance to record the alternating stress at specific locations in the drill pipe specimens. A static vertical load was applied by a hydraulic actuator at the point approximately located in the middle of the specimen, as highlighted in Figure 5a. The voltage signals indicated by the strain gauges were recorded and the nominal stress values at the strain gauges' locations were calculated by the beam theory, as shown in Figure 5b. Finally, the ratios between the nominal stress values and the voltage signals were calculated. In addition to this, the adequate calibration of the load cell at the end of the hydraulic actuator was verified to ensure its proper functioning. The vertical displacement of the load application point was calculated for a given load by using the classical Mohr integral, and it was also measured by the use of a comparator, as shown in Figure 5a. The two obtained results were very similar, thus confirming the proper functioning of the load cell.

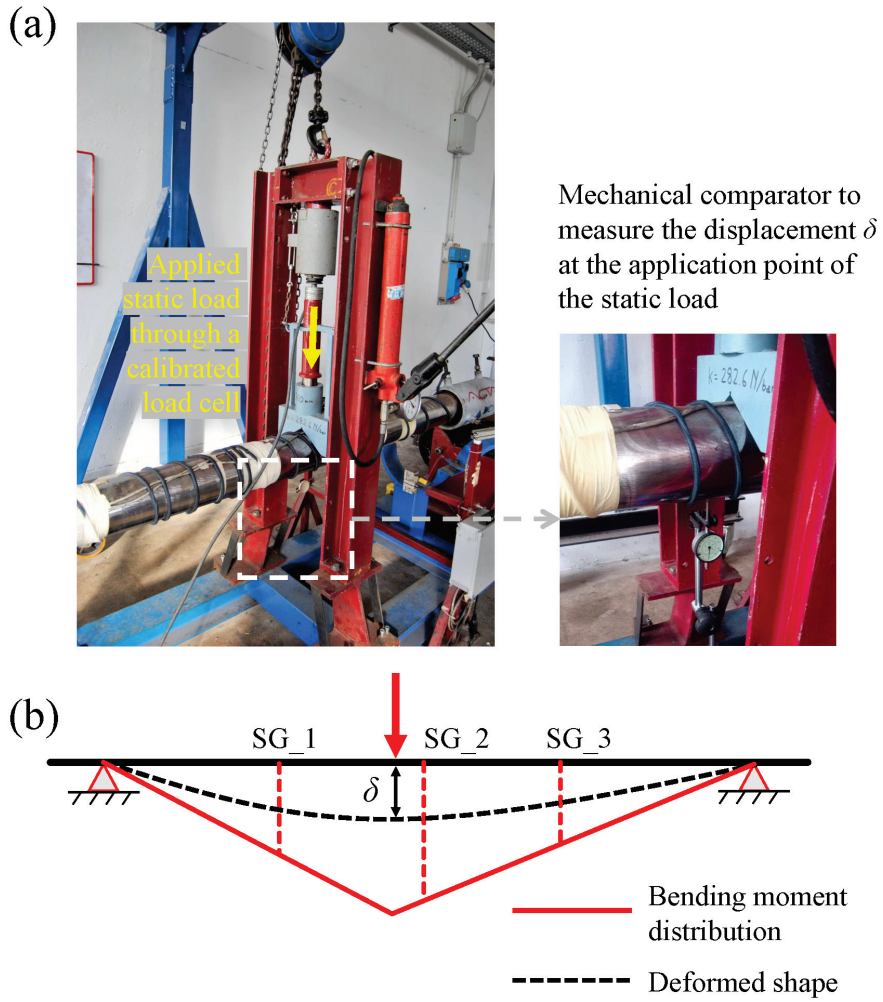



**Figure 5.** (**a**) Strain gauges' calibration and the use of a comparator to measure the displacement in accordance with the load application point and (**b**) beam scheme for strain gauges' calibration.

The proper calibration of the strain gauges was also essential for the correct functioning of the control system beyond the test rig. The pipe specimens were tested under an imposed alternating stress equal to $\sigma_{a,ref} = 270$ MPa at the SG_2 of Figure 3a,b, while the expected stress at the SG_1 and SG_3 was approximately equal to 90% of $\sigma_{a,ref}$. To accomplish this, a control system was necessary to reach and maintain the imposed level of stress. The voltage signal recorded from the SG_2 was converted into a stress value through the previously calculated scale factor, and it was then compared with the reference value

of $\sigma_{a,ref}$; thus, the error $e$ between the value of the stress obtained through the strain gauges and the corresponding reference value was obtained. The obtained value of $e$ was employed in a proportional integrative control where the output quantity was represented by a pulse–width modulation (digital) voltage signal, which was then converted into an averaged voltage signal (analog), and this latter became the input quantity of the inverter. The inverter output quantity was an alternating power current with a frequency $f$, which powered the electric asynchronous motor. The excitation frequency of the eccentric rotating mass was then $f^{'} = kf$, given that the electric asynchronous motor scaled the input frequency $f$ through the sliding factor $k$. Regardless of all the precautions taken during the gluing of the strain gauges, these latter may fail during the tests, and the voltage signal can then be recorded from one of the other strain gauges that did not fail, for example, the SG_1 and SG_3. The lasers can also be considered a valid alternative to the use of the strain gauges to control the imposed alternating stress during the tests after the stress amplitude is correctly imposed. During the initial phase of the tests, the alternating stress is controlled with the strain gauges up to the value of $\sigma_{a,ref}$, and the displacement amplitude $\delta_{a,ref}$ related to the lasers' application point is initially recorded. The value of $\delta_{a,ref}$ can be then assumed as the target displacement amplitude that should be maintained during the test. In case of failure of the strain gauges, the value of the displacement at the laser location can be compared with the value of $\delta_{a,ref}$, and then the error $e$ is found for the proportional integrative control. It should be noted that even if the quantity $\delta_{a,ref}$ measured by the lasers may be slightly incorrect, or does not perfectly match the FE simulation, it does not represent a problem for the control system given that it is calibrated with respect to the alternating stress during the initial phase.

### *3.3. Test Rig for the Polishing Operations*

In this research, the fatigue behaviour of polished drill pipe specimens was investigated. In particular, a polishing test rig was developed, as shown in Figure 6, to polish the external and corroded surface of the specimens. As shown in Figure 6a, a slow-rotation electric motor powered a self-centering chuck, which allowed for the specimens to be rotated along their longitudinal axis, as shown in Figure 6b. While rotating, the specimens underwent polishing operations via grinding. As indicated in Figure 6b, only small portions of the the extremities of the specimen remained unpolished, and these zones were needed to compare the surface morphology of the polished zones with the surface morphology of the corroded zones. The polishing operation consisted of three different phases, as shown in Figure 7, which are listed below:

- A first coarse grinding (Figure 7a).
- A second coarse polishing (Figure 7b).
- A final fine polishing (Figure 7c).

The technical data about the rotational speeds of the grinding wheel and the specimens to be polished and the dimensions of the diameters of the grinding wheels are reported in Table 1. The entire polishing operation for each pipe specimen was considered to be completed when the value of $R_a$, obtained by means of a portable roughness tester, was equal to or less than 0.4 μm over almost all the polished region's length. The roughness of 0.4 μm is generally considered a reference value for a well-performed grinding process. In specimen 1, the value of $R_a$ along the entire length of the polished region was even lower than 0.2 μm, while in specimen 2 the value of $R_a$ in the polished region was higher than that of the specimen 1; however, in any case, it was lower than 0.4 μm over almost all the polished region's length. As discussed in the following sections, the drill pipe specimen 2 featured several residual corrosion pits, which were too deep to be removed with a polishing operation of this kind.

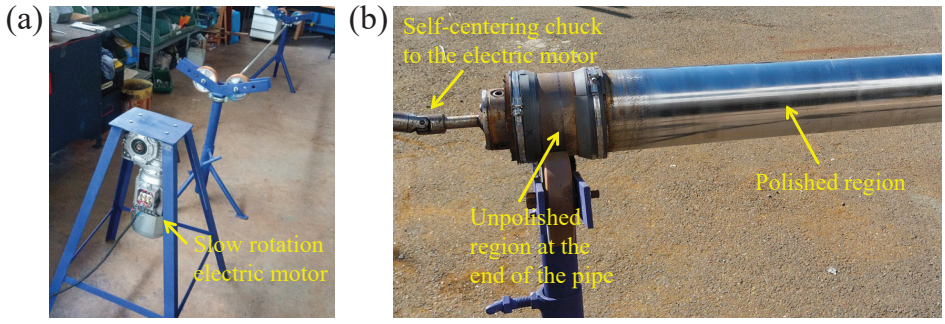



**Figure 6.** (**a**) Test rig for polishing operations and (**b**) pipe specimens on the test rig for polishing operation.

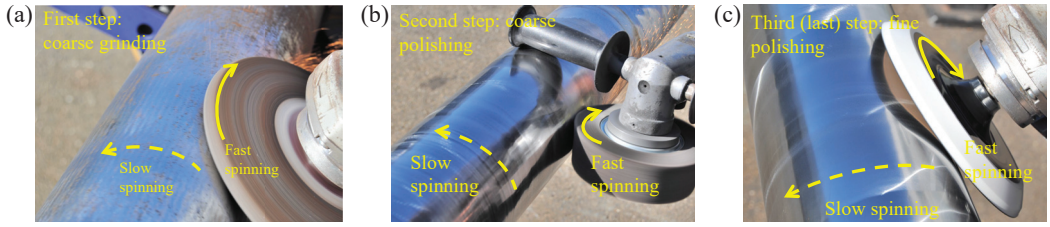



**Figure 7.** Steps during polishing operations: (**a**) coarse grinding, (**b**) coarse polishing, and (**c**) fine polishing.

**Table 1.** Significant technical data of the polishing operations.

| Step of the Polishing Operation | Grinding Wheel Rotational Speed (rpm) | Pipe Specimen's Rotational Speed (rpm) | Grinding Wheel Diameter (mm) |
|---|---|---|---|
| First step (coarse grinding | 5000 | 60 | 150 |
| Second step (coarse polishing) | 8000–10,000 | 60 | 100 |
| Third step (fine polishing) | 5000 | 60 | 125 |

## 4. Results

### *4.1. Fatigue Strength Results and Crack Location Analyses*

The fatigue test results of the polished pipe specimens in terms of stress amplitude and number of cycles to failure are reported in Figure 8, along with those of our previous research [50] for a direct comparison. Pipe specimen 1 failed after $N_f = 134{,}300$ cycles and at a stress amplitude $\sigma_a = 260$ MPa, while pipe specimen 2 failed after $N_f = 162{,}600$ cycles and at a stress amplitude $\sigma_a = 268$ MPa. The imposed alternating stress in both tests was $\sigma_{a,ref} = 270$ MPa. Among the specimens of the same group, the dispersion of the points of Figure 8 can be motivated by considering the quite large dimensions of the tested specimens compared to the laboratory scale specimens. As highlighted in Figure 8, the number of cycles to failure for these polished specimens was higher than the average value of the corroded pipe specimens of the experiment described in Ref. [50].However, the number of cycles to failure of these polished pipes was lower than the average value of the not-corroded pipes, again reported in Ref. [50]. This could be because the not-corroded drill pipe specimens were new; thus, both the inner and the outer surfaces were free of corrosion marks.

The crack location of the specimen 1 was found approximately in the middle of the specimen, as indicated in Figure 9a. The specimen region containing the crack location was extracted from the entire specimen via cutting, and it was evident that the crack initiated from the inner (not polished) diameter, as shown in Figure 9b. On the contrary, the crack location of pipe specimen 2 was not exactly in the middle of the specimen, while it started

near SG_3, as highlighted in Figure 10. In addition, the crack of pipe specimen 2 nucleated from the outer diameter, despite its being polished. To better investigate the role and the impact of the corrosion pits on the fatigue strength, several samples were extracted from specimens 1 and 2 to perform several observations using SEM. The samples extracted from specimen 1 are outlined in Figure 11: sample 1A was obtained from the corroded and unpolished zone, while sample 1B was extracted at the crack nucleation zone. The surface dimensions of both samples 1A and 1B were approximately equal to 50 × 10 mm. Other samples were also extracted from specimen 2, as shown in Figure 12: sample 2A was obtained from the corroded and unpolished zone, while samples 2B, 2C, and 2D were extracted at the crack nucleation zone. In particular, two nucleation sites were observed for specimen 2: the primary was found at sample 2B, while the secondary site was found where the 2D sample was extracted. The surface dimensions of samples 2A, 2B, and 2C were again equal to 50 × 10 mm, while the surface dimensions of sample 2D were smaller and approximately equal to 15 × 10 mm.

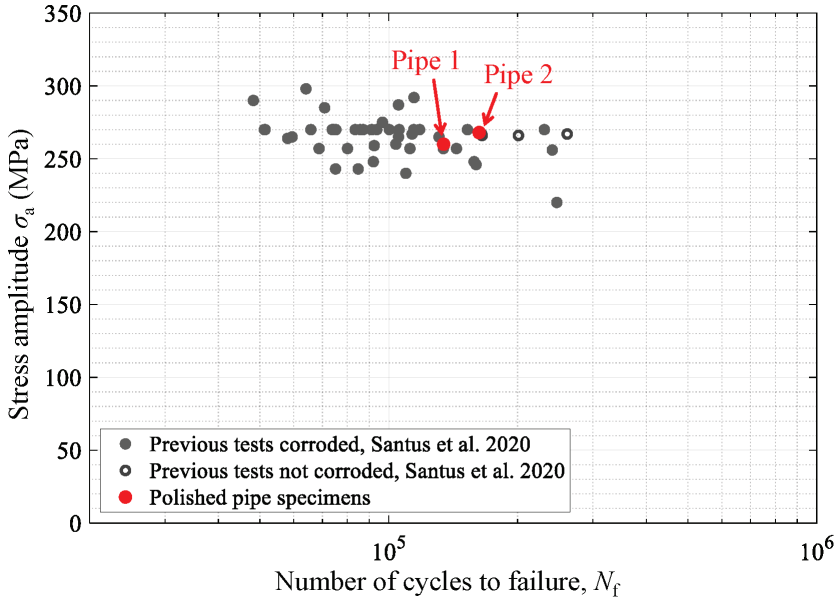



**Figure 8.** Fatigue test results of the present campaign compared with those of previous test series, including corroded and not-corroded pipes of a similar type [50].

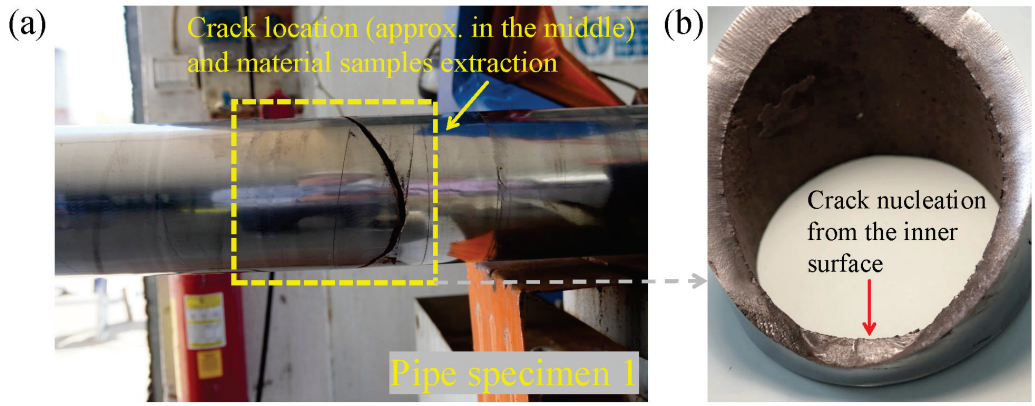



**Figure 9.** Analysis of the crack nucleation of pipe specimen 1: (**a**) location of the crack and (**b**) extracted part located at the crack nucleation zone.

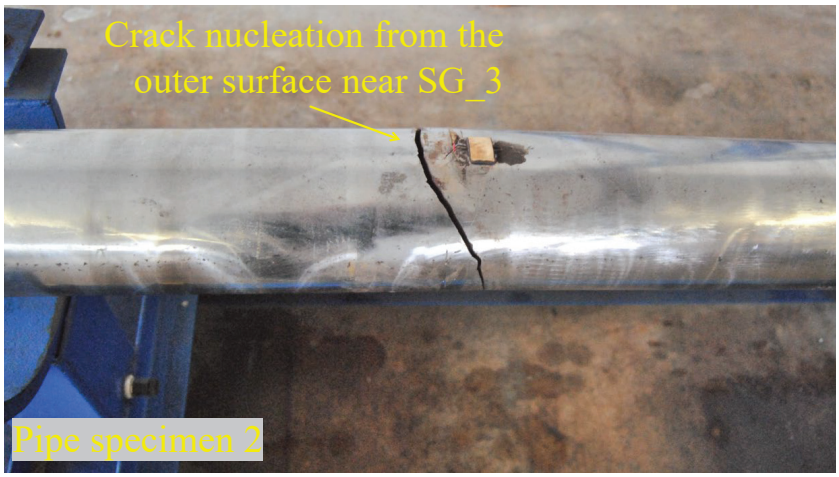



**Figure 10.** Analysis and location of the crack nucleation of pipe specimen 2.

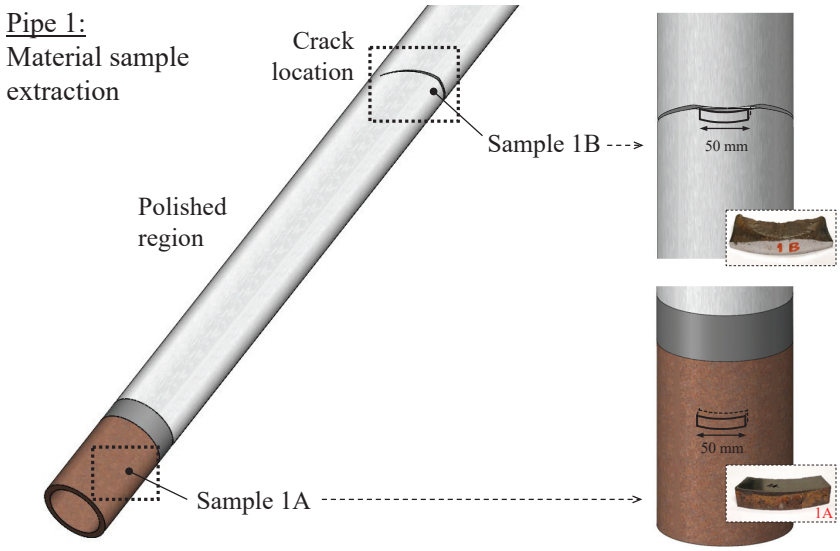



**Figure 11.** Extraction of the samples from the polished and corroded zones of pipe specimen 1.

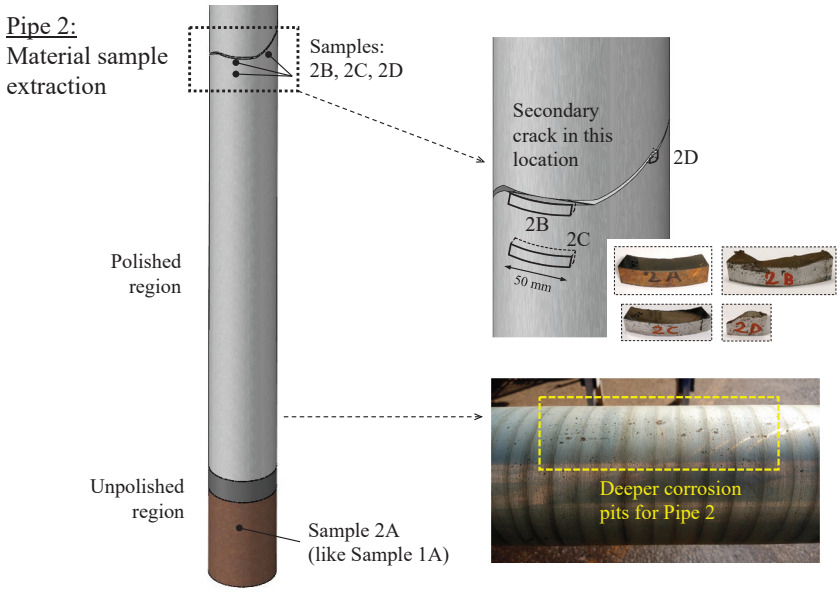



**Figure 12.** Extraction of the samples from the polished and corroded zones of pipe specimen 2.

*4.2. Performed Investigations with the SEM*

Before performing the SEM investigations, the samples were first cleaned in an ultrasonic bath to remove any residual grease or dirt. After that, the surfaces to be observed were polished using different grades of polishing papers up to grit 1200, and were then finally polished by using 1 µm diamond paste. Samples 1A and 1B were analyzed at both the inner diameter and the outer diameter, as shown in Figures 13 and 14. Samples 2A and 2C of the pipe specimen 2 were scanned at both the inner and the outer diameters, as shown in Figure 15, while samples 2B and 2D were only scanned near the crack location zone, which was at the outer diameter, as noted previously.

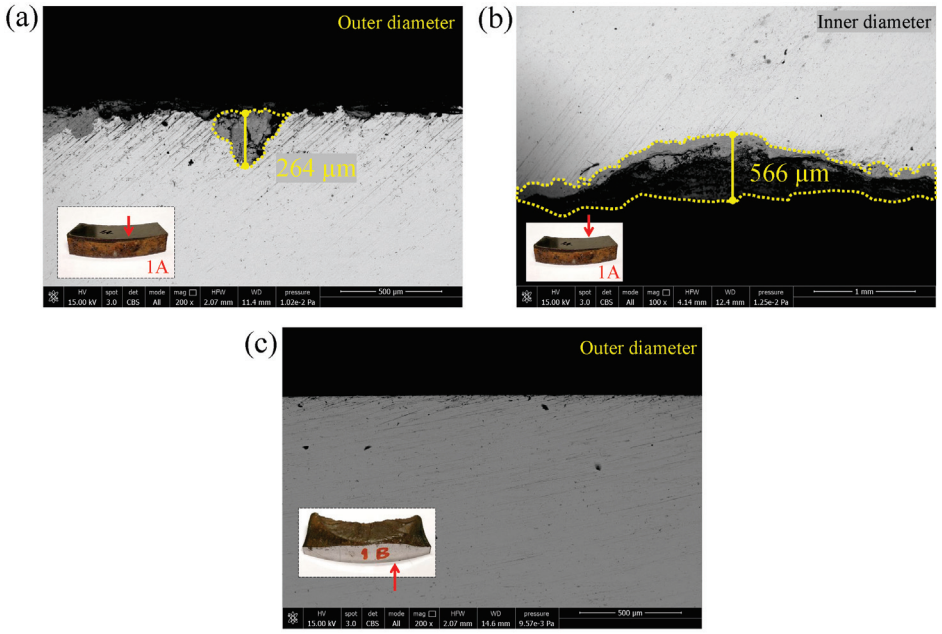



**Figure 13.** SEM investigations of drill pipe specimen 1, not at the crack location zone: (**a**) sample 1A, scanned at the outer diameter; (**b**) sample 1A, scanned at the inner diameter; and (**c**) sample 1B, scanned at the outer diameter.

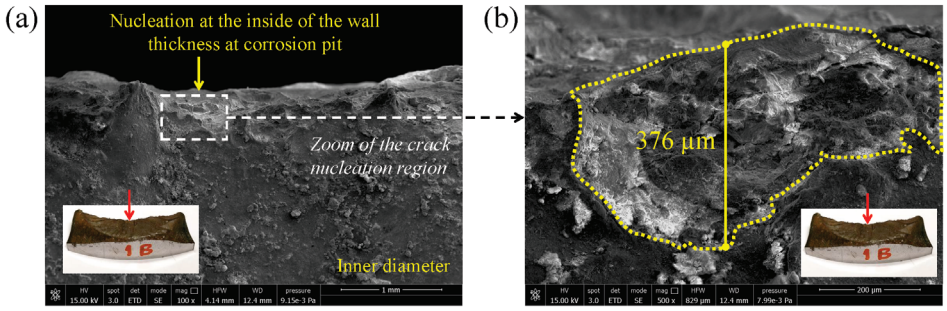



**Figure 14.** SEM investigations of the drill pipe specimen 1 at the crack location zone: (**a**) sample 1B, scanned at the inner diameter, and (**b**) zoom of sample 1B, scanned at the inner diameter.

Several observations were made of the extracted samples from specimens 1 and 2, and those reported in Figures 13–16 correspond to the largest obtained *area* of the corrosion pits for each kind of sample and location. The obtained numerical results of the parameter $\sqrt{area}$ for all the investigated samples and for the different locations are reported in Table 2. The values of this parameter for samples 1B and 2C at the outer diameter were not reported as, due to the polishing operation, no evident corrosion pits were found at the outer diameter, and this is evident in Figures 13c and 15c. In order to apply Equation (3), the Vickers hardness was measured with an AFFRI hardness tester where a load of 10 kg was applied for a duration of 10 s. The obtained Vickers hardness

values were $H_V = 378$ HV and $H_V = 351$ HV for drill pipe specimens 1 and 2, respectively. The obtained values of the Vickers hardness are similar, and they are also consistent with the fact that the pipe specimen 1 was made of S150 ($S_Y = 1034$ MPa or grater) while the pipe specimen 2 was made of S140 ($S_Y = 965$ MPa or grater); thus, the first specimen accordingly had a (slightly) higher Vickers hardness than the other one. After that, Equation (3) was applied, and the obtained results are reported in Table 2.

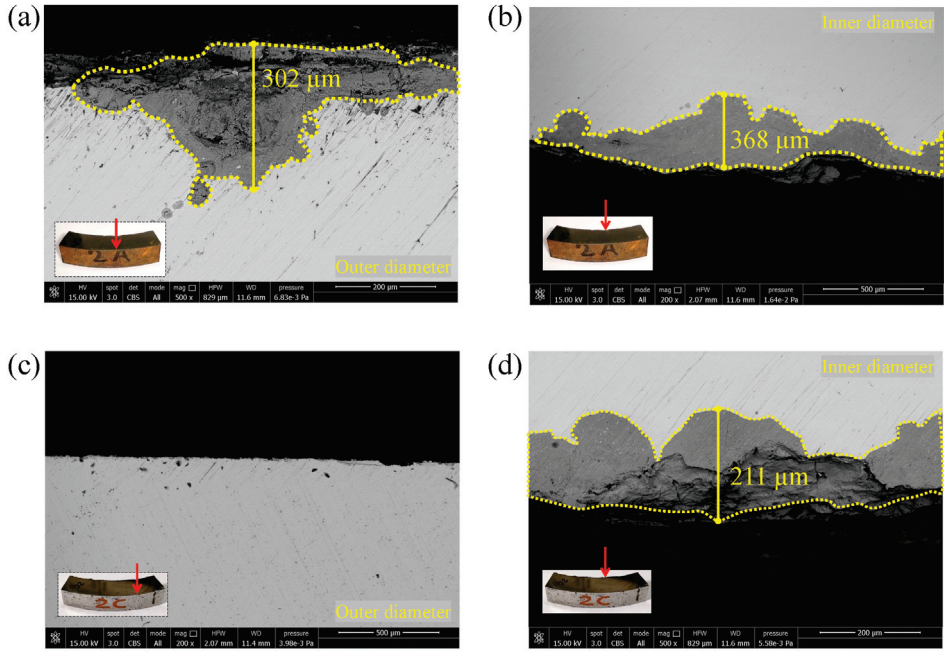



**Figure 15.** SEM investigations of drill pipe specimen 2, not at the crack location zone: (**a**) sample 2A, observed at the outer diameter; (**b**) sample 2A, observed at the inner diameter; (**c**) sample 2C, observed at the outer diameter; and (**d**) sample 2C, observed at the inner diameter.

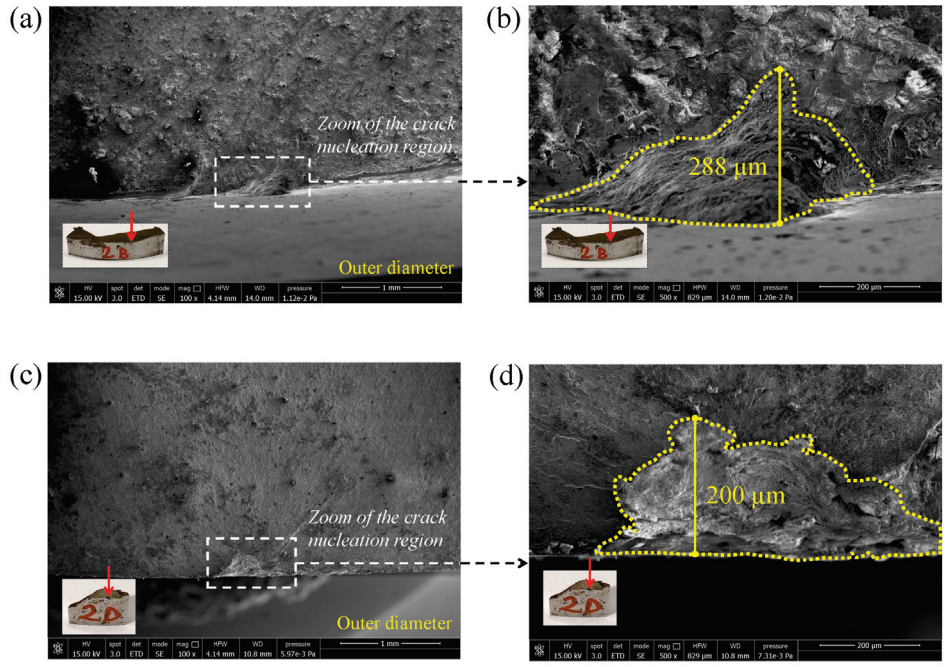



**Figure 16.** SEM investigations of drill pipe specimen 2 at the crack location zone: (**a**) sample 2B, observed at the outer diameter; (**b**) zoom of sample 2B, observed at the outer diameter; (**c**) sample 2D, observed at the outer diameter; and (**d**) zoom of sample 2D, observed at the outer diameter.

**Table 2.** Obtained values of the Murakami parameter $\sqrt{area}$ and of $\sigma_w$.

| Sample Number | Location | $\sqrt{area}$ (mm) | $\sigma_w$ (MPa) |
|---|---|---|---|
| Sample 1A | outer diameter | 0.263 | 281 |
| Sample 1A | inner diameter | 1.28 | 216 |
| Sample 1B | outer diameter | — | — |
| Sample 1B | inner diameter | 0.463 | 256 |
| Sample 2A | outer diameter | 0.333 | 256 |
| Sample 2A | inner diameter | 0.632 | 230 |
| Sample 2B | outer diameter | 0.327 | 257 |
| Sample 2C | outer diameter | — | — |
| Sample 2C | inner diameter | 0.349 | 254 |
| Sample 2D | outer diameter | 0.361 | 252 |

The values of $\sigma_w$ at the inner diameter are always lower than the corresponding values obtained at the outer diameter. This is quite obvious for the samples extracted from the polishing zones but is also true for the samples extracted from the corroded zones. The crack location of specimen 1 was at the inner surface of sample 1B, which was located in the middle of the specimen and thus experienced the maximum bending moment. The obtained value of $\sigma_w$ at the inner surface of sample 1B is lower than that expected at the outer surface, which was not calculated since there was no evident defect. This latter, despite the gradient stress distribution from the external to the internal surface, justifies the failure at the inner diameter. The obtained values of $\sigma_w$ for samples 2B and 2D at the outer diameter are similar to the corresponding value obtained at the inner diameter of sample 2C. For this reason, and considering the gradient stress distribution due to bending, the initiation at the outer diameter of samples 2B and 2D is acceptable. As previously shown in Figure 12, deeper corrosion pits were found in the outer surface of specimen 2, and they were not completely removed after the polishing operation. The failure of pipe specimen 2 was located near the SG_3; thus, the combination of a bending moment near to the maximum (90%) and the consistent dimensions of the corrosion pits led to failure.

## 5. Conclusions

In this research, the fatigue strength of polished drill pipe specimens made of S150 and S140 steel was investigated. The polishing operations of the specimens at the outer diameter were performed with a rig designed and commissioned for this purpose. The polished specimens were then tested, at an imposed alternating stress ($\sigma_{a,ref} = 270$ MPa), by means of the resonant test rig designed and implemented by the University of Pisa in collaboration with ACTA Srl. After the tests, some samples were then extracted from the specimens at different locations and were observed via SEM. In order to investigate the effects of the corrosion pits on the fatigue strength, the latter were then analysed with the Murakami model, which allowed for their impact on the fatigue strength to be quantified. After that, quantitative comparisons were made of the different samples, and the main findings of the study are reported below.

The FE modal analysis was initially performed to identify the node locations and the first natural frequency of the specimen tubular structure. After that, an FE model of the harmonic response was performed to extract the frequency which allowed to obtain the imposed value of the alternating stress in correspondence of the central strain gauge. As expected, the obtained value of this frequency was very close (but lower) to the corresponding value of the first natural frequency. However, the position of the node near the eccentric rotating mass changed appreciably with respect to that extracted from the modal analysis. As a consequence of this, FE simulations of the harmonic response are necessary to obtain the correct locations of the nodes during the tests.

The combination of corrosion pits and the high bending moment has a strong influence on the fatigue strength of the drill pipes and their crack initiation location. Regarding the sample extracted at the crack location zone of the pipe specimen 1, the calculated value of

parameter $\sigma_w$, with the Murakami model, at the inner surface is lower than the expected value of $\sigma_w$ at the outer surface, which could not be calculated since there was no evident defect in this region. This latter, despite the stress gradient from the outer to the inner diameter, justifies the nucleation of the crack at the inner diameter. On the other hand, the scans performed with the SEM on the samples extracted at the crack location zone of specimen 2 revealed that several corrosion pits were still found, despite the polishing, at the outer diameter; thus, similar values of $\sigma_w$ were obtained between the inner and outer surfaces. Considering the gradient stress distribution, specimen 2 failed at the outer diameter and near the SG_3, where the imposed alternating stress was approximately equal to 90% of the maximum alternating stress at the middle of the specimen; thus, the crack nucleation was driven by a synergistic combination of the corrosion pits and the high bending moment near to the maximum.

The results of the fatigue tests showed that the numbers of cycles to failure of the polished drill pipe specimens were higher than the average value of the corroded drill pipe specimens of previous research by the authors in Ref. [50], thus confirming the good impact of the polishing operation on the fatigue strength. However, the number of cycles to failure of the polished drill pipe specimens is lower than the average value of the not-corroded specimens presented in Ref. [50]. This can be easily explained by the fact that the specimens in this research were only polished at the outer diameter, while the not-corroded specimens had no defects at both the outer and at the inner diameters. According to this latter finding, the investigation into the fatigue strength of drill pipe specimens polished at both the inner and at the outer diameters could be a valid target for future research.

**Author Contributions:** Conceptualization, C.S., L.R., L.B. and A.B.; methodology, C.S., L.R., L.B. and A.B.; software, A.B.; validation, C.S., L.R., L.B. and A.B.; formal analysis, C.S., L.R. and L.B.; investigation, C.S., L.R., L.B. and A.B.; resources, C.S., L.R., L.B., A.B. and T.I.; data curation, C.S., L.R., L.B. and A.B.; writing—original draft preparation, C.S., L.R., L.B. and T.I.; writing—review and editing, C.S., L.R., L.B. and T.I.; visualization, C.S., L.R. and L.B.; supervision, T.I.; project administration, C.S., L.R., L.B. and T.I.; funding acquisition, T.I. All authors have read and agreed to the published version of the manuscript.

**Funding:** This research received no external funding.

**Data Availability Statement:** Data are contained within the article.

**Acknowledgments:** Scanning electron microscopy analyses were performed using a FEI QUANTA 450 ESEM-FEG at the Centro per la Integrazione della Strumentazione della Università di Pisa (CISUP).

**Conflicts of Interest:** Author Alessandro Burchianti was employed by the company ACTA Srl. The remaining authors declare that the research was conducted in the absence of any commercial or financial relationships that could be construed as a potential conflict of interest.

## Abbreviations

The following abbreviations are used in this manuscript:

| | |
|---|---|
| API | American petroleum institute |
| FE | Finite element |
| LET | Last engaged thread |
| FET | First engaged thread |
| SG_1 | Strain gauge 1 |
| SG_2 | Strain gauge 2 |
| SG_3 | Strain gauge 3 |
| SEM | Scanning electronic mycroscope |

## References

1. Dong, G.; Chen, P. A Review of the Evaluation, Control, and Application Technologies for Drill String Vibrations and Shocks in Oil and Gas Well. *Shock Vib.* **2016**, *2016*, 7418635. [CrossRef]
2. Ma, T.; Chen, P.; Zhao, J. Overview on vertical and directional drilling technologies for the exploration and exploitation of deep petroleum resources. *Geomech. Geophys. Geo-Energy Geo-Resour.* **2016**, *2*, 365–395. [CrossRef]

3. Inoue, T.; Wada, K.; Miyazaki, E.; Miyazaki, T. Scientific Drilling Program of Drilling Vessel Chikyu and Drilling Data Acquisition for Future Technical Development. In Proceedings of the Volume 5: Ocean Space Utilization; Ocean Renewable Energy. ASMEDC, Rotterdam, The Netherlands, 19–24 June 2011; OMAE2011. [CrossRef]
4. Inoue, T.; Kyo, M.; Sakura, K. Fatigue Strength Evaluation of Drill Pipe for Challenging Deep Drilling Project-Japan Trench Fast Drilling (JFAST). In Proceedings of the Twenty-Third International Offshore and Polar Engineering Conference, Anchorage, AK, USA, 30 June–5 July 2013.
5. Inoue, T.; Kyo, M.; Sakura, K.; Fukui, T. Fatigue Strength Investigation of Drill Pipe for Challenging Scientific Deep Drilling and Utilization of Drilling Data to Estimate Cumulative Fatigue. In Proceedings of the Offshore Technology Conference, Houston, TX, USA, 5–8 May 2014; 14OTC. [CrossRef]
6. American Petroleum Institute. *Specification for Rotary Drill Stem Elements*; American Petroleum Institute: Washington, DC, USA, 2006.
7. Santus, C. Fretting fatigue of aluminum alloy in contact with steel in oil drill pipe connections, modeling to interpret test results. *Int. J. Fatigue* **2008**, *30*, 677–688. [CrossRef]
8. Fangpo, L.; Yonggang, L.; Xinhu, W.; Caihong, L. Failure analysis of ∅ 127mm IEU G105 drill pipe wash out. *Eng. Fail. Anal.* **2011**, *18*, 1867–1872. [CrossRef]
9. Haagensen, P.J.; Grøttum, T.I. Fatigue Assessment of Drill Pipes. In Proceedings of the Volume 4: Materials Technology. American Society of Mechanical Engineers, Trondheim, Norway, 25–30 June 2017; OMAE2017. [CrossRef]
10. Luo, S.; Liu, M.; Zheng, X. Characteristics and life expression of fatigue fracture of G105 and S135 drill pipe steels for API grade. *Eng. Fail. Anal.* **2020**, *116*, 104705. [CrossRef]
11. Inoue, T.; Fujikubo, M. Fatigue evaluation of drill pipe by considering ship motions and its application in scientific drilling. *J. Mar. Sci. Technol.* **2020**, *26*, 525–540. [CrossRef]
12. Zamani, S.M.; Hassanzadeh-Tabrizi, S.A.; Sharifi, H. Failure analysis of drill pipe: A review. *Eng. Fail. Anal.* **2016**, *59*, 605–623. [CrossRef]
13. Ferjani, M.; Averbuch, D.; Constantinescu, A. A computational approach for the fatigue design of threaded connections. *Int. J. Fatigue* **2011**, *33*, 610–623. [CrossRef]
14. Tafreshi, A.; Dover, W. Stress analysis of drillstring threaded connections using the finite element method. *Int. J. Fatigue* **1993**, *15*, 429–438. [CrossRef]
15. Macdonald, K.; Deans, W. Stress analysis of drillstring threaded connections using the finite element method. *Eng. Fail. Anal.* **1995**, *2*, 1–30. [CrossRef]
16. Macdonald, K.A. The effectiveness of stress relief features in austenitic drillcollar connections. *Eng. Fail. Anal.* **1996**, *3*, 267–279. [CrossRef]
17. Van Wittenberghe, J.; De Pauw, J.; De Baets, P.; De Waele, W.; Ost, W.; De Roeck, G.; Bui, T.T. Fatigue investigation of threaded pipe connections. *Int. J. Sustain. Constr. Des.* **2010**, *1*, 182–189. [CrossRef]
18. Van Wittenberghe, J.; De Baets, P.; De Waele, W.; Galle, T.; Bui, T.T.; De Roeck, G. Design characteristics that improve the fatigue life of threaded pipe connections. *Int. J. Sustain. Constr. Des.* **2011**, *2*, 334–341. [CrossRef]
19. Luo, S.; Wu, S. Effect of stress distribution on the tool joint failure of internal and external upset drill pipes. *Mater. Des. (1980–2015)* **2013**, *52*, 308–314. [CrossRef]
20. Ozguc, O. Analysis of fatigue behaviour of drill pipe on pin-box connection. *Proc. Inst. Mech. Eng. Part M J. Eng. Marit. Environ.* **2020**, *235*, 68–80. [CrossRef]
21. Liu, H.; He, Y.; Wan, J.; Chen, L.; Yi, X.; Hou, S.; Wang, Y.; He, D.; Li, G. New design method of unequal taper thread (UTT) pairs and its application in API NC38 thread improvement. *Petroleum* **2023**, *9*, 439–453. [CrossRef]
22. Lin, Y.; Qi, X.; Zhu, D.; Zeng, D.; Zhu, H.; Deng, K.; Shi, T. Failure analysis and appropriate design of drill pipe upset transition area. *Eng. Fail. Anal.* **2013**, *31*, 255–267. [CrossRef]
23. Yonggang, L.; Fangpo, L.; Xin, X.; biyu, Y.; caihong, L. Simulation Technology in Failure Analysis of Drill Pipe. *Procedia Eng.* **2011**, *12*, 236–241. [CrossRef]
24. Zhu, H.; Lin, Y.; Zeng, D.; Zhou, Y.; Xie, J. Simulation analysis of flow field and shear stress distribution in internal upset transition zone of drill pipe. *Eng. Fail. Anal.* **2012**, *21*, 67–77. [CrossRef]
25. Spasova, D.; Argirov, Y.; Atanasov, N.; Yankova, R. Analysis of failure causes of S135 drill pipe. *Mater. Today Proc.* **2022**, *59*, 1719–1725. [CrossRef]
26. Yu, Z.; Zeng, D.; Hu, S.; Zhou, X.; Lu, W.; Luo, J.; Fan, Y.; Meng, K. The failure patterns and analysis process of drill pipes in oil and gas well: A case study of fracture S135 drill pipe. *Eng. Fail. Anal.* **2022**, *138*, 106171. [CrossRef]
27. Luo, S.; Liu, M.; Shen, Y.; Lin, X. Sulfide Stress Corrosion Cracking Behavior of G105 and S135 High-Strength Drill Pipe Steels in $H_2S$ Environment. *J. Mater. Eng. Perform.* **2019**, *28*, 1707–1718. [CrossRef]
28. Yu, H.; Peng, X.; Lian, Z.; zhang, Q.; Shi, T.; Wang, J.; Zhao, Z. Experimental and numerical simulation of fatigue corrosion behavior of V150 high-strength drill pipe in air and $H_2S$-dilling mud environment. *J. Nat. Gas Sci. Eng.* **2022**, *98*, 104392. [CrossRef]
29. Lu, S.; Feng, Y.; Luo, F.; Qin, C.; Wang, X. Failure analysis of IEU drill pipe wash out. *Int. J. Fatigue* **2005**, *27*, 1360–1365. [CrossRef]
30. Han, Y.; Zhao, X.; Bai, Z.; Yin, C. Failure Analysis on Fracture of a S135 Drill Pipe. *Procedia Mater. Sci.* **2014**, *3*, 447–453. [CrossRef]

31. Liu, W.; Liu, Y.; Chen, W.; Shi, T.; Singh, A.; Lu, Q. Longitudinal crack failure analysis of box of S135 tool joint in ultra-deep well. *Eng. Fail. Anal.* **2015**, *48*, 283–296. [CrossRef]
32. Liu, Y.; Lian, Z.; Lin, T.; Shen, Y.; Zhang, Q. A study on axial cracking failure of drill pipe body. *Eng. Fail. Anal.* **2016**, *59*, 434–443. [CrossRef]
33. Liu, M.; Luo, S.; Shen, Y.; lin, X. Corrosion fatigue crack propagation behavior of S135 high–strength drill pipe steel in $H_2S$ environment. *Eng. Fail. Anal.* **2019**, *97*, 493–505. [CrossRef]
34. Zeng, D.; Li, H.; Tian, G.; Liu, F.; Li, B.; Yu, S.; Ouyang, Z.; Shi, T. Fatigue behavior of high-strength steel S135 under coupling multi-factor in complex environments. *Mater. Sci. Eng. A* **2018**, *724*, 385–402. [CrossRef]
35. Han, L.; Liu, M.; Luo, S.; Lu, T.J. Fatigue and corrosion fatigue behaviors of G105 and S135 high–strength drill pipe steels in air and $H_2S$ environment. *Process Saf. Environ. Prot.* **2019**, *124*, 63–74. [CrossRef]
36. Peng, X.; Yu, H.; Lian, Z.; Dong, B.; Zhong, W.; Zhang, Y.; Hu, Z. Material optimization of drill pipe in complex wellbore environments by comparing fatigue life and cost. *Energy Rep.* **2021**, *7*, 5420–5430. [CrossRef]
37. Ziomek-Moroz, M. Environmentally Assisted Cracking of Drill Pipes in Deep Drilling Oil and Natural Gas Wells. *J. Mater. Eng. Perform.* **2011**, *21*, 1061–1069. [CrossRef]
38. Kryzhanivskyi, E.I.; Nykyforchyn, H.M.; Student, O.Z.; Krechkovska, H.V.; Chudyk, I.I. Role of Nonmetallic Inclusions in Premature Stress-Corrosion Fractures of Drill Pipes. *Mater. Sci.* **2020**, *55*, 822–830. [CrossRef]
39. Zhao, J.; Bai, X.; Qu, T.; Li, D.; Liu, W.; Wei, Z.; Xiaolong, L. Corrosion Failure Analysis of a S135 Drill Pipe. *J. Fail. Anal. Prev.* **2024**, *24*, 368–379. [CrossRef]
40. Santus, C.; Bertini, L.; Beghini, M.; Merlo, A.; Baryshnikov, A. Torsional strength comparison between two assembling techniques for aluminium drill pipe to steel tool joint connection. *Int. J. Press. Vessel. Pip.* **2009**, *86*, 177–186. [CrossRef]
41. Belkacem, L.; Abdelbaki, N.; Otegui, J.L.; Gaceb, M.; Bettayeb, M. Using a supperficially treated 2024 aluminum alloy drill pipe to delay failure during dynamic loading. *Eng. Fail. Anal.* **2019**, *104*, 261–273. [CrossRef]
42. Liu, W.; Li, J.; Zhong, Y.; Shi, T.; Zhang, J.; Li, S. Failure analysis on aluminum alloy drill pipe with pits and parallel transverse cracks. *Eng. Fail. Anal.* **2022**, *131*, 105809. [CrossRef]
43. Mou, Y.; Lian, Z.; Li, W.; Zhong, X.; Li, J.; He, Y.; Cao, J.; Eliaz, N. The effect of friction welding on the mechanical properties and corrosion fatigue resistance of titanium alloy drill pipe. *Fatigue Fract. Eng. Mater. Struct.* **2021**, *45*, 466–481. [CrossRef]
44. Miscow, G. Techniques to characterize fatigue behaviour of full size drill pipes and small scale samples. *Int. J. Fatigue* **2004**, *26*, 575–584. [CrossRef]
45. Teodoriu, C. Oil Country Tubular Goods Fatigue Testing: Do We Test Them Enough? In Proceedings of the Volume 4: Materials Technology. American Society of Mechanical Engineers, Trondheim, Norway, 25–30 June 2017; OMAE2017. [CrossRef]
46. Zou, H.; Tan, Z. Fatigue life analysis of rotary drill pipe. *Int. J. Press. Vessel. Pip.* **2023**, *201*, 104874. [CrossRef]
47. Huertas, J.I.; Navarrete, N.; Giraldo, M.; Uribe, J.D.; Gasca, J.J. Resonant fatigue test bench for shaft testing. *Fatigue Fract. Eng. Mater. Struct.* **2016**, *40*, 364–374. [CrossRef]
48. Bertini, L.; Beghini, M.; Santus, C.; Baryshnikov, A. Resonant test rigs for fatigue full scale testing of oil drill string connections. *Int. J. Fatigue* **2008**, *30*, 978–988. [CrossRef]
49. Santus, C.; Bertini, L.; Burchianti, A.; Inoue, T.; Sakurai, N. Fatigue resonant tests on drill collar rotary shouldered connections and critical thread root identification. *Eng. Fail. Anal.* **2018**, *89*, 138–149. [CrossRef]
50. Santus, C.; Burchianti, A.; Inoue, T.; Ishiguro, H. Fatigue resonant tests on S140 and S150 grade corroded drill pipe connections and pipe bodies. *Int. J. Press. Vessel. Pip.* **2020**, *184*, 104107. [CrossRef]
51. Santus, C.; Romanelli, L.; Burchianti, A.; Inoue, T. Resonant Fatigue Tests on Drill Pipe Connections with Different Geometries and Sizes. *Appl. Sci.* **2023**, *13*, 8006. [CrossRef]
52. Van Wittenberghe, J.; De Baets, P.; De Waele, W.; Ost, W.; Verstraete, M.; Hertelé, S. Resonant Bending Fatigue Test Setup for Pipes With Optical Displacement Measuring System. *J. Offshore Mech. Arct. Eng.* **2012**, *134*. [CrossRef]
53. Oku, Y.; Sugino, M.; Ando, Y.; Makino, T.; Komoda, R.; Takazaki, D.; Kubota, M. Fretting fatigue on thread root of premium threaded connections. *Tribol. Int.* **2017**, *108*, 111–120. [CrossRef]
54. Schneider, S.; Herrmann, R.; Marx, S. Development of a resonant fatigue testing facility for large-scale beams in bending. *Int. J. Fatigue* **2018**, *113*, 171–183. [CrossRef]
55. Schramm, C.; Birkner, D.; Marx, S. Resonance-based testing facility for fatigue tests of different axially loaded structural elements. *Eng. Struct.* **2024**, *298*, 117045. [CrossRef]
56. Thomas, C.; Sainz-Aja, J.; Setien, J.; Cimentada, A.; Polanco, J.A. Resonance fatigue testing on high-strength self-compacting concrete. *J. Build. Eng.* **2021**, *35*, 102057. [CrossRef]
57. Chuan, W.; Zhu, H.; Wang, D. Test System and Model for Fatigue Performance Evaluation of Marine Riser. *J. Appl. Sci.* **2013**, *13*, 854–861. [CrossRef]
58. Xu, Z.; An, C.; Xie, Z.; Zhang, J.; Lim, F.; Zhang, Y. Full-scale resonant bending fatigue testing of casing joints under bending moment load. *Int. J. Press. Vessel. Pip.* **2024**, *207*, 105105. [CrossRef]
59. Snowberg, D.; Dana, S.; Hughes, S.; Berling, P. *Implementation of a Biaxial Resonant Fatigue Test Method on a Large Wind Turbine Blade*; National Renewable Energy Lab.: Golden, CO, USA, 2014. [CrossRef]
60. Melcher, D.; Bätge, M.; Neßlinger, S. A novel rotor blade fatigue test setup with elliptical biaxial resonant excitation. *Wind Energy Sci.* **2020**, *5*, 675–684. [CrossRef]

61. Van Wittenberghe, J.; Vanden Haute, C.; Shirzadeh, R.; Thibaux, P. On the Feasibility of Large-Scale Resonant Fatigue Testing to Study Bolt Force Relaxation. In Proceedings of the Volume 3: Materials Technology; Pipelines, Risers, and Subsea Systems, Hamburg, Germany, 5–10 June 2022; American Society of Mechanical Engineers: New York, NY, USA, 2022; OMAE2022. [CrossRef]
62. Luo, S.; Liu, M.; Lin, X. Corrosion fatigue behavior of S135 high-strength drill pipe steel in a simulated marine environment. *Mater. Corros.* **2018**, *70*, 688–697. [CrossRef]
63. Murakami, Y. *Metal Fatigue*; Elsevier: Amsterdam, The Netherlands, 2019. [CrossRef]
64. Macoretta, G.; Romanelli, L.; Santus, C.; Romoli, L.; Lutey, A.H.A.; Uriati, F.; Nicoletto, G.; Raghavendra, S.; Benedetti, M.; Monelli, B.D. Modelling of the surface morphology and size effects on fatigue strength of L-PBF Inconel 718 by comparing different testing specimens. *Int. J. Fatigue* **2024**, *181*, 108120. [CrossRef]
65. Łagoda, T.; Vantadori, S.; Głowacka, K.; Kurek, M.; Kluger, K. Using the Smith-Watson-Topper Parameter and Its Modifications to Calculate the Fatigue Life of Metals: The State-of-the-Art. *Materials* **2022**, *15*, 3481. [CrossRef] [PubMed]
66. Santus, C.; Romanelli, L.; Grossi, T.; Neri, P.; Romoli, L.; Lutey, A.H.A.; Pedranz, M.; Benedetti, M. Torsional-loaded notched specimen fatigue strength prediction based on mode I and mode III critical distances and fracture surface investigations with a 3D optical profilometer. *Int. J. Fatigue* **2022**, *161*, 106913. [CrossRef]
67. Santus, C.; Romanelli, L.; Grossi, T.; Bertini, L.; Le Bone, L.; Chiesi, F.; Tognarelli, L. Elastic–plastic analysis of high load ratio fatigue tests on a shot-peened quenched and tempered steel, combining the Chaboche model and the Theory of Critical Distances. *Int. J. Fatigue* **2023**, *174*, 107713. [CrossRef]


**Disclaimer/Publisher's Note:** The statements, opinions and data contained in all publications are solely those of the individual author(s) and contributor(s) and not of MDPI and/or the editor(s). MDPI and/or the editor(s) disclaim responsibility for any injury to people or property resulting from any ideas, methods, instructions or products referred to in the content.

machines

MDPI

*Article*

# Research on Bolt Loosening Mechanism Under Sine-on-Random Coupling Vibration Excitation

**Jiangong Du, Yuanying Qiu * and Jing Li**

School of Mechano-Electronic Engineering, Xidian University, Xi'an 710071, China; dujg@stu.xidian.edu.cn (J.D.); j_li@xidian.edu.cn (J.L.)
* Correspondence: yyqiu@mail.xidian.edu.cn

**Abstract:** This paper primarily investigates the mechanism of bolt loosening under the Sine-on-Random (SOR) vibration excitation. Firstly, a theoretical model of bolt loosening response under the SOR synthesized excitation is established by a time–frequency conversion method, which converts the sine excitation into Power Spectrum Density (PSD) expression in the frequency domain and superimposes it with random vibration excitation to obtain the SOR synthesized excitation spectrum. Then, by means of a four-bolt fastened structure, the bolt loosening mechanisms under both the sine and random vibration excitation are deeply studied, respectively. Ultimately, based on the time–frequency conversion method of SOR synthesized excitation, the bolt loosening responses of the structure under SOR excitation with different tightening torques are analyzed. Furthermore, a three-stage criterion including the Steady Stage, Transition Stage, and Loosen Stage for bolt loosening under SOR excitation is revealed, and the relationship among the SOR synthesized vibration responses and the two forms of single vibration responses is explored based on a corrective energy superposition method by introducing the weight factors of the two single vibration responses under different tightening torques. Finally, test verifications for the four-bolt fastened structure are conducted and good consistencies with the results of the Finite Element Analysis (FEA) are shown. This study provides valuable insights into the detection and prevention of loosening in bolted connection structures under multi-source vibration environments and has important engineering reference significance.

**Keywords:** bolt loosening; sine-on-random vibration; energy superposition method; strain monitoring; vibration test

## 1. Introduction

The threaded connection structure has advantages of easy installation, conciseness, small size, etc., which make it one of the most widely used and important connection methods in practical engineering [1,2]. In many megaprojects such as aerospace, railways, bridges, etc., bolt connection failure is an important factor leading to structural safety hazards and accidents. High-strength fasteners play a critical role in carrying and transmitting loads, and their failure may cause structural detachment, component loosening, and other hazards, leading to major accidents. It is of great significance to investigate the mechanism of bolt loosening under vibration [3,4].

In the last century, scholars have conducted research on the causes and theories of bolt loosening. In 1969, the German engineer Junker [5] designed a reciprocating displacement vibrostand to study the phenomenon of bolt loosening and found that the main factor of bolt loosening was transverse vibration excitation, which was widely recognized by many

scholars in recent years [6–8]. In 1978, Sakai [9] reported that when the sliding torque of the bolt head is greater than the sliding torque of the threaded surfaces, the bolt will loosen. In 1997, Zadoks [10] conducted an experiment and found that the micro slip between the clamping parts and bolts was the main cause of bolt loosening. Hess et al. [11] established a three-dimensional finite element model and provided a new method to analyze the loosening of bolts by FEA. Otter et al. [12] used different materials for bolts and connected parts and found that the influence of the structural material on bolt loosening was also obvious. Li et al. [13] proposed that bolt loosening could be categorized as either bolt head loosening or nut loosening by investigating the process of bolt loosening.

One of the important research directions is the study of different vibration excitation forms that cause bolt loosening [14]. In practical engineering, bolts are usually subjected to both sine and random vibration excitations simultaneously [15]. For example, during the running of aerospace vehicles or automobiles, the system is not only subject to periodic vibrations from the engine but also encounters random vibration sources such as environmental noise or external disturbances [16]. The superposition effect of SOR excitation may exacerbate the occurrence of bolt loosening, especially under the interaction of high-frequency sine vibration and low-frequency random vibration, making the system response more complex and the loosening process of bolts more difficult to predict. Therefore, studying the bolt loosening mechanism under SOR excitation is not only of great significance for improving the reliability and safety of structures, but is also crucial for the development of related detection and prevention technologies. Kihma et al. [17] derived a statistical rain flow cycle histogram from the SOR spectrum of the test stress data, and then used the appropriate material fatigue curve to obtain the estimated life. Cornelis et al. [18] proposed a "Mission Synthesis" method to establish the corresponding SOR power spectrum based on fatigue damage equivalence. Brown et al. [19] examined the percentile of the Cumulative Distribution Function (CDF) obtained by integrating the joint probability density functions of sine and random components. These studies provide some inspiration for the SOR vibration excitation processing method in this study.

At present, there are in-depth studies on bolt loosening under independent excitation of sine or random vibrations from multiple perspectives in the existing literature [20–23]. However, there is no research on bolt loosening under SOR vibration excitation. Currently, studies on SOR vibration are mainly focused on structural fatigue analysis. Firstly, by combining theoretical derivation and simulation analysis, the bolt loosening mechanism under SOR vibration excitation is studied by using a time–frequency conversion method. Then, a corrective energy superposition method introducing weight factors $a_{T_i}$ and $b_{T_i}$ is proposed, which reveals the relationship between the SOR synthesized vibration response and the individual sine or random vibration response. Finally, the effectiveness of FEA is verified through a series of vibration tests on a four-bolt fastened structure.

The summaries of the sections are as follows.

In Section 2, the relationship between SOR vibration excitation and linear system response is established, which provides a theoretical basis for investigating bolt loosening under SOR excitation.

In Section 3, for a four-bolt fastened structure model, the strain responses of monitored points of bolt loosening under sine and random vibration excitations with different tightening torques are analyzed by FEA.

In Section 4, a frequency-domain SOR vibration analysis method is proposed by synthesizing the sine vibration and random vibration excitation in Section 3, and the responses of the four-bolt structure monitored points are analyzed under SOR vibration excitation. Furthermore, the response results of monitored points under SOR synthesized excitation and independent sine and random vibration excitation are compared and analyzed, and

a relationship model of the SOR synthesized vibration response and two forms of single vibration responses based on energy superposition method is established.

In Section 5, sine and random vibration tests are conducted to verify the FEA results with the same four-bolt fastened structure. It is found that the statistical analysis of the structural test data has good consistency with that of the FEA, which proves the effectiveness of FEA and the feasibility of the proposed method.

## 2. Theoretical Model of System Response Under SOR Synthesized Excitation

This section establishes theoretical models for the displacement response of a Multi-Degree-of-Freedom (MDOF) system under three different vibration excitation forms. The three types of vibration excitation are sine vibration, random vibration, and SOR vibration synthesized excitation. Then, the relationship between displacement responses of MDOF and structural strain is pointed out, providing a basis for the strain-based implicit monitoring method of bolt loosening.

### *2.1. Displacement Response of the MDOF System Under Sine Vibration Base Excitation*

Bolt loosening is evaluated through the strain responses of monitored points of the structure in this study. To achieve this, a structural theoretical model of responses under SOR vibration excitation is established.

The vibration differential equation for the MDOF system with vibration base displacement excitation is [24]

$$\mathbf{M}\ddot{\mathbf{x}} + \mathbf{C}\dot{\mathbf{x}} + \mathbf{K}\mathbf{x} = -\mathbf{M}\ddot{y}(t) \tag{1}$$

where $\mathbf{M}$ is the system mass matrix; $\mathbf{C}$ is the damping coefficient matrix; $\mathbf{K}$ is the system stiffness matrix; $\mathbf{x}$ is the displacement vector of the system; $-\mathbf{M}\ddot{y}(t)$ is the equivalent inertial force vector caused by base displacement excitation; $y(t)$ is the expression of the vibration base displacement excitation.

In practical vibration engineering such as aviation, aerospace, navigation, and vehicles, Equation (1) is often used to describe the structural vibration caused by the motion of the carrier foundation.

Supposing the base displacement excitation in sine form, it can be expressed as

$$y_{Sine}(t) = A_{Sine}\sin(\omega_{Sine}t) \tag{2}$$

where $A_{Sine}$ is the amplitude of sinusoidal displacement excitation; $\omega_{Sine} = 2\pi f$ is the angular frequency of sine displacement excitation.

According to Equation (2), the acceleration expression of the base displacement excitation of sine vibration should be

$$a_{Sine}(t) = \ddot{y}_{Sine}(t) = -A_{Sine}\omega_{Sine}^2\sin(\omega_{Sine}t) \tag{3}$$

According to the assumption of proportional damping, the eigenvectors of the system can be solved regardless of the damping term [25]. The eigenvalue equation of Equation (1) is

$$\left(\mathbf{K} - \omega_i^2\mathbf{M}\right)\boldsymbol{\Phi}_i = 0, \qquad i = 1, 2, \cdots, n \tag{4}$$

where $\omega_i$ is the $i$-th natural frequency of the system; $\boldsymbol{\Phi}_i$ is the corresponding modal vector; $n$ is the number of degrees of freedom.

We introduce a generalized coordinate vector $\mathbf{q}$ via coordinate transformation $\mathbf{x} = \boldsymbol{\Phi}\mathbf{q}$, where $\boldsymbol{\Phi} = [\boldsymbol{\Phi}_1, \boldsymbol{\Phi}_2, \ldots, \boldsymbol{\Phi}_n]$ is the modal matrix of the system. By substituting Equation (4) and the generalized coordinate vector $\mathbf{q}$ into Equation (1) and left-multiplying $\boldsymbol{\Phi}^T$ into the

equation of motion, the equation of motion for each mode of the system can be written as [24]

$$\ddot{\mathbf{q}}_i + 2\zeta_i\omega_i\dot{\mathbf{q}}_i + \omega_i^2\mathbf{q}_i = -\boldsymbol{\phi}_i^T\mathbf{M}\ddot{y}(t), \qquad i = 1, 2, \cdots, n \tag{5}$$

where $\zeta_i$ is the damping ratio of the $i$-th mode of the system.

For a system with zero initial conditions, according to Equations (3)–(5), its steady-state response under vibration base excitation is [26]

$$\mathbf{x} = \sum_{i=1}^{n} \boldsymbol{\phi}_i\mathbf{q}_i = \sum_{i=1}^{n} \boldsymbol{\phi}_i A_i \sin(\omega_{Sine}t + \varphi_i) \tag{6}$$

where the amplitude and phase are

$$\begin{cases} A_i = \frac{A_{Sine}\omega_{Sine}^2}{\sqrt{\left(\omega_i^2 - \omega_{Sine}^2\right)^2 + (2\zeta_i\omega_i\omega_{Sine})^2}} \\ \varphi_i = \arctan\left(\frac{2\zeta_i\omega_i\omega_{Sine}}{\omega_i^2 - \omega_{Sine}^2}\right) \end{cases} \tag{7}$$

It can be observed that the displacement response of a system under only sine vibration excitation is influenced not only by the system's own properties such as natural frequency $\omega_i$, damping ratio $\zeta_i$, and system stiffness matrix $\mathbf{K}$, but also by the amplitude $A_{Sine}$ and frequency $\omega_{Sine}$ of the sine excitation.

### *2.2. Displacement RMS Response of the MDOF System Under Random Vibration Base Excitation*

For random vibration excitation, frequency-domain analysis is usually required. In Equation (5), $\ddot{y}(t)$ is the base acceleration excitation of random vibration. Assuming $\ddot{y}(t)$ is a generalized stationary process, it is described by the acceleration PSD $\mathbf{S}_{a\_Rand}(\omega)$.

The frequency-domain generalized coordinate response of the system can be indicated as [27]

$$\mathbf{Q}_i(\omega) = H_i(\omega)\mathbf{S}_{a\_Rand}(\omega) \tag{8}$$

where $\mathbf{Q}_i(\omega)$ is the Fourier transform of the generalized coordinate response $\mathbf{q}_i(t)$; the frequency response function is

$$H_i(\omega) = \frac{1}{\omega_i^2 - \omega^2 + j2\zeta_i\omega_i\omega} \tag{9}$$

The acceleration PSD $\mathbf{S}_{a\_Rand}(\omega)$ of random vibration excitation represents the energy density of each frequency component in the frequency domain. According to Equation (8), the displacement response PSD $\mathbf{S}_{qi\_Rand}(\omega)$ of generalized coordinates can be obtained [27]

$$\mathbf{S}_{qi\_Rand}(\omega) = |H_i(\omega)|^2\mathbf{S}_{a\_Rand}(\omega) \tag{10}$$

where the square of the modulus of $H_i(\omega)$ is

$$|H_i(\omega)|^2 = \frac{1}{\left(\omega_i^2 - \omega^2\right)^2 + (2\zeta_i\omega_i\omega)^2} \tag{11}$$

According to Equation (6), the total displacement response $\mathbf{x}$ of the system is the sum of the modal responses of each order. $\mathbf{q}_i$ is an uncorrelated random process; the total displacement response PSD $\mathbf{S}_{x\_Rand}(\omega)$ is the sum of the power spectral densities of each mode [26]:

$$\mathbf{S}_{x\_Rand}(\omega) = \sum_{i=1}^{n} |\boldsymbol{\phi}_i|^2\mathbf{S}_{qi\_Rand}(\omega) \tag{12}$$

The response of the system under base random excitation is random, so the statistical average energy of the system response, i.e., the RMS values, can be used to represent the response. The RMS of the displacement response **x** can be obtained by integrating and taking the root of the displacement response PSD $\mathbf{S}_{x\_Rand}(\omega)$ in the frequency domain [26]:

$$RMS_{x\_Rand} = \sqrt{\int_0^\infty \mathbf{S}_{x\_Rand}(\omega)d\omega} \tag{13}$$

According to Equations (8)–(13), the displacement response of this system under random vibration excitation is not only related to the system's mass matrix **M**, stiffness matrix **K**, and damping ratio $\zeta_i$, but also to the excitation PSD $\mathbf{S}_{a\_Rand}(\omega)$.

### *2.3. Strain RMS Response of the MDOF System Under Base SOR Excitation*

After theoretical analysis of the displacement response of the MDOF system under sine and random vibration excitation, respectively, its response under SOR vibration synthesized excitation could be further analyzed.

Due to the fact that the sine vibration response is solved in the time domain, while the random vibration response is solved in the frequency domain, it is rather difficult to find the relationship between the SOR vibration response and individual sine and random vibration responses. Therefore, a frequency-domain analysis method is proposed, which converts sine vibration displacement excitation in the time domain into a frequency-domain acceleration PSD expression and superimposes it with random vibration excitation PSD to obtain the acceleration PSD under the SOR synthesized excitation. The advantage of this method is that it utilizes the mode-superposition method to achieve better computational accuracy in the frequency-domain analysis of the structure.

The time–frequency conversion method used in this study assumes that the RMS value of the excitation acceleration is one of the conditions for energy equivalence, which means the frequency domain PSD acceleration RMS values match the acceleration RMS values of the sine vibration excitation in the time domain. The relationship between the sine excitation acceleration RMS and its PSD spectrum is [26]

$$RMS_{a\_Sine} = \sqrt{\int_0^\infty \mathbf{S}_{a\_Sine}(\omega)d\omega} \tag{14}$$

The RMS value of the acceleration of the sine excitation is called the effective value of the signal, which is $1/\sqrt{2}$ times the amplitude of the sine excitation acceleration [28]. According to Equation (3), the acceleration RMS of the sine vibration excitation is

$$RMS_{a\_Sine} = \frac{A_{Sine}\omega_{Sine}^2}{\sqrt{2}} \tag{15}$$

Converting the sine vibration displacement excitation into acceleration PSD in the frequency domain, theoretically it represents a spectral value corresponding to a single frequency point in the PSD:

$$\mathbf{S}_{a\_Sine}(\omega) = \frac{\left(A_{Sine}\omega_{Sine}^2\right)^2}{2}\delta(\omega - \omega_{Sine}) \tag{16}$$

where $\delta(x)$ represents the Dirac delta function [29], which is widely used to express the "Concentration" effect. It has two fundamental properties: $\delta(x)$ is zero outside of $x = 0$; $\int_{-\infty}^{\infty}\delta(x)dx = 1$. These two fundamental properties enable it to effectively express the PSD components of sine signals without considering phase.

In practical applications, it is impossible to achieve infinite excitation at a single frequency, and the spectral lines in the excitation PSD need to have continuity and integrability. Therefore, other functions need to be used to approximate the Dirac function. According to Equation (16), the trigonometric function is used to approximate the expression of sine excitation in the PSD.

$$\mathbf{S}_{a\_Sine}(\omega) = \frac{\left(A_{Sine}\omega_{Sine}^2\right)^2}{2\pi\Delta f}\mathrm{tri}\left(\frac{\omega-\omega_{Sine}}{\pi\Delta f}\right) \tag{17}$$

where $\Delta f$ is the bandwidth of the sine function in the PSD that approximates a triangle; the function $\mathrm{tri}(x)$ is a triangular pulse function [30], defined as

$$\mathrm{tri}(x) = \begin{cases} 1-|x|, & |x| \le 1 \\ 0, & |x| > 1 \end{cases} \tag{18}$$

at the sine excitation frequency $\omega_{Sine}$, and the spectral line inside is an impulse triangle, while the spectral values in other frequency bands are zero.

Therefore, the sine excitation and the random excitation PSD can be superimposed in the frequency domain to solve the response of the SOR synthesized excitation PSD. According to Equations (10), (12) and (13), the displacement response RMS of the system under the SOR synthesized excitation in the frequency domain can be obtained:

$$RMS_{x\_SOR} = \sqrt{\int_0^\infty \sum_{i=1}^{n} |\boldsymbol{\Phi}_i|^2 |H_i(\omega)|^2 \mathbf{S}_{a\_SOR}(\omega) d\omega} \tag{19}$$

The expression of the SOR synthesized excitation in frequency-domain analysis involves a spike representing sine excitation on the basis of random vibration excitation, so the SOR synthesized excitation PSD can be expressed by

$$\mathbf{S}_{a\_SOR}(\omega) = \mathbf{S}_{a\_Sine}(\omega) + \mathbf{S}_{a\_Rand}(\omega) \tag{20}$$

Combining Equations (19) and (20), the relationship between the displacement response $RMS_{x\_SOR}$ of the system under the SOR synthesized excitation, the displacement response $RMS_{x\_Sine\_PSD}$ of sine excitation in spectral conversion, and the $RMS_{x\_Rand}$ of random excitation can be obtained:

$$\begin{aligned} RMS_{x\_SOR} &= \sqrt{\int_0^\infty \sum_{i=1}^{n} |\boldsymbol{\Phi}_i|^2 |H_i(\omega)|^2 \mathbf{S}_{a\_SOR}(\omega) d\omega} \\ &= \sqrt{\int_0^\infty \sum_{i=1}^{n} |\boldsymbol{\Phi}_i|^2 |H_i(\omega)|^2 (\mathbf{S}_{a\_Sine}(\omega) + \mathbf{S}_{a\_Rand}(\omega)) d\omega} \end{aligned} \tag{21}$$

Based on the obtained displacement response under SOR vibration excitation, the strain response of the MDOF system can be solved. For the MDOF system, the strain between two points $\alpha$ and $\beta$ can be expressed as [31]

$$\varepsilon_{\alpha\beta} = \sqrt{\varepsilon_{u_{\alpha\beta}}^2 + \varepsilon_{v_{\alpha\beta}}^2 + \varepsilon_{w_{\alpha\beta}}^2} \tag{22}$$

where $\varepsilon_{u_{\alpha\beta}}$, $\varepsilon_{v_{\alpha\beta}}$, and $\varepsilon_{w_{\alpha\beta}}$ are the components of strain between two points in the $u$, $v$, and $w$ directions, respectively, which can be defined as

$$\begin{cases} \varepsilon_{u_{\alpha\beta}} = \frac{(u_\beta - u_\alpha) - D_{u_{\alpha\beta}}}{D_{u_{\alpha\beta}}} \\ \varepsilon_{v_{\alpha\beta}} = \frac{(v_\beta - v_\alpha) - D_{v_{\alpha\beta}}}{D_{v_{\alpha\beta}}} \\ \varepsilon_{w_{\alpha\beta}} = \frac{(w_\beta - w_\alpha) - D_{w_{\alpha\beta}}}{D_{w_{\alpha\beta}}} \end{cases} \tag{23}$$

where $u$, $v$, and $w$ are the orthogonal displacement response components of the system response $\mathbf{x}$ at point $\alpha$ or $\beta$; $D\_{\alpha\beta}$ is the component of the initial distance between the two points $\alpha$ and $\beta$ in one direction among the $u$, $v$, and $w$ directions.

The strain PSD components between two points $\alpha$ and $\beta$ in three directions can be expressed as [32]

$$\begin{cases} \mathbf{S}_{\varepsilon\_u_{\alpha\beta}}(\omega) = \frac{1}{D^2_{u_{\alpha\beta}}}\left(\mathbf{S}_{u_{\alpha\alpha}}(\omega) + \mathbf{S}_{u_{\beta\beta}}(\omega) - 2\mathrm{Re}\left\{\mathbf{S}_{u_{\alpha\beta}}(\omega)\right\}\right) \\ \mathbf{S}_{\varepsilon\_v_{\alpha\beta}}(\omega) = \frac{1}{D^2_{v_{\alpha\beta}}}\left(\mathbf{S}_{v_{\alpha\alpha}}(\omega) + \mathbf{S}_{v_{\beta\beta}}(\omega) - 2\mathrm{Re}\left\{\mathbf{S}_{v_{\alpha\beta}}(\omega)\right\}\right) \\ \mathbf{S}_{\varepsilon\_w_{\alpha\beta}}(\omega) = \frac{1}{D^2_{w_{\alpha\beta}}}\left(\mathbf{S}_{w_{\alpha\alpha}}(\omega) + \mathbf{S}_{w_{\beta\beta}}(\omega) - 2\mathrm{Re}\left\{\mathbf{S}_{w_{\alpha\beta}}(\omega)\right\}\right) \end{cases} \tag{24}$$

where $\mathbf{S}_{\alpha\alpha}(\omega)$ and $\mathbf{S}_{\beta\beta}(\omega)$ are the displacement response self-PSD of $\alpha$ and $\beta$ in one direction among the $u$, $v$, and $w$ directions, respectively; $\mathbf{S}_{\alpha\beta}(\omega)$ is the cross-PSD between $\alpha$ and $\beta$; $\mathrm{Re}\{\cdot\}$ represents taking the real part of the cross-PSD.

According to Equations (13), (22) and (24), the strain response RMS between points $\alpha$ and $\beta$ is

$$\begin{aligned} RMS_{\varepsilon_{\alpha\beta}} &= \sqrt{\int_0^\infty \mathbf{S}_{\varepsilon_{\alpha\beta}}(\omega)d\omega} \\ &= \sqrt{\int_0^\infty \left(\mathbf{S}_{\varepsilon\_u_{\alpha\beta}}(\omega) + \mathbf{S}_{\varepsilon\_v_{\alpha\beta}}(\omega) + \mathbf{S}_{\varepsilon\_w_{\alpha\beta}}(\omega)\right)d\omega} \end{aligned} \tag{25}$$

Thus, the strain response RMS values of the MDOF system under SOR synthesized excitation are obtained.

## 3. Analysis of Bolt Loosening Mechanism Under Sine or Random Vibration Excitation

One of the main failure modes of bolted connection structures is loosening failure, and one of the main causes of bolt loosening failure is the influence of reciprocating vibration on the structure [33]. The study of bolt loosening failure under vibration excitation is usually sine vibration at a lower frequency, while there is a lack of research on higher frequency sine vibration and random vibration excitation.

Taking a four-bolt fastened structure as an example in this paper, the strain responses of the monitored points near the bolts under sine and random vibration excitations are analyzed independently to explore the mechanism of bolt loosening in complex vibration environments.

### *3.1. FEA Modeling and Modal Analysis for the Four-Bolt Fastened Structure*

#### 3.1.1. FEA Modeling for the Four-Bolt Fastened Structure

The four-bolt fastened structure is modeled with the modeling software SolidWorks 2016, as shown in Figure 1, which includes a disc-shaped base with 28 M8 thread holes distributed on the inner and outer circumferences, where 12 inner holes are used to connect the base and vibrostand, and 16 outer holes are used to connect the base and fixture, which

is a special-shaped fixture composed of two plates horizontally and vertically, a rectangular clamped part, and four M10 coarse threaded bolts. The clamped part is a 10 mm thick rectangular plate, and the bolt loosening monitoring method is used to monitor the strains on the surface of the clamped part.

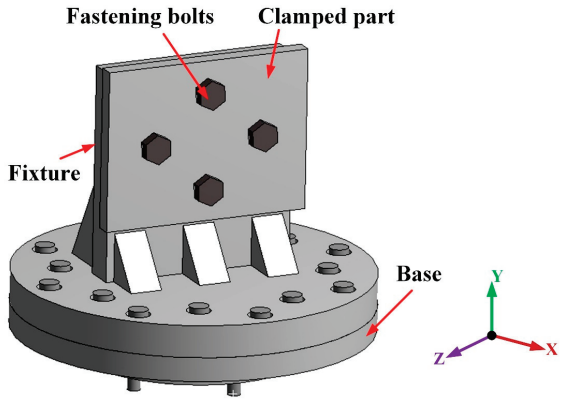



**Figure 1.** Model of the 4-bolt fastened structure.

In order to make the bolts and the clamped part have a more obvious difference in stiffness, carbon steel is used for the bolts and the nuts, and aluminum alloy is used for the clamped part and the fixture. The materials of the structure are shown in Table 1.

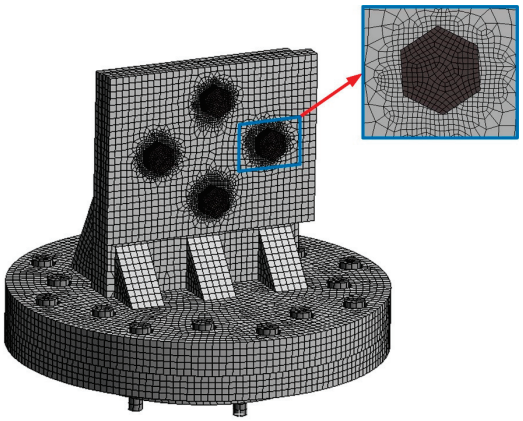
**Table 1.** The material information of the structure.

| Components | Material | Density ($kg/m^3$) | Elastic Modulus (GPa) | Poisson's Ratio |
|---|---|---|---|---|
| Clamped part/Fixture/Base | Aluminum alloy (7075-T6) | 2810 | 71 | 0.32 |
| Bolts/Nuts | Structure steel (16MnCr5) | 7800 | 210 | 0.28 |

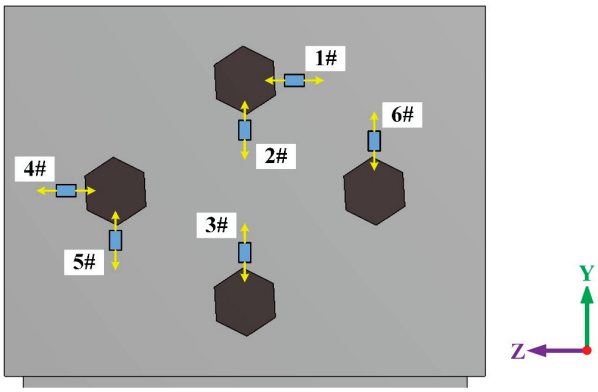
The finite element simulation software Ansys Workbench 15.0 is used to study the mechanism of bolt loosening of the four-bolt fastened structure. In modeling the FEA, the bottom of the base is set as a fixed support to simulate its connection with the vibrostand. The contact types of the following contact pairs are set as frictional type: the upper surface of the base and the bottom of the fixture; the fixture upright plate and the nut surfaces; the fixture upright plate and the contact surface of the clamped part; and the contact surface of the clamped part and the bolt heads. The frictional coefficient is set to 0.15 according to the engineering manual [34].

Multi-Point Constraints (MPCs) are used between the bolts and the nuts [35]. The MPC method is widely used for thread-region analysis in FEA. The MPC method describes the contact behavior of bolts and nuts by applying constraint relationships between their contact surfaces, which simplifies the contact problem between bolts and nuts into a coupling relationship between leader–follower nodes, without the need to establish an accurate thread model.

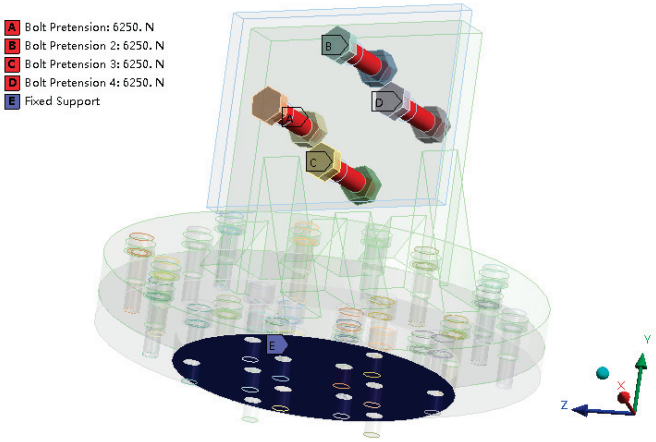
The mesh division of the FEA model is shown in Figure 2a. The global meshing type is hexahedral mesh, which has simple partitioning, high computational efficiency, and strong convergence. The global meshing element size is 4 mm, while the grid accuracy for the four fastening bolts, nuts, and their adjacent areas is refined to 1 mm to ensure the accuracy of the analysis solution.



(**a**) Model meshing of the structure




(**b**) Distribution and direction of the monitored points




(**c**) Schematic diagram of the structural load

**Figure 2.** Schematic diagram of the 4-bolt fastened structure.

The six monitored strain points are determined near the four bolts, with a distance of 15 mm from the center of the corresponding bolt. The monitoring direction of monitored points 1# and 4# is the Z-direction (horizontal direction), while the monitoring direction of monitored points 2#, 3#, 5#, and 6# is the Y-direction (vertical direction), as shown in Figure 2b.

Since the bottom surface of the base is connected to the vibrostand by bolts, the vibration excitation from the vibrostand is simulated by applying a Y-direction sinusoidal vibration displacement load to the bottom surface of the structure base. Figure 2c shows a schematic diagram of load application at a tightening torque of 15 N·m, where conditions A, B, C, and D represent the preload force of 6250 N applied to the four bolts, and condition E represents the surface subjected to sinusoidal vibration displacement load on the structure.

The vibration responses of the structure are analyzed under 15 different tightening torques. The following relationship exists between the bolt tightening torque $T$ and tightening force $F$ [34]:

$$T = KFd \tag{26}$$

where $K$ is the torque coefficient, and $K = 0.24$ in this investigation; $d$ is the nominal diameter of the bolts, and $d = 10$ mm in this investigation.

Equation (26) shows that for bolts with certain material and size information, the tightening force and tightening torque have a linearly positive correlation, which can be expressed by linear transformation in research. Through adjusting the tightening force successively, a set of corresponding tightening torques can be obtained.

In the FEA for this study, the finite element software Ansys Workbench 15.0 is used to exert axial force on a continuous surface cylinder (the screw surface of four bolts in this study) to achieve the corresponding bolt tightening force; 15 groups of tightening torque and their corresponding pre-tightening forces are shown in Table 2. For each analysis, a group of the same tightening torque is applied to the four bolts.

**Table 2.** Tightening torques of the bolts for the analysis.

| **Torque/N·m** | 3 | 5 | 7 | 9 | 11 | 13 | 15 | 17 |
|---|---|---|---|---|---|---|---|---|
| **Force/N** | 1250.0 | 2083.3 | 2916.7 | 3750.0 | 4583.3 | 5416.7 | 6250.0 | 7083.3 |
| **Torque/N·m** | 19 | 21 | 23 | 25 | 27 | 28.5 | 30 | |
| **Force/N** | 7916.7 | 8750 | 9583.3 | 10,416.7 | 11,250 | 11,875 | 12,500 | |

3.1.2. Modal Analysis for the Four-Bolt Fastened Structure

The first 20 modes of the four-bolt fastened structure are extracted for vibration excitation analysis. Different tightening torques will affect structural stiffness and natural frequency [36]; by taking the tightening torque of 15 N·m as an example, the structural nature frequencies are determined, and the first 10 orders of natural frequencies are shown in Table 3.

**Table 3.** The first 10 orders of natural frequencies of the 4-bolt fastened structure.

| **Modal Order** | **1** | **2** | **3** | **4** | **5** |
|---|---|---|---|---|---|
| **Natural Freq./Hz** | 1270.3 | 2504.8 | 2582.4 | 4122.1 | 4658.7 |
| **Modal order** | **6** | **7** | **8** | **9** | **10** |
| **Natural Freq./Hz** | 5172.6 | 5246.6 | 5321.9 | 5400.1 | 5882.3 |

According to Table 3, the first-order natural frequencies of the structure are above 1000 Hz, and only one order is below 2000 Hz, indicating that the structure has good stiffness.

### *3.2. Analysis of Bolt Loosening Mechanism of the Four-Bolt Fastened Structure Under Sine Vibration Excitation*

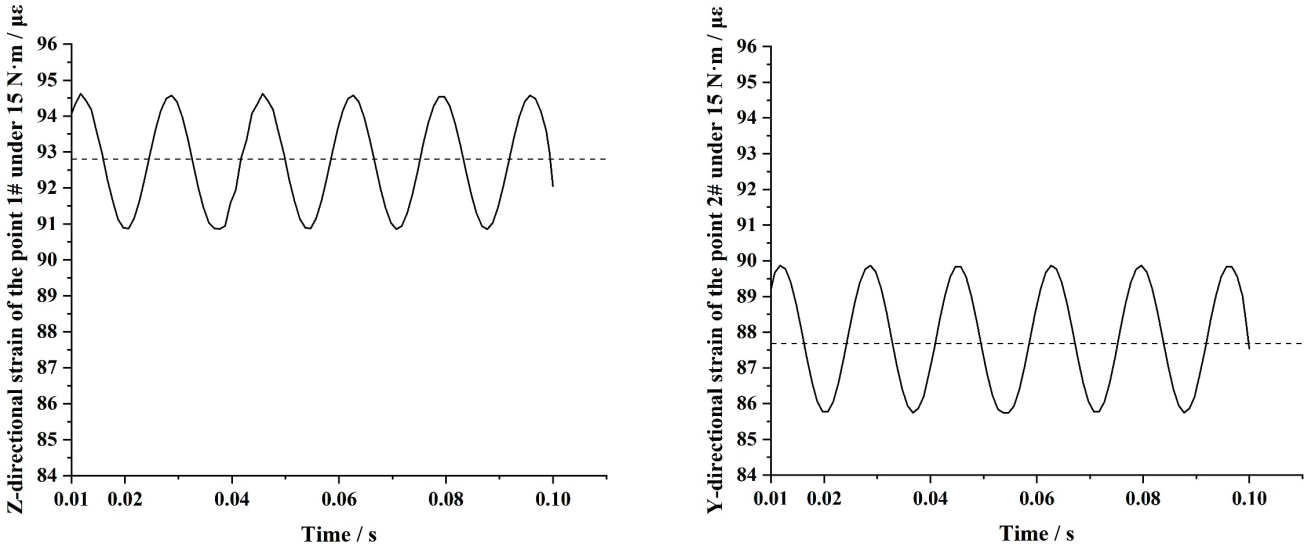
Based on the modal analysis results, the RMS strain response of the monitored bolt points in the four-bolt fastened structure under sine vibration excitation is analyzed.

The sine vibration excitation exerted to the bottom of the base in the Y-direction is given as Equation (2), supposing that the excitation amplitude $A_{Sine}$ is 1 mm and the excitation frequency $f_{Sine}$ is 60 Hz.

Sine vibration analyses of the structure under different tightening torques are carried out, and the strain responses of the six monitored points are obtained.

Taking the tightening torque of 15 N·m as an example, Figure 3 shows the normal strain response of monitored points 1# and 2# within 0.1 s.

As shown in Figure 3, the strain at a monitored point consists of two parts: one part is the pre-strain $\varepsilon^p$ generated by the tightening torque and the other part is the vibration strain $\varepsilon^v$ generated by the vibration excitation. Due to the different positions and directions, the response values of the six monitored points are different. However, their trends and patterns are the same.




(**a**) Normal strain response of 1# (**b**) Normal strain response of 2#

**Figure 3.** Normal strain responses of the monitored points within 0.1 s under 15 N·m tightening torque.

Since $\varepsilon^p$ is much larger than $\varepsilon^v$, it is possible that $\varepsilon^v$ would be covered up by $\varepsilon^p$. Thus, a workaround method is utilized in that $\varepsilon^p$ is removed from the monitored total strain first before vibration occurring, and then only $\varepsilon^v$ is extracted for mechanism analysis during the vibration process. It should be pointed out that $\varepsilon^v$ is influenced not only by vibration excitation but also by the bolt tightening torque [37]; it is reasonable that $\varepsilon^v$ can be chosen as an indicator for investigating the response of bolt loosening under the dual factors of vibration excitation and the bolt tightening torque.

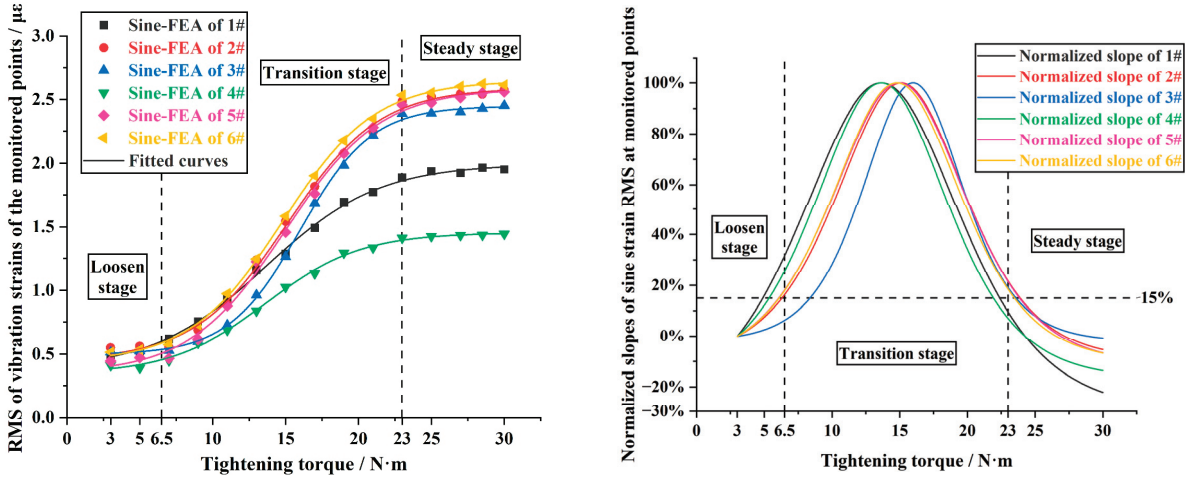
The effective value of a sine signal is called the Root Mean Square (RMS) value; the effect of vibration excitation on bolt loosening is reflected by monitoring the RMS values of vibration strains at monitored points. The following is the formula for calculating the RMS value of vibration strain at a monitored point:

$$\varepsilon^{vRMS} = \sqrt{\frac{\sum_{i=1}^{N}\left(\varepsilon^{vi}\right)^2}{N}} = \sqrt{\frac{\left(\varepsilon^{v1}\right)^2 + \left(\varepsilon^{v2}\right)^2 + \cdots + \left(\varepsilon^{vN}\right)^2}{N}} \tag{27}$$

where $N$ donates the number of sampled strain data in the time domain; $\varepsilon^{vi}$ is the $i$-th data point of the vibration strain.

The Matrix Laboratory software MATLAB R2018b is used to calculate and process the result data. The RMS values of the vibration strain response $\varepsilon^{vi}$ at the six monitored points are shown in Figure 4a.

It can be observed that the strain RMS curves of the six monitored points are roughly divided into three stages. To quantitatively divide these three stages, we considered using the slope change rates of the strain RMS curves. However, due to the different slope ranges of the strain RMS curves at different monitored points, in order to propose a unified standard, a normalized slope method is adopted. This method normalizes the slopes of the strain RMS curves at each monitored point when the tightening torque is 3 N·m to 0%, and the maximum slope of the RMS curve within the torque ranges up to 100%. In this way, the slopes of the strain RMS curves of the six monitored points can be unified to the same slope, and by using an appropriate slope boundary as the stage division, the three stages can be quantitatively divided, as shown in Figure 4b.




(**a**) Strain RMS curves of monitored points (**b**) Normalized slopes of strain RMS curves

**Figure 4.** Strain RMS of FEA results varying with tightening torque under sine vibration.

From Figure 4a, it can be found that the strain $\varepsilon^v$ RMS curves of the six monitored points have the same trend, which is because the distribution of the fastening bolts of the structure is generally symmetrical. It can be observed that the RMS values of strain responses at monitored points 1# and 4# are smaller compared to the responses of the other four monitored points. This is because the monitoring direction of monitored points 1# and 4# is the Z-direction, which is orthogonal to the vibration excitation direction of the Y-direction, while the monitoring direction of the other monitored points is the same as the excitation direction.

As shown in Figure 4b, the slopes of the strain RMS curves of the six monitored points are normalized. Using the mean tightening torque at the normalized slope of 15% for the strain RMS curves of six monitored points as the boundary torques, it can be divided into the Steady Stage, the Transition Stage, and the Loosen Stage.

For the Steady Stage, the strain RMS values always stay at a higher steady level when the tightening torque is larger than 23 N·m. This is because the bolt axial pretension remains at a high level, which ensures tightness between the bolts and fasteners.

For the Transition Stage, when the tightening torque is gradually reduced from 23 N·m to 6.5 N·m, the lower the preload, the lower the friction among the contact surfaces of the bolts and the clamped part; thus the looseness among the contact surfaces is more serious.

For the Loosen Stage, when the tightening torque is less than 6.5 N·m, the levels of strain RMS values at the six monitored points generally remain at a lower level, which means that the bolts have completely loosened and failed.

Some pivotal contact regions are assigned the frictional contact type, which is a typical nonlinear contact type and an important factor in the occurrence of nonlinear response in structures. On the other hand, the loosening mechanism of bolts is studied under vibration excitation by applying different tightening torques to bolts. The changing tightening torque is also one of the reasons for the boundary nonlinear response.

### *3.3. Analysis of Bolt Loosening Mechanism of the Four-Bolt Fastened Structure Under Random Vibration Excitation*

Based on the mode-superposition method, the RMS strain responses of the monitored bolt points in the four-bolt fastened structure under random vibration excitation are analyzed.

In this section, a white-noise waveform acceleration PSD is applied to the bottom of the base of the structure. Figure 5 is a schematic diagram of the random vibration excitation

PSD. The frequency range of the PSD is set as 15–1000 Hz, and the spectral value is 0.2 $g^2$/Hz.

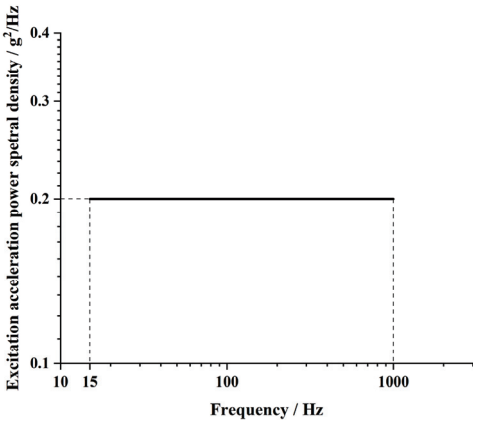
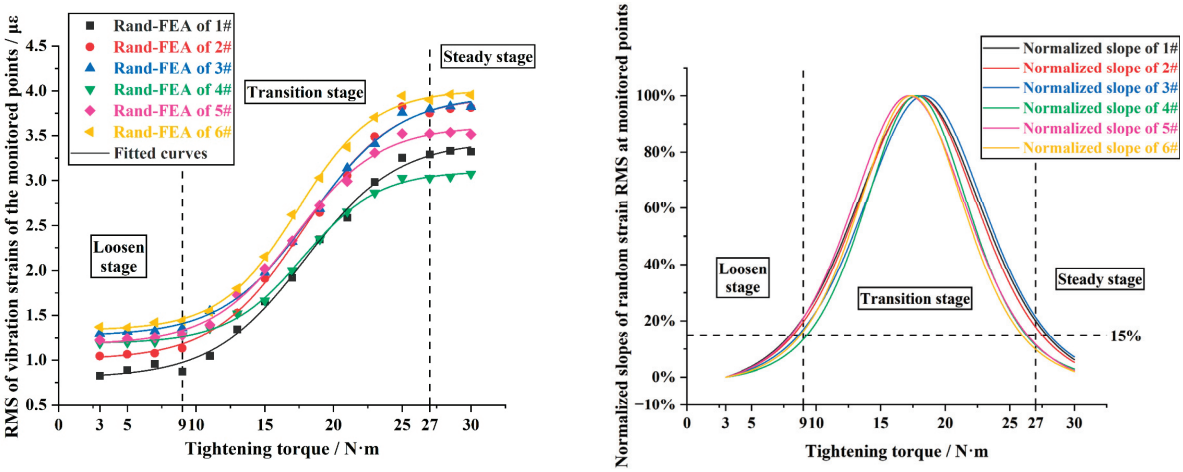



**Figure 5.** Random vibration excitation spectrum.

The RMS values of the strain responses of the six monitored points under random vibration with different tightening torques are extracted. Figure 6 shows the curves of the RMS values of the strain responses with varying tightening torques and the normalized slopes of the strain RMS curves.




(**a**) Strain RMS of monitored points (**b**) Normalized slopes of strain RMS curves

**Figure 6.** FEA strain RMS varying with tightening torques under random vibration.

It can be found that under random vibration excitation, the strain RMS values of the six monitored points have the same trend of varying with tightening torques, and the process of bolt loosening can be divided into three stages: the Steady Stage, the Transition Stage, and the Loosen Stage. This is similar to the three stages of bolt loosening under sine vibration excitation. Compared with the other four monitored points, the RMS values of the strain responses at monitored points 1# and 4# are relatively smaller because their monitoring directions are orthogonal to the excitation direction.

From Figure 6b, similarly, using a relative initial slope change of more than 15% as the boundary, the boundary tightening torques of the three loosening stages under random vibration are 27 N·m and 9 N·m, respectively, while those under sine vibration are 23 N·m and 6.5 N·m. This indicates that under random vibration, bolts will enter the Transition Stage and the Loosen Stage earlier than that under sine vibration. The reasons for this phenomenon are multifaceted. The acceleration RMS values of the two excitations are different, resulting in different bolt loosening boundaries. Considering the

energy distribution, the energy of the random vibration excitation distributes over a wide frequency range, and its upper limit is close to the structural natural frequency, while the sine vibration is only excited at a single fixed frequency of 60 Hz.

## 4. Investigation of Bolt Loosening Mechanism Under SOR Vibration Excitation

### *4.1. A Synthetic Excitation Analysis Method of SOR Vibration*

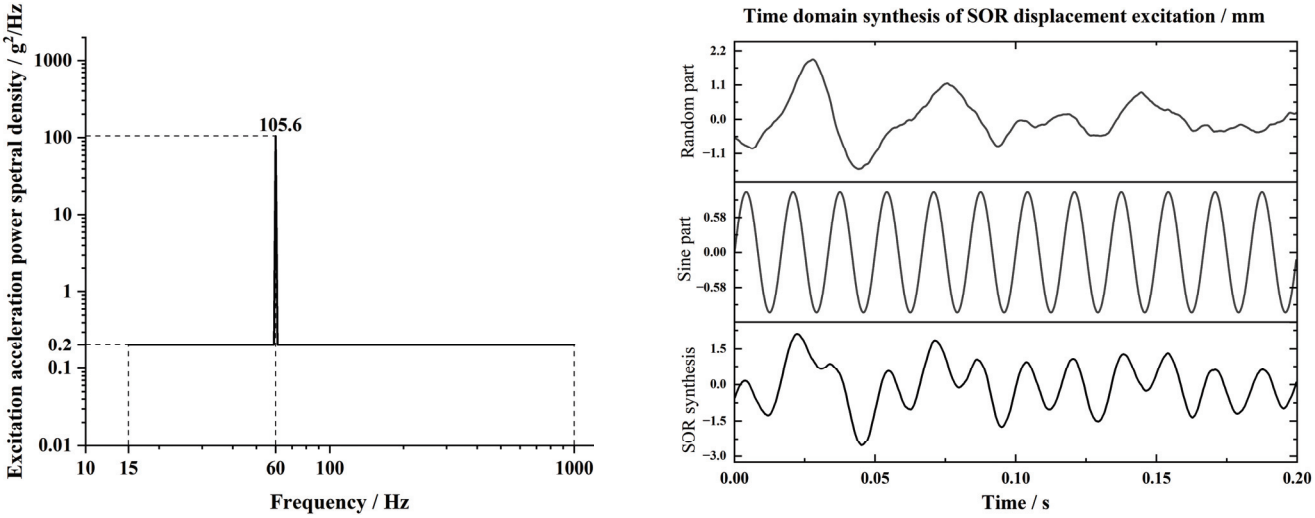
In order to analyze the effect of SOR vibration excitation on the response of bolt loosening, FEA of the strain responses of the monitored points under synthesized excitation is carried out.

A frequency-domain analysis method is proposed, which transforms sine vibration excitation into PSD expression and superimposes it with random vibration excitation PSD to obtain SOR vibration synthesized excitation PSD. The advantage of this method is that frequency-domain analysis relies on the mode-superposition method, which brings better analysis efficiency.

The excitation PSD value of sine vibration can be calculated with the excitation acceleration of the sine vibration, which can be obtained from Equation (3). Theoretically, there should be a definite spectrum value at the sine excitation frequency. However, the spectrum line of the PSD must have continuity and integrability, so it is necessary to perform spectral approximation on the PSD conversion of the sine excitation.

The meaning of PSD is the distribution function of energy in the corresponding frequency range. According to Equation (17), the frequency-domain transformation of the sine excitation is expressed approximatively as an isosceles triangle spectrum with a bottom bandwidth of only 2 Hz. The peak value of the excitation PSD can be calculated as 105.16 $g^2$/Hz by using the sine excitation amplitude of 1 mm and the excitation frequency of 60 Hz in Section 3.2.

To construct the synthetic excitation spectrum of the SOR vibration excitation, the sine triangle spectrum is superimposed to the white-noise excitation spectrum of the random vibration, as shown in Figure 7a, the dashed lines in Figure 7a are auxiliary lines for reading the values. The frequency-domain expression of SOR synthesized excitation PSD is not intuitive, so a more intuitive expression of SOR displacement excitation in the time domain is shown in Figure 7b.

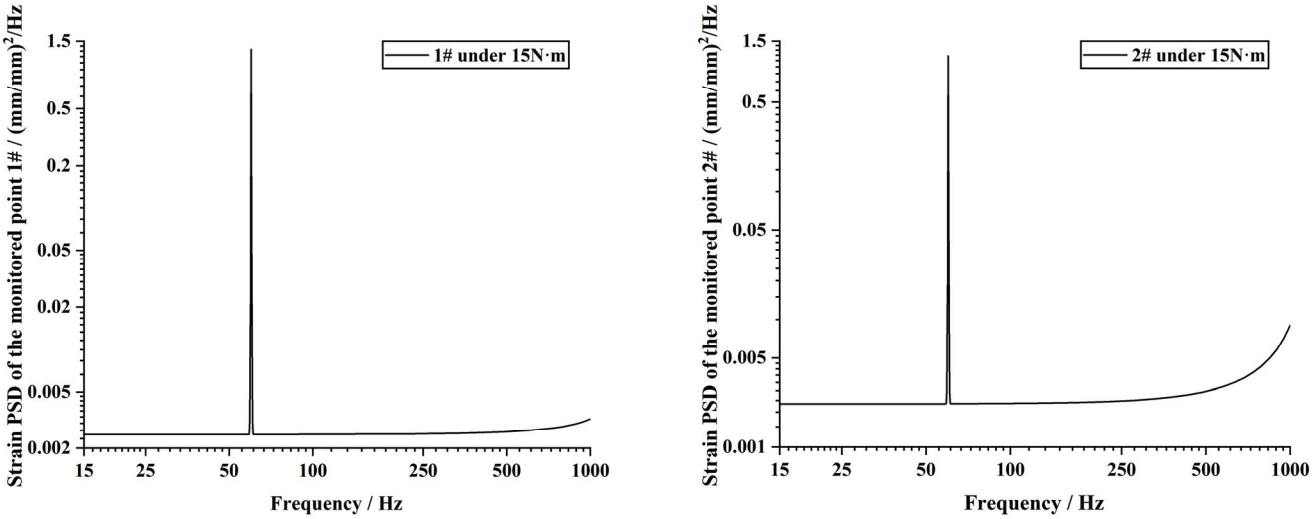



(**a**) SOR synthesize PSD in the frequency domain (**b**) SOR synthesis excitation in the time domain

**Figure 7.** Diagram of SOR synthesized excitation in different domains.

*4.2. Response Analysis of the Monitored Points of Bolt Loosening Under SOR Vibration Excitation*

Taking 15 N·m as an example, Figure 8 shows the strain response PSD of monitored points 1# and 2# under SOR synthesized excitation.

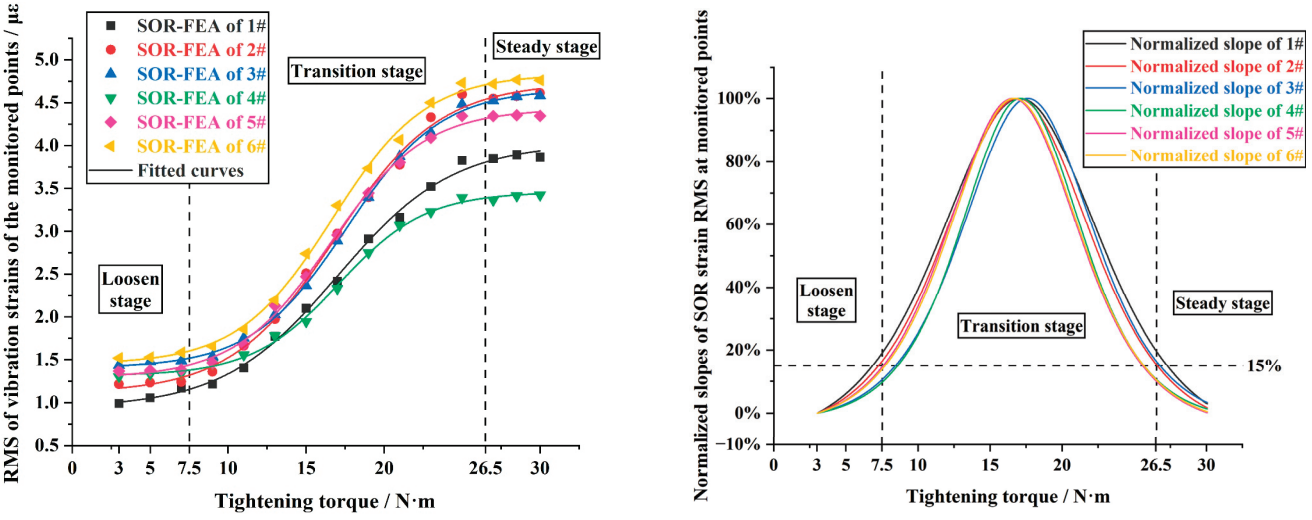



(**a**) Strain PSD of monitored point 1# (**b**) Strain PSD of monitored point 2#

**Figure 8.** Strain response PSD of the monitored points under SOR excitation with 15 N·m tightening torque.

It can be seen from Figure 8 that under the SOR synthesized excitation, the strain response of each monitored point only has a high peak at the sine excitation frequency of 60 Hz and maintains a stable response outside of this frequency. The response gradually increases in the latter part of the frequency range, which is because the response frequency gradually approaches the structural first-order natural frequency.

Figure 9 shows the curves of strain RMS of the six monitored points and the normalized slopes of the strain RMS curves under SOR excitation.




(**a**) Strain RMS of monitored points (**b**) RMS normalized slopes of monitored points

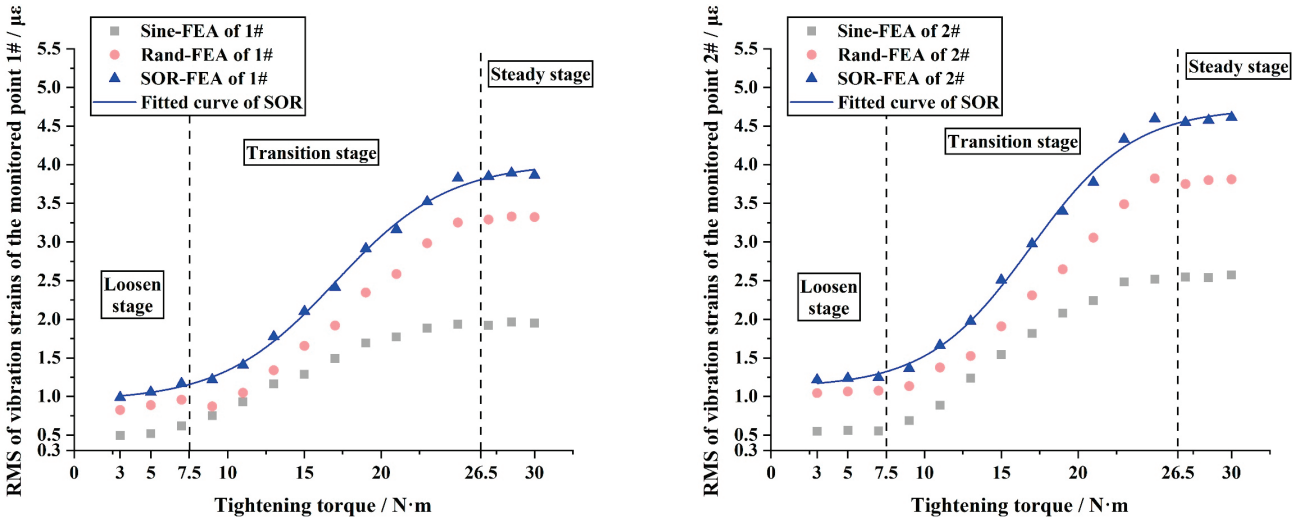
**Figure 9.** Curves of strain RMS of monitored points versus tightening torques under SOR synthesized excitation.

From Figure 9b, using the mean tightening torque at the normalized slope of 15% for the strain RMS curves of six monitored points as the boundary torques, which are 26.5 N·m

and 7.5 N·m, respectively, it can be divided into the Steady Stage, the Transition Stage, and the Loosen Stage.

The boundary torques of bolt loosening under SOR excitation are not the same as those under sine or random vibration excitations. When the bolts enter the Transition Stage from the Steady Stage, the boundary torque under SOR excitation is closer to the boundary torque under random excitation. And when the bolts enter the Loosen Stage from the Transition Stage, the boundary torque under SOR excitation is in the middle of the two boundary torques of the two single excitations. This indicates that under SOR excitation, random vibration dominates the bolt loosening mechanism.

Taking monitored points 1# and 2# as examples, the RMS response results of monitored points under three forms of vibration excitations are compared and analyzed, as shown in Figure 10.




(**a**) Results comparison of monitored point 1# (**b**) Results comparison of monitored point 2#

**Figure 10.** Comparison curves of strain RMS at monitored points under three forms of vibration.

It can be found that the strain RMS of the monitored point under SOR excitation is greater than that under single sine or random vibration excitation, but its curve trend is similar to the trends of the single vibration excitation results. Furthermore, it should be pointed out that the strain RMS values under SOR excitation are not equal to the linear superposition of that under the two single excitations.

### *4.3. A Relation Model Among the SOR Vibration Excitation Results and the Single Vibration Excitation Results Based on the Corrective Energy Superposition Method*

In order to study the response relationship of the monitored points among SOR synthesized excitation and two forms of single vibration excitations, we take 5 N·m, 15 N·m, and 25 N·m as examples to compare their responses, as shown in Table 4.

It can be found from Table 4 that the responses under sine vibration, random vibration, and SOR vibration synthesized excitation do not simply show a linear superposition relationship. In order to investigate the nonlinear correlation among the strain RMS responses of monitored points under three forms of vibration excitations, the corrective energy superposition method (ESM) introducing weight factors is proposed, which assumes that the contributions of sine and random vibration responses to the SOR vibration response are influenced by their respective "energies".

$$RMS_{\varepsilon\_SOR} = \sqrt{a_{T_i} \times RMS^2_{\varepsilon\_Sine} + b_{T_i} \times RMS^2_{\varepsilon\_Rand}} \tag{28}$$

where $RMS_{\varepsilon\_Sine}$ represents the vibration strain response RMS values of the time-domain sine excitation; $RMS_{\varepsilon\_Rand}$ represents the vibration strain response RMS values of the random excitation; $a_{T_i}$ represents the energy weight factor of the sine vibration response in the SOR vibration response under the tightening torque of $T_i$; and $b_{T_i}$ represents the energy weight factor of the random vibration response in the SOR vibration response under the tightening torque of $T_i$. It should be inferred that the weight factors $a_{T_i}$ and $b_{T_i}$ may be different under different tightening torques.

**Table 4.** RMS values of strain response of 6 monitored points under 3 forms of vibration excitation at 3 torques.

| Torque (N·m) | Excitation | 1# (με) | 2# (με) | 3# (με) | 4# (με) | 5# (με) | 6# (με) |
|---|---|---|---|---|---|---|---|
| 5 | Sine | 0.5211 | 0.5611 | 0.5247 | 0.3907 | 0.4721 | 0.5349 |
| | Random | 0.8892 | 1.0657 | 1.3179 | 1.1952 | 1.2427 | 1.3588 |
| | SOR | 1.0577 | 1.2355 | 1.4822 | 1.3345 | 1.3775 | 1.5293 |
| 15 | Sine | 1.2859 | 1.544 | 1.2638 | 1.0265 | 1.4577 | 1.5843 |
| | Random | 1.4929 | 1.9091 | 1.9775 | 1.6643 | 2.0178 | 2.1514 |
| | SOR | 2.1029 | 2.5095 | 2.3644 | 1.948 | 2.4711 | 2.7393 |
| 25 | Sine | 1.9372 | 2.5212 | 2.3915 | 1.4252 | 2.4753 | 2.5546 |
| | Random | 3.2532 | 3.824 | 3.7561 | 3.0278 | 3.5234 | 3.944 |
| | SOR | 3.8282 | 4.5956 | 4.4814 | 3.3924 | 4.3433 | 4.7294 |

The specific idea for obtaining the optimal weight factors $a_{T_i}$ and $b_{T_i}$ is shown in Figure 11.

As shown in Figure 11, for each set of tightening torques, according to Equation (28), the corresponding weight factors $a_{T_x,i,j}$ and $b_{T_x,i,j}$ can be obtained, which represent the set of weight factors obtained from the RMS responses of monitored points *i*# and *j*# under three forms of vibration excitation at the tightening torque $T_x$ of $x$ N·m.

Based on the weight factors $a_{T_x,i,j}$ and $b_{T_x,i,j}$, using Equation (28) with the sine vibration responses $RMS_{FEA-Sine\_T_x\_n\#}$ (where *n*# represents any one monitored point) and random vibration responses $RMS_{FEA-Rand\_T_x\_n\#}$ of the six monitored points, the theoretical SOR vibration responses $RMS_{Theo-SOR\_T_x\_n\#}$ of the corresponding monitored points are obtained.

Thus, the error between the theoretical calculated SOR response $RMS_{Theo-SOR\_T_x\_n\#}$ and the FEA SOR response $RMS_{FEA-SOR\_T_x\_n\#}$ of each monitored point can be obtained. There are six monitored points, so the $C_6^2 = 15$ groups of weight factors can be obtained when the tightening torque is $x$ N·m. By introducing the Least Squares Method, the average errors between the $RMS_{Theo-SOR\_T_x\_n\#}$ and $RMS_{FEA-SOR\_T_x\_n\#}$ of the six monitored points for each set of weight factors are taken as the optimal objective function, which can obtain the optimal weight factors $a_{T_x}$ and $b_{T_x}$ under the tightening torque $T_x$ of $x$ N·m.

Finally, the same steps are carried out for responses under all groups of tightening torque, and the optimal weight factors $a_{T_i}$ and $b_{T_i}$ under each group of tightening torque can be obtained.

The curves of the optimal weight factors $a_{T_i}$ and $b_{T_i}$ under all tightening torques are shown in Figure 12.

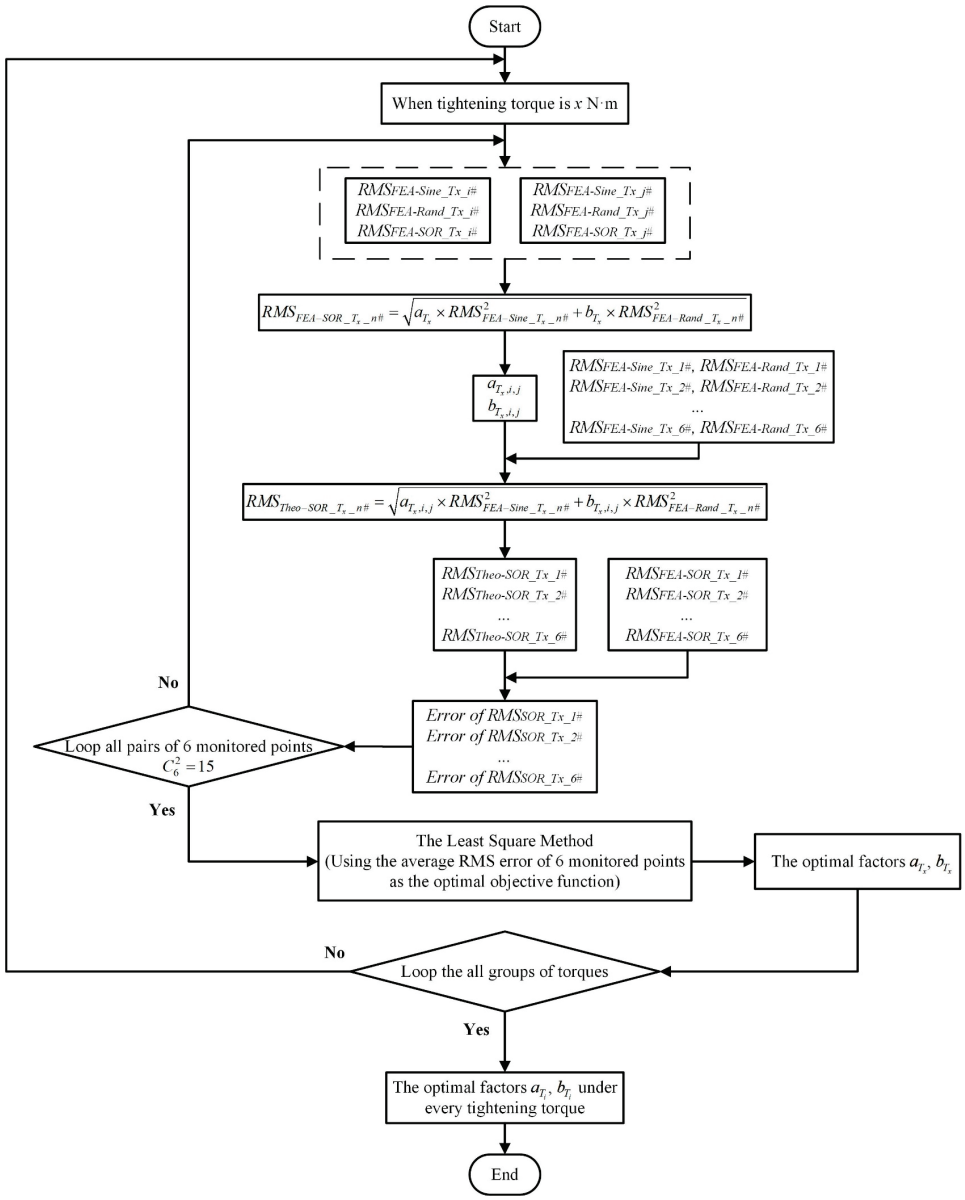



**Figure 11.** The calculation flowsheet for all optimal weight factors $a_{T_i}$ and $b_{T_i}$.

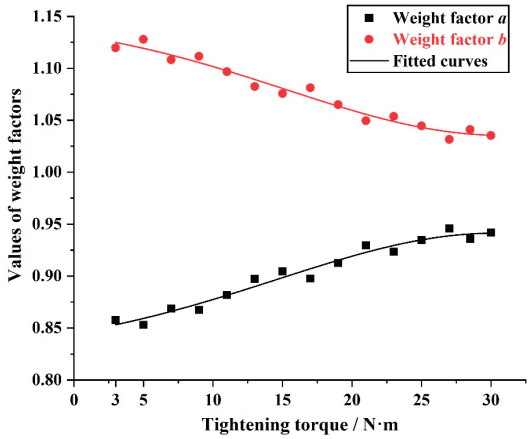



**Figure 12.** Curves of weight factors $a_{T_i}$ and $b_{T_i}$ as a function of tightening torque.

Figure 12 shows that with the increase in the tightening torques, the weight factor $a_{T_i}$ representing the sine vibration response gradually increases, while the weight factor $b_{T_i}$

representing the random vibration response gradually decreases. It is also found that the weight factors $a_{T_i}$ and $b_{T_i}$ are basically symmetrically distributed.

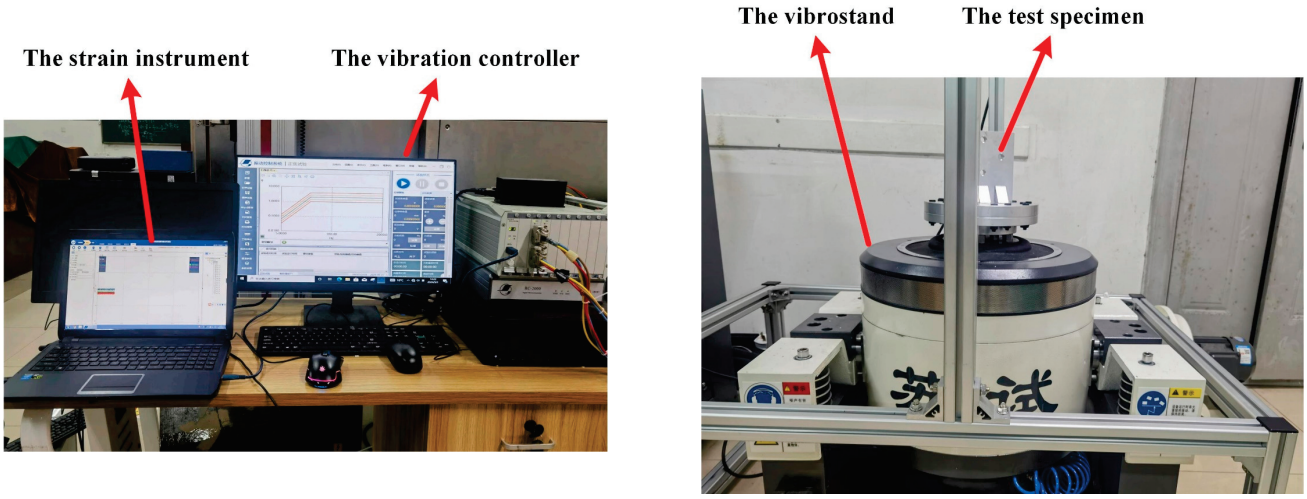
At the same time, it can be found from the numerical relationship between the weight factors $a_{T_i}$ and $b_{T_i}$ that, on the one hand, the factor $b_{T_i}$ is greater than the factor $a_{T_i}$, which means that the random vibration response accounts for a larger proportion in the response under the SOR vibration synthesized excitation, which can also be reflected in Figure 10. On the other hand, the difference between the two weight factors gradually decreases with the increase in the tightening torques, which means that the proportions of the two forms of vibration response in the SOR synthesized vibration response gradually approach each other, because the more tight the bolts are, the less effect the vibration excitation has on the strain responses.

## 5. Test Verification of Bolt Loosening Detection Under Vibration Excitation

A vibration test is carried out for the four-bolt fastened structure subjected to sine vibration excitation and random vibration excitation from the vibrostand to show the agreement between the test and FEA and prove the effectiveness and feasibility of the proposed method.

### *5.1. Test Devices and Conditions*

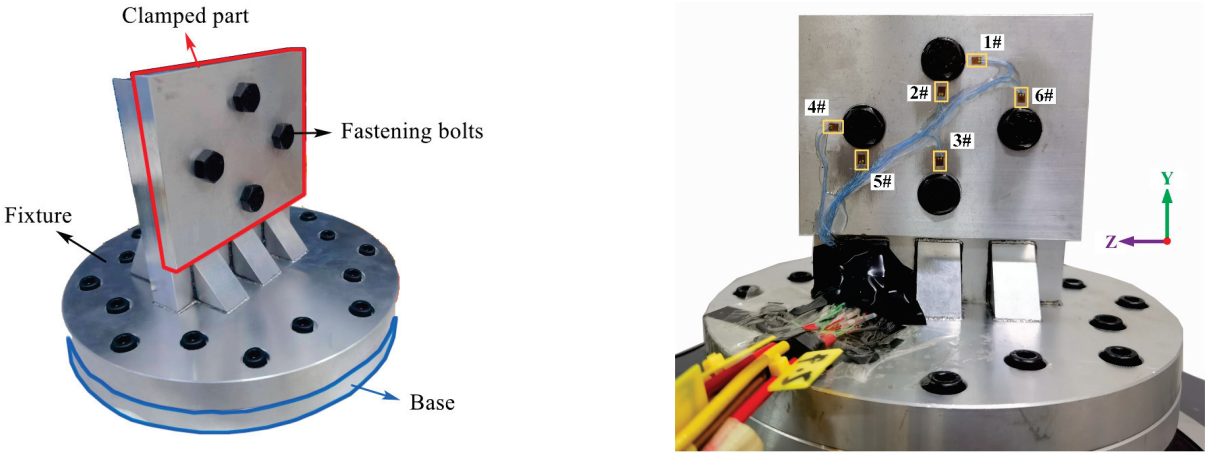
To verify the effectiveness of the loosening mechanism of the four-bolt fastened structure, a strain monitoring test for the structure under vibration is conducted. The test device including the vibration control system, the vibrostand, the test specimen, and the strain instrument is shown in Figure 13.




(**a**) The vibration controller and the strain instrument (**b**) The vibrostand and the test specimen

**Figure 13.** The test devices and test specimen.

The test structure, including four pairs of M10 bolts and nuts connected to 10 mm and 15 mm thick connected pieces, is shown in Figure 14. The materials and dimensions of the test structure are the same as the FEA model in Section 3.1. The base of the structure is fixed to the vibrostand by 12 bolts.




(**a**) The structure components (**b**) The distribution of the strain gauges

**Figure 14.** The test structure and distribution of the strain gauges.

As shown in Figure 14b, the distribution of the six monitored points 1#, 2#, 3#, 4#, 5#, and 6# on the four-bolt clamped part is consistent with that in the previous FEA. The direction of monitored points 1# and 4# is the Z-direction, and the direction of the other monitored points is the Y-direction.

A torque wrench, shown in Figure 15, is used to apply the tightening torques to the bolts, whose accuracy is 4%; 15 groups of tightening torques are applied to the bolts, as shown in Table 2. A manually preset ratchet torque wrench is utilized, with a maximum tightening torque of 50 N·m and an adjustment precision of 1 N·m per increment.



**Figure 15.** The torque wrench.

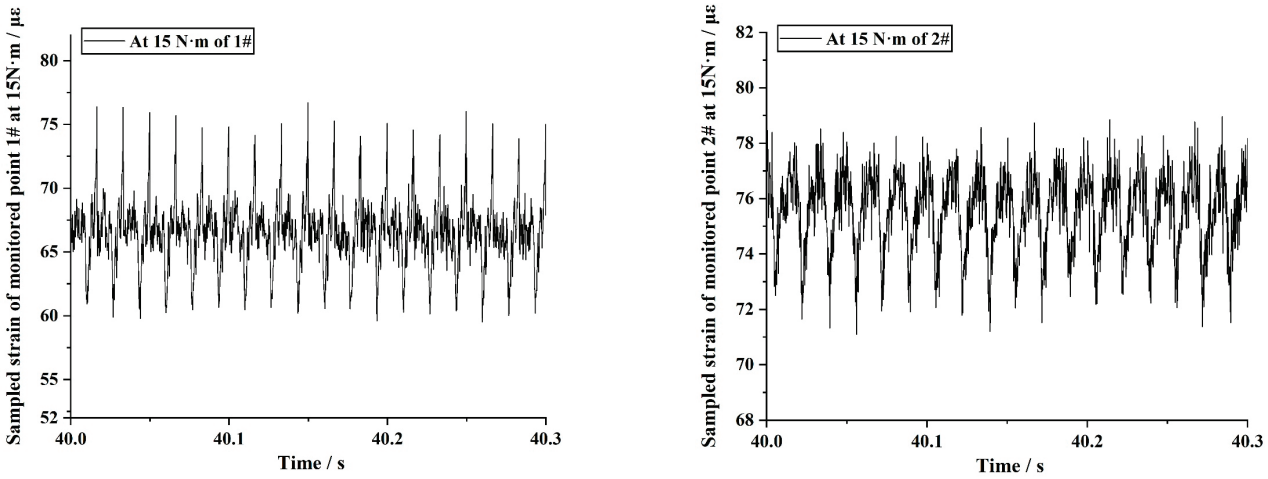
Before each group of vibration tests, the same tightening torque is applied to the four studied bolts with the torque wrench. There are 15 groups of tightening torques, as shown in Table 2 in Section 3.1. Each group of test data is sampled for 180 s. Due to the fact that the maximum frequency of random vibration excitation is 1000 Hz, to ensure that the data are not distorted and satisfy Shannon's sampling theorem [38], the sampling frequency of the strain gauge is set to 5000 Hz. To reduce the impact of random errors on the test, all of the vibration tests are conducted three times under each set of torque for the sine vibration and random vibration.

### *5.2. Result Analysis of the Structural Vibrations*

(1) Result analysis of the structure under the sine vibration test

When conducting the sine vibration test, the excitation conditions were consistent with the FEA of the sine vibration, where the excitation amplitude was 1 mm and the excitation frequency was 60 Hz.

Taking tightening torque 15 N·m as an example, Figure 16 shows the sampled strain data of monitored points 1# and 2# from 40 to 40.3 s. There is a "warm-up period" after the vibrostand is started, during which the vibration intensity gradually increases until it reaches the target excitation parameters and remains stable. Therefore, the strain response of monitored points within the first 30 s of each group of vibration tests is not the ideal stable data. So, Figure 16 shows a section of strain response data after the vibrostand reaches stability. On the other hand, the excitation frequency for the sine vibration test conducted is 60 Hz. If a longer period of strain data is shown in the figure, it is difficult to clearly observe the strain waveform of the monitored points. When the vibrostand reaches stability, the strain data of the monitored points have the same waveform. Therefore, Figure 16 chooses to display the monitored point data within 0.3 s, which includes suitable numbers of cycles and can also show clear waveforms.




(**a**) Strain data of the monitored point 1# (**b**) Strain data of the monitored point 2#

**Figure 16.** Strain sampling data under sine vibration excitation with 15 N·m tightening torque.

However, it should be noted that in the subsequent data processing, this study does not use only strain data within 40 to 40.3 s, but also all valid data after the vibrostand reaches stability.

As shown in Figure 16, the sampled strain data of the monitored points include the pre-strain with the vibration strain part fluctuating on its basis. There is a slight difference in the strain mean values at different monitored points, which is caused by the fact that the two monitored points are located in different parts of the structure.

At the same time, it can be found that the sampled strain data are not a perfectly smooth sine waveform, which is due to the inevitable electromagnetic interference inside the circuit of the strain instrument. Therefore, after data sampling, it is necessary to perform filtering processing on the strain data. Through bandpass filtering of the sampled signals in the frequency band of 59–61 Hz, the strain data could be retained within the frequency band that corresponds to the sine vibration excitation frequency of 60 Hz. Furthermore, the bolt loosening stage is reflected by studying the RMS values of the vibration strains at the monitored points. Therefore, it is necessary to eliminate the pre-strain (i.e., strain mean value) generated by the tightening torque and obtain zero mean strain data. The RMS values of the strains at the monitored points can be obtained through Equation (27).

The test strain RMS values of the six monitored points varying with tightening torques are shown in Figure 17.

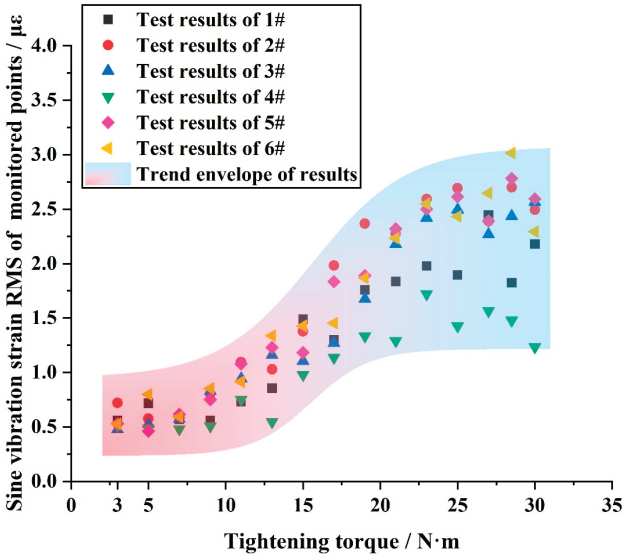
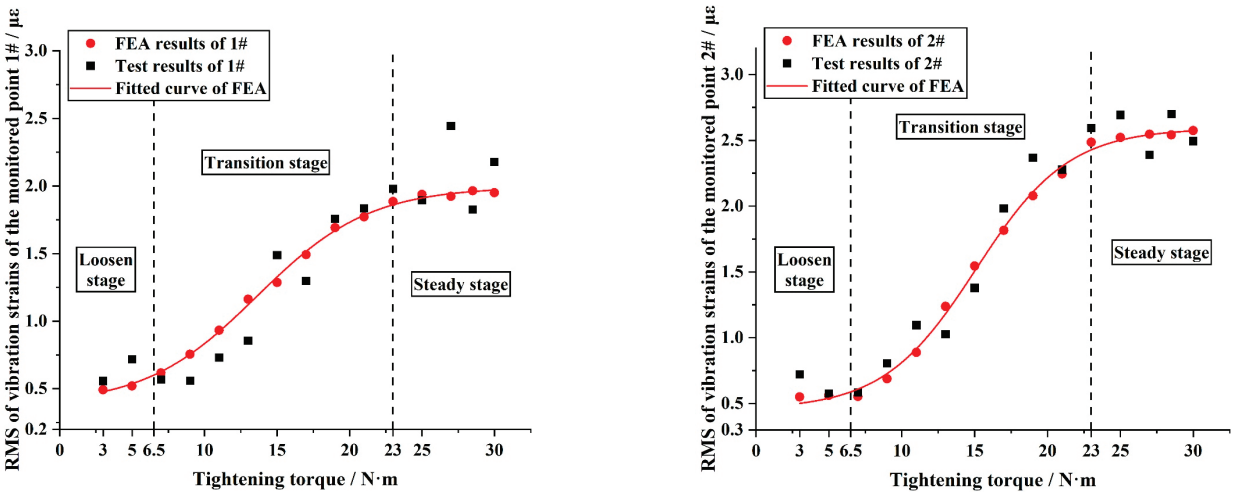



**Figure 17.** RMS results of strain response at the six monitored points under sine vibration test.

The approximate envelope area of the colored background in Figure 17 covers all data points. The strain RMS of monitored points 1# and 4# is smaller compared to other monitored points, because the monitoring direction of these two points is orthogonal to the excitation direction, while the others are horizontal to the excitation direction. Overall, the strain RMS of the six monitored points in the sine vibration test results showed three-stage characteristic bolt loosening.

Taking monitored points 1# and 2# as examples, a comparison between test results and FEA results under the same conditions is shown in Figure 18.




(**a**) Strain RMS comparison of 1# (**b**) Strain RMS comparison of 2#

**Figure 18.** Comparison between the test and FEA results of strain RMS at monitored points under sine vibration.

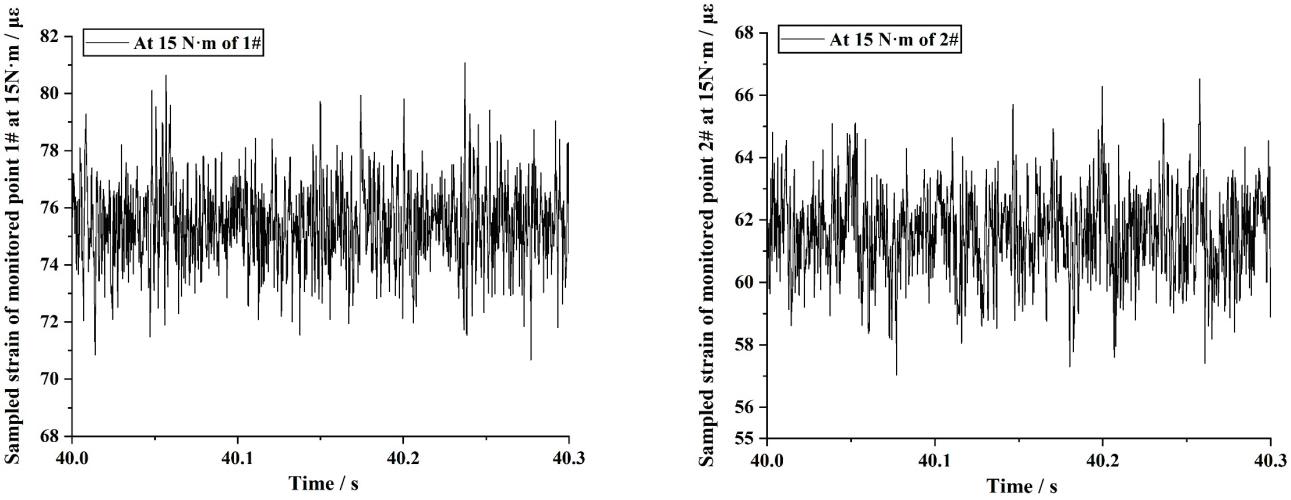
As shown in Figure 18, the black block data points represent the vibration strain RMS results of the monitored points of the sine vibration test, while the red dot data points and the fitted curves represent the FEA results under the same conditions. It can be found that the sine vibration test results are in good agreement with the FEA results, and the vibration test results can also be divided into the Steady Stage, the Transition Stage, and the Loosen Stage, which indicates the effectiveness and feasibility of both the simulation analysis method and the bolt loosening monitoring method proposed.

The average relative error between the experimental and simulation results is 8.33%. The errors between the test results and the simulation results may be caused by many factors, such as the difference between the excitation of the test vibrostand and the simulation, torque wrench error, the simplified surface contact type of the FEA model, the simulated friction coefficient, etc.

(2) Result analysis of the structure under the random vibration test

A bolt loosening test under random vibration of the structure was also conducted. The random vibration test conditions are consistent with the FEA in Section 3. The random vibration excitation is a broadband white-noise acceleration excitation PSD with a frequency range of 15–1000 Hz and a spectral value of 0.2 $g^2$/Hz.

Taking 15 N·m tightening torque as an example, the sampled strain data of strain gauges 1# and 2# under random vibration excitation are shown in Figure 19, with a 0.3 s duration.




(**a**) Strain data of the monitored point 1# (**b**) Strain data of the monitored point 2#

**Figure 19.** Strain sampling data under random vibration excitation with 15 N·m tightening torque.

It can be observed that the characteristics of sampled strain data under random vibration are not obvious. It is not possible to directly distinguish between the vibration strain data (the valid data) and the electrical noise signals (the invalid data). Therefore, it is necessary to filter the sampled strain data from the random vibration test.

The Kalman filter is a recursive linear optimal estimation method [39], suitable for handling time-varying signals and noise in dynamic systems. It can more accurately handle the dynamic changes between noise and signals. It dynamically estimates the system state and noise characteristics by assuming that the signal and noise satisfy certain statistical properties, without the need for explicit noise signal input.

The Kalman filtering method is applied to the sampled strain data, which obtains the strain data after removing the electrical noise signal. Then, the pre-strain is removed to obtain the zero mean random vibration strain responses. According to Equation (27), the RMS results of the vibration strain at the monitored points are obtained.

The test strain RMS values of the six monitored points varying with tightening torques are shown in Figure 20.

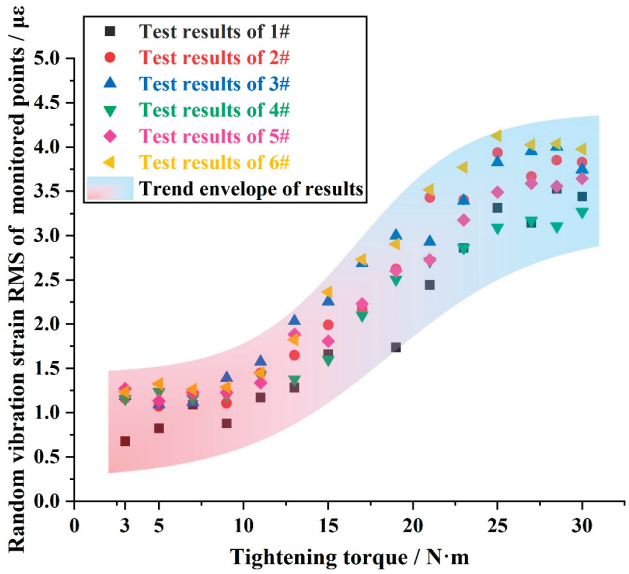
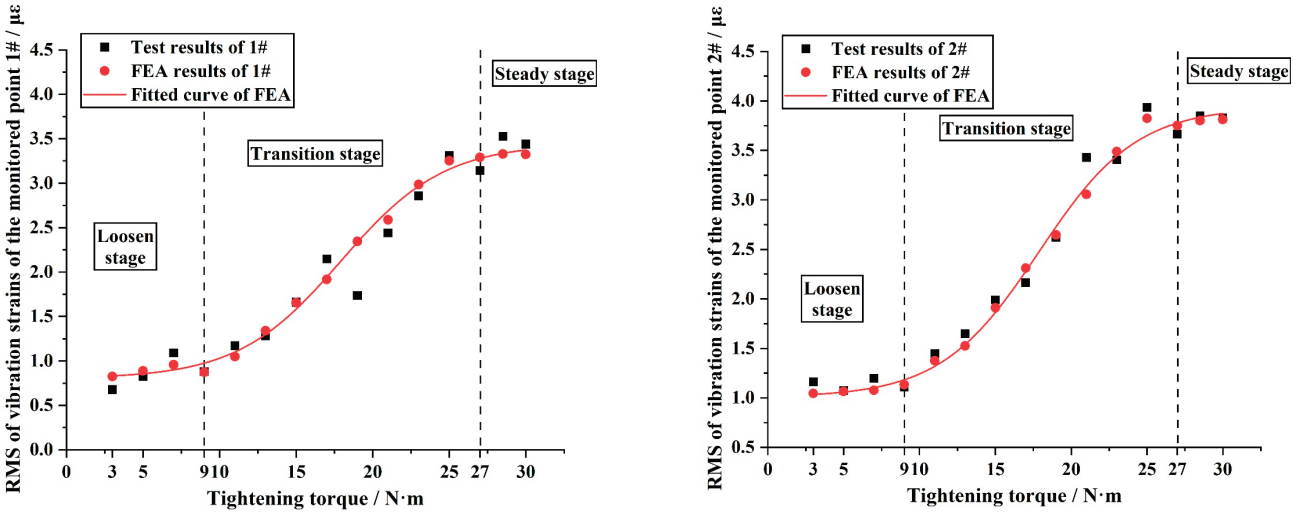



**Figure 20.** RMS results of strain response at the six monitored points under random vibration test.

The approximate envelope area of the colored background in Figure 20 covers all data points. The strain RMS of the six monitored points in the random vibration test results showed three-stage characteristic bolt loosening.

Taking monitored points 1# and 2# as examples, Figure 21 shows the curve of strain RMS values varying with tightening torques in the random vibration test and includes the FEA results under the same conditions.




(**a**) Strain RMS comparison of 1# (**b**) Strain RMS comparison of 2#

**Figure 21.** Comparison between the test and FEA results of strain RMS at monitored points under random vibration.

As shown in Figure 21, the black block data represent the test strain RMS results; the red dot data represent the FEA results. It can be observed that the test results have good consistency with the FEA results and exhibit the same trend. The curve of the RMS results of each strain gauge varying with tightening torques can be divided into three stages as well.

In summary, the vibration test results are in good agreement with the FEA results, which verifies the effectiveness of the three-stage criterion for bolt loosening under vibration excitation and the feasibility of the bolt loosening simulation analysis method proposed

herein. It also provides a reference method and ideas for bolt loosening test research for engineers or scholars in related fields.

## 6. Conclusions

Regarding the issue of bolt loosening under independent excitation of sine and random vibrations, some studies have conducted in-depth research from multiple perspectives. However, there is no related study on bolt loosening under Sine-on-Random vibration excitation. The bolt loosening mechanism under common Sine-on-Random vibration excitation is investigated by using a time–frequency conversion method, and the relationship between the Sine-on-Random synthesized vibration response and two forms of single sine and random vibration responses is revealed through a corrective energy superposition method with weight factors. Finally, the effectiveness of FEA is verified through the vibration tests for a four-bolt fastened structure. The main conclusions are as follows:

(a) The displacement response model of monitored points under SOR synthesized excitation is established. Based on the differential equation of motion, the response of the monitored point to sine base displacement excitation and random base acceleration PSD excitation are solved in the time domain and frequency domain, respectively. Further, by utilizing the $\mathrm{tri}(x)$ function, the sine base displacement excitation is converted as frequency-domain base acceleration excitation triangular PSD. The sine vibration and random vibration are superposed as the SOR synthesized vibration excitation according to the characteristics of the linear system. Finally, a response expression of the MDOF system under the SOR vibration synthesized excitation is deduced.

(b) The three-stage criterion for bolt loosening under SOR excitation is revealed. Through the strain RMS of the monitored points, an implicit monitoring method is used to analyze the strain response under sine, random, and synthesized excitation. It is found that there is the Steady Stage, Transition Stage, and Loosen Stage for bolt loosening.

(c) A transformed energy superposition model based on the weight factors is proposed to reflect the energy proportion of sine and random vibration responses in the SOR synthesized vibration response. In each group of tightening torque, $C_6^2 = 15$ sets of weight factors $a_{T_i}$ and $b_{T_i}$ can be obtained from $C_6^2 = 15$ pairs of monitored points responses under three forms of excitation (sine vibration, random vibration, and SOR synthesized vibration), where the weight factors $a_{T_i}$ and $b_{T_i}$ represent sine and random vibration response weights, respectively. By using the Least Square Method, the relative error between the theoretical calculated SOR response and the FEA SOR response is taken as the objective function to obtain the optimal weight factors under each group of tightening torque. Further, the influence of tightening torque on the weight factors of vibration response is studied. It can be found that there is a certain difference between the weight factors of the two forms of vibration responses when the tightening torques are small, while the weights of the two forms of vibration responses tend to be close with the increase in tightening torques. It can be found that when the bolts tend to loosen, random vibration excitation has a more significant impact on bolt loosening than sine vibration excitation, while as the bolt connections become more secure, the impacts of sine vibration and random vibration on bolt loosening are almost as much.

(d) Both sine and random vibration verification tests are conducted for a four-bolt fastened structure using a vibrostand and a specially designed clamp. The test results are highly consistent with the FEA results and reveal the approximate envelope area of the three-stage criterion for bolt loosening.

**Author Contributions:** Conceptualization, Y.Q. and J.L.; methodology, J.D. and Y.Q.; software, J.D.; validation, J.D., Y.Q., and J.L.; formal analysis, J.D.; investigation, J.D., Y.Q., and J.L.; resources, Y.Q. and J.L.; data curation, J.D.; writing—original draft preparation, J.D.; writing—review and editing, Y.Q. and J.L.; visualization, J.D.; supervision, Y.Q.; project administration, Y.Q. and J.L.; funding acquisition, Y.Q. and J.L. All authors have read and agreed to the published version of the manuscript.

**Funding:** This work is supported by the China Aerospace Science and Technology Corporation (Grant No. JSZL2017203C012), the Natural Science Basic Research Program of Shaanxi Province (Program No. 2023-JC-YB-328), and the Fundamental Research Funds for the Central Universities (Program No. ZYTS23014).

**Data Availability Statement:** Data are contained within the article.

**Conflicts of Interest:** The authors declare no conflicts of interest.

## References

1. Jiang, Y.; Zhang, M.; Lee, C.-H. A study of early stage self-loosening of bolted joints. *J. Mech. Des.* **2003**, *125*, 518–526. [CrossRef]
2. Gong, H.; Liu, J.; Feng, H. Review on anti-loosening methods for threaded fasteners. *Chin. J. Aeronaut.* **2022**, *35*, 47–61. [CrossRef]
3. Huang, J.; Liu, J.; Gong, H.; Deng, X. A comprehensive review of loosening detection methods for threaded fasteners. *Mech. Syst. Signal Process.* **2022**, *168*, 108652. [CrossRef]
4. Du, J.; Qiu, Y.; Li, J. Study on the effect mechanism of vibration excitation parameters on bolt loosening based on an implicit monitoring method. *Proc. Inst. Mech. Eng. C J. Mech. Eng. Sci.* **2024**, 09544062241296930. [CrossRef]
5. Junker, G.H. New criteria for self-loosening of fasteners under vibration. *SAE Trans.* **1969**, *78*, 314–335.
6. Du, C.; Liu, J.; Gong, H.; Huang, J.; Zhang, W. Percussion-based loosening detection method for multi-bolt structure using convolutional neural network DenseNet-CBAM. *Struct. Health Monit.* **2024**, *23*, 2183–2199. [CrossRef]
7. Lin, Q.; Zhao, Y.; Sun, Q.; Chen, K. Reliability evaluation method of anti-loosening performance of bolted joints. *Mech. Syst. Signal Process.* **2022**, *162*, 108067. [CrossRef]
8. He, Z.; Shi, Z.; Qin, D.; Wen, J.; Shao, J.; Liu, X.; Xie, X. Study on Comprehensive Performance of Four-Point Contact Ball Slewing Bearings Based on a Bearing Support Bolt-Integrated Model. *Machines* **2024**, *12*, 814. [CrossRef]
9. Sakai, T. Investigations of bolt loosening mechanisms. *Bull. JSME* **1978**, *21*, 1385–1390. [CrossRef]
10. Zadoks, R.I.; Yu, X. An investigation of the self-loosening behavior of bolts under transverse vibration. *J. Sound Vib.* **1997**, *208*, 189–209. [CrossRef]
11. Pai, N.G.; Hess, D.P. Three-dimensional finite element analysis of threaded fastener loosening due to dynamic shear load. *Eng. Fail. Anal.* **2002**, *9*, 383–402. [CrossRef]
12. Otter, D.C.; Maljaars, J. Preload loss of stainless steel bolts in aluminium plated slip resistant connections. *Thin Wall. Struct.* **2020**, *157*, 106984. [CrossRef]
13. Li, Z.; Chen, Y.; Sun, W.; Jiang, P.; Pan, J.; Guan, Z. Study on self-loosening mechanism of bolted joint under rotational vibration. *Tribol. Int.* **2021**, *161*, 107074. [CrossRef]
14. Gong, H.; Ding, X.; Liu, J.; Feng, H. Review of research on loosening of threaded fasteners. *Friction* **2022**, *10*, 335–359. [CrossRef]
15. Barredo, E.; Zhao, Z.; Mazón-Valadez, C.; Larios, J.G.M.; Maldonado, I.A. A grounded inerter-based oscillating TMD for suppressing harmonic and random vibrations. *Int. J. Mech. Sci.* **2023**, *254*, 108438. [CrossRef]
16. Richards, D.; Neale, M. Effects of phase relationship in helicopter vibrations. *J. IEST* **1994**, *37*, 26–31. [CrossRef]
17. Kihm, F.; Halfpenny, A.; Ferguson, N.S. Fatigue life from sine-on-random excitations. *Procedia Eng.* **2015**, *101*, 235–242. [CrossRef]
18. Cornelis, B.; Manzato, S.; Peeters, B.; der Vorst, R.V.; Hiatt, J. A mission synthesis procedure for sine-on-random excitations in a helicopter application. In *Shock & Vibration, Aircraft/Aerospace, Energy Harvesting, Acoustics & Optics, Proceedings of the 35th IMAC, A Conference and Exposition on Structural Dynamics 2017*; Springer: Cham, Switzerland, 2017; pp. 197–209.
19. Brown, A.; McGhee, D. Statistical comparison and improvement of methods for combining random and harmonic loads. In Proceedings of the 45th AIAA/ASME/ASCE/AHS/ASC Structures, Structural Dynamics & Materials Conference, Palm Springs, CA, USA, 19–22 April 2004; p. 1535.
20. Yang, X.; Nassar, S.A. Effect of thread profile angle and geometry clearance on the loosening performance of a preloaded bolt-nut system under harmonic transverse excitation. In Proceedings of the ASME 2011 Pressure Vessels and Piping Conference, Baltimore, MD, USA, 17–21 July 2011; pp. 393–404.
21. Zheng, Z.; Huang, X.; Miao, X.; Qiu, K.; Jiang, Z.; Ding, P. Probabilistic analysis of bolted joint anti-loosening under cyclic transverse load. *Mech. Based Des. Struct. Mach.* **2024**, *52*, 7985–8011. [CrossRef]

22. Liu, G.; Zhang, L.; Han, J.; Li, M.; Su, H.; Qiao, T. Study on the influence of galloping alternating load on bolt loosening of tower. In Proceedings of the Ninth International Conference on Energy Materials and Electrical Engineering (ICEMEE 2023), Guilin, China, 25–27 August 2023; Volume 12979, pp. 895–901.
23. Dong, G.; Chen, J.; Zhao, F. Monitoring of the looseness in cargo bolts under random excitation based on vibration transmissibility. *Shock Vib.* **2021**, *2021*, 8841940. [CrossRef]
24. Geradin, M.; Rixen, D.J. *Mechanical Vibrations: Theory and Application to Structural Dynamics*, 3rd ed.; Wiley: West Sussex, UK, 2014.
25. Schmitz, T.L.; Smith, K.S. *Machining Dynamics*, 2nd ed.; Springer: Cham, Switzerland, 2019.
26. Inman, D.J. *Engineering Vibration*, 4th ed.; Pearson Education: Harlow, UK, 2014.
27. Melchers, R.E.; Beck, A.T. *Structural Reliability Analysis and Prediction*; John Wiley & Sons: Hoboken, NJ, USA, 2018.
28. Silva, C.W.d. *Vibration and Shock Handbook*, 1st ed.; CRC Press: Boca Raton, FL, USA, 2005.
29. Eftekhari, S.A. A note on mathematical treatment of the Dirac-delta function in the differential quadrature bending and forced vibration analysis of beams and rectangular plates subjected to concentrated loads. *Appl. Math. Model.* **2015**, *39*, 6223–6242. [CrossRef]
30. Wu, Z.; Lei, L.; Dong, J.; Zhang, X. Triangular-shaped pulse generation based on self-convolution of a rectangular-shaped pulse. *Opt. Lett.* **2014**, *39*, 2258–2261. [CrossRef] [PubMed]
31. Lurie, A.I.; Belyaev, A. *Theory of Elasticity*; Springer Science & Business Media: Berlin/Heidelberg, Germany, 2010.
32. Humar, J. *Dynamics of Structures*; CRC Press: Boca Raton, NJ, USA, 2012.
33. Croccolo, D.; De Agostinis, M.; Fini, S.; Mele, M.; Olmi, G.; Scapecchi, C.; Tariq, M.H. Failure of threaded connections: A literature review. *Machines* **2023**, *11*, 212. [CrossRef]
34. Childs, P. *Mechanical Design Engineering Handbook*, 2nd ed.; Butterworth-Heinemann: Oxford, UK, 2019.
35. Guzas, E.; Behan, K.; Davis, J. 3D Finite Element Modeling of Single Bolt Connections under Static and Dynamic Tension Loading. *Shock Vib.* **2015**, *2015*, 205018. [CrossRef]
36. Du, J.; Qiu, Y.; Wang, Z.; Li, J.; Wang, H.; Wang, Z.; Zhang, J. A three-stage criterion to reveal the bolt self-loosening mechanism under random vibration by strain detection. *Eng. Fail. Anal.* **2022**, *133*, 105954. [CrossRef]
37. Wang, D.; Geng, Q.; Li, Y. Effect of static load on vibro-acoustic behaviour of clamped plates with geometric imperfections. *J. Sound Vib.* **2018**, *432*, 155–172. [CrossRef]
38. Yang, Y.; Dorn, C.; Mancini, T.; Talken, Z.; Nagarajaiah, S.; Kenyon, G.; Farrar, C.; Mascareñas, D. Blind identification of full-field vibration modes of output-only structures from uniformly-sampled, possibly temporally-aliased (sub-Nyquist), video measurements. *J. Sound Vib.* **2017**, *390*, 232–256. [CrossRef]
39. Grewal, M.S.; Andrews, A.P. *Kalman Filtering: Theory and Practice Using MATLAB*, 3rd ed.; John Wiley & Sons: Hoboken, NJ, USA, 2008.


**Disclaimer/Publisher's Note:** The statements, opinions and data contained in all publications are solely those of the individual author(s) and contributor(s) and not of MDPI and/or the editor(s). MDPI and/or the editor(s) disclaim responsibility for any injury to people or property resulting from any ideas, methods, instructions or products referred to in the content.

machines

MDPI

*Article*

# Study on Dynamic Behaviors of Hypoid Gears Under Variable Tidal Current Energy Harvesting Conditions

**Dequan Huang [1], Yan Li [2], Xingyuan Zheng [3,4] and Gang Li [5,*]**

[1] School of Equipment Manufacture, Zhenjiang College, Zhenjiang 212028, China; max-huang@zjc.edu.cn
[2] School of Mechanical Engineering, University of Shanghai for Science and Technology, Shanghai 200093, China; 221170121@st.usst.edu.cn
[3] College of Mechanical and Vehicle Engineering, Chongqing University, Chongqing 400044, China; zhengxingyuan@cqu.edu.cn
[4] Department of Mechanical Engineering, University of Utah, Salt Lake City, UT 84112, USA
[5] Michael W. Hall School of Mechanical Engineering, Mississippi State University, Starkville, MS 39762, USA
* Correspondence: gli@me.msstate.edu

**Abstract:** This study investigates dynamic behaviors of hypoid gear rotor systems under variable tidal current energy harvesting conditions through numerical simulations and experimental validation. The study examines dynamic responses of a hypoid gear rotor system induced by cyclical tidal current variations, which generate fluctuating loads and bidirectional rotational speeds in tidal energy conversion systems. Two hypoid gear pairs, modified through precise manufacturing parameters, are evaluated to optimize tooth contact patterns for bidirectional tidal loading conditions. A coupled torsional vibration model is developed, incorporating variable transmission error and mesh stiffness. Experimental validation of dynamic performances of hypoid gear pairs was conducted on a bevel gear testing rig, which can measure both torsional and translational vibrations across diverse tidal speed profiles. The experimental results demonstrate that second-order primary resonances exhibit heightened vibration intensity during flow-reversal phases. This phenomenon has significant implications for system power efficiency and acoustic emissions. The findings extend the current understanding of hypoid gear optimization for tidal energy-harvesting applications.

**Keywords:** hypoid gears; dynamic behaviors; transmission error; mesh stiffness; tidal current energy

## 1. Introduction

Hypoid gears serve as critical power transmission components in tidal current energy converters (TCECs), where they facilitate the conversion of bidirectional tidal flows into rotational mechanical energy [1]. In tidal energy applications, these gears encounter distinct challenges due to the cyclical nature of tidal current loading and the periodic flow reversals characteristic of tidal environments [2]. A cross-axis hypoid gear pair in a TCEC enables optimal spatial configuration of the power take-off system between a horizontal-axis turbine and a vertically mounted generator [3]. While conventional performance metrics such as transmission error (TE), tooth root strength, and surface wear remain crucial considerations, dynamic behaviors of hypoid gears under variable tidal current conditions introduce additional complexities due to bidirectional loading patterns. The time-varying TE and mesh stiffness (MS) function as primary internal excitation sources, whose characteristics are significantly influenced by the predictable yet varying loads and reversing operational speeds inherent in TCECs [4]. Variations in TE and MS parameters,

amplified by tidal current fluctuations and flow reversals, can induce complex dynamic behaviors in the rotor system's speed and load responses across different tidal cycles. These dynamic behaviors are further complicated by variations in tooth contact conditions, which emerge from micro-scale deviations in gear tooth form geometry and become particularly critical during tidal flow transitions and reversal periods. Within tidal energy applications, multiple gear tooth contact patterns may manifest across different hypoid gear pairs of identical design specifications. These are attributable to manufacturing tolerances and machining parameter variations, which become especially significant under bidirectional loading. Preventing edge-tooth contact during flow reversals is particularly important in TCECs. This necessitates comprehensive inspection protocols for hypoid gears prior to deployment in tidal environments, as such contact patterns could induce severe vibrations in the rotor system under cyclical tidal loading conditions. Hypoid gear pairs enable efficient mechanical power transmission between intersecting shafts in TCECs, converting the high-torque, low-speed rotations of tidal turbines into optimized generator inputs through precision-engineered tooth geometry and mesh characteristics. Dynamic behaviors of hypoid gear pairs of TCECs under bidirectional tidal loading conditions significantly influence their power conversion efficiency and operational reliability. It is essential for rigorous analysis of gear dynamics and transmission error of hypoid gear pairs under TCEC operational conditions to advance the performance of tidal energy harvesting technologies.

Recent studies on TCECs have predominantly focused on their hydrodynamic performances and structural reliability, with limited attention to drivetrain dynamics. Zhang et al. [5] studied unsteady effects on hydrodynamic performances of a horizontal-axis tidal turbine system, including bevel gears and a gearbox. Power fluctuations and weak characteristics of a TCEC were analyzed under wave-current interactions in [6], but neither addressed those influences on its mechanical transmission system. Chen and Wu [7] presented a comprehensive review of hybrid wave-tidal technologies, highlighting the need for improved power take-off systems, e.g., gearboxes, but without detailed expectations of gear dynamics. Avalos et al. [8] considered gearbox integration in wave energy converters. Glennon et al. [9] focused on composite blade testing methodologies for operational life prediction, emphasizing the critical need for mechanical component reliability in marine environments. These studies demonstrated a research gap regarding gear system dynamics under bidirectional tidal loading conditions, particularly concerning the interrelationship between tooth contact patterns, TE, and MS of drivetrains in TCECs under variable flow speed conditions.

Researchers assumed that the time-varying TE and MS are the prominent, exciting sources for the gearing systems. Many researchers specialized their studies on TE and MS to evaluate dynamic performances of their interest through static performances of the gearing system. Hypoid gears have much more complex tooth surface geometry, typically quasi-conjugated, than that of involute gears. Extensive research work in recent decades found it difficult to carry out the loaded tooth contact analysis (LTCA) of hypoid gears by a purely analytical approach to obtain exact solutions for load distribution, tooth contact deformation, tooth bending and shear, TE, and MS by certain formulas based on intermediate results. In all cases, the finite element (FE)-based semi-analytical LTCA approach is significantly developed, and it is powerful enough to give the desired results in the past decade, benefiting from the computational efficiency. Wang et al. [10] proposed a methodology to avoid trial and error in obtaining a satisfied design of hypoid gears, and the FE-based semi-analytic LTCA is applied in their work to calculate the bending stress of the tooth root. Liu et al. [11] investigated the impact of work-holding equipment errors on contact characteristics of face-hobbed hypoid gears and a mathematical model considering both radial and angular eccentric errors. Liang et al. [12] investigated the effects on the

tooth contact characteristics for the face-hobbed hypoid gears under different blade sections, and the contact pattern is compared between the linear, circular, and polynomial blades based on the FE tooth contact model. Cooley [13] proposed two determining approaches for spur gears mesh stiffness, average slope, and local slope using the FE method and a local slope difference formula for dynamic studies. In addition to the FE model, other researchers searched for numerical solutions to loaded transmission error (LTE) of hypoid gears. Huang et al. [14] used the conjugate approach to frictional loss and surface wear studies of hypoid gears. Simon [15] presented a novel hypoid gear grinding method that combines generating and Waguri motions, which can model the tooth surface roughness by considering spherical grinding wheel grains. This method achieved mapping the 3D topography to both pinion and gear tooth surfaces through their respective motions and investigating how grain size and motion relationships influence the resultant surface roughness characteristics. Liu et al. [11] used a quasistatic LTCA method to investigate contact characteristics and gear geometry with radial and angular eccentric errors.

Concerning dynamic studies of hypoid gears, researchers developed many dynamic models and explored the influence of various factors on dynamic performances. Shi et al. [16] presented a dynamic model for hypoid gears, considering the influences of dynamic MS due to time-variable contact loads. Liu et al. [17] proposed a semi-analytical LTCA method for spiral bevel gears that integrated ease-off surface computation with high-precision virtual generating tooth surfaces. Wang et al. [18] proposed a general nonlinear time-varying torsional model of hypoid gears to investigate dynamic behaviors, and typical behaviors reported in spur gears were observed, jump discontinuities, subharmonic and chaotic states from the computational results. Karagiannis et al. [19] proposed an alternative formulation for dynamic transmission error (DTE) of hypoid gears. Mohammadpour et al. [20] studied the coupling relationship between dynamics and tribology in vehicle differential hypoid gears. Athanasopoulos et al. [21] presented a sliding and rolling speed calculation method along the full path of contact on a meshing tooth surface of hypoid gears. Song et al. [22] proposed a hybrid dynamic model to investigate hypoid gears coupled with off-sized bearing rollers. Huangfu et al. [23] investigated the effects of tooth modifications on dynamic characteristics of thin-rimmed gears under surface wear conditions to optimize load distribution and reduce vibration throughout the wear process. Zheng et al. [24] presented an analytical approach to modeling the MS of high-speed spur gears, considering the centrifugal effect and its influence on gear deformation and load sharing. Li and Zhu [25] proposed a loaded contact pattern optimization method for hypoid gears, considering high-order TE functions and face-milling machine-tool settings. The integration of these diverse research efforts provides a comprehensive understanding of the current state of the field. An et al. [26] focused on improving load capacity and minimizing the effects of misalignment through development of a point contact model featuring normal cross-sectional circular arc tooth profiles. Shen et al. [27] investigated the fault mechanism and dynamic characteristics of planetary gears with gear wear and analyzed the impacts of wear on MS, TE, and gear backlash of gear tooth profiles. A dynamic model incorporating wear-related factors was developed to analyze the influences of wear on planetary gear vibration responses. Yi et al. [28] proposed a nonlinear dynamic model for spur gear systems that accounts for time-varying behaviors of pressure angle and gear backlash, providing a more realistic representation of gear dynamics and potentially influencing system stability and tooth impact states. Wei et al. [29] studied dynamic characteristics of spur gear systems with uncertain parameters, such as MS and support stiffness.

This study investigates the dynamic behavior variations between two hypoid gear configurations under distinct tooth contact conditions specifically designed for tidal current energy harvesting applications. The logical diagram of the simulation calculation that

yields the load and speed responses is shown in Figure 1. Experimental tests for hypoid gear dynamics are conducted in the meantime and compared to the simulation.

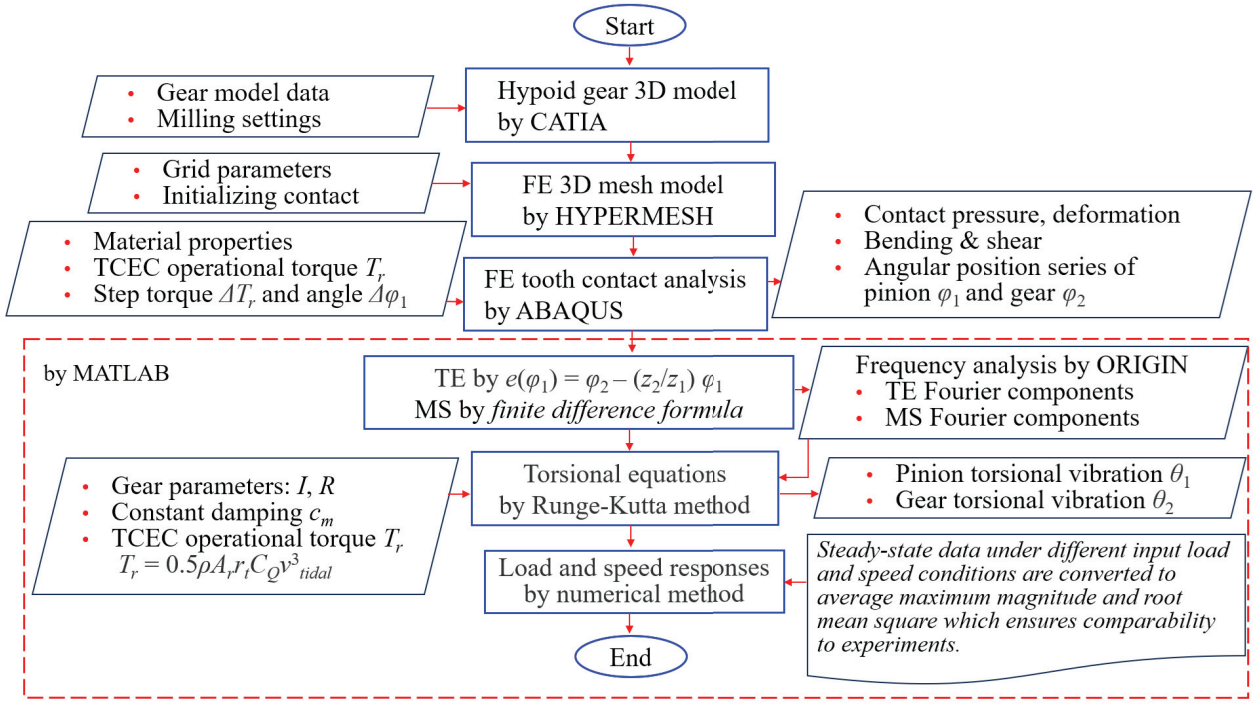



**Figure 1.** Logic diagram of dynamic behavior analysis for hypoid gears in TCECs

The baseline hypoid gear design, adapted from a commercial vehicle transmission, is modified for bidirectional tidal flows, featuring two gear pairs produced under different milling parameters. One pair is optimized for tidal applications, while the other provides marginal edge contact to assess system sensitivity. A comprehensive nonlinear dynamic torsional model is developed that incorporates the time-varying TE and MS parameters derived from the FE-based LTCA model, specifically accounting for bidirectional loading conditions of tidal current variations. Dynamic responses under variable tidal loading conditions are numerically solved using the Runge–Kutta method, with particular attention to behaviors during flow-reversal phases. Experimental validation is performed with a bevel gear pair testing rig that uses high-precision rotary encoders to measure torsional vibrations of both the pinion and gear, along with triaxial accelerometers to capture the full dynamic response under simulated tidal flow conditions. Numerical and experimental results are systematically analyzed to evaluate the influence of tooth contact patterns on system performance under variable tidal current conditions, leading to significant insights for optimizing hypoid gear designs in tidal energy harvesting applications. This study advances the field through three key innovations: (1) development of a coupled torsional-translational dynamic model that incorporates time-varying TE and MS under bidirectional variable tidal loading conditions; (2) experimental validation using purpose-built testing apparatus capable of measuring both torsional and translational vibrations across variable tidal speed profiles; and (3) quantitative characterization of the relationship between tooth contact patterns and system dynamics during flow-reversal phases, particularly regarding second-order primary resonances and their implications for power conversion efficiency.

## 2. Power Conversion Modeling of Drivetrains in Tidal Current Energy Converters

The enhancement of TCEC power generation capabilities necessitates optimized design of power conversion systems that enable energy capture at reduced cut-in velocities, facilitating the conversion of fluctuating low-speed turbine rotations to stable high-rated outputs. Performance validation of the drivetrain system under varying tidal velocities was accomplished through experimental studies using a TCEC configuration incorporating both hydro-turbine and drivetrain components in controlled flume conditions. Figure 2 illustrates the experimental TCEC configuration, including a hydro-turbine, a gearbox, and a hypoid gear pair. The extractable hydrokinetic power from tidal currents via a hydro-turbine can be expressed as

$$P_r = \frac{1}{2}\rho A_r C_p v_{tidal}^3, \tag{1}$$

where $A_r$ is the hydro-turbine swept area, $\rho$ is the seawater density, $C_p$ is the power coefficient, and $v_{tidal}$ is the tidal current velocity. Equation (1) quantifies the extractable energy for a specified hydro-turbine's swept area operating at a defined power coefficient $C_p$ within a tidal stream. The hydro-turbine's power coefficient $C_p$ primarily correlates with its tip-speed ratio (TSR), which is

$$C_p(\lambda, \beta) = C_Q(\lambda, \beta)\lambda, \tag{2}$$

where $C_Q(\lambda, \beta)$ is the design-dependent torque coefficient and $\lambda$ is the TSR, which is

$$\lambda = \frac{\omega_t r_t}{v_{tidal}}, \tag{3}$$

with $r_t$ is the rotor radius and $\omega_t$ is hydro-turbine's angular velocity. For this study, the hydro-turbine's torque coefficient is [30]

$$C_Q(\lambda, \beta) = 0.5\left(\frac{116}{\gamma} - 0.4\beta - 5\right)e^{-\frac{21}{\lambda}} + 0.0068\lambda, \tag{4}$$

where

$$\frac{1}{\gamma} = \frac{1}{\lambda + 0.08\beta} - \frac{0.035}{\beta^3 + 1}, \tag{5}$$

with $\beta$ is the pitch angle, i.e., 15° in this study. Using the TSR in Equation (3), hydro-turbine's angular velocity is

$$\omega_r = \frac{\lambda v_{tidal}}{r_t}. \tag{6}$$

The TCEC operational torque, crucial for drivetrain load distribution analysis, can be expressed as

$$T_r = \frac{1}{2}\rho A_r r_t C_Q v_{tidal}^3. \tag{7}$$

This operational torque serves as the primary input parameter for the drivetrain system. The drivetrain facilitates energy transfer from the generated power $P_r$ to the generator assembly. Maintaining optimal performance across variable tidal velocities requires consistent TSR regulation at its designed optimal value.

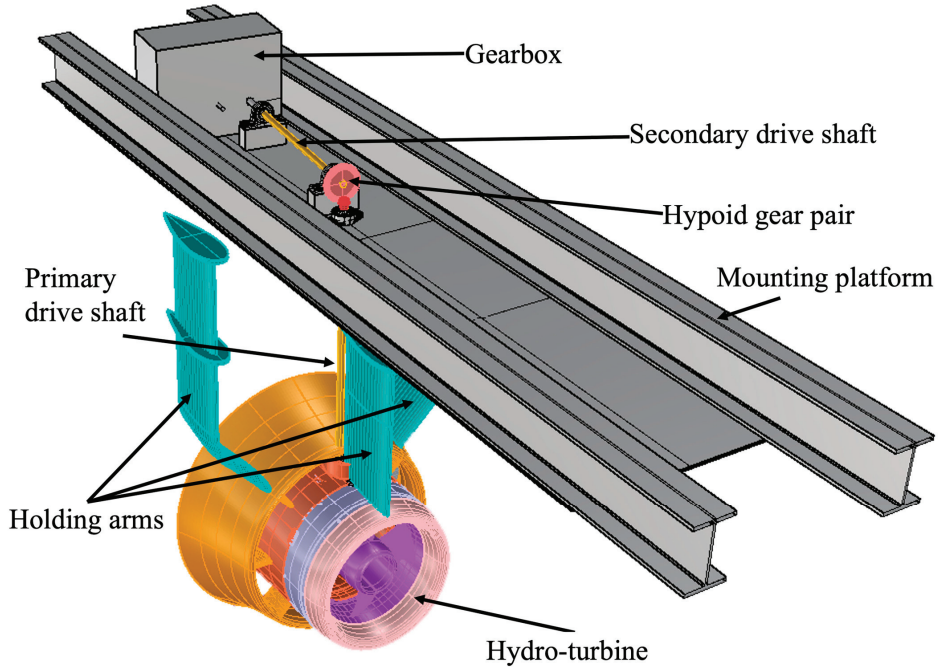



**Figure 2.** Layout structure of the TCEC, including the hydro-turbine, a hypoid gear pair, and the gearbox [30].

The dynamic torsional model of the hypoid gear under variable tidal current energy-harvesting conditions is shown in Figure 3, and its torsional equations include Equations (8) and (9), which serves to solve the torsional vibrations of the pinion and gear, respectively. This study confines attention to the dynamic behavior under two different tooth contact conditions subject to different milling settings [31]. Thus, TE and MS of two pairs of gears obtained from the respective milling settings are used as parametric input conditions to the torsional equations. The dynamic model excludes the translational vibrations of bearing systems of the rotor system, focusing instead on extensive experimental tests using data from a 3-axis accelerometer.

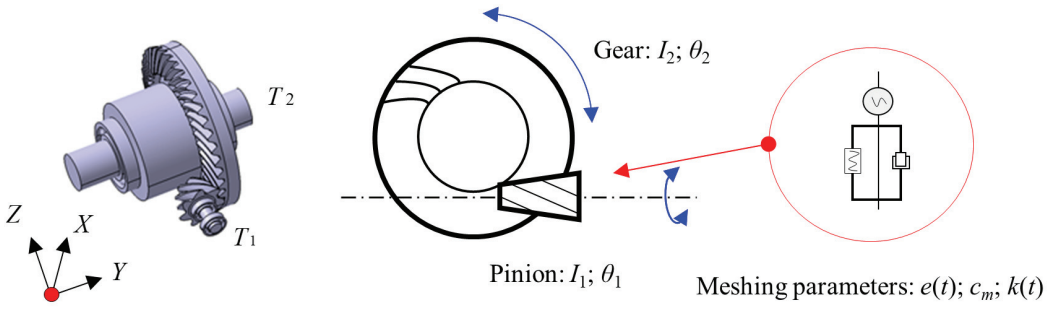



**Figure 3.** A dynamic model of a hypoid gear system to reflect its angular vibrations.

The torsional equations to solve the torsional vibrations of the pinion and gear are written as

$$I_1\frac{d^2\theta_1}{dt^2} + R_1c_m\left(R_1\frac{d\theta_1}{dt} - R_2\frac{d\theta_2}{dt} - R_1\frac{de(t)}{dt}\right) + R_1k_m(t) = T_r(t), \tag{8}$$

$$I_2\frac{d^2\theta_2}{dt^2} + R_2c_m\left(R_1\frac{d\theta_1}{dt} - R_2\frac{d\theta_2}{dt} - R_2\frac{de(t)}{dt}\right) + R_2k_m(t) = i_hT_r(t), \tag{9}$$

where $\theta_1$ and $\theta_2$ are rotation angles of the pinion and the gear, respectively, $R_1$ and $R_2$ are radii of contact points on the pinion and gear, respectively, $I_1$ and $I_2$ are the moment of

inertia of the pinion and the gear, respectively, $i_h$ is the gear ratio, $c_m$, $k_m(t)$, and $e(t)$ are meshing damping, MS, and TE of the hypoid gear rotor system, respectively. Meshing damping $c_m$, which reflects the effects of viscous and friction, is assumed to be constant in this study. The time-varying MS is an unknown function that can be expressed as $k_m(t) = f(R_1\theta_1 - R_2\theta_2 - e(t))$, which means its value is affected by the combination of angular deviations from the theoretic conjugate position $R_1\theta_1 - R_2\theta_2$ of the contact point on the pinion and the gear tooth surfaces, and the static TE $e(t)$ over meshing cycles.

## 3. FE Tooth Contact Model Under Variable Tidal Current Conditions

This investigation analyzes the dynamic behavior characteristics of hypoid gear rotor systems under variable tidal current conditions, focusing on the comparative assessment of different tooth contact patterns generated through specialized milling parameters. TE and MS variations for two distinct gear pair configurations are computed using a high-fidelity FE tooth contact model, which incorporates bidirectional loading profiles characteristic of tidal current fluctuations. The precision of the three-dimensional hypoid gear model, particularly critical for the precise computation of TE and MS under reversing tidal flows, is established through an advanced geometric construction methodology that accounts for time-varying contact conditions. This methodology enables a detailed analysis of the behavior of tooth contact during critical tidal flow transition periods, where the loading direction changes significantly impact gear mesh characteristics.

### *3.1. Tooth Contact Model*

This section presents the modeling method of 3D hypoid gears and the FE analysis of the 3D model for the approach in detail to TE and MS. CATIA is well known for the ability of model work to construct complex surfaces, so software is applied to construct the 3D model of hypoid gears. In the simulation of this study, special machines Gleason 116 and 609 are chosen to generate the tooth surface of the specified pair of hypoid gears in CATIA. The face-milled process is applied to machine the pinion and the gear. Basic Visual programming codes drive the milling process through the Macro interface of CATIA, which simulates Gleason 116 generating the pinion and Gleason 609 forming the gear. Figure 4 shows the grinding settings of the Gleason 116 machine tool in Figure 4b and 609 in Figure 4c, respectively, and Figure 4a the grinding process of the pinion and the gear that illustrates the relative positions of the 3D cutter head and the workpiece. The pinion generating settings include ten: four workpiece settings, axial position $X_{p1}$, horizontal position $X_1$, vertical position $E_{01}$ and root angle $\delta_{M1}$; four cutter-head settings, $S$, $q$, $i$, and $j$; and the rolling angle of the workpiece $\Psi$, and the cradle angle $q = \Psi/m_{1c}$, where $m_{1c}$ is the rolling ratio. Gear formation settings include six: four workpiece positioning settings, i.e., $X_2$, $X_{p2}$, $E_{02}$, and $\delta_{M2}$; and two cutter-head positioning settings, i.e., $H$ and $V$.

Figure 4a shows that Boolean operations remove the cutter-head solid from the intersection with the workpiece solid at each predetermined workpiece angular position according to the rolling ratio in CATIA's Part Design module. The tooth groove, thereby, is composed of a number of strip surfaces that should be stitched together. In CATIA's Generative Shape Design module, strip surfaces are extracted and joined together, and uniformly distanced partition planes that are vertical to the pinion shaft axis are created. The intersection curves where the generated tooth groove intersects with the partition planes are extracted, and they are replaced by spline curves in CATIA's multi-sectional surface module. An integrated tooth surface is thereby constructed from these spline curve sections in CATIA's Generative Shape Design module. A cover is added to the integrated tooth surface and is sealed together, and in the Part Design module, the sealed tooth surface again becomes a solid tooth through the close-surface operation. Following some other

solid editing work, the 3D pair of solid hypoid gears are finally worked out as shown in Figure 5a.

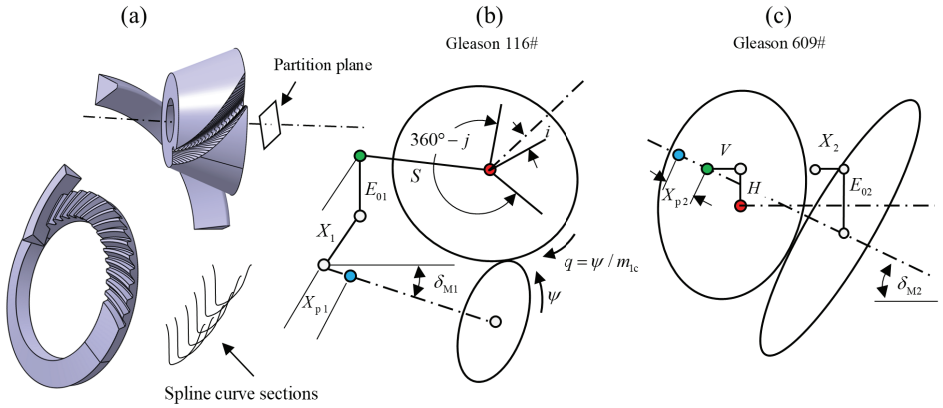



**Figure 4.** Machining simulations of hypoid gears: (**a**) 3D face-milled process showing relative positions of cutter-head and workpiece of the pinion and the gear, (**b**) generating settings of machine tool for the pinion, and (**c**) forming settings of machine tool for the gear.

Figure 5b shows a piece of the FE model split from the complete hypoid gears in the HYPERMESH version 9.0 software. This study only requires a six-tooth pinion and gear for analysis, which significantly saves computing time and provides sufficient accuracy. The incompatible mode of element C3D8I is configured in HYPERMESH to perform grid division of the FE model, which is good at a high resolution of contact stress. Details of the six-tooth FE model of hypoid gears include that the pair has a total of 308,988 elements with 350,998 nodes, mesh density is 25 × 62 nodes for the master tooth surface (drive side of the pinion), and 32 × 72 nodes for slave tooth surface (driven side of the gear). The element density of the surface of the slave tooth is predefined higher than the surface of the master tooth at 149% to avoid any penetration into each other. However, the same density would give more accurate results. Physical parameters include material characteristics: Young's modulus and Poisson's ratio predetermined as $E = 2.1 \times 108$ N/mm$^2$, and $v = 0.3$ in this study. TE and MS simulations were managed by ABAQUS. To promote convergence, a small approach angle of 0.001 is set as an initial angle, which is an effective measure to ensure that the pinion and gear teeth are in slight contact.

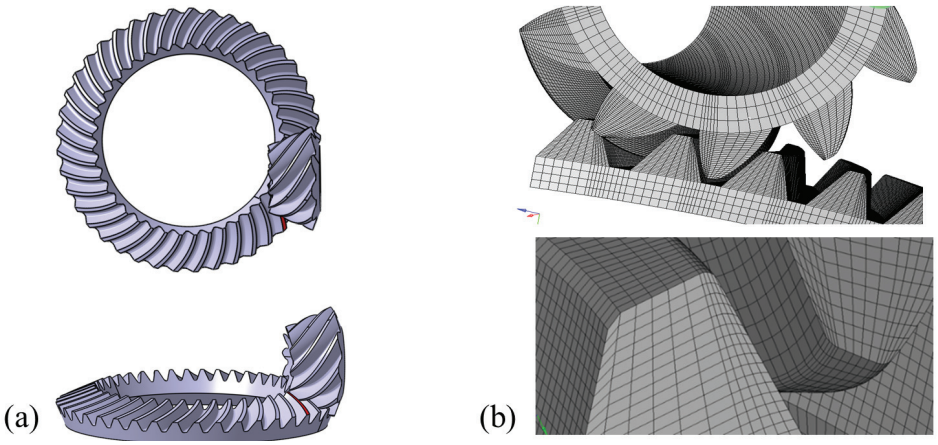



**Figure 5.** 3D modeling of the hypoid gear pair: (**a**) 3D model of the hypoid gear pair in CATIA, and (**b**) its FE tooth contact model using HYPERMESH.

### *3.2. TE and MS of the Hypoid Gear Pair*

TE of gears, including the unloaded UTE and the loaded LTE, is commonly defined as the angular difference of the actual angular position of the driven gear from

its mathematical conjugate angular position. Therefore, TE is conceptually expressed as $e(\varphi_1) = \varphi_2 - (z_2/z_1)\varphi_1$, where $z_1$, $z_2$, $\varphi_1$, $\varphi_2$ denote the tooth number and the actual angular positions of the pinion and gear, respectively. TE of hypoid gears is caused by multiple factors, such as geometric tooth-form deviation and assembly error under unloaded conditions and loaded conditions. TE also involves surface compression, bending and shear, and torsion of the pinion and the gear and its shaft systems. For hypoid gears, the geometric tooth-form deviation relates to its generating method, and the theoretic conjugate point only exists at the reference point on the center of the pinion and the gear tooth surfaces, which is the biggest difference from the involute gears. Missing the mathematic reference tooth surface makes it extremely difficult to obtain an accurate TE of hypoid gears by either the analytic or the numeric method; in contrast, involute gears have a reference datum involute surface. The FE method that relies on computing power is increasingly becoming an effective tool to produce a relatively accurate TE with the development of computing technology. However, TE by the FE method is still dependent on the accuracy of the tooth contact model to simulate the generating process of actual milling machines. The detailed construction process of 3D and FE models of hypoid gears, which serve to compute TE and MS of this section, are presented in Section 3.1.

In addition to TE, the FE method is also wildly involved in the MS calculation of involute gears. Cooley [13] proposed two determining approaches of the average slope and the local slope to calculate the MS of the spur gears using the FE method. In Cooley's two approaches, the FE tooth contact model of spur gears is utilized for obtaining tooth contact compression, tooth bending and shear for a span of specified torque loads. Cooley made careful comparisons between the two approaches and came up with suggestions that the average slope more resembles a static analysis and that the local slope can work well on dynamics. The average slope mathematically is an arithmetic formula, and the local slope is a finite-difference formula. The local slope approach is applied to calculate the time-varying MS for hypoid gears supported by the data from the FE tooth contact model.

Stiffness refers to the ability of a material or structure to resist elastic deformation subject to force. The composite elastic deformation of a geared system should include many components, such as Hertz tooth contact compression, tooth bending and shear, shaft system torsions, etc. Thereby, the composite static mesh stiffness of a geared rotor system at an instant time can be expressed as

$$\frac{1}{k_m} = \frac{1}{k_c} + \frac{1}{k_b} + \frac{1}{k_s} + \frac{1}{k_t}, \tag{10}$$

where $k_m$ is the composite mesh stiffness, $k_c$, $k_b$, and $k_s$ are the separated stiffness caused by the tooth contact compression, tooth bending, and shear, respectively, $K_t$ is the local stiffness of the mesh caused by shaft torsions as it transmits the torque. Typically, a hyoid gear pair has multiple teeth in contact simultaneously. Chang [32] thought that the mesh stiffness of multi-tooth contact is something like a set of parallel contact springs and suggested that the global composite stiffness of gears is expressed by summing up all discrete contact points to cover all major contact lines, giving

$$K_m = \sum_{i=1}^{N} k_m^{(i)}, \tag{11}$$

where $N$ is the amount total of discrete segments, and $k_m$ is the mesh stiffness of the $m$th tooth pair in contact. The finite-difference stiffness formula of the local slope approach for the $m$th single tooth pair in contact is represented as

$$k_m = \frac{F_n(q_n + \Delta q_n) - F_n(q_n - \Delta q_n)}{2\Delta q_n}, \tag{12}$$

where $F_n$ is tooth contact force, $q_n$ is composite mesh deflection of single tooth contact corresponds to the total approaching distance of a tooth contact segment caused by tooth contact compression, tooth bending, and shear, and $\Delta q_n$ is a specified small increment of mesh deflection, i.e., finite-difference term. Equation (12) can also be rewritten as

$$k_m^{-1} = \frac{q_n(F_n + \Delta F_n) - q_n(F_n - \Delta F_n)}{2\Delta F_n}. \tag{13}$$

It is much more convenient to give a desired incremental size of $\Delta T$, and correspondingly it yields $\Delta F_n$. It should be noted that excellent convergence is reported by setting the increment size at 1% of the nominal torque load [13]. This approach may cover all interesting torque ranges and avoid possible multiple stiffness curves due to the nonlinearity of contact deformation.

## 4. Experimental Testing and Data Process

### *4.1. Experimental Setup*

A bevel gear testing rig in Figure 6 integrates high-precision rotary encoders for measuring torsional vibrations and a triaxial accelerometer for capturing translational responses under simulated turbine speed profiles ranging from 50 to 1400 rpm and torque loads up to 450 Nm. Measurement facilities in the testing rig maintain sampling frequencies at four times the mesh frequency to ensure adequate resolution of second-order primary resonances during flow transitions, enabling comprehensive characterization of dynamic behaviors across both rotational and spatial domains. Measurement facilities of the testing rig include (1) a magnetic brake, (2) a hypoid gear pair, (3) rotary encoders, (4) torque sensors, (5) a motor, and (6) a PCB Piezotronics 3-axis accelerometer. LTE is produced using measured data on the angular positions on the pinion and gear sides according to its definition formula in Section 3.2. LTE is obtained when the rotor system runs under quasistatic conditions for a certain number of angles at a very low speed. Translational vibrations in the $x$, $y$, and $z$-axis directions are measured by the 3-axis accelerometer on the upper surface of the hypoid gearbox.

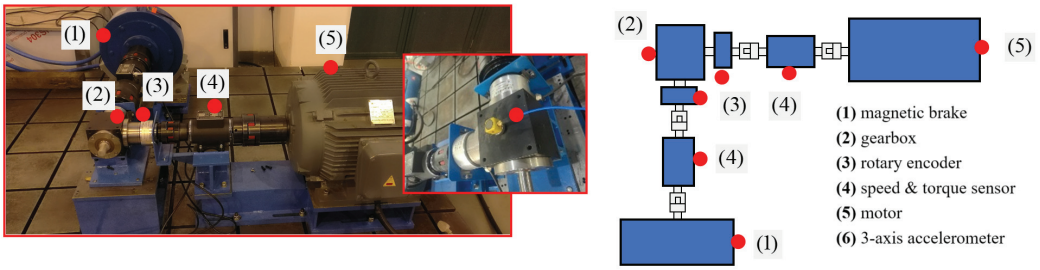



**Figure 6.** Bevel gear pair testing rig to measure torsional and translational vibrations by rotary encoders and a 3-axis accelerometer, respectively.

The measurable finest angle of the optical rotary encoders on the input side is $2\pi/2^{17}$ rad, and the output side is $2\pi/2^{21}$ rad. Such resolution ratios on both sides can ensure the desired precision for the research objective of this study. The details of the acceleration meter are as follows: A PCB Piezotronics 3-axis accelerometer to measure translational vibrations in the x, y, and z directions, type 356B18, and a National Instruments NI-9234 data acquisition board that connects to the sensor to collect vibration data in three directions. Key performances are: sensitivity $\pm$ 10% of 102 mV/(m/s$^2$); measurable

frequency range 0.5–3000 Hz with ±5% sensitivity and bandwidth 110,000 Hz. Data of $x$, $y$, and $z$ vibrations are processed by ORIGIN to analyze frequency components and by MATLAB R2024b for comprehensive analysis and reprocessing. The mesh frequency is calculated by $f_m = n$ rpm $\times N_1$ / 60 s, where $n$ rpm is the speed of input on the pinion side, and the sampling frequency must meet $f_s > 2 - 5f_m$ according to the sampling theory.

The investigation requires a large number of tests so that the steady-state data are collected by continuously increasing the load and speed within the respective ranges in Section 5.3. The particular concern is that the investigation avoids directly comparing torsional vibrations of the rotor system of the test rig with simulations. Torsional motion equations in Equations (8) and (9) cannot analyze real-world conditions that neglect certain factors such as manufacturing errors, friction, material nonlinearity, and temperature variations. The direct comparison between experiment and simulation is likely to become endless discussions about the accuracy of tests and how factors are considered in simulation. The response of loads and speeds in the frequency domain is a desirable method to eliminate the high-frequency components of exciting sources caused by most manufacturing errors.

### *4.2. Data Process*

The data collected from experimental tests are not suitable for direct comparison with simulations, which means that the data have to be processed in a certain form before being compared to the simulations. It is extremely difficult to capture the transient state to compare simulations and experiments under dynamic conditions of the rotor system of hypoid gears at a certain instant time of interest in practice. However, it is more practical to compare the load response and the speed response in the steady state, which reflects typical dynamic behaviors of hypoid gears but can also be easily compared between simulations and experiments. The comparison is conducted mainly in the frequency domain and in the form of average maximum magnitude (AMM) and root mean square (RMS) in a steady state after a specified period of time. The time-domain data of vibrations picked from simulations and experiments are processed into the form of AMM and RMS before they are compared to each other. The load and speed responses are used to evaluate the dynamic behaviors of hypoid gear rotor systems under different tooth contact conditions. Detailed comparisons are performed next in Section 5 for hypoid gears of a domestic popular vehicle. The design data and generating settings are listed in Table 1.

**Table 1.** Basic design specifications of the hypoid gear pair 41 × 11 on the driving side.

| **Design Parameters** | **Symbols** | **Pinion** | **Gear** |
|---|---|---|---|
| Number of teeth | $z_1, z_2$ | 11 | 41 |
| Spiral direction | | Left | Right |
| Pitch diameter | $d_2$ | N/A | 295.00 |
| Shaft offset (mm) | $E$ | | 25.40 |
| Face width (mm) | $b_1, b_2$ | 44.57 | 41.00 |
| Outer cone diameter (mm) | $d_{e1}, d_{e2}$ | 156.32 | 273.57 |
| Mean spiral angle (deg) | $\beta_{01}, \beta_{02}$ | 45.08 | 48.08 |
| Pitch cone angle (deg) | $\delta_1, \delta_2$ | 11.82 | 77.92 |
| Face cone angle (deg) | $\delta_{a1}, \delta_{a2}$ | 16.18 | 78.57 |
| Root cone angle (deg) | $\delta_{f1}, \delta_{f2}$ | 11.17 | 73.45 |
| Face cone point | $O_{a1}, O_{a2}$ | −0.68 | 0.64 |
| Pitch cone point | $O_{H1}, O_{H2}$ | −7.24 | 0.39 |
| Root cone point | $O_{f1}, O_{f2}$ | −1.62 | 0.08 |

For torsional vibrations, the angular positions in the unit of μrad of the pinion and the gear are measured by two rotary encoders on both shafts. Respective torsional vibrations of the pinion and the gear are combined as DTE when the rotor system of

the hypoid gears runs at high speed, and the dynamic effect must be considered. Let $\Delta\varphi(\tau)|_k = [\Delta\varphi_1, \Delta\varphi_2, \Delta\varphi_3, \Delta\varphi_4, \ldots, \Delta\varphi_n]$ denote the $n$ number of dynamic LTEs collected from its theoretic formula $\Delta\varphi = \varphi_o - \gamma\varphi_I$ in steady state for a specified period, where $\tau$ is the specified period of the measurement operation, $\Delta\phi_n$ is the error value for a predefined time interval by dividing $\tau$, and $k$ is one of the tests or measurement operations, i.e., different $k$ corresponds to any of the load and speed differences of the numbers of test operations. For each test operation $k$ under different load and speed conditions, $q_a$ denotes the AAM operation obtained from $q_a = maxium(\Delta\varphi_n)|_k$, and $q_{rms}$ denotes the RMS operation obtained from $q_{rms} = [\sum(\Delta\varphi_n|_k)/n]^{0.5}$.

For translational vibrations, let $X|_k = [x_1, x_2, x_3, \ldots, x_n]$, $Y|_k = [y_1, y_2, y_3, \ldots, y_n]$, and $Z|_k = [z_1, z_2, z_3, \ldots, z_n]$ denote the collected vibration data in $x$, $y$ and $z$-axis directions, respectively, where $k$ is the $k$th test operation under different load and speed conditions $[T, \omega_p]|_k$. The collected time-domain vibration data $[x_t, y_t, z_t]|_k$ in an instant of time t of experiments is transformed into frequency domain vibration data $[x_f, y_f, z_f]|_k$ in the Origin software by performing the fast Fourier transform (FFT). Let $n$, $\omega_p$, $f_r$, and $f_m$ denote the order number, the pinion speed, the revolution, and the mesh frequencies of the rotor system, respectively. Thus, the revolution frequency is $f_r = 60\omega_p$, the mesh frequency is $f_m = z_1 f_r$, and the frequency of the primary resonances at the $n$th order ($n$ = 1, 2, 3, …) is $f_n = nz_1 f_r = 60nz_1\omega_p$. The RMS operation that expresses the overall intensity of the vibration is $d_{rms} = [\sum(x_{fn}^2 + y_{fn}^2 + z_{fn}^2)/3)]^{0.5}|_k$ obtained from vibrational magnitudes of the frequency domain of $[x_{fn}, y_{fn}, z_{fn}]|_k$ in $x$, $y$ and $z$ directions at frequencies $f_n$ of different orders $n$.

## 5. Results and Discussion

This study uses two hypoid gear pairs for experimental testing, with the gear and pinion produced by Gleason 116 and 609 machine tools, respectively. Design specifications for hypoid gear pairs are listed in Table 1.

The pinion speed is set to different test conditions for testing variation effects in tidal current and flow reversals. For this study, the hypoid gear model 41 × 11 is subject to two different machine-tool settings to produce two pairs of gears under two different tooth contact conditions according to the machine-tool settings in Tables 2 and 3, respectively. One hypoid gear pair has a normal tooth contact condition, and the other has a slight edge contact condition to generate a different LTE and MS. Two hypoid gear pairs are obtained in two different tooth contact conditions by modifying the cutter radius and the other machine-tool settings, the details of which are omitted here.

**Table 2.** Machine-tool settings of gear pair No. 1 in the normal tooth contact condition.

| Settings of Machine Tool | Symbols | Pinion | Gear |
|---|---|---|---|
| Sliding base | $X_1, X_2$ | 28.78 | 87.94 |
| Machine center to back | $X_{p1}, X_{p2}$ | 2.63 | −3.63 |
| Flank offset | $E_{01}, E_{02}$ | 24.38 | 76.59 |
| Machine root angle (deg) | $\delta_{M1}, \delta_{M2}$ | 357.78 | 20.40 |
| Cradle radius | $S; V, H$ | 117.12 | 25.38, 99.50 |
| Cutter-head title angle (deg) | $i$ | 18.59 | 0 |
| Cutter-head swivel angle (deg) | $j$ | −43.53 | 0 |
| Cutter-head diameter | $2r_{c1}, 2r_{c2}$ | 229.36 | 112.95 |
| Cutter-head blade angle (deg) | $\alpha_{01}, \alpha_{02}$ | 14 | 20 |
| Roll ratio | $m_{1c}, m_{1c}$ | 3.67 | 0 |
| Milling method | | generating | forming |

**Table 3.** Machine-tool settings of gear pair No. 2 in the tooth edge contact condition.

| Settings of Machine Tool | Symbols | Pinion | Gear |
|---|---|---|---|
| Sliding base | $X_1, X_2$ | 23.57 | 87.94 |
| Machine center to back | $X_{p1}, X_{p2}$ | −0.86 | −3.63 |
| Flank offset | $E_{01}, E_{02}$ | 22.39 | 76.59 |
| Machine root angle (deg) | $\delta_{M1}, \delta_{M2}$ | 358.35 | 20.40 |
| Cradle radius | $S; V, H$ | 115.68 | 25.38, 99.50 |
| Cutter-head title angle (deg) | $i$ | 17.95 | 0 |
| Cutter-head swivel angle (deg) | $j$ | −40.67 | 0 |
| Cutter-head diameter | $2r_{c1}, 2r_{c2}$ | 245.45 | 112.95 |
| Cutter-head blade angle (deg) | $\alpha_{01}, \alpha_{02}$ | 14 | 20 |
| Roll ratio | $m_{1c}, m_{1c}$ | 3.63 | 0 |
| Milling method | | generating | forming |

### *5.1. LTE and Its Harmonic Components*

LTEs are obtained from the simulation and the experiments under a torque load of 50 to 450 Nm, respectively, under quasistatic conditions. The speed is fixed at a very low 50 rpm, at which the dynamic effect can be neglected. In an ABAQUS-based FE analysis, the angular positions of the pinion and the gear can be read, respectively, at each step of mutual rotations from pre-setting in the software. In experimental tests, the angular positions of the pinon and the gear can be collected from rotary encoders. LTEs are therefore calculated according to its definition formula in Section 3.2. The two pairs of solid gears of the hypoid gears are produced by Gleason 116 and 609 milling machines, and two 3D tooth contact models for FE analysis are constructed in CATIA according to the generating methods in Section 3, based on the model data in Table 1 and two different settings of the machine tool in Tables 2 and 3, respectively. Then, two 3D models are transformed into FE tooth contact models by completing the mesh division. The tooth contact analysis for two different FE models is performed in ABAQUS, and experimental tests for two solid gear pairs are conducted on the test rig of Figure 6. Figures 7–9 show their respective contact patterns, LTE, and their harmonic components of the primary resonances in the frequency domain under two different contact conditions of the teeth of interest when the pinion shaft has exerted a torque of 350 Nm. Under normal tooth contact conditions, LTE curves from both the FE model and experiments have a regular sine shape, whereas, under edge tooth contact conditions, they do not. The fast Fourier transformation (FFT) is performed for the LTE data in the time domain of the simulation and experiment, and Figure 9 shows their respective harmonic components of the primary resonances from frequencies $1f_m$ to $8f_m$, where $f_m$ is the mesh frequency. The simulation result is similar to the experiment, which suggests that hypoid gears under edge tooth contact conditions have more harmonic components than under normal tooth contact conditions. Experimental results suggest that in the frequency domain, LTE has a lot of high-frequency harmonic components under both edge and normal tooth contact conditions. In addition, tooth contact patterns demonstrate high sensitivity to milling parameter variations under bidirectional tidal loading conditions, resulting in distinct TE and MS characteristics during flow reversals.

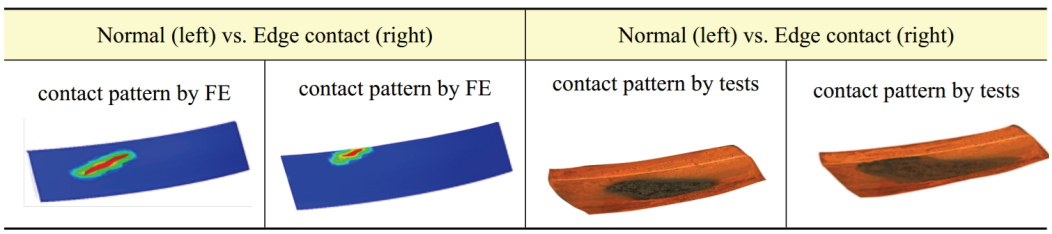



**Figure 7.** Contact pattern comparisons between two gear pairs under different tooth contact conditions.

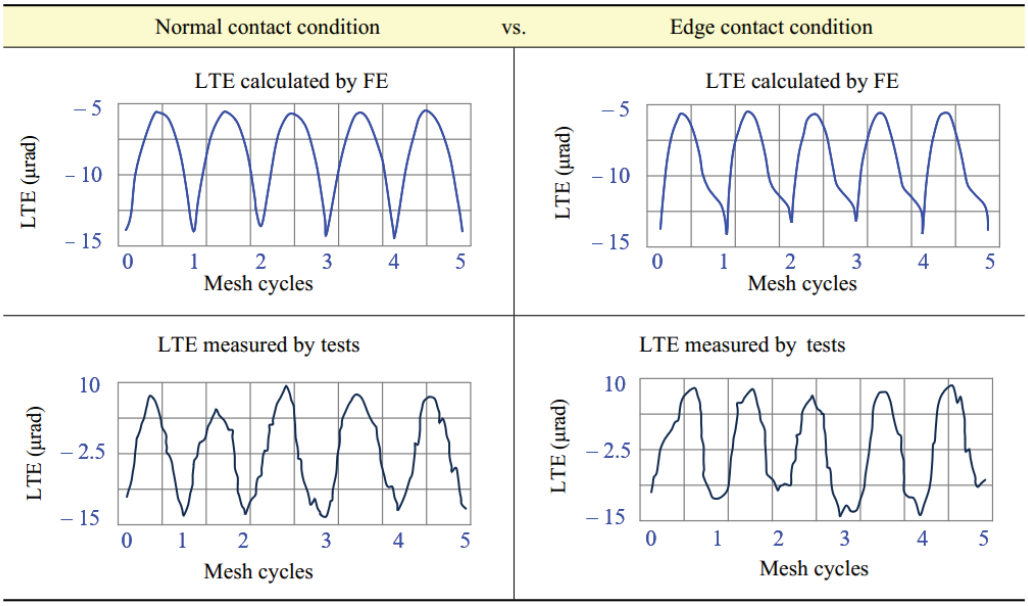



**Figure 8.** LTE yielded from the FE method and rolling tests under input torque 350 Nm in two different contact conditions.

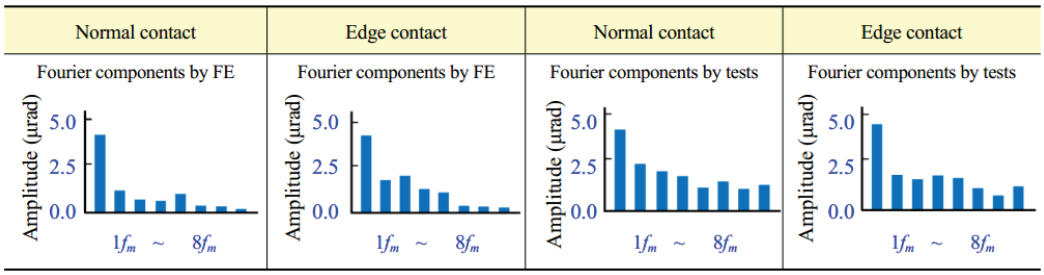



**Figure 9.** Fourier components of LTE under different contact conditions.

LTE, as one of the primary exciting sources, contributes to the unique dynamic characteristics of hypoid gears, and loaded TE is often used to predict possible dynamic behaviors of the rotor system. However, the exact dynamic behaviors of the hypoid gear rotor system have to be evaluated by torsional vibrations; in most cases, it is reflected by the dynamic TE in the form.

Primary resonances of the first five orders of the Fourier series of LTE $e(t)$ thus can be written as

$$e(t) = e_0 + \sum_{i=1}^{5} e_i \cos(i\omega_h t + \phi_i) \tag{14}$$

where $i$ and $\omega_h$ are harmonic order and mesh frequency, respectively, $e_0$ and $e_i$ are the fundamental and the $i$th order harmonic component of LTE, respectively, and $\phi_i$ is phase position.

### *5.2. MS and Its Harmonic Components*

MS is extremely difficult to measure directly from rotary encoders in experimental tests, according to the accessible public literature. In this study, MS under two different tooth contact conditions is obtained from the Cooley local slope approach using the finite-difference formula presented in Section 3.2, based on the angular position data of the FE tooth contact model.

Figure 10 shows the MS of two pairs of gears of the chosen commercial hypoid gears model, which are obtained from the finite-difference formula of Cooley's local slope approach under two different normal and edge tooth contact conditions in the simulations

using data from the FE tooth contact analysis. The MS of the gears is usually shaped like the letter "n", i.e., there are steep rises and falls on two sides, suggesting that the contact shift occurs on different teeth. The Fourier series of MS yielded from FFT replaces time-domain MS as input nonlinear exciting source to perform dynamic analysis using the dynamic motion model presented in Section 2, which provides a direct correlation between the exciting and response frequencies for this study. The time-varying MS $k_m(t)$ for primary five orders of Fourier series shown in Figure 11 thus can be written as

$$k(t) = k_0 + \sum_{j=1}^{5} k_j \cos(j\omega_h t + \varphi_j), \tag{15}$$

where $j$ and $\omega_h$ are harmonic orders and mesh frequency, respectively, $k_0$ and $k_j$ are the fundamental and the $j$th order harmonic components, respectively, and $\varphi_j$ is phase position of the $j$th harmonic component. In parametric theory, the time-varying MS of the gear pair may enhance the second-order harmonic vibration of its rotor system.

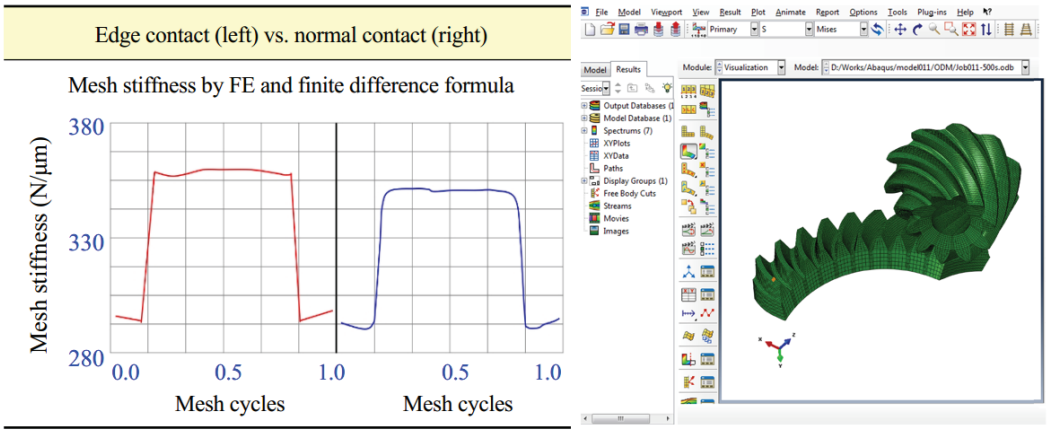



**Figure 10.** MS simulation results under two different tooth contact conditions and its Abaqus analysis image.

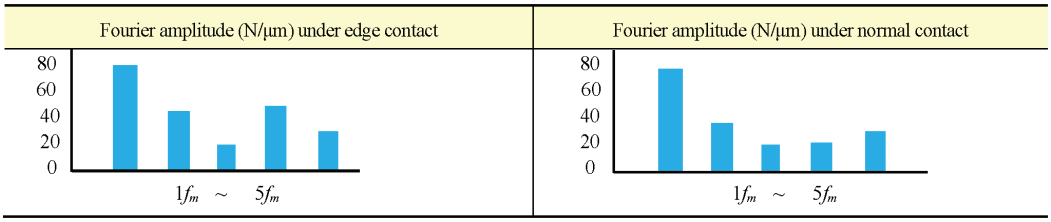



**Figure 11.** Harmonic components of MS under two different tooth contact conditions.

### *5.3. Torsional Vibrations*

The torsional vibrations of the pinion $\theta_1$ and the gear $\theta_2$ are usually illustrated by DTE $(\theta_1, \theta_2)$ which graphically assesses the dynamic characteristics of the geared systems. Figure 12 compares two DTEs in steady state under two different tooth contact conditions of normal and edge, and the results of two tooth contact conditions are obtained from Equations (8) and (9). The DTE figures suggest that the periodicity in the case of normal tooth contact is better than in the case of edge tooth contact, or in the case of edge tooth contact, the rotor system may behave periodically for a sufficiently long period. Comparisons also suggest that the dynamic behavior of hypoid gears under the edge tooth contact condition has more complex harmonic components. In contrast, LTEs under two different tooth contact conditions in a quasistatic state have perfect periodicity due to the milling consistency in each tooth-form geometric deviation shown in Figure 8.

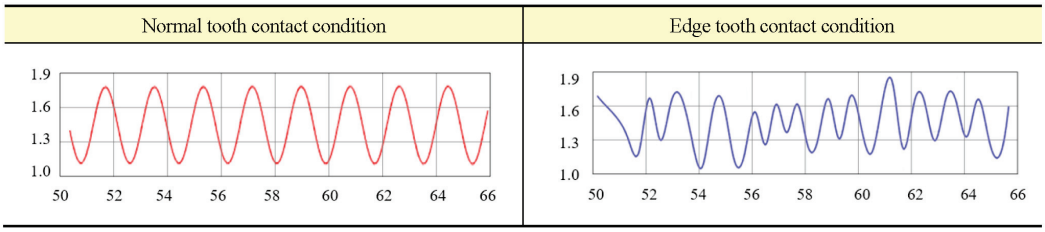



**Figure 12.** Dimensionless dynamic TE under two different tooth contact conditions of normal and edge in steady state.

It is difficult to compare DTEs directly between simulations and experiments, which are yielded, respectively, from the torsional equations and data of rotary encoders as measured. In reality, torsional vibrations of experiments are resultant signals that may include various harmonic components such as shaft revolution and noise of bearing systems, in addition to mesh frequency and harmonic frequencies excited by TE and MS. The DTEs of experimental results are filtered to eliminate the shaft revolution signal in low frequency and the noise signal of bearing systems in high frequency before compared to that of simulations. Comparisons of load and speed responses are performed between the filtered experimental data and the simulation data, which are evaluated by AMM and RMS under two different tooth contact conditions. The proposed comparisons of the load and speed responses in AMM and RMS are expected to provide a comprehensive and accurate understanding of the dynamic characteristics of the gear systems. In simulations, the torsional vibrations of the pinion $\theta_1$ and the gear $\theta_2$ are solved numerically using the Runge–Kutta method in Equations (8) and (9), which adopts $c_m$, $e(t)$, and $k(t)$ to be used as equation parameters to investigate the response of load and speed to exciting sources of TE and MS. The mesh damping is a constant $c_m$ = 500 N·s/m. In experiments, the torsional vibrations of the gear pair are measured by two rotary encoders under different experimental testing conditions: the speed ranges from 50 to 1400 rpm on the pinion side, giving a mesh frequency $f_m$ = 0.55–15.4 kHz; and the sampling frequency $f_s$ is set four times the mesh frequency $f_m$ in each sufficiently high test; and the load ranges from 50 to 450 Nm.

AMM and RMS of the load and speed responses are computed according to the data process method presented in Section 4.2, and they are compared between simulations and experiments. Two gear pairs of the normal and the edge tooth contacts are tested under the aforementioned conditions in the previous paragraph, and the measurement procedure starts after the rotor system runs for a long period, which ensures the system has been in a steady state. The blue and red curves in Figure 13 are experimental data in units of $10^{-2}$ μrad in the left ordinate and simulation data scaled by dimensionless coordinates in the right ordinate, respectively.

Figure 13a,b are load responses (LRs) in AMM and RMS of simulations and experiments, which are observed roughly the same between two different tooth contact conditions of the edge denoted by the dotted line and the normal denoted by the solid line. The load responses in AMM and RMS decrease slightly during light load and then increase continuously, and experiments suggest that the rotor system of hypoid gears is in an unstable state in which behaviors sustained angular vibrations between 50 and 75 Nm of the light input load condition.

Figure 13c–f are the speed response (SR) in AMM and RMS to the pinion speed between simulations and experiments under two different tooth contact conditions of the normal and the edge. Primary resonance vibrations are observed from both simulations and experiments, which are put together in figures. According to Section 4.2, primary resonances at the $n$th order are $f_n = 60nz_1\omega_p$. Experimental tests of the two pairs of hypoid

gears suggest that primary resonances of first and second orders occur at $f_1$ = 858 kHz and $f_2$ = 1716 kHz, which correspond to pinion speeds of 1300 rpm and 2800 rpm, respectively. Figure 13c–f show that simulations and experiments share similar dynamic behaviors in SRs evaluated by AMM and RMS. Importantly, SR figures show that the gear pair under edge tooth contact condition has a larger magnitude of AMM and RMS during flow reversals according to experiments and simulations, and edge tooth contact has more complex harmonic components, which confirms empirical predictions.

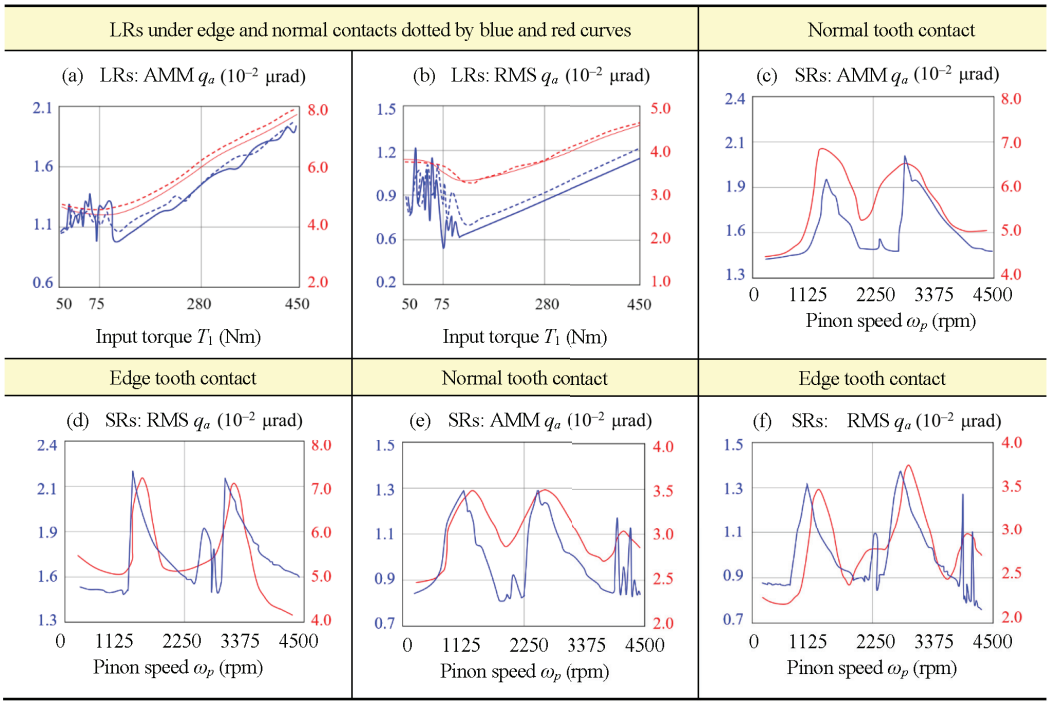



**Figure 13.** Angular LRs and SRs between experiments and simulations denoted by blue and red curves, respectively.

### *5.4. Translational Vibrations*

Translational vibrations of two pairs of hypoid gears are also investigated by experiments that use an accelerometer shown in Figure 6 to collect vibrational accelerations $[x_t, y_t, z_t]$ of the time domain in $x$, $y$, and $z$ directions. The data in the time domain are transformed by FFT into the data in the frequency domain $[x_f, y_f, z_f]$ and then processed into $d_{rms}$, which reflects the overall intensity of the vibration. The overall intensity of vibrations is for further analysis of gear pairs, and the detailed data process is presented in Section 4.2. Figure 14 shows the vibrational accelerations collected $[x_t, y_t, z_t]$ of the time domain from one of multiple experimental tests under different load and speed conditions. The time-domain vibrational accelerations suggest that $z_t$ in the up and down direction has a slightly smaller magnitude than in the horizontal directions $x_t$ and $y_t$. Figure 15 shows the vibrations in the frequency domain to examine consistency in different directions $x$, $y$, and $z$ under the condition that the pinion speed remains at 3000 rpm. At the remaining speed, frequencies of the first three orders of primary resonances are 1980 kHz, 3960 kHz, and 5940 kHz, respectively. The multiple experimental tests suggest that the magnitudes of primary resonances of the gear pairs of hypoid gears in different directions are different.

The general intensity of vibration $d_{rms}$ that goes with the increase of the pinion speed $\omega_p$ is obtained from the accelerations in the collected time domain at each increase in the pinion speed, which corresponds to the $n$th order vibrational frequency $f_n = 60nz_1\omega_p$. The vibration order $n$ in the gear vibration refers to a dimensionless quantity that represents the frequency of vibration normalized by the rotational speed of a reference component,

e.g., the gear shaft. It defines how many times a vibration event occurs per revolution of the component. For example, in the first order $n = 1$, vibration corresponds to a frequency equal to the rotational frequency of the shaft, and the order $n$ typically relates to the gear meshing frequency multiplied by $n$ times the shaft speed generated by periodic tooth engagement. The overall intensity of vibration $d_{rms}$ in the frequency domain is compared between two pairs of gears under two different tooth contact conditions by a large number of experimental tests, as shown in Figure 16. The proposed comparisons suggest that the gear pair in the case of edge tooth contact has higher vibrational intensity $d_{rms}$ than in the case of normal tooth contact. The general increase in the intensity of the vibration $d_{rms}$ is significantly correlated with the increase in the pinion speed of the order $n = 2$, which means that the second order of the pair of gears of the hypoid gears increases the power losses in the conversion of the tidal energy. According to the figures, two pairs of gears under different tooth contact conditions of normal in solid line and edge in dashed line share a similar trend in three all orders $n = 1$, 2, and 3. However, the overall vibration intensity $d_{rms}$ in the case of the edge tooth contact increases higher than in the case of the normal tooth contact, along with the rotation speed of order $n = 2$.

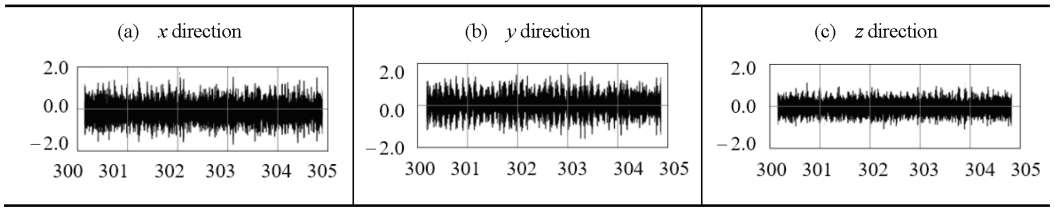



**Figure 14.** Measured accelerations in unit of $g$ in $x$, $y$ and $z$ directions for 5 s at pinion speed 3000 rpm.

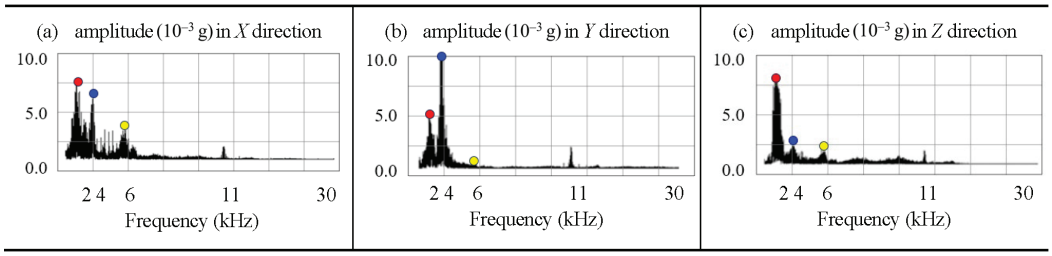



**Figure 15.** Primary resonances of the first three orders at 1980 kHz, 3960 kHz, and 5940 kHz in $x$, $y$, and $z$ directions.

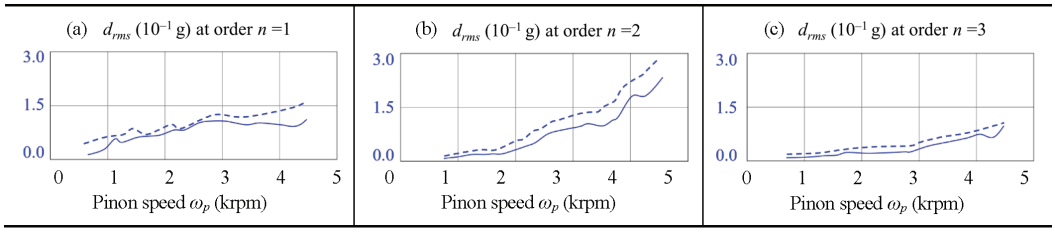



**Figure 16.** Translational SRs in RMS at orders of $n = 1$, 2, 3, and vibrational frequencies $f_n = 60\,nz_1\omega_p$.

Based on experimental findings and numerical analyses, several key solutions can be proposed for optimizing hypoid gear transmissions in tidal energy-harvesting systems, including: (1) implementation of modified tooth profile parameters during the manufacturing process, specifically adjusting the cutter radius and machine-tool settings to achieve optimal contact patterns that can better accommodate bidirectional loading; (2) development of specialized inspection protocols that focus on characterizing tooth contact patterns under simulated tidal loading conditions prior to deployment, particularly examining behavior during flow-reversal phases where edge contact is most prevalent; and

(3) integration of advanced monitoring systems utilizing high-precision rotary encoders and triaxial accelerometers to detect early signs of adverse contact patterns, especially monitoring second-order primary resonances, which this study identified as key indicators of edge contact development.

## 6. Conclusions

This study presents a comprehensive investigation of the dynamic behaviors of hypoid gears under variable tidal current energy-harvesting conditions, with particular emphasis on the effects of tooth contact patterns during bidirectional loading cycles. The study focuses on dynamic responses induced by internal excitation sources, specifically TE and MS, under characteristic tidal current variations and flow reversals. Comparison of torsional and translational vibrations between the two gear configurations, supported by both numerical simulations and experimental validation, yields the following significant findings.

(1) tooth contact patterns demonstrate high sensitivity to milling parameter variations under bidirectional tidal loading conditions, resulting in distinct TE and MS characteristics during flow reversals.

(2) Frequency domain analysis reveals that marginal edge tooth contact significantly amplifies the high-frequency harmonic components of TE and MS, particularly during tidal flow transition periods.

(3) Speed response measurements in multiple experimental trials confirm that edge contact-induced harmonic components generate additional angular vibrations in the high-frequency domain during flow reversals, validating the numerical predictions from the torsional model.

(4) Under variable tidal current conditions, tooth contact patterns significantly influence the dynamics of the system, with second-order primary resonances that exhibit elevated vibration intensities during flow transitions, leading to increased power losses in the conversion of tidal energy.

Generally, edge contact deteriorates the dynamic performance of hypoid gears, adding vibrations to the rotor system, particularly in high-frequency components. The short contact pattern decreases the contact load capacity, and the long contact pattern increases the risk of edge contact according to the tooth contact analysis and the pattern check obtained from the FE analysis and experimental rolling tests. The radius of the cutter head, along with the other generating settings of the pinion, significantly changes the contact length so that the appropriate radius of the cutter head is important, and the recommended cutter head for the pinion of the $41 \times 11$ hypoid gear pair is the radius between $2r_c = 225.10$ mm and $2r_c = 241.48$ mm. The findings demonstrating heightened vibration intensity and complex harmonic components during flow reversals suggest that future TCEC designs must incorporate advanced tooth contact optimization strategies and precision manufacturing controls to mitigate edge contact conditions under bidirectional loading. These results have significant implications for drivetrain reliability and power conversion efficiency, particularly in terms of tooth profile modifications and MS characteristics to accommodate the unique combination of high-torque loads and cyclic flow reversals that characterize tidal energy-harvesting conditions.

**Author Contributions:** Conceptualization, methodology and writing: D.H., Y.L. and X.Z.; software and validation: D.H. and Y.L.; formal analysis, data curation: D.H.; investigation and resources: X.Z.; writing—review and editing, supervision, project administration, and funding acquisition: G.L. All authors have read and agreed to the published version of the manuscript.

**Funding:** This research was funded by the U.S. National Science Foundation under Grant No. 2329791.

**Data Availability Statement:** Data are contained within the article.

**Acknowledgments:** The authors would like to thank Zhonghou Wang for his technical support on gear experimental investigation at the University of Shanghai for Science and Technology.

**Conflicts of Interest:** The authors declare no conflicts of interest.

## References

1. Li, G.; Zhu, W. A review on up-to-date gearbox technologies and maintenance of tidal current energy converters. *Energies* **2022**, *15*, 9236. [CrossRef]
2. Khare, V.; Khare, C.; Nema, S.; Baredar, P. *Tidal Energy Systems: Design, Optimization and Control*; Elsevier: Amsterdam, The Netherlands, 2018.
3. Li, G.; Zhu, W. Tidal current energy harvesting technologies: A review of current status and life cycle assessment. *Renew. Sustain. Energy Rev.* **2023**, *179*, 113269. [CrossRef]
4. Elasha, F.; Mba, D.; Togneri, M.; Masters, I.; Teixeira, J.A. A hybrid prognostic methodology for tidal turbine gearboxes. *Renew. Energy* **2017**, *114*, 1051–1061. [CrossRef]
5. Zhang, D.; Liu, D.; Liu, X.; Xu, H.; Wang, Y.; Bi, R.; Qian, P. Unsteady effects of a winglet on the performance of horizontal-axis tidal turbine. *Renew. Energy* **2024**, *225*, 120334. [CrossRef]
6. Zhang, Z.; Zhang, Y.; Zheng, Y.; Zhang, J.; Fernandez-Rodriguez, E.; Zang, W.; Ji, R. Power fluctuation and wake characteristics of tidal stream turbine subjected to wave and current interaction. *Energy* **2023**, *264*, 126185. [CrossRef]
7. Chen, P.; Wu, D. A review of hybrid wave-tidal energy conversion technology. *Ocean Eng.* **2024**, *303*, 117684. [CrossRef]
8. Avalos, G.O.G.; Shadman, M.; Estefen, S.F. Application of the latching control system on the power performance of a wave energy converter characterized by gearbox, flywheel, and electrical generator. *J. Mar. Sci. Appl.* **2021**, *20*, 767–786. [CrossRef]
9. Glennon, C.; Finnegan, W.; Kaufmann, N.; Meier, P.; Jiang, Y.; Starzmann, R.; Goggins, J. Tidal stream to mainstream: Mechanical testing of composite tidal stream blades to de-risk operational design life. *J. Ocean Eng. Mar. Energy* **2022**, *8*, 163–182. [CrossRef] [PubMed]
10. Wang, Q.; Zhou, C.; Gui, L.; Fan, Z. Optimization of the loaded contact pattern of spiral bevel and hypoid gears based on a kriging model. *Mech. Mach. Theory* **2018**, *122*, 432–449. [CrossRef]
11. Liu, S.; Song, C.; Zhu, C.; Liang, C.; Yang, X. Investigation on the influence of work holding equipment errors on contact characteristics of face-hobbed hypoid gear. *Mech. Mach. Theory* **2019**, *138*, 95–111. [CrossRef]
12. Liang, C.; Song, C.; Zhu, C.; Liu, S.; Yang, X. Investigation of the effects with linear, circular and polynomial blades on contact characteristics for face-hobbed hypoid gears. *Mech. Mach. Theory* **2020**, *146*, 103739. [CrossRef]
13. Cooley, C.G.; Liu, C.; Dai, X.; Parker, R.G. Gear tooth mesh stiffness: A comparison of calculation approaches. *Mech. Mach. Theory* **2016**, *105*, 540–553. [CrossRef]
14. Huang, D.; Wang, Z.; Kubo, A. Hypoid gear integrated wear model and experimental verification design and test. *Int. J. Mech. Sci.* **2020**, *166*, 105228. [CrossRef]
15. Simon, V.V. Grinding of hypoid gears by applying generating and Waguri motions. *Mech. Mach. Theory* **2023**, *179*, 105100. [CrossRef]
16. Shi, Z.; Li, S. Nonlinear dynamics of hypoid gear with coupled dynamic mesh stiffness. *Mech. Mach. Theory* **2022**, *168*, 104589. [CrossRef]
17. Liu, Y.; Chen, L.; Mao, X.; Shangguan, D. A semi-analytical loaded contact model and load tooth contact analysis approach of ease-off spiral bevel gears. *Machines* **2024**, *12*, 623. [CrossRef]
18. Wang, J.; Lim, T.C.; Li, M. Dynamics of a hypoid gear pair considering the effects of time-varying mesh parameters and backlash nonlinearity. *J. Sound Vib.* **2007**, *308*, 302–329. [CrossRef]
19. Karagiannis, I.; Theodossiades, S. An alternative formulation of the dynamic transmission error to study the oscillations of automotive hypoid gears. *ASME J. Vib. Acoust.* **2014**, *136*, 011001. [CrossRef]
20. Mohammadpour, M.; Theodossiades, S.; Rahnejat, H. Multiphysics investigations on the dynamics of differential hypoid gears. *ASME J. Vib. Acoust.* **2014**, *136*, 041007. [CrossRef]
21. Athanasopoulos, E.; Salpistis, C.; Mohammadpour, M.; Mihailidis, A.; Theodossiades, S.; Grekoussis, R. Calculation of the kinematics of hypoid gears towards developing a method for an equivalent crossed helical gear pair selection for use in tribological experimental evaluations. *Proc. Inst. Mech. Eng. Part K J. Multi-Body Dyn.* **2017**, *231*, 519–537. [CrossRef]
22. Song, C.; Bai, H.; Zhu, C.; Wang, Y.; Feng, Z.; Wang, Y. Computational investigation of off-sized bearing rollers on dynamics for hypoid gear-shaft-bearing coupled system. *Mech. Mach. Theory* **2021**, *156*, 104177. [CrossRef]
23. Huangfu, Y.; Zhao, Z.; Ma, H.; Han, H.; Chen, K. Effects of tooth modifications on the dynamic characteristics of thin-rimmed gears under surface wear. *Mech. Mach. Theory* **2020**, *150*, 103870. [CrossRef]
24. Zheng, X.; Luo, W.; Hu, Y.; He, Z.; Wang, S. Analytical approach to mesh stiffness modeling of high-speed spur gears. *Int. J. Mech. Sci.* **2022**, *224*, 107318. [CrossRef]

25. Li, G.; Zhu, W. An active ease-off topography modification approach for hypoid pinions based on a modified error sensitivity analysis method. *ASME J. Mech. Des.* **2019**, *141*, 093302. [CrossRef]
26. An, L.; Zhang, L.; Qin, S.; Lan, G.; Chen, B. Mathematical design and computerized analysis of spiral bevel gears based on geometric elements. *Mech. Mach. Theory* **2021**, *156*, 104131. [CrossRef]
27. Shen, Z.; Qiao, B.; Yang, L.; Luo, W.; Yang, Z.; Chen, X. Fault mechanism and dynamic modeling of planetary gear with gear wear. *Mech. Mach. Theory* **2021**, *155*, 104098. [CrossRef]
28. Yi, Y.; Huang, K.; Xiong, Y.; Sang, M. Nonlinear dynamic modelling and analysis for a spur gear system with time-varying pressure angle and gear backlash. *Mech. Syst. Signal Process.* **2019**, *132*, 18–34. [CrossRef]
29. Wei, S.; Chu, F.L.; Ding, H.; Chen, L.Q. Dynamic analysis of uncertain spur gear systems. *Mech. Syst. Signal Process.* **2021**, *150*, 107280. [CrossRef]
30. Li, G.; Zhu, W. Control and flume flow experiments of a tidal current energy converter with an infinitely variable transmission. *IEEE/ASME Trans. Mechatron.* **2024**, *29*, 2803–2811. [CrossRef]
31. Liu, Y.; Chen, L.; Li, G. Multi-points control for face-milled spiral bevel gears with a predesigned fourth-Order motion curve. *Machines* **2024**, *12*, 34. [CrossRef]
32. Chang, L.; Liu, G.; Wu, L. A robust model for determining the mesh stiffness of cylindrical gears. *Mech. Mach. Theory* **2015**, *87*, 93–114. [CrossRef]


**Disclaimer/Publisher's Note:** The statements, opinions and data contained in all publications are solely those of the individual author(s) and contributor(s) and not of MDPI and/or the editor(s). MDPI and/or the editor(s) disclaim responsibility for any injury to people or property resulting from any ideas, methods, instructions or products referred to in the content.

machines

MDPI

*Article*

# Analysis of Performance and Noise on an Asymmetric Double-Suction Fan with Non-Uniformity Inlet Conditions

**Yougen Huang [1], Bin Li [2], Haohui Chen [2], Weigang Yang [2], Qianhao Xiao [3,4] and Jun Wang [1,*]**

[1] School of Energy and Power Engineering, Huazhong University of Science and Technology, Wuhan 430074, China; huangyga@hust.edu.cn
[2] Ningbo Fotile Kitchenware Co., Ltd., Ningbo 315336, China
[3] School of Energy and Power Engineering, Changsha University of Science and Technology, Changsha 410205, China
[4] Key Laboratory of Renewable Energy Electric-Technology of Hunan Province, School of Energy and Power Engineering, Changsha University of Science and Technology, Changsha 410114, China
* Correspondence: wangjhust@hust.edu.cn

**Abstract:** Asymmetric double-suction centrifugal fans are commonly employed in home kitchens to remove cooking pollutants, and their performance is critical to maintaining a healthy indoor environment. However, inlet condition variations significantly influence the aerodynamic efficiency and noise levels. This study utilizes a combination of performance testing and a large eddy simulation to analyze the impact of different inlet conditions on the performance curve, impeller outlet pressure pulsation, unsteady flow structures, and sound quality of an asymmetric double-suction centrifugal fan. A non-uniform air distribution at the inlet is proposed to enhance the fan's aerodynamic and noise characteristics. The findings reveal that when the inlet area is reduced to less than 70% of its fully open state, the aerodynamic performance declines with decreasing intake area. The amplitude of the superimposed blade-passing frequency is minimized when only the left inlet is open; the pressure coefficient's fluctuation amplitude in the time domain reaches 0.4, with sharpness peaking at 3.1. In the optimized design, the maximum deviation in total pressure efficiency is limited to 1.96%, with loudness reduced by four sones and improved sharpness and roughness. These results provide valuable insights into the design and noise reduction of asymmetric double-suction squirrel-cage fans.

**Keywords:** inlet condition; large eddy simulation; vortex structure; pressure pulsation; acoustic quality characteristics

## 1. Introduction

Squirrel-cage fans are widely used in ventilation, fire protection, and smoke exhaust fields due to their high flow rate and low noise [1,2]. These fans are the core power of range hoods, mainly used to remove the fumes generated during cooking. They are also an important source of noise in home environments and will impact human health [3,4]. During the actual operation of the range hood, the inlet conditions and structure will be dynamically adjusted according to the working status of the stoves on both sides below to improve the capture efficiency, forming different intake conditions, which can bring about non-uniform inflow, thereby affecting the aerodynamic performance, internal unsteady flow, and noise of the fan [5–7]. On the other hand, under the influence of the motor's structure and space size limitations, the flow separation inside the double-suction squirrel-cage fan is further increased [8–11].

Currently, research methods for analyzing the internal pressure pulsation characteristics of fans include numerical simulations, experimental studies, and theoretical approaches. Kirchhofer et al. [12] conducted a comparative study using different turbulence models (S-A, k-ε, and SST k-ω) to simulate the flow field within a fan and compared these results with particle image velocimetry measurements. Their findings showed that the SST k-ω model provided the most accurate predictions for the characteristic curves and internal velocity fields. Similarly, Yang et al. [13] demonstrated that the SST model offers the lowest error in performance predictions when simulating a range hood equipped with a squirrel-cage fan.

The known literature indicates that the pressure and its fluctuations are highly consistent with the noise characteristics of the fan. It is feasible to study the pressure pulsation characteristics inside the fan to reflect the noise characteristics of the fan. Ballesteros-Tajadura et al. [14], Li et al. [15], and Xu et al. [16] all used numerical simulation methods to obtain the pressure pulsation inside the fan impeller, and the numerical calculation results matched well with experimental values. Zhang et al. [17] calculated the three-dimensional unsteady flow and acoustic field of the fan via direct computational aeroacoustics based on the lattice Boltzmann method. Experimental data from the performance test bench and the semi-anechoic chamber were used to validate the accuracy of the numerical simulation results. Min et al. [18] used URANS and FFT to analyze the interaction between the rotors of a centrifugal fan and its impact on acoustic performance. Zhang et al. [19] proposed an experimentally based vibration noise optimization control method for a particular centrifugal fan, leading to a 6.23 dB reduction. Xiao et al. [20] introduced a new empirical noise model to more accurately predict fan noise. Velarde-Su'arez et al. [21,22] found a significant circumferential asymmetry in the magnitude and direction of the velocity of a squirrel-cage fan. Oro et al. [23–25] presented a numerical methodology to evaluate the flow unsteadiness and impeller-tongue interaction. Kato [26] captured the large eddies in the flow and found that the large eddies were the primary noise source. Liu et al. [27], using large eddy simulation and acoustic analogy theory, analyzed the flow noise at a natural gas transmission and distribution station. A small hole muffler was designed to effectively reduce low-frequency noise by up to 37.4 dB, with an average noise reduction of approximately 20.9 dB. Deng et al. [28–30] mentioned more efficient and advanced CFD tools that could improve the LES results.

In the study of internal flow characteristics and optimization improvements for double-suction squirrel-cage fans, the primary areas of focus include flow deflectors, blade profiles, and volute designs. Gholamian et al. [31] studied the impact of four inlet nozzle sizes on fan performance and found that the inlet nozzle size and the impeller inner diameter are crucial for fan efficiency. Huang et al. [32] found that range hood noise predominantly consists of discrete low-frequency components, with most of the noise being transmitted through the inlet. Lv et al. [33] demonstrated that biomimetic volutes can significantly enhance aerodynamic performance under rated conditions. Lei et al. [34] showed that installing flow straighteners can notably reduce vortex intensity. Liu et al. [35] introduced a non-axisymmetric D-type inlet nozzle to mitigate severe backflow development at the volute tongue. Jiang et al. [36] explored a random modulation method to reduce tonal noise and reshape the noise spectrum. Xiao et al. [37] optimized the blade shape of the squirrel-cage fan within a range hood using a surrogate model, resulting in a 2.9% increase in maximum volume flow rate in the optimal design. In recent years, several scholars [38–42] have developed optimization design methods to enhance the aerodynamic performance and reduce the noise of centrifugal fans, achieving positive results in engineering applications.

In conclusion, the noise sources within squirrel-cage fans are intricate, primarily stemming from complex, unsteady flows. However, existing research predominantly addresses uniform air intake, fan placement within equipment, and steady-state simulations. These

approaches fall short in examining the internal flow dynamics and noise distribution characteristics of asymmetric double-suction squirrel-cage fans under non-uniform air intake conditions. There is a significant gap in understanding noise quality. The present study employs large eddy simulation (LES) numerical methods to analyze the internal flow of asymmetric double-suction centrifugal fans integrated within complete equipment. It investigates the impact of varying air intake conditions on impeller outlet pressure pulsation, internal complex flow patterns, and noise characteristics at the operator position. This research aims to offer valuable insights and a solid theoretical foundation for optimizing the design of dual-suction centrifugal fans.

This study introduces a non-equal flow inlet scheme, derived from unsteady simulation analysis and noise testing, that enhances the aerodynamic performance and reduces noise in asymmetric double-suction centrifugal fans. While this approach offers significant engineering guidance, further research is necessary. Future work should include integrating kitchen space considerations, performing multi-phase flow coupling analysis, accounting for human behavior and smoke exhaust conditions, accumulating measurement data, and developing a reduced-order analysis model for inlet parameters, aerodynamic noise, and air pollution concentration. Additionally, establishing a multi-objective optimization model for air quality and kitchen noise levels, dynamically optimizing inlet conditions, and ensuring superior performance of squirrel-cage fans across various operating scenarios will be essential.

## 2. Aerodynamic Performance Analysis

### *2.1. Fan Model*

This study focuses on an asymmetric double-suction squirrel-cage fan used in range hoods. Figure 1a illustrates the internal structure of the device, where the test fan is mounted in the upper fan frame. The square intake chamber is divided into two paths by the double-suction fan: the front and rear. The front path is associated with the narrow blade side, while the rear path corresponds to the wider impeller side. Airflow is drawn from a narrow, tapered duct below, passing through the front and rear intake chambers before entering the fan via the respective intake nozzles. A motor and its support structure are located in the narrow impeller channel, and these elements, along with the dimensions of the intake chambers and airflow conditions on both sides of the range hood, create asymmetric intake conditions. Consequently, the flow field analysis in the subsequent sections primarily compares the flow structures between the wide and narrow impellers corresponding to the front and rear paths.

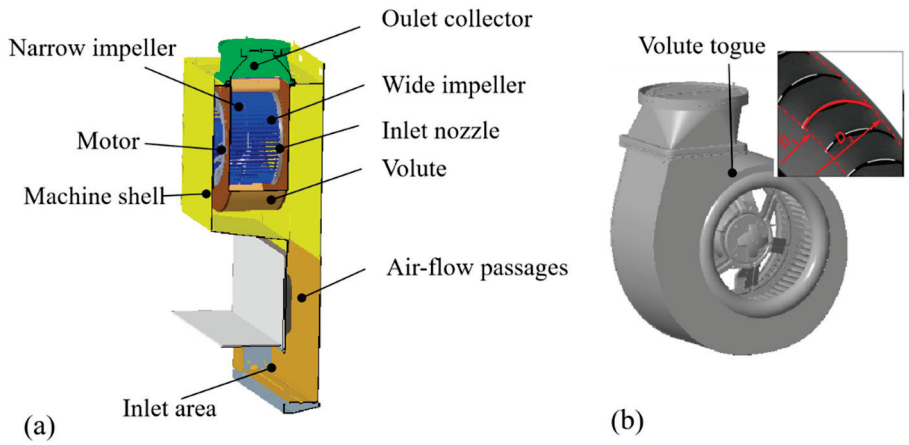



**Figure 1.** Schematic of the test range hood: (**a**) entire machine; (**b**) squirrel-cage fan.

The critical parameters of the test fan are illustrated in Figure 1b, with the specific values provided in Table 1. The rotor inner and outer diameters are 210 mm and 254 mm, respectively. The blade design features a single circular arc structure, with inlet and outlet angles of 105° and 167°. The impeller widths are 128 mm on the wide side and 50 mm on the narrow side. In this study, a fan speed of 1200 rpm and a flow rate of 12 $m^3$/min were chosen based on typical operating conditions for residential kitchen range hoods. These parameters represent common usage scenarios, ensuring that the results are applicable to real-world situations. These parameters represent common usage scenarios, ensuring that the results are applicable to real-world situations.

**Table 1.** Design parameters of a double-suction centrifugal fan.

| Parameter | Value |
|---|---|
| Impeller inlet diameter | 209 mm |
| Impeller outlet diameter | 232 mm |
| Impeller width | 128 mm/50 mm |
| Blade inlet angle | 105° |
| Blade outlet angle | 167° |
| Volume flow rate | 12 $m^3$/min |

### *2.2. Test Device*

The aerodynamic performance testing apparatus is based on the Chinese range hood measurement standard GB/T 17713 [43]. The experimental setup in Figure 2 has a flow measurement range of 0–35 $m^3$/min. Local atmospheric pressure, temperature, and humidity are recorded using an environmental temperature and humidity sensor and input into the aerodynamic performance measurement software, with temperature measurement errors of ±0.5 °C and humidity measurement accuracy of 1%. An air conditioning system in the laboratory maintains the experimental environment at around 20 °C and 85% relative humidity. The motor current is controlled via different settings on the electronic control panel to adjust the fan speed displayed on the control panel. Various nozzle combinations are used to simulate different fan operating conditions.

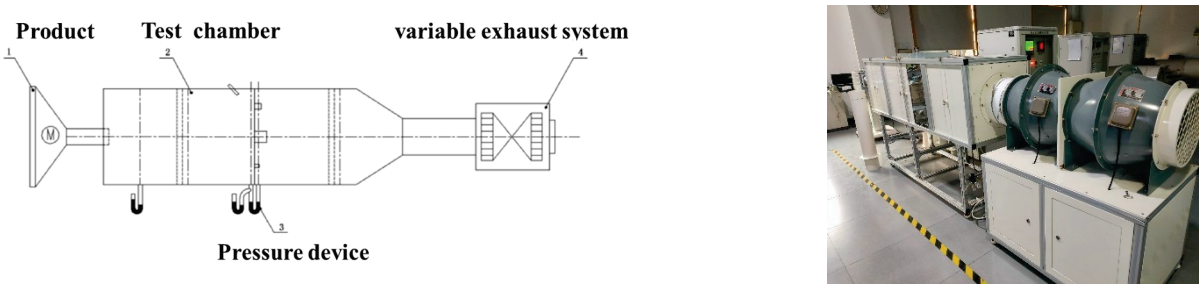



**Figure 2.** The aerodynamic performance testing device.

### *2.3. Analysis of Aerodynamic Performance*

Given the variation in cooking habits, long-term use of range hoods can lead to oil accumulation, potentially causing blockages in the inlet structure. On the other hand, dynamically adjusting the inlet conditions and structure according to the working state of the stoves on both sides below becomes a scheme to improve the effect of cooking fume absorption. Additionally, the rotational direction of the impeller may result in uneven inlet flow fields. To address these issues, nine specific inlet conditions have been defined, as illustrated in Figure 3.

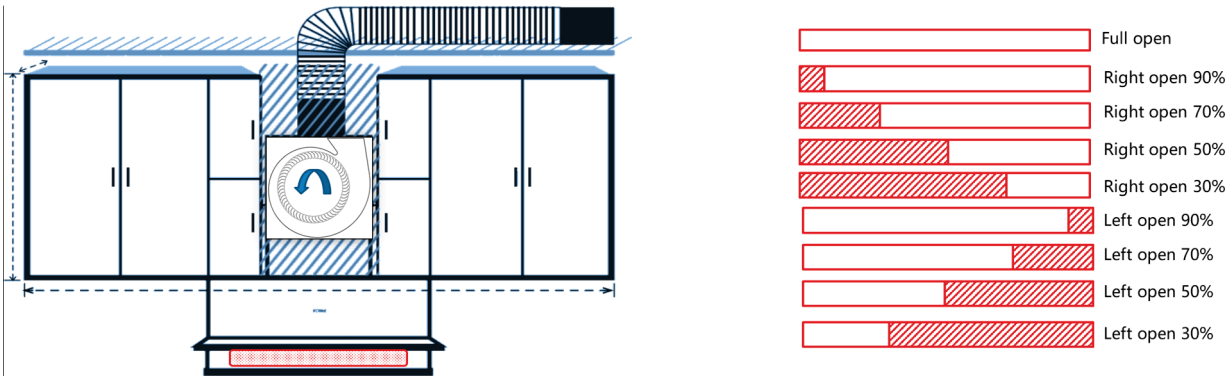
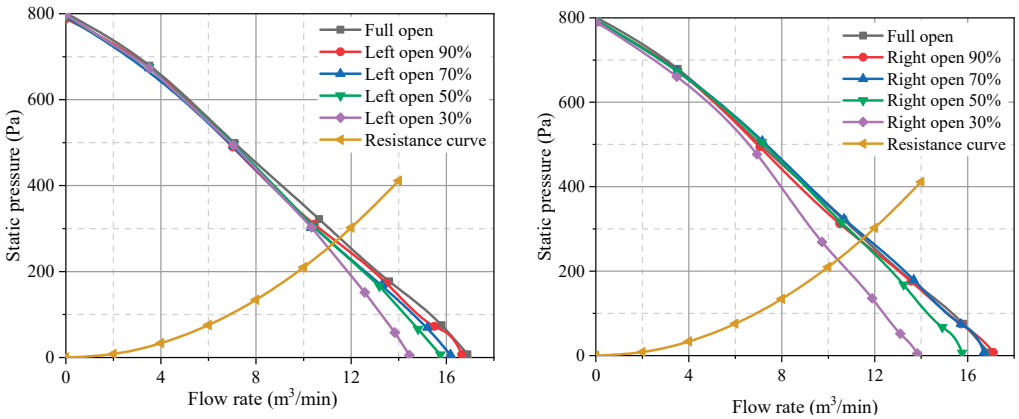



**Figure 3.** Nine inlet conditions with considering the direction of rotation.

The data are derived from aerodynamic performance tests. To ensure accuracy, we compared measurements taken at different times and with various fan products, maintaining a deviation in air volume measurement of no more than 1%. Data were collected while testing nine different inlet conditions at a constant fan speed. For each condition, we gathered 13 sets of data on air volume, static pressure, total pressure, and power by adjusting the nozzles. Using this information, we calculated the total pressure efficiency. The experimental results presented in Figure 4 demonstrate that the size of the range hood's air inlet area has a substantial impact on its aerodynamic performance. Interestingly, the fan's performance is better when the inlet is 90% open on both sides compared to when it is fully open. This improvement is likely due to excessive airflow velocity changes from the range hood's inlet to the fan's inlet, which leads to flow loss. However, when the inlet area is reduced to less than 70% of the fully open condition, the aerodynamic performance declines as the inlet area decreases. Additionally, at 30% left and right openings, a noticeable difference in aerodynamic performance is observed, suggesting that the optimal inlet area is asymmetrical between the left and right sides.




(**a**) Left open (**b**) Right open

**Figure 4.** Aerodynamic performance of nine inlet conditions.

Figure 5 illustrates the maximum total pressure efficiency for the nine different inlet conditions, revealing distinct patterns between the left and right inlet areas. The highest efficiency occurs under fully open and 90% right opening conditions. Conversely, the maximum total pressure efficiency drops significantly when the right inlet is only 30% open. This suggests that as the left opening area decreases, the resistance in the air duct increases in a nonlinear manner, while the left side shows a linear decrease in efficiency.

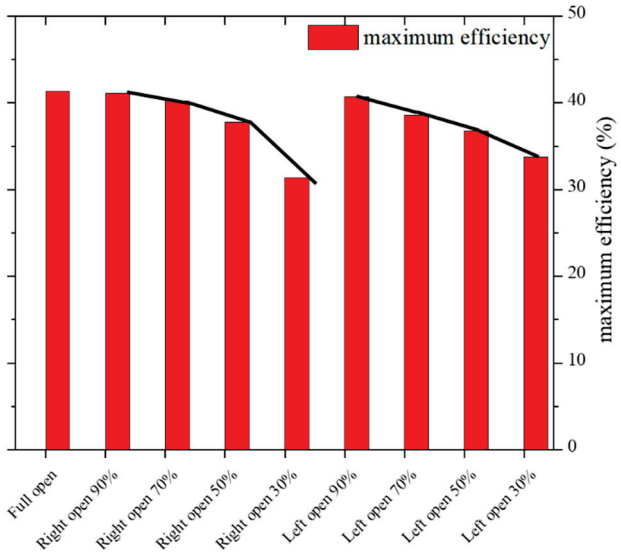



**Figure 5.** Maximum efficiency of nine inlet conditions.

## 3. Analysis of Internal Flow Characteristics

### *3.1. Numerical Method*

The kitchen model in this paper represents a typical household kitchen layout, as shown in Figure 6, with overall kitchen dimensions of 3.6 m × 2.1 m × 2.1 m. There are 60 blades in the impeller, consisting of a wide and narrow impeller, forming a double-suction structure. Moreover, a 1200 rpm speed resulted in a blade-passing frequency of 1200 Hz and a shaft frequency of 20 Hz. Other parameters are listed in Table 1. The entire computational domain is meshed using ANSYS ICEM 2022R1, with hexahedral mesh division for the impeller and refinement of the impeller blade wall mesh shown in Figure 7, ensuring a rotational domain with $y^+ \leq 1$. The remaining areas are meshed using tetrahedral elements.

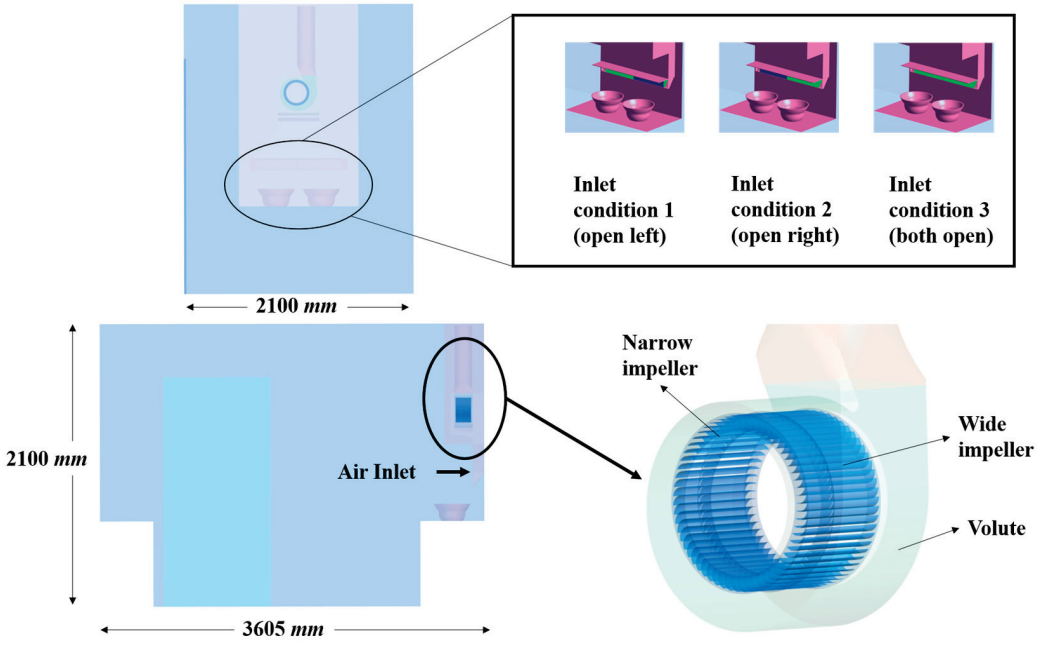



**Figure 6.** Three-dimensional layout.

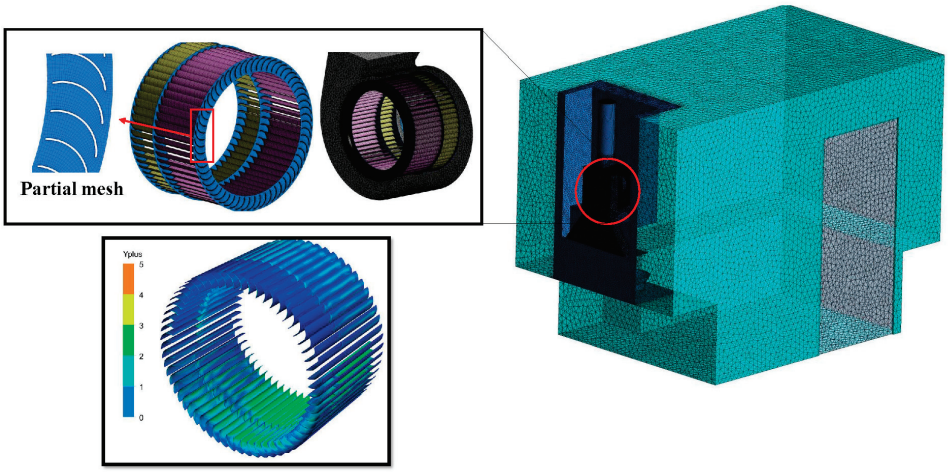



**Figure 7.** Schematic diagram of the grid.

Based on the aerodynamic performance analysis in the previous text, an internal flow study was conducted on the inlet conditions of 50% left opening, 50% right opening, and full opening. These conditions were named inlet condition 1, inlet condition 2, and inlet condition 3, respectively, to further analyze the internal mechanism for the performance differences.

At the rated operating conditions, the LES was employed to numerically simulate seven different mesh partitioning schemes. This turbulence model can derive the LES governing equations by adding a filtering function to the Navier–Stokes equations.

$$\frac{\partial \overline{u_i}}{\partial t} + \frac{\partial}{\partial x_j}\left(\overline{u_i u_j}\right) = -\frac{1}{\rho}\frac{\partial \overline{p}}{\partial x_i} + \frac{\partial}{\partial x_j}\left[\nu\left(\frac{\partial \overline{u_i}}{\partial x_j} + \frac{\partial \overline{u_j}}{\partial x_i}\right)\right] + \frac{\partial \overline{\tau_{ij}}}{\partial x_j} + S_i \tag{1}$$

$\overline{\tau_{ij}}$ is the subgrid-scale stress, abbreviated as SGS stress, expressed as:

$$\overline{\tau_{ij}} = \overline{u_i u_j} - \overline{u_i}\,\overline{u_j} \tag{2}$$

The most commonly used subgrid-scale model is the Smagorinsky–Lilly model.

$$\overline{\tau_{ij}} - \frac{1}{3}\delta_{ij}\overline{\tau_{kk}} = -2v_T\overline{S_{ij}} \tag{3}$$

$\overline{S_{ij}}$ is the strain tensor, $v_T$ is the subgrid-scale turbulent viscosity.

$$v_T = (C_s\Delta)^2\left|\overline{S}\right| \tag{4}$$

$$\left|\overline{S}\right| = \sqrt{2\overline{S_{ij}S_{ij}}} \tag{5}$$

$\Delta$ is the filter width, $C_s$ is the Smagorinsky–Lilly constant, take $C_s = 0.1$.

The computational domain was evaluated based on whether the total fan pressure stabilized as the grid number increased to verify mesh independence. When the grid number exceeded $9.18 \times 10^6$ under consistent computational conditions, changes in the total fan pressure became negligible. A grid total of $9.18 \times 10^6$ was selected for the numerical simulation to balance computational efficiency and accuracy. The mesh configuration is illustrated in Figure 8.

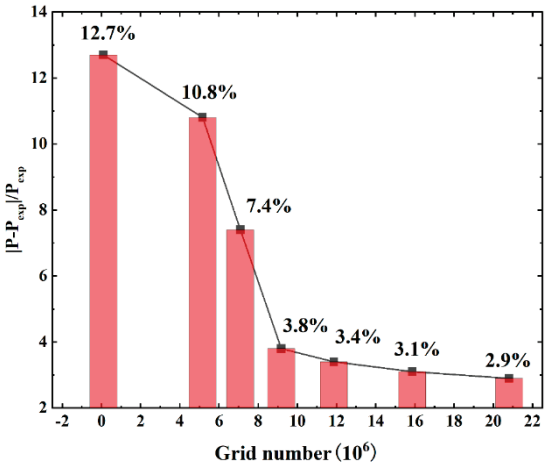



**Figure 8.** Relative error with grid number.

Steady-state simulations were conducted using the SST k-ω turbulence model, chosen for its comprehensive accuracy as the optimal eddy-viscosity model. The entire computational process was carried out in ANSYS Fluent. The inlet boundary condition was defined as a pressure inlet, while the outlet was set as a mass flow outlet with a flow rate of 12 $m^3$/min. Interfaces were applied at the boundaries between different regions to enable efficient data transfer.

The steady-state results are used as initial values for unsteady simulations. The sliding mesh model facilitates data transfer at the dynamic–static interface. The numerical calculations are set to rotate the impeller by 0.5 degrees per step, with a corresponding time step of $6.9444 \times 10^{-5}$ s. Moreover, a comparison of the pressure curves obtained from the experiment and CFD calculation is shown in Figure 9. The results from both the simulation and experiments show a strong correspondence in the high flow rate region. In the low flow rate area, the trends of both results are generally consistent, with the maximum error kept within 3%.

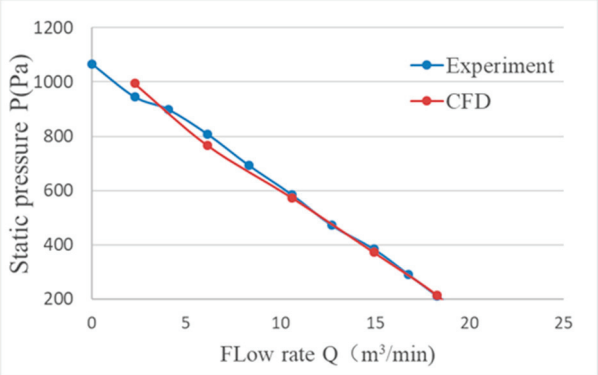
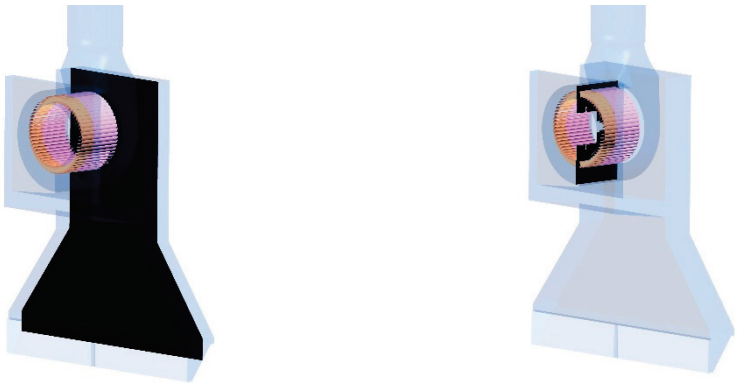



**Figure 9.** Comparison of experiment and CFD calculation.

### *3.2. Flow Field Analysis*

In the overall streamlined analysis (Figure 10), inlet condition 3 demonstrates lower velocities and more uniform streamlines at the fan inlet compared to inlet conditions 1 and 2. The figure reveals that fluid entering the fan inlet does not do so uniformly, which is a critical factor to consider in numerical simulations when modeling the kitchen environment. To examine the flow state near the impeller, two planes (Planes 1 and 2) were created. Figure 11 shows that while the flow under inlet condition 3 is relatively uniform, there is a distinct low-speed zone in the middle area. Under inlet conditions 1 and 2, the velocity

distribution within the intake chamber is uneven, with large low-speed zones in non-intake regions and increased vortex separation. Given the impeller rotation direction, airflow under inlet condition 1 enters from the left side, affecting the impeller's rotation direction.



(**a**) Plane 1 (**b**) Plane 2

**Figure 10.** Slice schematic diagram.

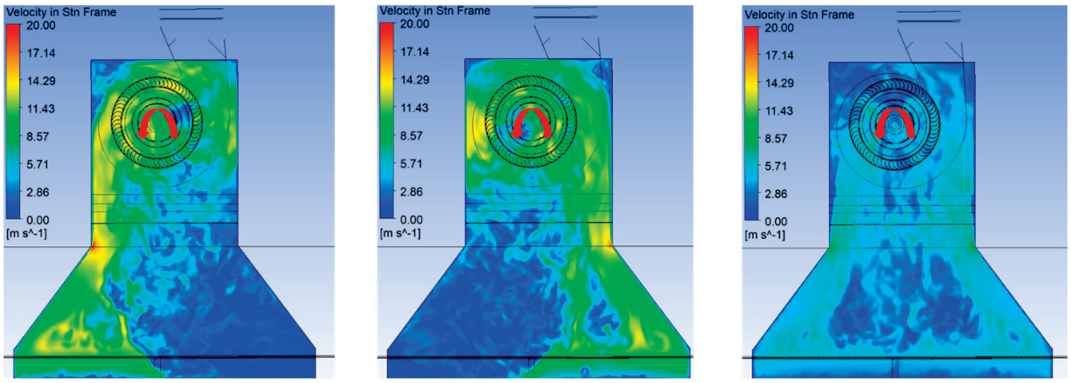



**Figure 11.** Vorticity and streamline distribution (Plane 1).

Figure 12 further illustrates that asymmetric inlet conditions generate large-scale circulation in another dimension, directly caused by the impeller's uneven air intake. From the perspective of plane 1, where the impeller rotates counterclockwise, inlet condition 1 shows that flow entering from the left side opposes the impeller's rotation, resulting in higher impact forces on the fluid and more complex flow characteristics. In contrast, inlet condition 2, where flow enters from the right side, aligns with the impeller's rotation direction, leading to a more stable internal flow state compared to condition 1.

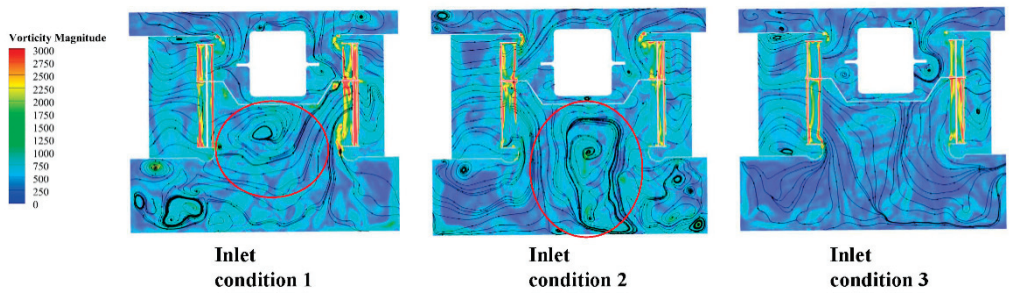



**Figure 12.** Vorticity and streamline distribution (Plane 2).

### *3.3. Influence of Inlet Conditions on the Pressure Fluctuation of Impeller Outlet*

The arrangement of all pressure fluctuation measurement points in this study is shown in Figure 13. Eight monitoring points (C1~C8, D1~D8) are uniformly arranged around the

outlet of the wide and narrow impellers. Pressure fluctuations data within a certain period are dimensionless processed, defining the pressure coefficient $C_p$ and the root mean square of pressure fluctuation coefficient $C_p$-RMS:

$$C_p = \frac{p - \overline{p}}{0.5\rho u_2^2} \tag{6}$$

$$C_p - RMS = \sqrt{\frac{\sum_{i=1}^{n} \left(C_{pi} - \overline{C}_p\right)^2}{n}} \tag{7}$$

where $p$ is the instantaneous pressure value. $\overline{p}$ is the mean value of pressure data in a specific time period. $u_2$ is the circumferential velocity of the impeller outlet. $n$ is the number of selected pressure coefficient samples.

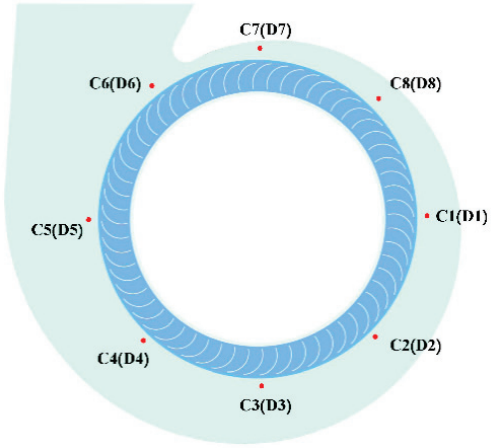



**Figure 13.** Location distribution of monitoring points.

The computational results indicate that the impact of different inlet conditions on the time domain is generally similar. Time-domain analysis offers a detailed description of the instantaneous characteristics of pressure signals, while frequency-domain analysis provides a deeper understanding of the frequency components and their sources. By combining both approaches, we gain a more comprehensive understanding of the fan's flow field characteristics and their relationship with noise and vibration. As shown in Figure 14, inlet condition 3 provides more stable time-domain characteristics, with a higher mean pressure coefficient ($C_p$), suggesting that the fluid gains more energy under this condition. Figure 15 illustrates that under inlet condition 1, the pressure signals at various monitoring points exhibit a distinct peak–valley pattern over time. This pattern is due to the periodic impact of the blades on the surrounding air as the impeller rotates, with each cycle producing 60 distinct peaks corresponding to the number of blades. Notably, under inlet condition 1, there are significant fluctuations in the $C_p$ near the C1 measurement point for the wide impeller and near the D5 measurement point for the narrow impeller. The time-domain characteristics for the wide impeller are comparatively more stable, with a maximum $C_p$ pulsation amplitude of 0.25, while the narrow impeller experiences a higher amplitude of 0.4. Subsequent analysis will focus on the flow characteristics near the C1 measurement point for the wide impeller and the D5 measurement point for the narrow impeller under inlet condition 1.

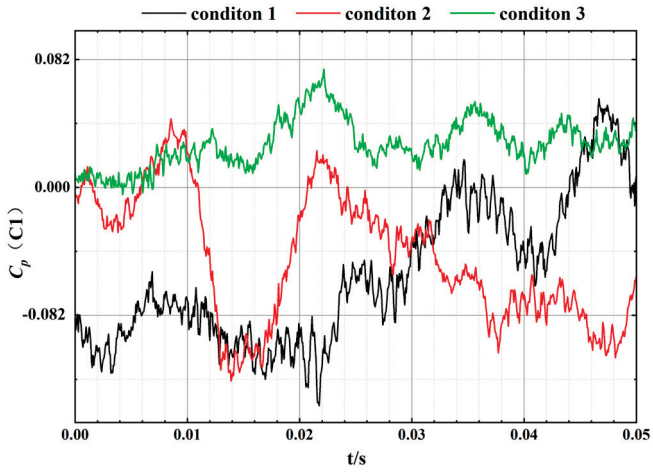



**Figure 14.** Time-domain characteristics of C1 measuring point under different inlet conditions.

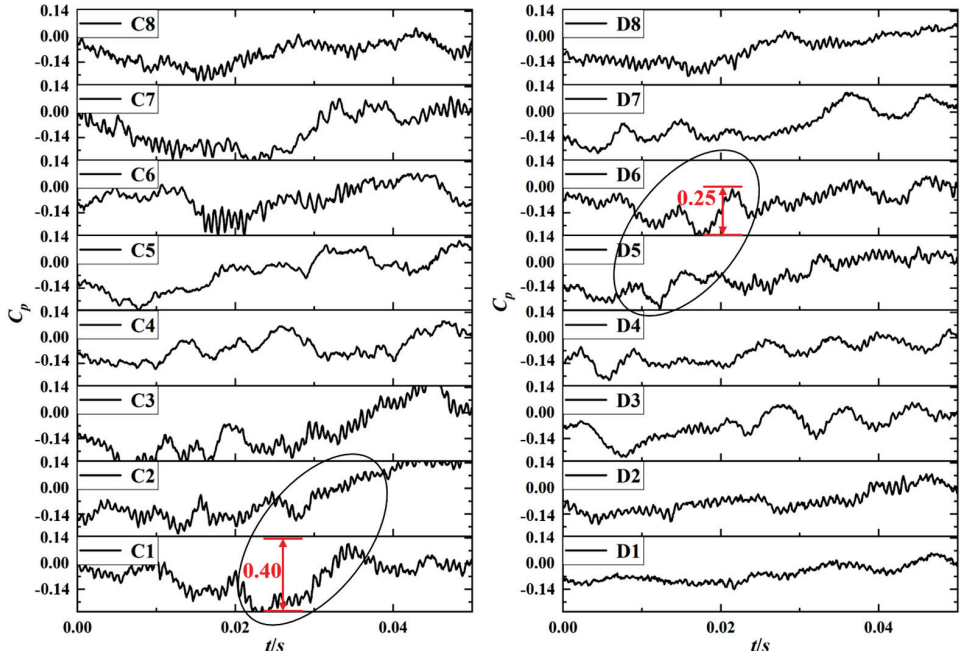



**Figure 15.** Time-domain characteristics of impeller outlet measuring points (inlet condition 1).

The rotor–stator interaction at the impeller outlet serves as the main source of internal unsteady pulsations in the fan. To capture the pulsation characteristics in this region and assess the impact of different inlet conditions on the rotor–stator interaction, eight monitoring points (C1~C8 and D1~D8) are evenly distributed at the outlet of each impeller. The time-domain signals from these points are processed using Fast Fourier Transform (FFT) with a Hanning window to analyze the frequency-domain signals under various inlet conditions.

Figure 16 illustrates the pressure pulsation frequency spectrum at the outlet under inlet condition 1. The central peak values of pressure pulsations at different monitoring points are all observed at the blade-passing frequency ($f_{BPF}$), though the amplitude varies significantly. Under inlet condition 1, a broad-frequency signal is evident in the low-frequency range and near the blade-passing frequency. The rotor–stator interaction is characterized by peak pressure pulsation energy at the blade-passing frequency and its harmonics. The spectrum reveals that the blade-passing frequency dominates the pressure pulsation spectrum at the impeller outlet, contributing the most energy and exhibiting a higher amplitude compared to its harmonics. The development of complex flow structures

appears to suppress the rotor–stator interaction, as indicated by the broad-frequency characteristics and reduced amplitude of the blade-passing frequency in the frequency-domain plot.

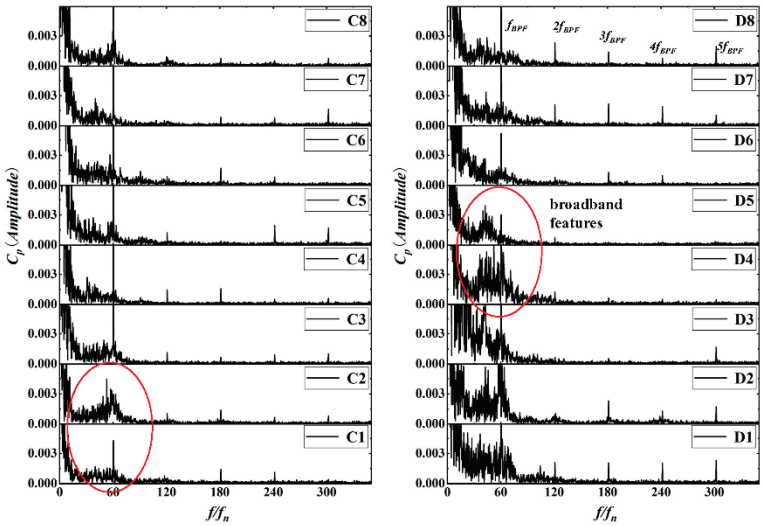



**Figure 16.** Frequency-domain characteristics of measuring points at the outlet of the wide impeller and narrow impeller under inlet condition 1.

Figure 17a,b illustrate the distribution of blade-passing frequency amplitude for pressure pulsations at various circumferential monitoring points at the impeller outlet. The superimposed amplitudes of the wide and narrow impellers at corresponding section monitoring points are shown in Figure 17c. Under inlet condition 1, the minimum superimposed BPF amplitude is 0.0018, while under inlet condition 2, it is 0.0038. For inlet condition 3, the minimum superimposed BPF amplitude reaches 0.009.

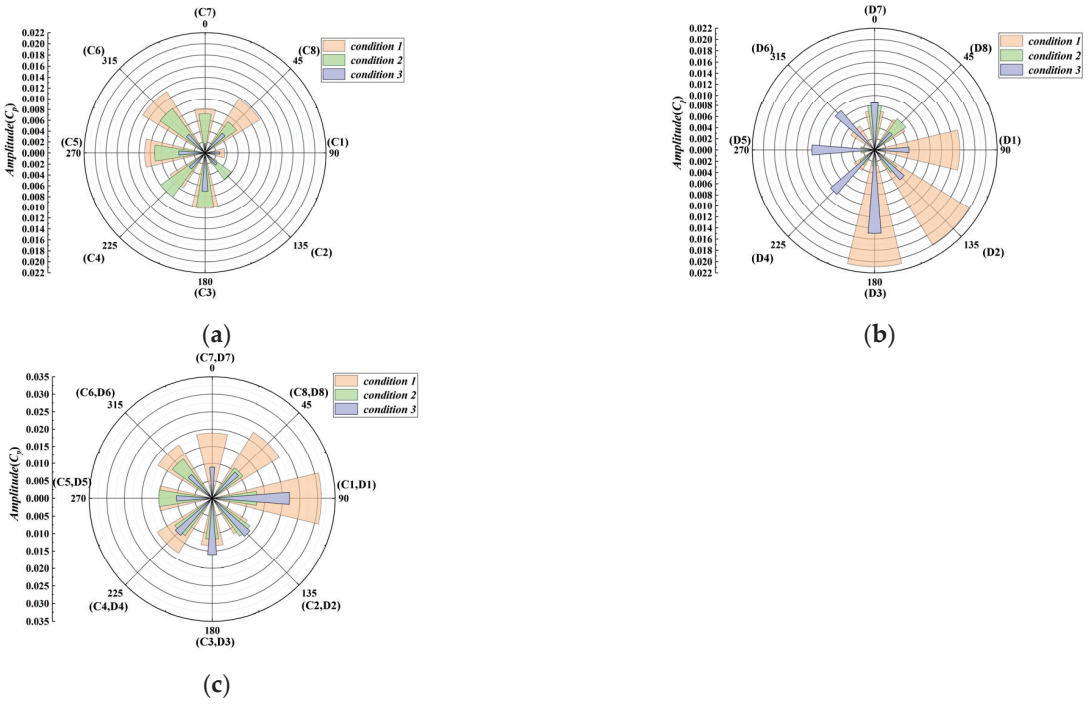



**Figure 17.** Circumferential distribution of $C_p$ amplitude at blade-passing frequency ($f_{BPF}$). (**a**) From the wide impeller monitors. (**b**) From the narrow impeller monitors. (**c**) Superimposed values of measuring points on the same section.

Under inlet condition 1, the internal flow within the impeller is notably complex, leading to the highest amplitude of low-frequency broadband pulsations. This complex flow significantly reduces the BPF amplitude. Specifically, under this condition, the minimum BPF amplitude for the wide impeller is observed at monitoring point C2 (the fourth section), while for the narrow impeller, it is at monitoring point D5 (the seventh section). Under inlet condition 2, the minimum BPF amplitude for the wide impeller is at monitoring point C1 (the third section), and for the narrow impeller, it is at monitoring point D1 (the third section). For inlet condition 3, the minimum BPF amplitude for the wide impeller is recorded at monitoring point C7 (the first section), whereas for the narrow impeller, it is at monitoring point D8 (the second section).

### *3.4. Correlation Between Flow Structures and Pressure Pulsation*

To investigate the relationship between pressure pulsation signals and unsteady flow structures within the fan, vortex structures in the impeller are identified using the Q-criterion. Developed by Hunt et al., the Q-criterion highlights areas of the flow field where the second invariant of the velocity gradient tensor reveals vortex structures. This criterion is expressed as follows:

$$Q = \frac{1}{2}\left(\|B\|_F^2 - \|A\|_F^2\right) \tag{8}$$

where A and B represent the symmetric and anti-symmetric matrices, respectively. $||\ ||_F$ denotes the Frobenius norm of the matrix.

Figure 18 shows that complex transient structures with high vortices appear near monitoring point C1 for the wide impeller section and near monitoring point D5 for the narrow impeller section. These two points correspond to the locations with the minimum amplitude of pressure pulsations at the blade-passing frequency (BPF). The reason for this is the inhibitory effect of the evolution of complex vortices on aerodynamic interference. The time interval Δt in the subsequent analysis is set to 0.0083 s (60°) to analyze the evolution process of internal impeller vortex structures within one rotation cycle.

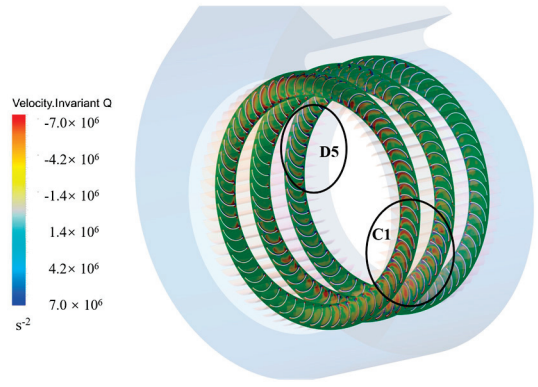
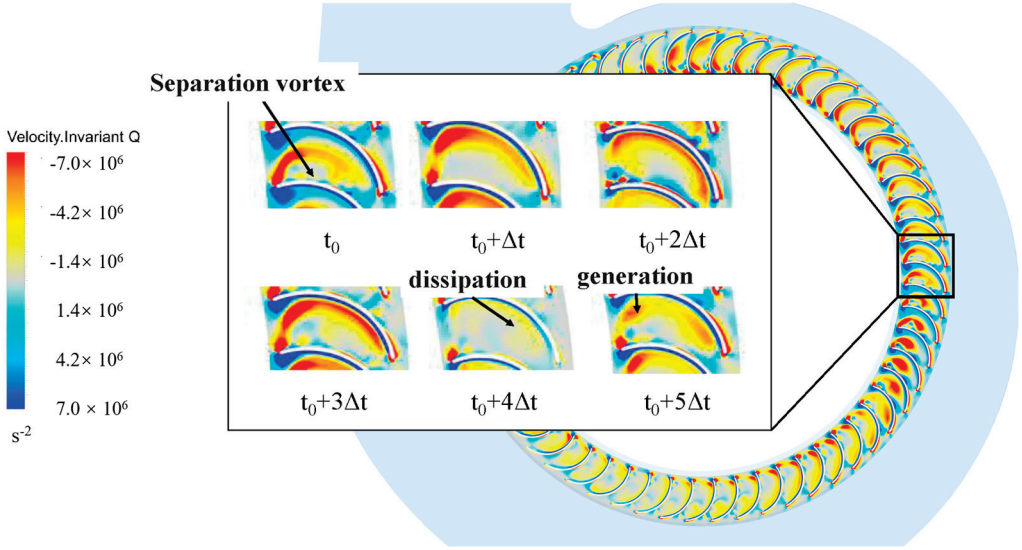


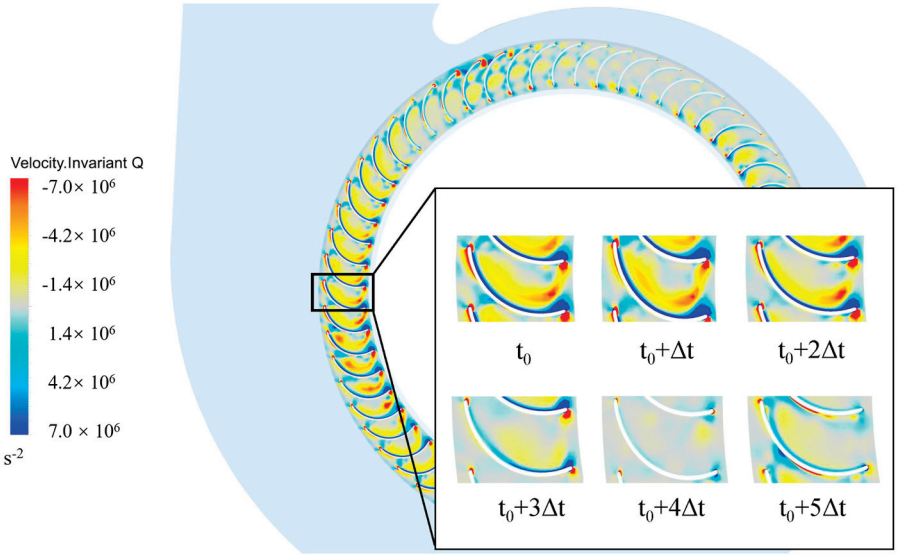

**Figure 18.** Vortex distribution of different axial sections.

Figure 19 illustrates that the high-vortex region near monitoring point C1 on the wide impeller originates from the blade's leading edge. The forward blade design positions negative vortices near the pressure side, while positive vortices emerge from the leading edge and merge with negative vortices near the pressure side of the adjacent blade. This interaction results in the shedding of large-scale vortices on the pressure side, while smaller-scale separation vortices predominantly shed on the suction side. At time $t_0$, the large-scale vortices peak in intensity, nearly filling the entire impeller passage. By time t0 + Δt, these vortices impact the pressure side, breaking up and dissipating within the passage. At time t0 + 5Δt, regeneration of the large-scale vortices begins. Throughout this cycle, the intensity

of the smaller separation vortices remains largely unaffected, which primarily influences the amplitude of the blade-passing frequency (BPF) due to the large-scale vortices. In contrast, near monitoring point D5 on the narrow impeller, the transient vortex structure lacks smaller separation vortices. Only a pair of large-scale vortices is observed, with weaker vortex energy and a reduced impact on the BPF signal.



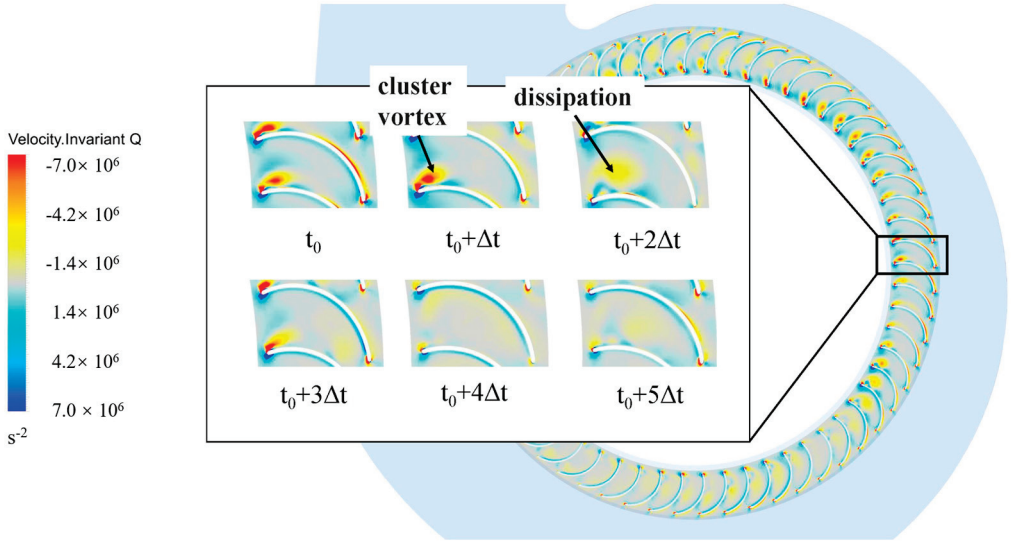

(**a**) Wide impeller



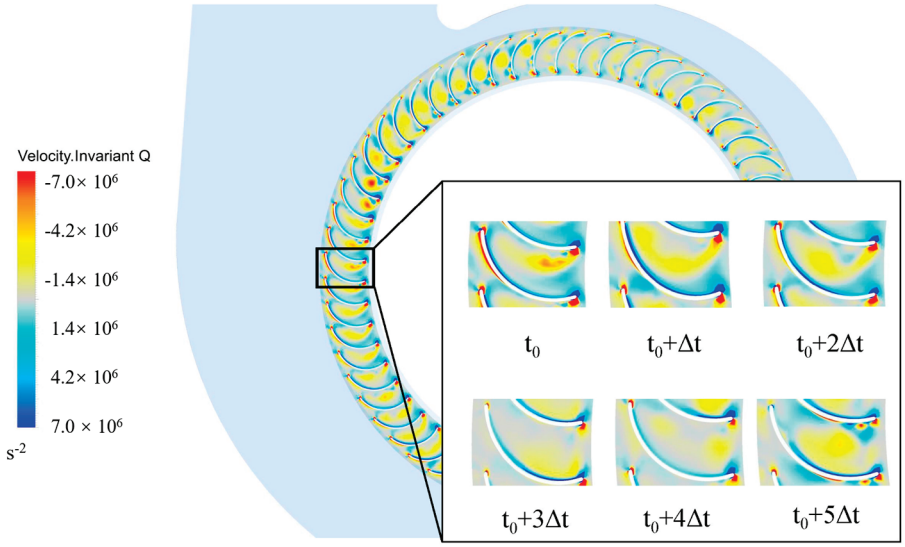

(**b**) Narrow impeller

**Figure 19.** Flow structure transient evolution in the flow passage of inlet condition 1.

In Figure 20, under inlet condition 2, the overall vortex strength is significantly reduced compared to inlet condition 1. The vortex structure within the wide blade passage shifts from a striped pattern to a predominantly clustered formation. Throughout a single rotation cycle, the vortex originates from the leading edge at time $t_0$ and gradually fragments as it progresses towards the trailing edge, eventually forming an isolated positive vortex cluster that persists within the passage. By time t0 + 4Δt, the strength of this vortex cluster reaches its minimum before regenerating from the leading edge in the next time step. In contrast, the transient vortex structure within the narrow blade passage maintains its striped pattern, as the high-energy vortex clusters generated at the leading edge do not undergo fragmentation.




(**a**) Wide impeller



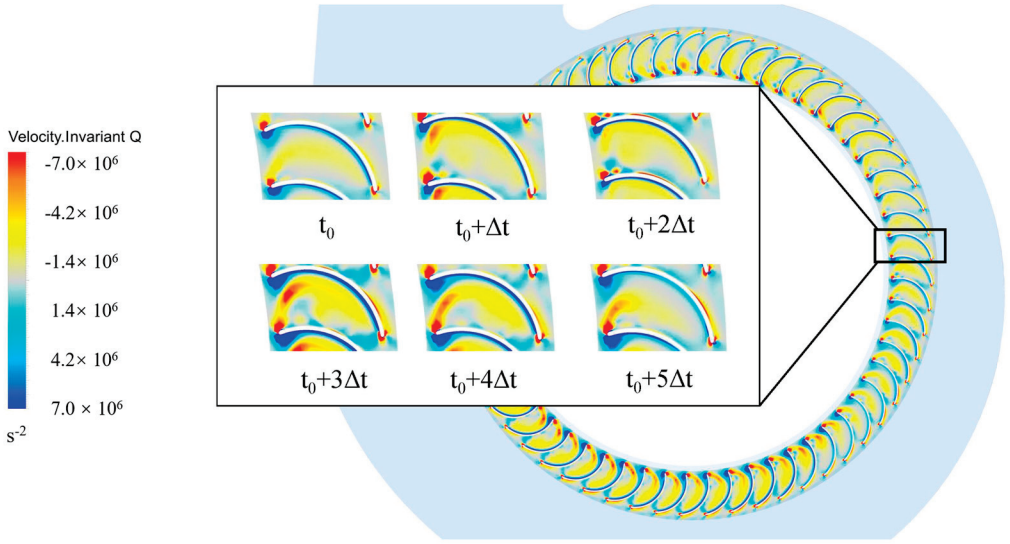

(**b**) Narrow impeller

**Figure 20.** Flow structure transient evolution in the flow passage of inlet condition 2.

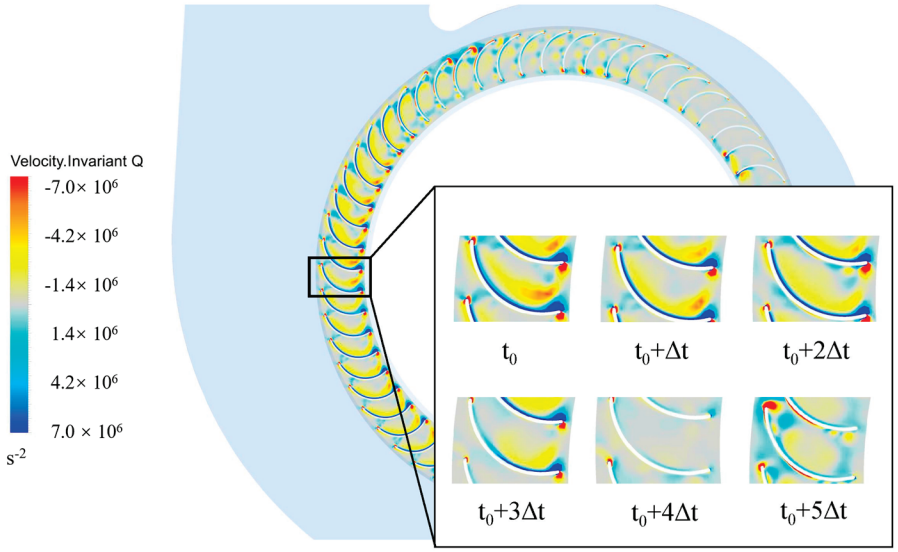
Figure 21 demonstrates that under inlet condition 3, vortex shedding within both the wide and narrow blade passages exhibits a striped pattern. The vortex structures maintain consistent strength and distribution throughout the passages, both spatially and temporally. This inlet condition achieves an optimal internal flow state for the impeller, characterized by a pronounced dynamic–static interference effect. Furthermore, there are no significant broad-frequency signals detected near the blade-passing frequency.

Under non-uniform inlet conditions, the flow at the impeller inlet is complex, featuring significant variations in both velocity and direction. These fluctuations result in unbalanced aerodynamic forces acting on the blades during rotation, leading to pressure fluctuations at the impeller outlet. For instance, when the left inlet serves as the primary air source, the left blades experience greater impact forces during rotation, which causes more pronounced pressure fluctuations on the left side of the impeller outlet. This observation aligns with the higher amplitude of low-frequency and broadband fluctuations noted near the monitoring points on the left side, as illustrated in Figures 19–21. The asymmetric vortex structures also influence the pressure distribution. As demonstrated in Figure 21, the vortex structures within both the wide and narrow impellers display a striped distribution.

The consistent strength and arrangement of these vortices contribute to relatively stable pressure fluctuations at the impeller outlet, characterized by a smaller amplitude of the pressure coefficient.




(**a**) Wide impeller




(**b**) Narrow impeller

**Figure 21.** Flow structure transient evolution in the flow passage of inlet condition 3.

## 4. Sound Quality

The acoustic field test was carried out in a simulated kitchen laboratory, with the experimental platform arranged as shown in Figure 22. The kitchen floor, walls, and ceiling were constructed from smooth, reflective materials such as concrete, metal, or ceramic tiles. To reduce interference with the sound source during testing, only one operator was allowed in the lab, and they were required to avoid wearing clothing with significant sound-absorbing properties that could impact the results. To evaluate human perception of noise, dummy heads (depicted in Figure 23) were placed at measurement points to capture data on how personnel in front of the stove perceive fan noise through the left and right ears of the artificial head.

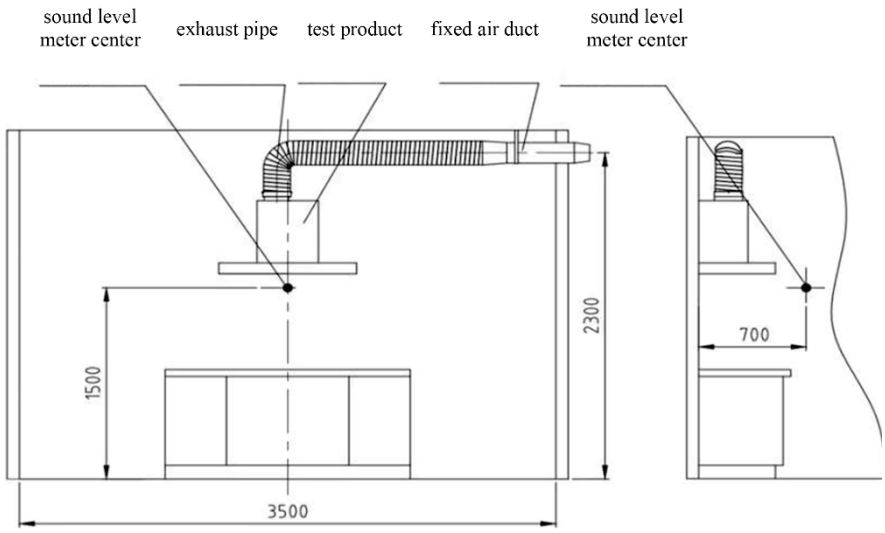



**Figure 22.** Layout diagram of the test bench.



**Figure 23.** Artificial head schematic diagram.

The process of collecting sound signals and developing models involves several key steps: gathering sound samples from range hoods, objectively evaluating the samples' parameters, subjectively assessing the samples, performing statistical analysis, and creating models. Initially, the loudness (L), sharpness (S), roughness (R), and articulation index (AI) of the range hood sound samples are measured. The method for calculating these four parameters refers primarily to the standard TCAS 341-2019 [44], which outlines the test methods for noise and sound quality of range hoods. A selected group of participants then listens to these samples under controlled conditions to ensure accurate representation, providing subjective comfort ratings for the sound quality. A regression model is then established to correlate the objective parameters with the subjective comfort ratings, leading to a final calculation formula for sound quality comfort Q.

$$Q = 10.7067 - 0.026 \times L - 0.5 \times S - 2.4298 \times R + 3.1657 \times AI \quad (9)$$

Loudness quantifies how the human ear perceives the overall volume of sound, measured in sones. For reference, the loudness of a pure 1 kHz tone at a sound pressure level of 40 dB is defined as 1 sone. The second row of Figure 19 displays the variations in loudness over time, recorded from the left and right ears of an artificial head. The data reveal from Figure 24 that under inlet condition 1, the left ear perceives a loudness of 26.6 sones, while the right ear perceives 28 sones. Under inlet condition 2, the average

loudness decreases to 24.2 sones in the left ear and 25.2 sones in the right ear. Inlet condition 3 further reduces loudness to 21.8 sones in the left ear and 22.7 sones in the right. The highest loudness, observed under inlet condition 1, indicates that the fan's internal noise is most intense under this condition.

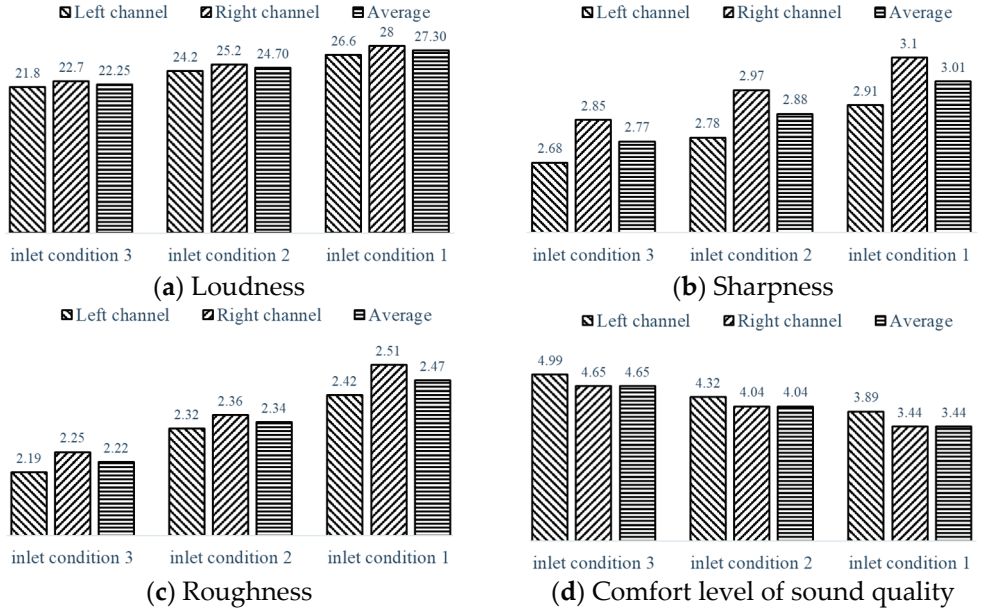
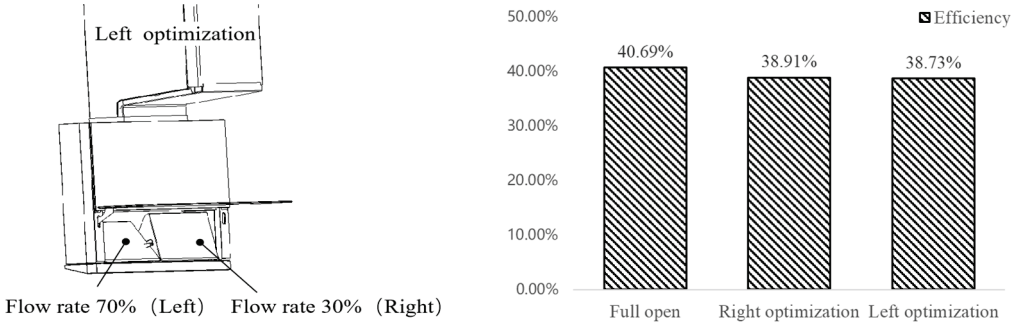



**Figure 24.** Comparison of sound quality parameters under three different intake conditions.

Sharpness is a psychoacoustic measure that evaluates the presence of high-frequency components in sound, expressed in acum. The third row of figures shows that sharpness is highest under inlet condition 1, with values of 2.91 acum in the left ear and 3.1 acum in the right ear. This suggests a higher concentration of high-frequency signals in the sound, corresponding to the broadband pulsation signal near the mid-frequency of the pressure pulsation, and is associated with the periodic evolution of large-scale vortices in the impeller flow passage.

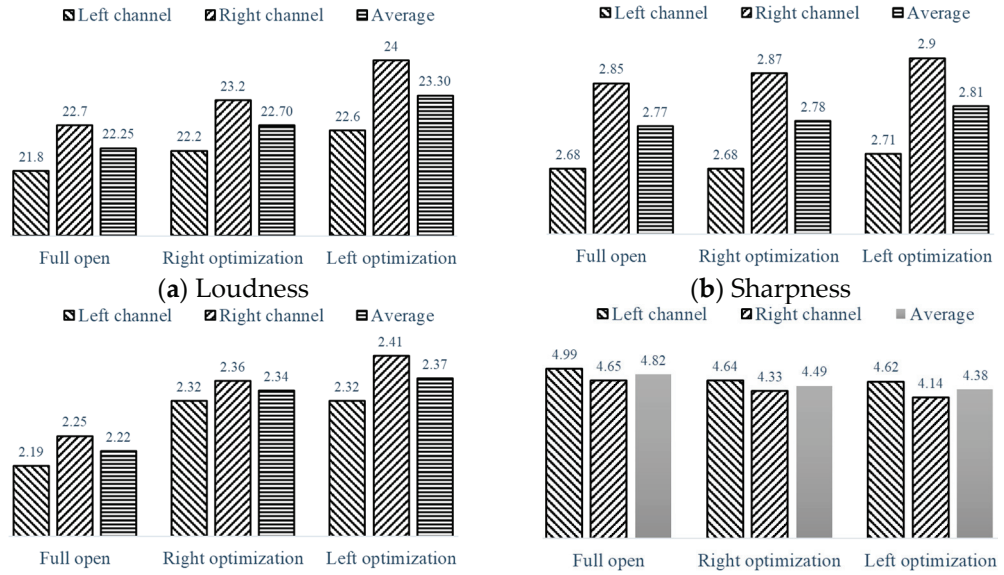
Sharpness of sound is a psychological measure used to assess the amount of high-frequency signal components in sound, and it is measured in acum. The data can be seen in the third row of the figures. Under inlet condition 1, the sharpness in the left and right ears is the highest, at 2.91 acum and 3.1 acum, respectively. Thus, it can be seen that under this inlet condition, the high-frequency signal in the sound is relatively high, corresponding to the wideband pulsation signal near the mid-frequency of the pressure pulsation, manifested as the periodic evolution of a pair of large-scale vortices in the impeller flow passage.

Based on inlet condition 1, a new inlet scheme with a non-uniform air volume distribution has been proposed to enhance aerodynamic performance and noise quality while preventing uneven oil fume escape. This scheme involves adjusting the angle of the guide plate at the intake structure, where the left side is fully opened and the right side is partially opened, resulting in an airflow ratio of 7:3. Alternatively, when the right side is fully opened and the left side is partially opened, the airflow ratio becomes 3:7. This approach aims to ensure that airflow is distributed evenly across the entire intake surface. Details of this optimization can be found in Figure 25. Figure 26 illustrates that, following the implementation of this optimization scheme, the aerodynamic performance parameters, including the maximum total pressure efficiency under the three intake conditions, remain consistent, with the maximum deviation in total pressure efficiency not exceeding 1.96%.




(**a**) Non-uniform inlet condition scheme (**b**) Maximum total pressure efficiency

**Figure 25.** The non-uniform inlet condition scheme and maximum total pressure efficiency.




(**a**) Loudness (**b**) Sharpness

(**c**) Roughness (**d**) Comfort level of sound quality

**Figure 26.** Comparison of sound quality parameters of optimization.

Figure 26 demonstrates that the optimization scheme effectively reduces the differences in loudness, sharpness, and roughness between the left and right ears. Specifically, the left-side optimization reduces the average loudness by four sones. Both optimization schemes achieve a deviation from the average loudness under fully open conditions of no more than 0.3 sones, sharpness by no more than 0.3 acum, and roughness by no more than 0.15 asper. These results suggest that the distribution characteristics of the internal vortex are consistent across the optimized conditions.

## 5. Conclusions

This study utilizes numerical simulations to explore how various inlet conditions influence the internal flow field and pressure pulsation of a dual-inlet centrifugal fan. The key findings are as follows:

(1) Time-domain analysis indicates that inlet condition 1 is the most unstable. This instability is characterized by significant fluctuations in the pressure coefficient and the presence of broadband signals in the frequency domain. These broadband features are particularly pronounced at measurement point C1, located on the wide impeller, and measurement point D5, located on the narrow impeller.

(2) Analysis of transient vortex structures reveals that the observed broadband characteristics and the absence of the blade-passing frequency at these measurement points are associated with the periodic evolution of large-scale vortices within the flow passage.

Under inlet condition 1, the intensity of the vortex peaks is due to the alignment between the inlet direction and the impeller's rotation direction, which has a substantial impact on flow within the passage.

(3) Sound quality analysis shows that under inlet condition 1, the sound sharpness is greater than under the other conditions. This observation suggests a higher presence of high-frequency signals in the pressure pulsation near the blade-passing frequency, further linking the flow structures to the characteristics in the frequency domain.

(4) A non-uniform air volume distribution scheme is proposed. This scheme enhances aerodynamic performance and reduces noise discrepancies between the left and right sides, leading to an overall reduction in average loudness by four sones.

**Author Contributions:** Conceptualization, Y.H.; methodology, Y.H. and Q.X.; software, Y.H. and B.L.; validation, W.Y., H.C. and J.W.; formal analysis, Y.H.; investigation, Y.H. and B.L.; resources, Y.H.; data curation, Q.X.; writing—original draft preparation, Y.H.; writing—review and editing, Y.H.; visualization, Y.H.; supervision, J.W. and Q.X.; project administration, W.Y. and Q.X.; funding acquisition, Y.H. All authors have read and agreed to the published version of the manuscript.

**Funding:** This research was supported by the National Key Research and Development Program of China (2023YFC3708405), the Open Research Fund of Science and Technology Innovation Platform of Key Laboratory of Renewable Energy Electric-Technology of Hunan Province, Changsha University of Science & Technology (2024ZNDL005).

**Data Availability Statement:** Data are contained within the article.

**Acknowledgments:** The authors thank the SCTS/CGCL HPCC of HUST for providing computing resources and technical support. The authors also appreciate Ningbo Fotile Kitchenware Co., Ltd. for their advice and assistance in improving this article.

**Conflicts of Interest:** Author Bin Li, Haohui Chen and Weigang Yang were employed by the company Ningbo Fotile Kitchenware Co., Ltd. The remaining authors declare that the research was conducted in the absence of any commercial or financial relationships that could be construed as a potential conflict of interest.

## References

1. Darvish, M.; Frank, S.; Paschereit, C.O. Numerical and experimental study on the tonal noise generation of a radial fan. *J. Turbomach.* **2015**, *137*, 101005. [CrossRef]
2. Akbari, G.; Montazerin, N.; Akbarizadeh, M. Stereoscopic particle image velocimetry of the flow field in the rotor exit region of a forward-blade centrifugal turbomachine. *Proc. Inst. Mech. Eng. Part A J. Power Energy* **2012**, *226*, 163–181. [CrossRef]
3. Pretzsch, A.; Seidler, A.; Hegewald, J. Health Effects of Occupational Noise. *Curr. Pollut. Rep.* **2021**, *7*, 344–358. [CrossRef]
4. Bolm-Audorff, U.; Hegewald, J.; Pretzsch, A.; Freiberg, A.; Nienhaus, A.; Seidler, A. Occupational Noise and Hypertension Risk: A Systematic Review and Meta-Analysis. *Int. J. Environ. Res. Public Health* **2020**, *17*, 6281. [CrossRef]
5. Wen, X.; Mao, Y.; Yang, X.; Qi, D. Design Method for the Volute Profile of a Squirrel Cage Fan with Space Limitation. *J. Turbomach.* **2016**, *138*, 081001. [CrossRef]
6. Wang, K.; Ju, Y.; Zhang, C. Numerical investigation on flow mechanisms of a squirrel cage fan. *Proc. Inst. Mech. Eng. Part A J. Power Energy* **2019**, *233*, 3–16. [CrossRef]
7. Cho, G.R.; Kawahashi, M.; Hirahara, H.; Kitadume, M. Application of Stereoscopic Particle Image Velocimetry to Experimental Analysis of Flow through Multiblade Fan. *JSME Int. J. Ser. B* **2005**, *48*, 25–33. [CrossRef]
8. Wang, C.; Wang, M.; Mai, K.; Li, H.; Liu, N. Structure design of low-frequency broadband sound-absorbing volute for a multi-blade centrifugal fan. *Appl. Acoust.* **2020**, *165*, 107315. [CrossRef]
9. Benchikh Le Hocine, A.E.; Poncet, S.; Fellouah, H. CFD modeling and optimization by metamodels of a squirrel cage fan using OpenFoam and Dakota: Ventilation applications. *Build. Environ.* **2021**, *205*, 108145. [CrossRef]
10. Xiong, J.; Tang, J.; Guo, P.; Li, J. Flow Capacity Optimization of a Squirrel Cage Fan with a New Rounded Rectangle Volute under Size Limitation. *Machines* **2023**, *11*, 283. [CrossRef]
11. Wang, K.; Ju, Y.; Zhang, C. Aerodynamic optimization of forward-curved blade centrifugal fan characterized by inclining bionic volute tongue. *Struct. Multidiscip. Optim.* **2021**, *63*, 2493–2507. [CrossRef]

12. Kirchhofer, M.; Krieger, M.; Hofer, D. A Comparative Study on Numerical Flow Simulations of a Centrifugal Electronic Cooling Fan Using Four Different Turbulence Models. *Energies* **2023**, *16*, 7864. [CrossRef]
13. Yang, X.; Jiang, B.; Wang, J.; Huang, Y.; Yang, W.; Yuan, K.; Shi, X. Multi-objective optimization of dual-arc blades in a squirrel-cage fan using modified non-dominated sorting genetic algorithm. *Proc. Inst. Mech. Eng. Part A J. Power Energy* **2020**, *234*, 1053–1068. [CrossRef]
14. Ballesteros-Tajadura, R.; Velarde-Suárez, S.; Hurtado-Cruz, J.P.; Santolaria-Morros, C. Numerical Calculation of Pressure Fluctuations in the Volute of a Centrifugal Fan. *J. Fluids Eng.* **2005**, *128*, 359–369. [CrossRef]
15. Li, Z.; Cao, W.; Ye, X.; Wei, Y. Experimental Investigation on the Noise Characteristics of a Squirrel-Cage Fan with Different Blade Lengths. *Energies* **2022**, *16*, 69. [CrossRef]
16. Xu, L.; Hansen, A.C.; Li, Y.; Liang, Z.; Yu, L. Numerical and Experimental Analysis of Airflow in a Multi-Duct Cleaning System for a Rice Combine Harvester. *Trans. ASABE* **2016**, *59*, 1101–1110.
17. Zhang, H.; Yang, J.; Li, B.; Xia, C.; Zhang, Y. Noise reduction and aerodynamic performance improvement of a multiblade centrifugal fan. *Phys. Fluids* **2024**, *36*, 125168. [CrossRef]
18. Min, Y.H.; Kang, S.; Hur, N.; Lee, C.; Park, J. Performance assessment of the RANS turbulence models in prediction of aerodynamic noise for air—Conditioner indoor unit. *J. Comput. Fluids Eng.* **2012**, *17*, 81–86. [CrossRef]
19. Zhang, J.; Chu, W.; Zhang, J. Numerical study of volute casing vibro-acoustics in a marine centrifugal fan. *Aust. J. Mech. Eng.* **2021**, *19*, 502–520. [CrossRef]
20. Xiao, Q.; Wang, J.; Yang, X.; Ding, Y.; Jiang, B. An Empirical noise model of centrifugal fans with different volute tongues based on Langevin regression. *J. Build. Eng.* **2023**, *79*, 107876. [CrossRef]
21. Velarde-Suárez, S.; Ballesteros-Tajadura, R.; Santolaria-Morros, C.; González-Pérez, J. Unsteady Flow Pattern Characteristics Downstream of a Forward-Curved Blades Centrifugal Fan. *J. Fluids Eng.* **2001**, *123*, 265–270. [CrossRef]
22. Velarde-Suárez, S.; Ballesteros-Tajadura, R.; Pérez, J.G.; Pereiras-García, B. Relationship between volute pressure fluctuation pattern and tonal noise generation in a squirrel-cage fan. *Appl. Acoust.* **2009**, *70*, 1384–1392. [CrossRef]
23. Oro, J.M.; García, J.; Parrondo, J. Numerical investigation of the unsteady flow in a centrifugal fan: Impeller-tongue interaction. *J. Fluids Eng.* **2010**, *132*, 051102.
24. Oro, J.M.; García, J.; Parrondo, J. Experimental validation of numerical simulations of unsteady flow in a centrifugal fan. *Exp. Therm. Fluid Sci.* **2011**, *35*, 1–10.
25. Oro, J.M.; García, J.; Parrondo, J. Optimization of impeller-tongue interaction in centrifugal fans using CFD. *J. Turbomach.* **2014**, *136*, 031001.
26. Kato, C.; Kaiho, M.; Manabe, A. An Overset Finite-Element Large-Eddy Simulation Method With Applications to Turbomachinery and Aeroacoustics. *J. Appl. Mech.* **2003**, *70*, 32–43. [CrossRef]
27. Liu, E.; Yan, S.; Peng, S.; Huang, L.; Jiang, Y. Noise silencing technology for manifold flow noise based on ANSYS fluent. *J. Nat. Gas Sci. Eng.* **2016**, *29*, 322–328. [CrossRef]
28. Deng, X. A unified framework for non-linear reconstruction schemes in a compact stencil. Part 1: Beyond second order. *J. Comput. Phys.* **2023**, *481*, 112052. [CrossRef]
29. Deng, X. A new open-source library based on novel high-resolution structure-preserving convection schemes. *J. Comput. Sci.* **2023**, *74*, 102150. [CrossRef]
30. Cheng, L.; Deng, X.; Xie, B. An accurate and practical numerical solver for simulations of shock, vortices and turbulence interaction problems. *Acta Astronaut.* **2023**, *210*, 1–13. [CrossRef]
31. Gholamian, M.; Rao, G.K.M.; Bhramara, P. Numerical investigation on effect of inlet nozzle size on efficiency and flow pattern in squirrel cage fans. *Proc. Inst. Mech. Eng. Part A J. Power Energy* **2013**, *227*, 896–907. [CrossRef]
32. Huang, J.; Zhang, K.; Li, H.; Wang, A.; Yang, M. Numerical simulation of aerodynamic noise and noise reduction of range hood. *Appl. Acoust.* **2021**, *175*, 107806. [CrossRef]
33. Lv, H.; Yang, W.; Zhang, W.J. Numerical simulation and analysis of the aerodynamic noise of a nautilus-inspired bionic multiblade centrifugal fan. *J. Mech. Sci. Technol.* **2022**, *36*, 4475–4489. [CrossRef]
34. Lei, J.; Jia, C.; Cui, Q.; Cheng, W.; Qin, G. Cause analysis and suppression method of the vortex at the impeller outlet of the multiblade centrifugal fan. *Energy Sci. Amp; Eng.* **2023**, *11*, 3364–3378. [CrossRef]
35. Liu, H.; Jiang, B.; Wang, J.; Yang, X.; Xiao, Q. Numerical and experimental investigations on non-axisymmetric D-type inlet nozzle for a squirrel-cage fan. *Eng. Appl. Comput. Fluid Mech.* **2021**, *15*, 363–376. [CrossRef]
36. Jiang, B.; Wang, J.; Yang, X.; Wang, W.; Ding, Y. Tonal noise reduction by unevenly spaced blades in a forward-curved-blades centrifugal fan. *Appl. Acoust.* **2019**, *146*, 172–183. [CrossRef]
37. Xiao, Q.; Jang, B.; Wang, J. Volute profile design of the squirrel cage fan based on a B-spline curve under space limitation. *Proc. Inst. Mech. Eng. Part A J. Power Energy* **2020**, *234*, 889–899. [CrossRef]
38. Zhou, W.; Zhou, P.; Xiang, C.; Wang, Y.; Mou, J.; Cui, J. A Review of Bionic Structures in Control of Aerodynamic Noise of Centrifugal Fans. *Energies* **2023**, *16*, 4331. [CrossRef]

39. Yuan, Y.; Xiao, Y.; Ming, P.; Lu, H. The aerodynamic and noise characteristics of centrifugal fan with partially tilted tongue. *Phys. Fluids* **2023**, *35*, 127113. [CrossRef]
40. Paramasivam, K.; Rajoo, S.; Romagnoli, A.; Yahya, W.J. Tonal noise prediction in a small high speed centrifugal fan and experimental validation. *Appl. Acoust.* **2017**, *125*, 59–70. [CrossRef]
41. Zhang, A.T.; Zhou, B.S.; Mao, C.Z.; He, D.J.; Fang, E.X. A design method of volute profile of multi-blade centrifugal fan based on DRBF model. *Phys. Fluids* **2023**, *35*, 125127. [CrossRef]
42. Wang, J.; Liu, X.; Tian, C.; Xi, G. Aerodynamic performance improvement and noise control for the multi-blade centrifugal fan by using bio-inspired blades. *Energy* **2023**, *263*, 125829. [CrossRef]
43. Zhou, S.; Zhou, H.; Yang, K.; Dong, H.; Gao, Z. Research on blade design method of squirrel-cage fan for building efficient ventilation based on Hicks-Henne function. *Sustain. Energy Technol. Assess.* **2021**, *43*, 100971.
44. *T/CAS 341-2019*; Test Method for Sound Quality of Range Hood Noise. Chinese Group Standards: Beijing, China, 2019.


**Disclaimer/Publisher's Note:** The statements, opinions and data contained in all publications are solely those of the individual author(s) and contributor(s) and not of MDPI and/or the editor(s). MDPI and/or the editor(s) disclaim responsibility for any injury to people or property resulting from any ideas, methods, instructions or products referred to in the content.

machines

MDPI

*Article*

# Rapid Dismantling of Aluminum Stranded Conductors: An Automated Approach

**Zhinan Cao [1,2], Jie Feng [1,2], Shijun Xie [1,2], Qian Peng [2], Jiahui Chen [2,*], Cheng Wen [3] and Jigang Huang [3]**

[1] Sichuan Shuneng Dianke Energy Technology Co., Ltd., Chengdu 610041, China; fj2004.cdut@126.com (J.F.)
[2] State Grid Sichuan Electric Power Research Institute, Chengdu 610041, China
[3] Department of Mechanical Engineering, Sichuan University, Chengdu 610065, China
* Correspondence: cjh13w@163.com

**Abstract**

Currently, the dismantling of aluminum stranded conductors remains predominantly manual due to their structural complexity. To enhance the efficiency and reduce the labor intensity for dismantling aluminum stranded conductors, this study presents an innovative torque-driven dismantling method validated through dynamic simulation analysis. To demonstrate the proposed method, a modular prototype machine that includes four main functional modules (transmission, untwisting, separation, and shearing) was developed. Experimental results from the prototype dismantling machine demonstrated that when processing JL/G3A-500/65 conductors (Sichuan Star Cable Co., Ltd., Leshan, China) under the following operational parameters—0.5 rad/s rotational speed, 10 cm extension length, 2400 N clamping force, and 40 N·m torque application—the system achieved a single-layer dismantling efficiency exceeding 98%. This represents a significant improvement in operational speed compared to traditional manual methods. The developed machine achieved collaborative control of axial feed, reverse untwisting, and automatic shearing, elevating the untwisting qualification rate to 95%. This solution provides an efficient and safe approach to conductor inspection, demonstrating substantial engineering application value.

**Keywords:** aluminum conductor steel-reinforced (ACSR); torque method; simulation analysis; modular design

## 1. Introduction

In recent years, with the advancement of China's "Dual Carbon" goals and accelerated energy structure transition, ultra-high voltage (UHV) power grids have emerged as critical network infrastructures supporting national strategic initiatives such as "West-East Power Transmission" and "new energy grid integration". By 2025, the State Grid Corporation of China will have completed and operationalized 35 UHV projects, achieving an annual electricity transmission capacity exceeding 3 trillion kilowatt-hours, which significantly enhances inter-regional power allocation capabilities. Overhead transmission lines, leveraging their economic efficiency and adaptability advantages, undertake more than 90% of national power transmission tasks, serving as the "arterial network" of the power system. The aluminum conductor steel-reinforced (ACSR) cables predominantly employed in high-voltage and UHV overhead transmission systems feature a composite structure of steel cores and aluminum strands. This innovative configuration achieves synergistic optimization of mechanical strength and electrical conductivity, establishing its dominance in high-voltage and UHV transmission applications [1–3].

The widespread adoption of ACSR cables stems from their dual-functional advantages: the internal steel core effectively withstands extreme meteorological conditions in heavy-ice zones and long-span configurations while bearing mechanical stresses in both large-span and conventional installations. Concurrently, the outer aluminum strands reduce overall resistivity and enhance current-carrying capacity, fulfilling long-distance power transmission requirements. A representative application is evidenced in the Xinjiang-to-Chongqing ±800 kV UHV DC transmission project, where large-section ACSR cables with enhanced reliability effectively mitigate conductor fracture risks induced by complex southwestern terrain and high-altitude conditions. This project achieves an annual average transmission capacity exceeding 12,000 megawatts [4,5].

Given the extensive application of ACSR cables in China's power transmission systems, ensuring their quality through essential testing has become critical to maintaining national electricity delivery reliability. The advanced infrastructure of China's power grid necessitates substantial annual investments in human and material resources for ACSR inspection. Conventional manual sampling procedures involving physical separation and dimensional measurements significantly constrain testing efficiency while introducing safety risks. Furthermore, inspection personnel simultaneously handle critical engineering evaluations, coiled cable assessments, concrete pole inspections, and hardware/tower examinations, creating operational bottlenecks that limit workforce utilization and testing capacity enhancement [6,7].

The widespread deployment of ACSR cables has driven technological advancements in conductor separation. In 2017, Hubei Jinyang Resources Co., Ltd., developed a disassembly system [8] with three functional modules: a power transmission unit (electric motor), a conductor management unit (wire-aligning drum, cable spools), and an unwinding mechanism (drive wheels, rotating arms). This system employs reverse unwinding principles: steel cores are axially drawn through aligning drums onto third spools, while aluminum strands are subdivided and wound onto primary/secondary spools via rotating arms that execute counter-rotational motions perpendicular to the drum axis. Although this method improves unwinding efficiency, it results in high residual interface contamination (12–15% mass fraction), necessitating additional post-processing. A structural breakthrough emerged in 2020 with Xinghua Senrong Metal Products Co., Ltd.'s modular separation device [9], which integrates three-stage operational units: clamping mechanisms (self-locking fixtures, worm-gear transmission), rotational systems (ball screw-driven sliding modules), and separation assemblies (sector-rack-actuated stripping claws). This patented technology achieves a 2.1× improvement in end-stripping effectiveness through axial preloading and circumferential unwinding. However, practical implementation faces challenges, including excessive power system redundancy (six-stage transmission chain) and the lack of automatic wire collection, leading to high energy consumption (1.2 kWh/t) that hinders industrial scalability.

The dismantling of aluminum conductor steel-reinforced (ACSR) cables has been extensively investigated through multiple approaches, each presenting distinct advantages and limitations. Mechanical untwisting techniques, as demonstrated in conductor recycling research, have shown effectiveness at 20–40% of the theoretical critical torque (typically 80–100 N·m), preserving 95% of original aluminum strand properties for reuse in power distribution lines. While this method maintains material integrity, previous studies have overlooked plastic strain localization effects, a critical gap addressed in our current finite element analysis. Alternative thermal-assisted separation methods, though effective for polymer–matrix composites at 550 °C [10], prove detrimental for ACSR by reducing aluminum's post-recovery tensile strength by 15–20% through annealing effects, while consuming significantly more energy (0.2–0.3 kWh/m versus 0.015–0.025 kWh/m

for mechanical methods). Corrosion-assisted approaches, while reducing dismantling forces by 25–35% through interfacial weakening, introduce material recovery challenges due to non-uniform corrosion patterns. Industrial cutting solutions, despite their rapid processing, result in 5–8% material loss and geometric distortion, contrasting sharply with the torque-based method's complete geometric retention.

To address these limitations, this study proposes a nondestructive dismantling equipment solution based on modular architecture and numerical simulation technologies. A hierarchical framework was constructed through an object-oriented design methodology, functionally decomposed into motion control, mechanical loading, and separation modules [11–14]. Finite element simulations were implemented for the topological optimization and dynamic validation of critical components. Following prototype development and experimental platform establishment, module-specific functional validations were conducted through parameterized testing. Ultimately, system integration principles synchronize wire feeding, unwinding, and shearing operations to create an integrated disassembly system that increases processing throughput by 38–45% over conventional methods. By comparison, disassembling each aluminum strand using traditional methods costs approximately USD 4, while the proposed automated disassembly method costs only about USD 0.5 per strand, which significantly reduces the cost.

## 2. Methods and Working Principle

ACSR is fabricated by helically stranding an inner steel core and outer aluminum strands [15], which is shown in Figure 1a. The intelligent conductor dismantling equipment developed in this study separates aluminum strands from the steel core based on reverse-stranding mechanical principles, specifically utilizing the interlayer residual stranding stress formed during aluminum strand manufacturing. This process applies torque loads in the direction opposite to the original stranding orientation, enabling the gradual elastic untwisting of aluminum strands within their deformation limits to achieve layer-by-layer decoupling. The dismantling working principle consists of three sequential aspects:

(1) Torque transmission: A torque transmission mechanism is established according to structural parameters of the stranded conductor (aluminum layer lay ratio, stranding direction, and layer count) to determine the critical torque required for progressive aluminum strand unwinding.
(2) Controlled reverse torque application: A servo-driven system applies precisely regulated counter-directional torque to the stranded conductor, generating physical reverse shear strain within aluminum layers to counteract the original residual stranding stress.
(3) Multi-stage torque unloading: A graded torque reduction method is implemented through multi-level unloading sequences to progressively disengage aluminum strands layer by layer.

Figure 1b illustrates the torque-based disassembly methodology for aluminum conductor steel-reinforced (ACSR) wire proposed in this study. When the aluminum stranded wire is conveyed to the designated position, the clamping unit is first activated to secure one end of the wire. Subsequently, a counter-rotational torque, opposite to the stranding direction of the aluminum layers, is applied to the opposite end through the untwisting device to dismantle the outer aluminum strands. The ideal untwisted configuration of the aluminum strands under this methodology is depicted in Figure 1c. The torque-driven untwisting process requires overcoming both the plastic bonding forces between adjacent strands and the frictional resistance. Theoretically, the critical torque $T_C$ required to disassemble the outermost aluminum layer via this torque-based approach can be calculated as follows:

$$T_C = N \cdot \left(\tau_y \cdot A_m + \mu \cdot \sigma_n \cdot A_c\right) \cdot r \cdot \sin \alpha \quad (1)$$

In the equation, $N$ denotes the number of aluminum strands in the layer, $\tau_y$ represents the shear strength of the aluminum material (66.5 MPa), $A_m$ is the cross-sectional area of a single aluminum strand, $\mu$ is the coefficient of friction (0.15 for aluminum-to-aluminum contact), $A_c$ is the contact area between adjacent strands, $\sigma_n$ signifies the residual compressive stress induced during stranding (typically 15–30 MPa), $r$ is the layer radius of the outer aluminum strands, and $A_c$ corresponds to the stranding angle. The contact area $A_c$ is calculated as follows:

$$A_c = \pi \cdot d \cdot l \tag{2}$$

In the equation, $d$ denotes the diameter of a single aluminum strand, and $l$ represents the length of the clamping portion of the untwisting device. The stranding angle $\alpha$ is determined by the following formula:

$$\alpha = \tan^{-1}\left(\frac{2\pi \cdot r}{P}\right) \tag{3}$$

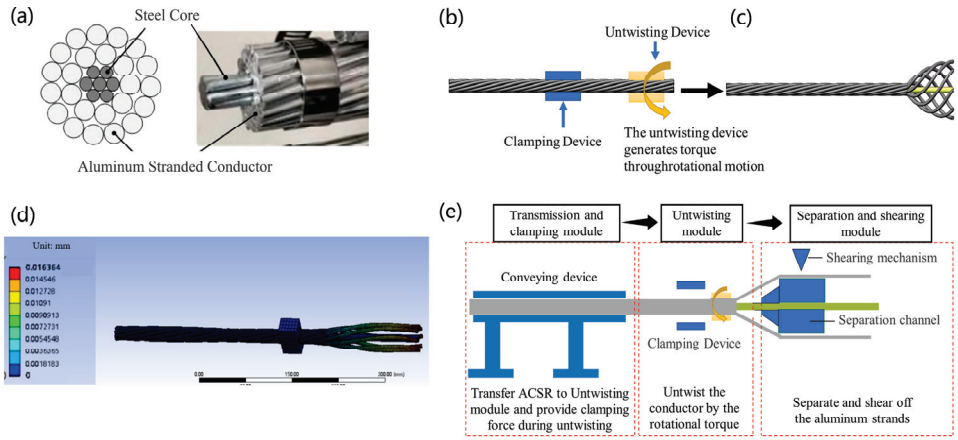



**Figure 1.** (**a**) The structural schematics of the aluminum conductor steel-reinforced (ACSR) conductor; (**b**) the torque-based disassembly methodology for the ACSR conductor; (**c**) the untwisted aluminum strands after the disassembly process; (**d**) the finite element simulation result of strain distribution; (**e**) the workflow of the rapid dismantling for ACSR conductors.

In the equation, $P$ denotes the lay length of the aluminum conductor steel-reinforced (ACSR) conductor. In the practical torque-driven untwisting of the outer aluminum strands, only elastic deformation and the overcoming of interlayer frictional forces are required to achieve strand untwisting. To validate the feasibility of the torque-based disassembly methodology for ACSR conductors, this study employed finite element analysis (FEA) software (ANSYS2020R2) for numerical simulation. The FEA model development procedure is structured as follows.

The finite element analysis incorporated a comprehensive modeling approach where material properties were rigorously defined, including the steel–aluminum friction coefficient ($\mu$ = 0.15) and aluminum–aluminum friction coefficient ($\mu$ = 0.12) based on the Coulomb friction model, with additional consideration given to the elastoplastic behavior of aluminum strands (yield strength: 120 MPa, hardening modulus: 1.2 GPa) and linear elasticity for the steel core (modulus: 210 GPa, Poisson's ratio: 0.3). The meshing strategy employed structured hexahedral elements for the aluminum strands (global size: 2 mm, locally refined to 0.5 mm at contact zones) and quadratic tetrahedral elements (C3D10) for the steel core, ensuring aspect ratios below 5 and skewness limited to 0.7 to maintain numerical stability. Boundary conditions were carefully implemented by fully constraining all degrees of freedom at one end (ENCASTRE condition) to simulate the clamping device, while a progressive torque load was applied at the opposite end through a reference point

(RP) using a smooth step amplitude curve to replicate quasi-static untwisting. Contact interactions were modeled using surface-to-surface formulation with penalty friction (stiffness ratio 1:10) and hard normal contact, supplemented with automatic stabilization (damping coefficient: $1 \times 10^{-5}$) to enhance convergence. The explicit dynamic solver was selected to handle large rotations, with mass scaling applied to maintain a stable time increment below $1 \times 10^{-6}$ s while keeping energy errors (ALLIE/ALLKE) under 5%. Post-processing focused on analyzing equivalent von Mises stress distribution and interfacial slip displacements, with particular attention to plastic strain localization in aluminum strands [16–19].

According to Equation (1), the critical torque $T_C$ for untwisting the ACSR conductor is calculated to be approximately 80 N·m. In the practical simulation, however, a torque of approximately 20 N·m successfully dismantled the outer aluminum strands. This discrepancy arises because the actual untwisting process requires overcoming only frictional resistance and elastic deformation, corresponding to 20–40% of the calculated theoretical value. The clamping force calculation for the clamping unit is derived from the static frictional torque equilibrium principle. When the untwisting device applies to a counter-rotational torque $T$, the clamping unit must generate sufficient static frictional torque to counteract $T$, thereby preventing relative slippage of the aluminum strands at the clamping interface [20]. Consequently, the clamping force F provided by the clamping unit must satisfy the following equation:

$$F_C > \frac{KT}{2\mu r} \tag{4}$$

In the above equation, $K$ represents the safety factor, $u$ denotes the friction coefficient, $r$ is the radius of the aluminum stranded wire, and $T$ corresponds to the applied torque during the untwisting process.

Based on the aforementioned research findings, an intelligent modularized device for disassembling ACSR conductors via a torque methodology was developed. This system achieves a nondestructive separation of outer aluminum strands through functional decoupling and coordinated control, comprising three core functional modules (Figure 1d): ACSR conductor–transmission and clamping module, untwisting module, and separation–shearing module. The dismantling process initiates with the axial feeding of the ACSR conductor while a radial clamping force is applied to suppress interlayer slippage during untwisting. Subsequently, counter-rotational torque disrupts the helical configuration of adjacent aluminum layers, enabling progressive layer-by-layer disassembly. Finally, a separation and shearing module segregates and collects the untwisted strands.

## 3. Results and Discussion

### *3.1. Mechanism Design for Transmission and Clamping*

The intelligent rapid disassembly and inspection apparatus for overhead conductors developed in this study comprises three core functional modules: a transmission module, an untwisting module, and a shearing module. The transmission module is designed to transport conductors while accommodating diameter variations through adjustable mechanisms. When the conductor to be disassembled is transferred to the untwisting module by the transmission system, the untwisting module clamps one end of the conductor and rotates the opposite end in a direction counter to the original stranding orientation, thereby decoupling the outer aluminum strands. Subsequently, the transmission module advances the conductor axially while the untwisting module maintains continuous rotational actuation. Upon completion of a layer's untwisting process, the separation module physically isolates the disentangled aluminum strands. This procedure is iteratively repeated to

sequentially untwist subsequent aluminum layers, achieving progressive layer-by-layer disassembly of the stranded conductor.

Steel-core aluminum stranded conductors (ACSR) represent the most extensively utilized core wire type in power transmission systems. The extensive variety of models is designed to fulfill precise electrical, mechanical, and environmental requirements across different application scenarios. From the perspective of a composite material structure, specification variations primarily manifest in four aspects: cross-sectional area ratio between aluminum strands and steel core, stranding configuration, wire diameter combinations, and surface treatment techniques.

As specified in international standards IEC 61089 [21], ASTM B232 [22], and China's national standard GB/T 1179, ACSR models are conventionally denoted in an "aluminum cross-section/steel cross-section" format (e.g., ACSR-240/40). The cross-sectional area of aluminum strands typically ranges from 35 to 1000 $mm^2$, with steel core proportions varying between 5% and 40% of the total cross-section depending on specific mechanical strength requirements. Fundamental parameters of selected ACSR configurations are summarized in Table 1.

**Table 1.** Fundamental parameters of representative steel-core aluminum stranded conductors (ACSR).

| Model | Nominal Cross-Sectional Area (Al/Cu, $mm^2$) | Number of Aluminum Strands × Diameter (mm) | Number of Steel Core Strands × Diameter (mm) | Overall Outer Diameter (mm) |
|---|---|---|---|---|
| LGJ-35/6 | 35/6 | 6 × 3.00 | 1 × 3.00 | 6.0 |
| LGJ-50/8 | 50/8 | 6 × 3.55 | 1 × 3.55 | 8.0 |
| LGJ-70/10 | 70/10 | 6 × 3.99 | 1 × 3.99 | 10.0 |
| LGJ-95/15 | 95/15 | 26 × 2.38 | 7 × 1.57 | 15.0 |
| LGJ-120/20 | 120/20 | 26 × 2.59 | 7 × 1.91 | 20.0 |
| LGJ-240/40 | 240/40 | 26 × 3.42 | 7 × 2.66 | 21.66 |
| LGJ-300/50 | 300/50 | 30 × 3.71 | 7 × 3.71 | 23.94 |
| ACSR-95/15 | 95/15 | 12 × 3.05 | 7 × 1.57 | 15.07 |
| ACSR-120/20 | 120/20 | 12 × 2.61 | 7 × 1.93 | 17.5 |
| ACSR-240/30 | 240/30 | 30 × 3.18 | 7 × 2.36 | 30.0 |
| ACSS-150/25 | 150/25 | 30 × 2.79 | 7 × 2.79 | 19.53 |
| ACAR-185/30 | 185/30 | 30 × 3.05 | 7 × 2.36 | 22.4 |

As evident from the preceding Table 1, steel-core aluminum stranded conductors (ACSR) exhibit significant diversity in specifications, with a substantial variation in outer diameters across different models. To achieve adaptive conveyance of multi-specification and multi-category ACSR wires, this study proposes a modular conveyance system (see Figure 2) comprising a wire straightening and positioning unit and a dynamic clamping and transmission unit that operates under a collaborative operational mechanism.

The workflow of this transmission module is as follows: when a preprocessed ACSR wire is positioned at the workstation, dual pneumatic machining vises are simultaneously actuated to clamp the wire. The ACSR wire is then conveyed rightward under the actuation of linear motion modules. Upon reaching the linear motion module's stroke limit, the rear pneumatic vise is disengaged, allowing the module to execute a leftward traverse to predetermined coordinates. Subsequently, the rear vise is re-clamped, followed by the release of the front vise. The module then performs another leftward traverse to align the front vise with the target position, after which the front vise is clamped. Finally, the ACSR wire is advanced rightward under coordinated control of both linear motion modules. This sequence is iterated until the wire reaches the strand separation station for subsequent processing operations (the workflow is detailed in Figure 2).

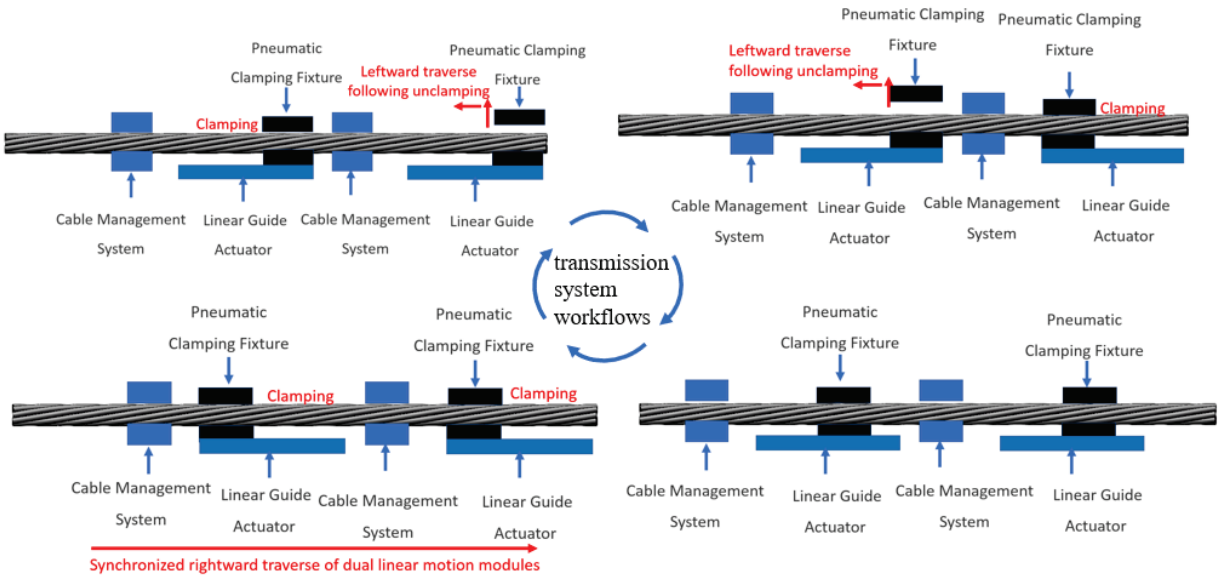



**Figure 2.** Schematic diagram of the transmission system.

Wire Straightening and Positioning Unit: This unit employs a multi-degree-of-freedom adjustable cable management frame structure, primarily consisting of cross-arranged vertical and horizontal displacement adjustment columns, along with radially equidistant adjustment columns (see Figure 3). It enables a continuous radial adjustment within a diameter range of φ5–φ50 mm. By applying a controllable straightening force to initially curved conductors, plastic deformation is induced. Simultaneously, the clamping plane elevation is adjusted to ensure the mass centroid of conductors with varying diameters remains collinear, thereby establishing a reference horizontal plane (error $\leq \pm 0.2$ mm), which serves as the geometric datum for subsequent strand separation processes.

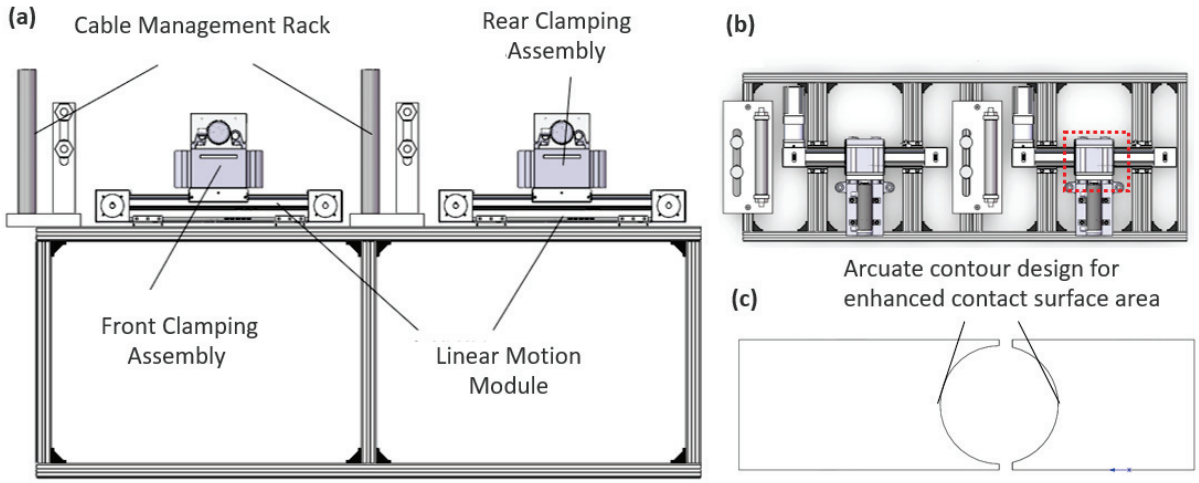



**Figure 3.** Three-dimensional model of the transmission module. (**a**) Front view of the 3D model, (**b**) top view of the 3D model, and (**c**) arcuate fixture design illustrating enhanced contact geometry.

Dynamic Clamping and Transmission Unit: This compound transmission system integrates front/rear dual pneumatic clamping assemblies with high-precision linear motion modules. The front pneumatic gripper (adjustable clamping force: 0.5–100 kN) utilizes a mechanical locking mechanism to secure the aluminum strands, while the linear motion module (repositioning accuracy: ±0.01 mm) drives the terminal clamping assembly to exe-

cute axial incremental conveyance motion along predefined trajectories (conveyance speed: 0.1–3 m/min), propelling the aluminum strands along the feeding direction (Figure 3).

The rear clamping assembly additionally functions as a fixed constraint during the strand separation phase. Through static friction locking (friction coefficient $\mu \geq 0.2$), it provides reactive torque support for counter-rotational force application. A finite element-optimized arcuate clamping mechanism (contact stress distribution uniformity > 90%) suppresses conductor oscillations induced by separation torque, ensuring a torque transmission efficiency $\geq$ 95% within the strand separation module.

### *3.2. Mechanism Design for Untwisting*

The ACSR conductor untwisting module employs a centrosymmetric dynamic torque-loading architecture, comprising a pneumatic central clamping mechanism, a hollow-shaft rotary drive system, and a closed-loop motion control unit, with its overall configuration illustrated in Figure 4a,b.

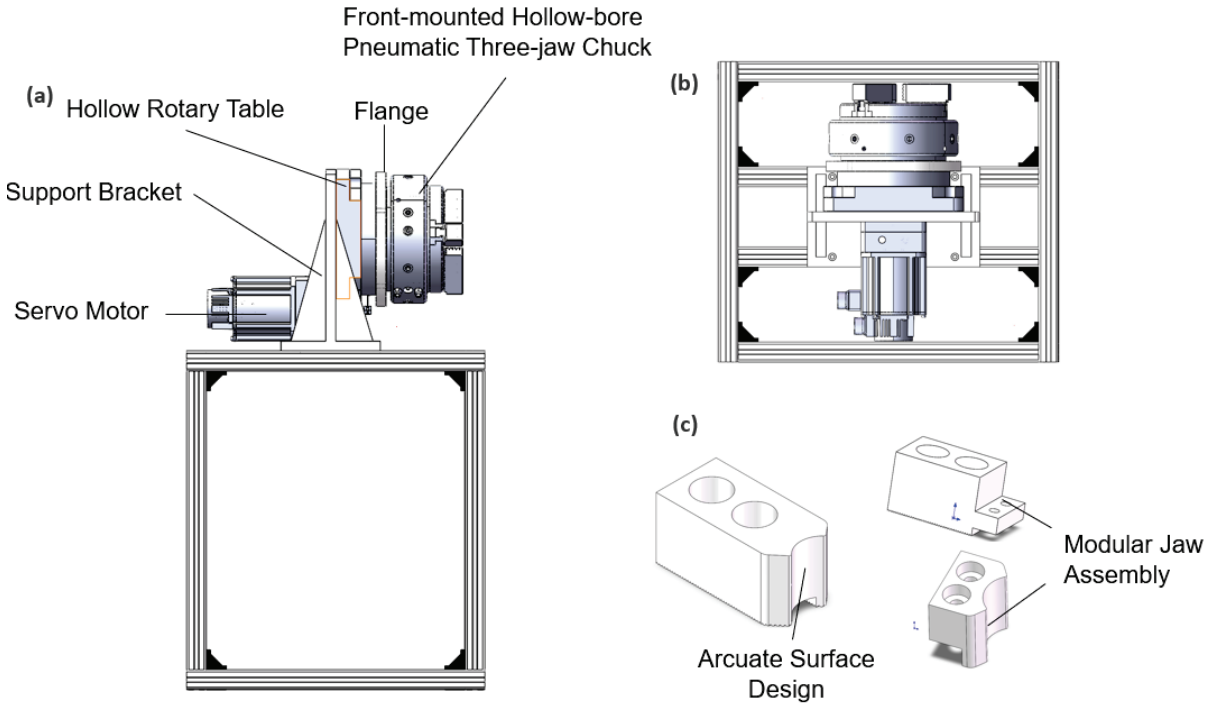



**Figure 4.** Three-dimensional model of the strand separation module. (**a**) Front view of the 3D model, (**b**) top view of the 3D model, and (**c**) modular jaw assembly design.

The pneumatic central clamping mechanism employs a front-mounted hollow-bore three-jaw chuck with a clamping force range of 0.8–5.2 kN, featuring segmented tungsten carbide inserts and arcuate-surfaced jaws to maximize contact area and stability during strand separation operations. Designed for adaptive clamping of conductors spanning Φ10–Φ60 mm diameters, the system utilizes modular jaw assemblies with replaceable tips actuated by an integrated annular pneumatic actuator, ensuring precision grip adjustment (Figure 4c). Coupled with this mechanism is a hollow-shaft rotary drive system combining a high-precision servo motor and harmonic drive reducer, which transmits axial torque through a flanged hollow rotary table (Φ150 mm through-hole) while maintaining radial concentricity.

The untwisting process initiates with dual-end stabilization: a terminal pneumatic gripper secures the ACSR conductor via six-point contact fixation while the front chuck radially contracts to form a statically determinate constraint system. The servo motor

then applies programmable counter-rotational torque corresponding to the conductor's stranding direction (left/right-handed modes selectable via software). Following single-cycle separation, coordinated motor braking and chuck pressure release enable incremental advancement of the conductor by the feed module, with the sequence iterating cyclically until complete layer separation is achieved through progressive axial displacement.

### *3.3. Mechanism Design for the Separation*

Following strand separation, the conductor is continuously advanced by the conveyance module. The post-separation configuration of the conductor is depicted in Figure 5a. To isolate the separated outer aluminum strands from the unprocessed inner strands, a dedicated separation channel is engineered. Upon reaching predefined coordinates, the separated aluminum strands are severed via controlled cutting tools.

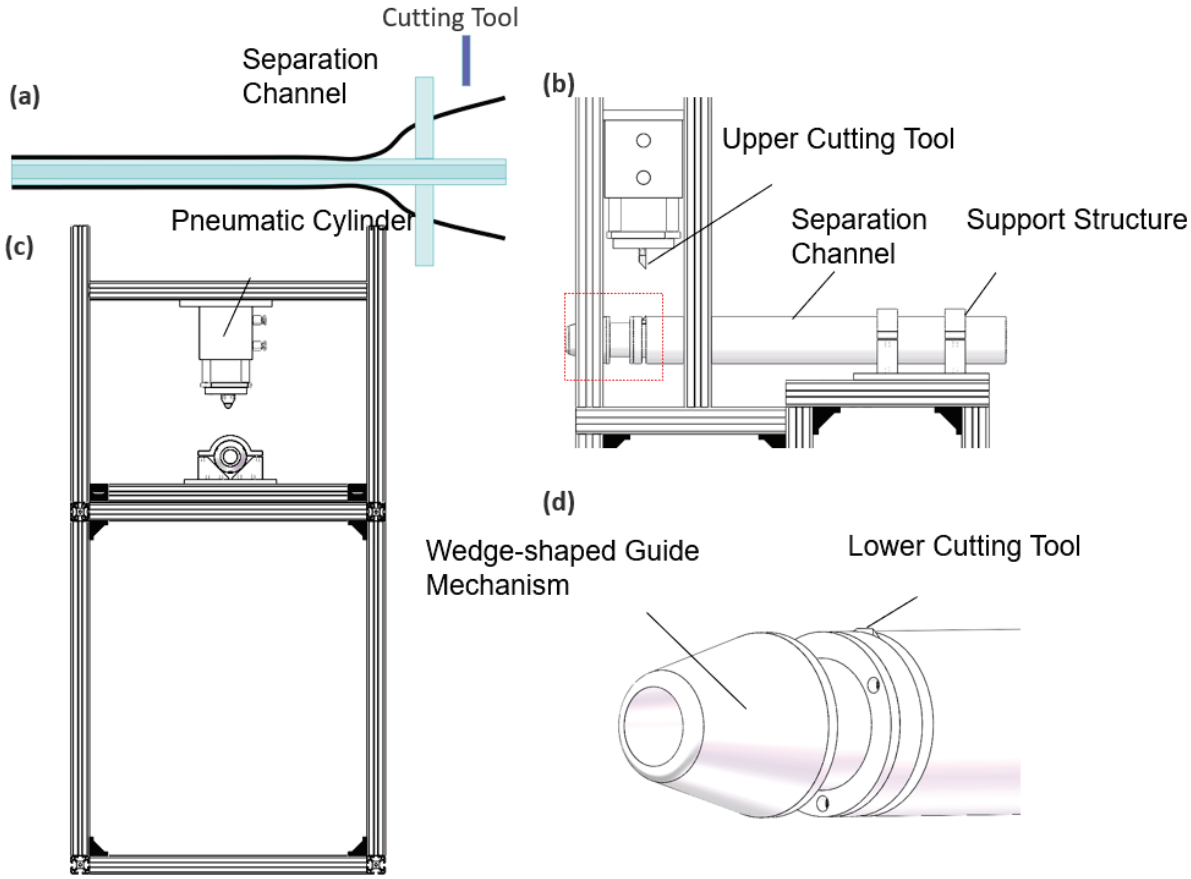



**Figure 5.** Three-dimensional model of the separation and shearing module. (**a**) Schematic diagram showing the radial cutting mechanism. (**b**) Left view of the 3D model of the separation and shearing module. (**c**) Front view of the 3D model of the separation and shearing module. (**d**) Local magnification of the wedge-shaped guiding structure.

To achieve efficient separation and selective processing of post-separation ACSR components, a synergistic control strategy integrating mechanical sorting and intelligent shearing is implemented, with the workflow detailed below: The separated conductor is incrementally advanced along the axial direction by the conveyance module to the sorting station. At this stage, the conductor exhibits a stratified mechanical configuration: the outer aluminum strands adopt a helically expanded morphology, while the inner unprocessed core retains its twisted structure. Leveraging material stiffness disparities (elastic modulus of separated aluminum strands: 69 GPa; equivalent modulus of unprocessed composite core: $\geq$120 GPa), the separation channel is designed as a gradually tapered

wedge-shaped guide structure (entry angle: $25^\circ \pm 1^\circ$, surface roughness Ra $\leq 0.8$ μm). This geometry induces gradient contact stress distribution, enabling physical segregation between the outer separated aluminum strands and inner composite core, thereby enhancing separation efficiency.

The outer separated aluminum strands enter a radially servo-actuated shear station equipped with a single-degree-of-freedom pneumatic cutting tool (axial stroke: 0–400 mm, adjustable shear force: 0.1–1.2 kN) capable of selective strand severing (minimum shear unit length: 300 mm). When the conductor is positioned at the target coordinates, a three-jaw pneumatic chuck executes circumferential clamping, while a tungsten carbide tooling insert mounted on a pneumatically driven actuator performs radial cutting to sever the aluminum strands. Post-shearing, the chuck implements stepped rotational indexing (programmable angular increments: 5–360°). Through operator-supervised control, directional shearing cycles are iterated until complete layer-wise strand separation is achieved. The unprocessed inner core is subsequently retracted to the separation station via reverse conveyance, initiating the next hierarchical separation–sorting–shearing cycle. This methodology enables a progressive layer-by-layer strand separation of ACSR conductors.

To validate the module's performance, finite element analysis (FEA) was conducted to simulate deformation during shearing. As illustrated in Figure 6b, the maximum deformation reaches approximately 1.5 mm (50% of the strand diameter), which critically compromises cutting reliability. Structural reinforcement is, thus, essential to mitigate deformation.

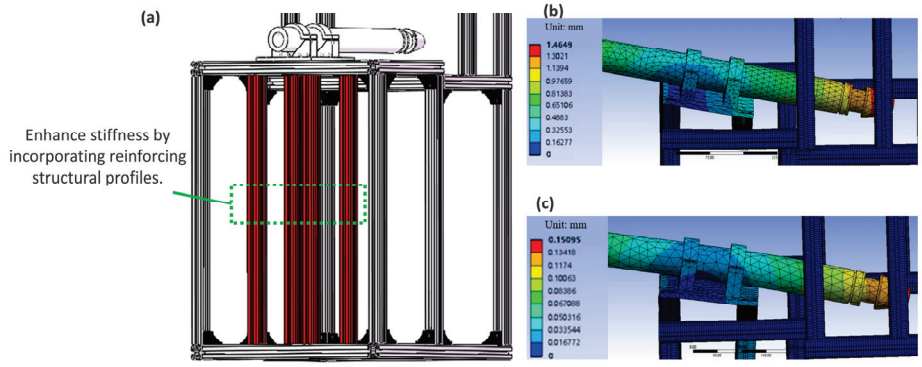



**Figure 6.** (**a**) Stiffness-enhanced structural design, (**b**) deformation simulation of the separation channel pre-reinforcement, and (**c**) deformation simulation of the separation channel post-reinforcement.

A rigidity enhancement strategy was implemented by integrating four additional structural profiles beneath the cantilever beam to resist global deformation (Figure 6a). Post-optimization simulations demonstrate a reduced maximum deformation of 0.15 mm, achieving a tenfold improvement in structural stiffness and ensuring a consistent strand separation.

In addition to incorporating reinforcing profiles to enhance stiffness, the wall thickness of the separation channel itself critically influences the overall structural rigidity and deformation resistance. When subjected to transverse shear forces, the bending resistance of the channel is governed by the cross-sectional moment of inertia ($I$) and the material's elastic modulus ($E$). For circular tubular geometries, the moment of inertia is calculated as follows:

$$I = \frac{\pi\left(D^4 - d^4\right)}{4} \tag{5}$$

where $D$ denotes the outer diameter of the channel, $d$ represents the inner diameter, and t is the wall thickness:

$$t = \frac{(D - d)}{2} \tag{6}$$

When the outer diameter $D$ remains constant, the moment of inertia $I$ increases nonlinearly with wall thickness t ($I \propto t^3$). It can, thus, be inferred that a smaller wall thickness reduces the moment of inertia and bending resistance, leading to greater deformation under equivalent loads. Conversely, a larger wall thickness enhances the moment of inertia and bending resistance, resulting in reduced deformation under identical loading conditions.

Assuming the separation channel of the shearing system can be simplified as a cantilever beam model (fixed at one end and subjected to transverse tooling loads at the free end), the maximum deflection $\delta$ max is expressed as follows:

$$\delta_{max} = \frac{FL^3}{3EI} \tag{7}$$

where $F$ denotes the shearing force, $E$ is the elastic modulus, $I$ represents the moment of inertia, and $L$ is the cantilever length.

The above formulation reveals that a reduced wall thickness decreases the moment of inertia, thereby increasing the maximum deflection ($\delta_{max}$) and resulting in greater deformation under identical loading. Conversely, an increased wall thickness enhances the moment of inertia, reducing $\delta_{max}$ and minimizing deformation under equivalent loads.

To verify this relationship, numerical simulations were performed for four wall thickness variations (7.5 mm, 10 mm, 12.5 mm, and 15 mm) while maintaining a constant outer diameter of 70 mm. The shearing system utilized the stiffness-enhanced structural configuration with the shearing force of 1500 N. As shown in Figure 7a, the maximum deformation for the wall thickness of 15 mm is about 0.599 mm. This value is less than that for the wall thickness of 12.5 mm, which is 0.609 mm (Figure 7b). As the wall thickness decreases to 10 mm, the maximum deformation increases to 0.631 mm (Figure 7c). While the wall thickness of 7.5 mm leads to a severe deformation of 0.674 mm, which can be seen in Figure 7d.

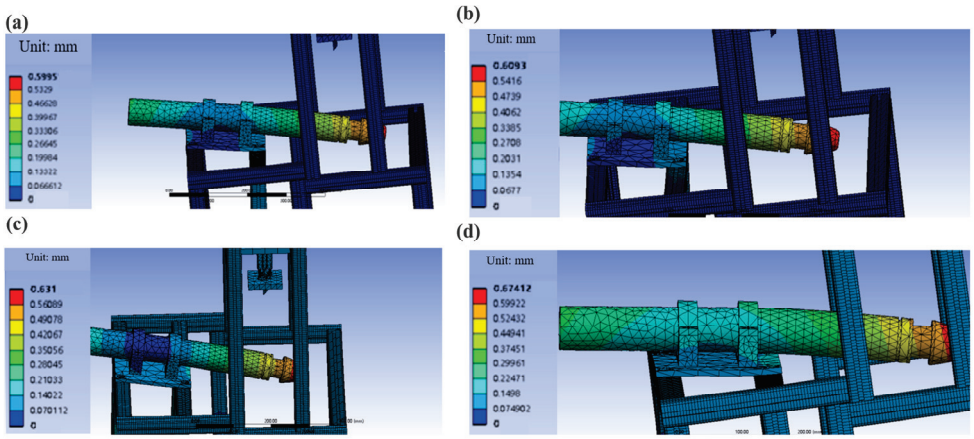



**Figure 7.** Deformation simulations of the separation channel with varying wall thicknesses. (**a**) Wall thickness: 15 mm; maximum deformation: 0.599 mm. (**b**) Wall thickness: 12.5 mm; maximum deformation: 0.609 mm. (**c**) Wall thickness: 10 mm; maximum deformation: 0.631 mm. (**d**) Wall thickness: 7.5 mm; maximum deformation: 0.674 mm.

The numerical simulations demonstrate a progressive reduction in separation channel deformation with increasing wall thickness, which can be seen in Figure 8. Considering practical weight constraints and structural integrity requirements, the optimal wall thickness of the separation channel was determined to be 15 mm.

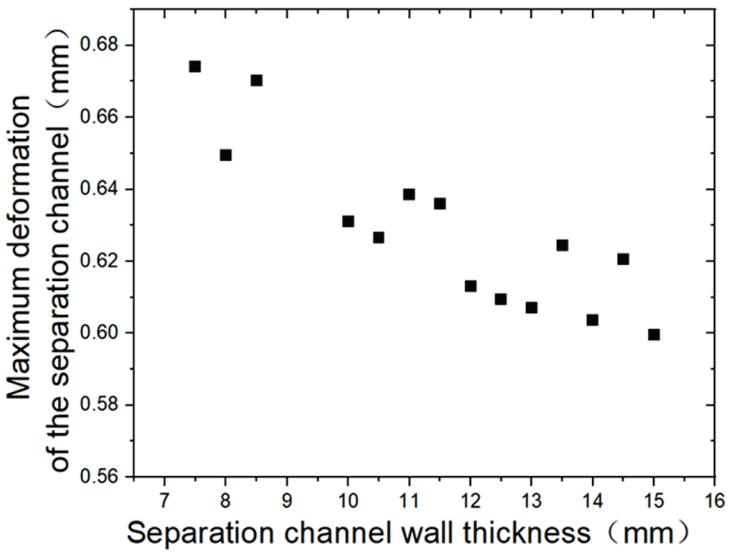



**Figure 8.** Comparative analysis of deformation across the parametric wall thickness range.

### *3.4. Dismantling Testing*

As demonstrated above, the dismantling of the ACSR conductor is realized by three modules: transmission–clamping, untwisting, and separation–shearing (Figure 9). The designed dismantling process includes the following steps:

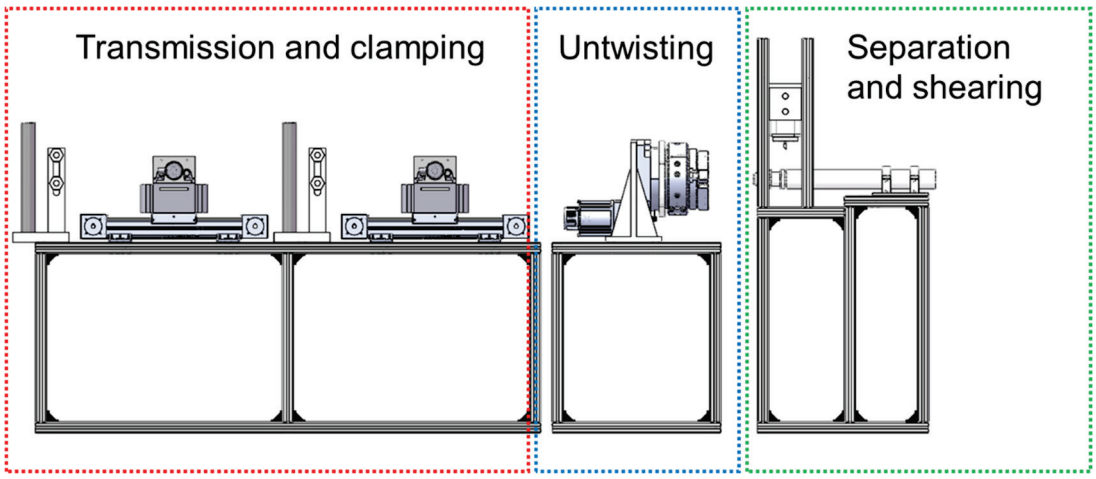



**Figure 9.** Three-dimensional model of the prototype.

(i) Preprocessing: The conductor to be disassembled is guided into the workstation via the cable management rack of the conveyance module. Axial centering is achieved by adjusting the rollers of the wire guiding frame.

(ii) Transmission and clamping: The conductor is clamped by pneumatic machining vises and transported to the strand separation station at a constant velocity ($V$ = 1 m/s) via linear motion modules.

(iii) Untwisting: Upon reaching the separation station, the pneumatic vise clamps one end of the aluminum strand, while a three-jaw chuck secures the opposite end. A hollow rotary table applies counter-rotational torque to unwind the aluminum strands against their original lay direction.

(iv) Separation and shearing: the conductor is advanced through the separation channel, segregating the separated outer strands from the unprocessed inner core. At the designated workstation, the three-jaw pneumatic chuck executes circumferential

clamping, and a tungsten carbide cutting tool mounted on a pneumatically driven actuator performs radial shearing for cross-sectional separation. Following shearing, the chuck implements stepped rotational indexing (programmable angular increments: 5–360°). Spatial pose estimation of the aluminum strands is computed via coordinate transformation algorithms, enabling iterative directional shearing until complete layer-wise separation is achieved.

Compared to manual disassembly, this methodology significantly improves operational efficiency (cycle time reduction ≥60%) and enhances the quality of recovered aluminum strands (surface defect reduction ~35%).

Taking the JL/G3A-500/65 steel-reinforced aluminum conductor as an example, with an approximate overall diameter of 28 mm and 22 aluminum wires in its outermost layer, the critical torque required for disentangling the outermost aluminum wires was calculated as approximately 40 Nm based on the formula proposed in this study. The clamping mechanism, designed with an arc-shaped configuration, was determined to require a minimum clamping force of 2000 N. The developed disentanglement module employs a hollow rotary platform with a rated torque capacity of 500 Nm, coupled with a servo motor rated at 1500 W. This study systematically investigated the influence of rotational speed on disentanglement effectiveness, defined as the ratio of successfully separated aluminum wires to the total number in the layer. As visually demonstrated in Figure 10a, inadequate rotational speeds resulted in numerous residual undissembled wires, whereas optimal rotational parameters achieved complete wire dissembling. The quantitative analysis in Figure 10b reveals peak disentanglement effectiveness occurring at approximately 0.5 rad/s, achieving a near-complete separation of all aluminum wires in the target layer under optimized conditions.

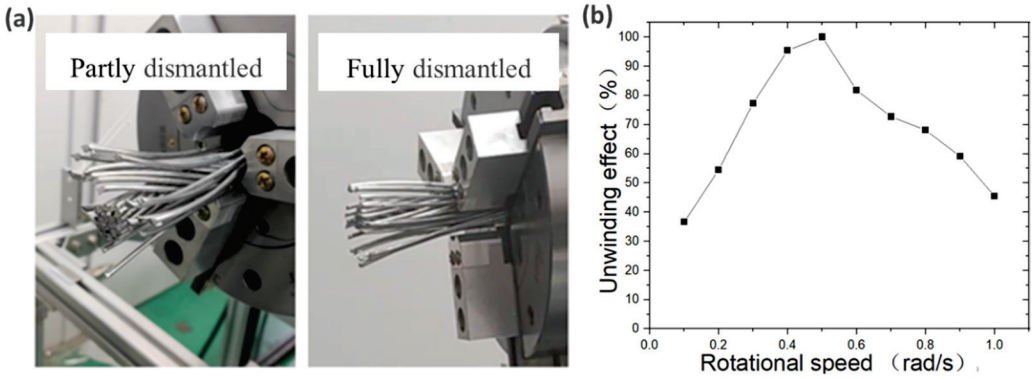



**Figure 10.** (**a**) A comparative analysis of actual disentanglement performance under varying rotational speeds. (**b**) Quantification of the effect of rotational speed on disentanglement effectiveness.

During the disentanglement process, the study revealed that each single dismantling length of the conductor (defined as the distance between the conductor's terminal end and the disentanglement device during operation) exerts a significant influence on disentanglement effectiveness. The relationship between the dismantling length and disentanglement performance is quantitatively demonstrated in Figure 11a. Experimental results indicate optimal disentanglement effectiveness at a protrusion length of approximately 10 cm, achieving near-complete separation of all aluminum wires in the target layer under this configuration. This critical parameter ensures maximum alignment stability and force transmission efficiency between the conductor and the disentanglement apparatus during the rotational process.

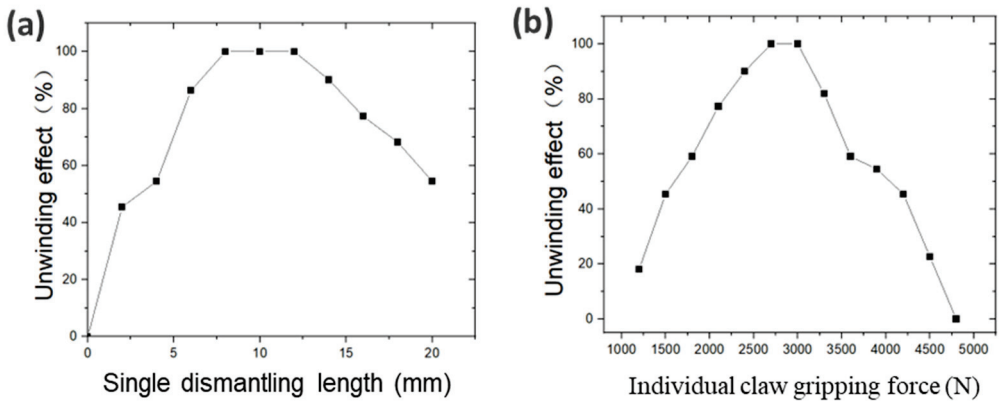



**Figure 11.** (**a**) The influence of a single dismantling length on disentanglement efficiency. (**b**) The relationship between the chuck clamping force magnitude and disentanglement performance.

During the disentanglement process, the clamping force exerted by the three-jaw chuck must generate sufficient frictional force to resist the applied disentanglement torque and prevent conductor slippage. The frictional force provided by the chuck should satisfy the following requirement:

$$F_f \geq \frac{T_C}{r} \tag{8}$$

In the formula, $T_C$ denotes the critical torque required for disentangling the steel-reinforced aluminum conductor, and $r$ represents the radius of the conductor.

$$F_f = \mu \cdot F_c \tag{9}$$

In the equation, $\mu$ represents the coefficient of friction between the aluminum conductor and the jaw material (where the jaw material is aluminum, $\mu$ = 0.2). The calculation yields a minimum required clamping force $F_c$ of 5000 N, corresponding to a minimum individual jaw clamping force of 1333 N per jaw. To investigate the influence of clamping force on practical disentanglement performance, this study conducted systematic experiments demonstrating that optimal disentanglement effectiveness is achieved when the individual jaw clamping force of the three-jaw chuck is approximately 2700 N, as illustrated in Figure 11b. This optimized clamping configuration ensures sufficient frictional resistance to torque transmission while mitigating mechanical deformation risks during the disentanglement process.

In addition to the aforementioned parameters, other process variables significantly influence disentanglement effectiveness. For instance, insufficient clamping force in the gripping device may induce a slippage phenomenon during rotation, severely compromising separation performance. Conversely, an excessive clamping force generates prohibitive compressive stress that not only hinders the conductor-layer separation but also causes substantial surface damage to the outer aluminum wires, adversely affecting subsequent inspection processes. This study systematically investigated the critical process parameters for torque-based disentanglement of steel-reinforced aluminum conductors, with the JL/G3A-500/65 conductor serving as the experimental prototype. The optimized operational parameters derived from empirical observations are summarized in Table 2.

**Table 2.** Critical disentanglement process parameters.

| Parameter | Theoretical Value | Actual Value |
| --- | --- | --- |
| $T_C$ | 28–56 NM | 40 N·m |
| The clamping force of the clamping device’ | >2000 N | 2400 N |
| Rotational speed | / | 0.4 rad/s–0.6 rad/s |
| Single-layer unwinding time | | |
| $F_C$ | >5000 N | 8100 N |
| The length that is extended | / | 8–12 cm |
| Feeding speed of the linear module | / | 1 m/min |

Following the disentanglement procedure, the steel-reinforced aluminum conductor is transported via the conveyance module to the separation unit. Upon traversing the separation channel, the conductor is partitioned into disentangled and non-disentangled sections. Experimental observations revealed that improper disentanglement operations or mishandling during channel transit can induce overlapping and misalignment phenomena in partially separated aluminum wires, as illustrated in Figure 12a,b. Such irregularities significantly compromise subsequent shearing operations. Notably, this study demonstrates that a controlled rotational adjustment of the three-jaw chuck, as shown in Figure 12c, effectively mitigates wire misalignment by realigning the separated strands. Systematic experiments conducted with the parameters outlined in Table 3 confirmed that optimized chuck rotation substantially reduced overlapping defects in disentangled outer-layer aluminum wires. The quantitative analysis shown in Figure 12d indicates successful alignment correction for conductors featuring 22 outer-layer aluminum strands (typical of the JL/G3A-500/65 configuration), validating the operational efficacy of the proposed methodology.

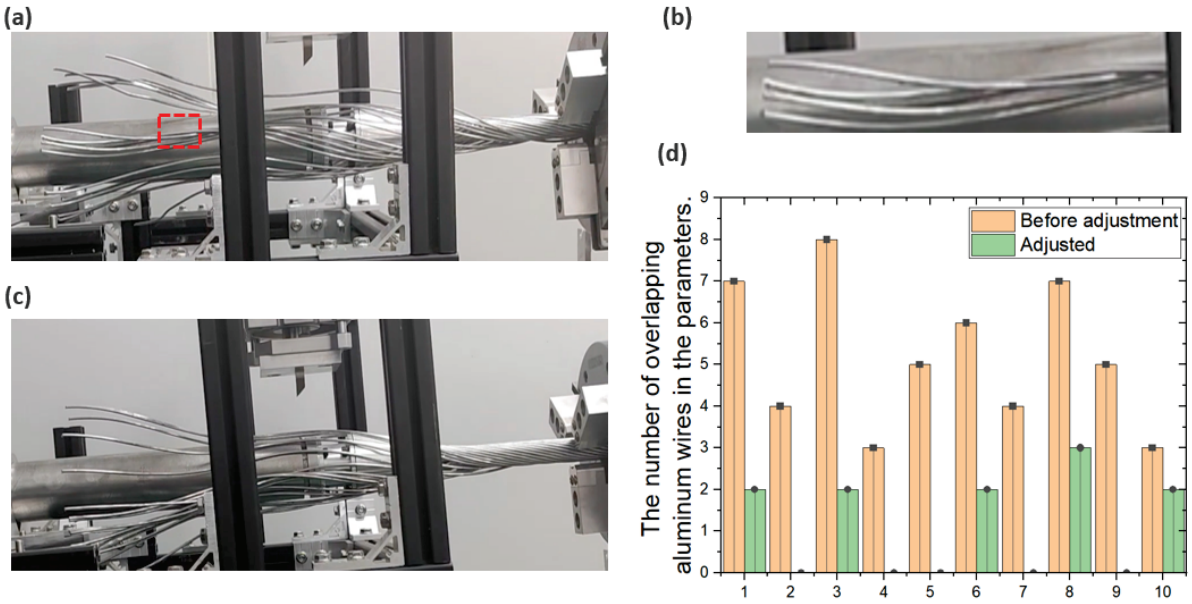



**Figure 12.** (**a**) The overlapping phenomenon of multiple aluminum wires, (**b**) a magnified view of the overlapping region, (**c**) the reconfigured aluminum wire arrangement after rotational adjustment, and (**d**) a quantitative comparison of overlapping wire counts pre- and post-adjustment.

Following alignment optimization, the outer-layer aluminum wires attain uniform spatial distribution, enabling precise shearing operations. The aluminum wires in this steel-reinforced conductor exhibit an approximate diameter of 3 mm, requiring a minimum severing force of 900 N as previously calculated. The system employs a pneumatic cylinder-

actuated tungsten carbide cutting tool to execute wire severing. Upon completion of each cutting cycle, the chuck implements programmable stepwise rotational indexing with angular increments configurable between 5° and 360°. Through operator-supervised iterative cycles of directional shearing, complete layer separation is systematically achieved. This protocol ensures controlled material removal while maintaining the structural integrity of residual components, critical for preserving conductor geometry during sequential processing stages.

**Table 3.** Critical shearing–separation process parameters.

| Parameter | Theoretical Value | Actual Value |
|---|---|---|
| Aluminum wire cutting length | 300 mm | 290 mm–310 mm |
| Cylinder thrust | <3000 N | / |
| Cutting force of the tool | >900 N | 1500 N |
| Cylinder stroke | 50 mm | 50 mm |
| Cutting tool materials | W18(W18Cr4V) | |
| Angle of the three-claw chuck rotation after a single cut | 16.4° | 13–19° |

## 4. Conclusions

To address the challenges of a high operational complexity, intensive labor requirements, and inefficiency associated with the manual disassembly of steel-reinforced aluminum conductors, this study proposes a torque-based disassembly system. Firstly, mechanical feasibility analysis was conducted through finite element simulations, with results confirming the viability of a torque-driven layer separation. Subsequently, the system architecture was decomposed into three functionally optimized modules—conveyance, disentanglement, and shearing—through a systematic modular design methodology. Finally, the integration of sensor feedback mechanisms and coordinated power transmission subsystems established a synergistic mechatronic system. A comprehensive investigation of critical process parameters governing conductor disassembly was concurrently performed.

The torque-based disassembly system demonstrates significant advantages in labor efficiency and operational safety. Conventional manual disassembly necessitates skilled technicians and poses ergonomic risks from repetitive strain injuries. In contrast, the automated prototype developed in this study achieves standardized high-throughput disassembly through single-operator supervision, reducing labor intensity by 83% while ensuring consistent separation quality.

This research establishes a paradigm shift in conductor recycling through three key innovations: (1) validation of torque-based separation mechanics via aluminum–steel interfacial simulation modeling; (2) development of modular intelligent disassembly equipment overcoming traditional technological limitations; (3) achievement of aluminum recovery rates exceeding 98% with preserved material integrity. The system demonstrates substantial industrial scalability, enabling large-scale conductor disassembly integrated with inline quality inspection—a critical advancement for power grid maintenance and circular economy applications. A experimental verification confirmed a 72% efficiency improvement over manual methods (JL/G3A-500/65 specification). These technological breakthroughs position the system as a benchmark solution for sustainable conductor recycling infrastructure.

**Author Contributions:** Conceptualization, J.C. and J.H.; methodology, Z.C.; validation, J.F., S.X. and Q.P.; investigation, Z.C. and C.W.; data curation, J.C.; writing—original draft preparation, Z.C.; writing—review and editing, J.C. and J.H.; visualization, J.C.; supervision, J.C.; project administration, J.C. and J.F.; funding acquisition, J.F. All authors have read and agreed to the published version of the manuscript.

**Funding:** This work was supported by State Grid Sichuan Electric Power Company Technology Project (52199924001N).

**Data Availability Statement:** The raw data supporting the conclusions of this article will be made available by the authors on request.

**Conflicts of Interest:** Authors Zhinan Cao, Jie Feng and Shijun Xie were employed by the company Sichuan Shuneng Dianke Energy Technology Co., Ltd. The remaining authors declare that the research was conducted in the absence of any commercial or financial relationships that could be construed as a potential conflict of interest.

## References

1. You, C.Y. Research on the Application of Capacity-Expanded Conductors in Overhead Transmission Lines. *Electr. Power Equip.* **2006**, *10*, 1–7.
2. You, C.Y. Research on the Application of Steel-Cored Soft Aluminum Stranded Wires in Overhead Transmission Lines. *Electr. Power Constr.* **2006**, *27*, 1–4+30.
3. Milad, J.; Jordi-Roger, R.; Pooya, P. Aluminum Conductor Steel-Supported Conductors for the Sustainable Growth of Power Line Capacity: A Review and Discussion. *Mater* **2024**, *17*, 4536.
4. Huang, X.C.; Chen, C.; Wang, F.; Zhao, Q.J.; Bai, X.L.; Wen, X.X. Study on Stress Distribution Characteristics of Aluminum Strands in Steel-Cored Aluminum Conductors for Long-Span Overhead Transmission Lines. *J. China Three Gorges Univ.* **2016**, *38*, 76–81.
5. Zhang, X.S.; Niu, H.J.; Liu, S.C.; Yi, Q. Anti-vibration Measures of Ultrahigh Strength Steel Cored Aluminum Strand for Long-Span Overhead Line. *Int. J. Front. Eng. Technol.* **2022**, *4*, 10.
6. Xie, Y.; Wang, S.D.; Zhang, C.; Ouyang, K.J.; Jiang, X.F. Study on Nondestructive Testing Methods for Crimping Quality of Steel Cored Aluminum Strand. *IOP Conf. Ser. Earth Environ. Sci.* **2019**, *295*, 032097. [CrossRef]
7. Liu, F.; Findlay, R.D. Investigation of mechanical properties of single layer ACSR based on an Integrated Model. *Electr. Power Syst. Res.* **2007**, *78*, 209–216. [CrossRef]
8. Hubei Jinyang Resources Co., Ltd. Disassembly and Separation Machine for Steel-Cored Aluminum Conductors. CN 207127482 U, 20 April 2018.
9. Xinghua Senrong Metal Products Co., Ltd. Steel-Aluminum Wire Separation Device for Aluminum Conductor Recycling. CN 214107542 U, 22 June 2021.
10. Gopalraj, S.K.; Kärki, T. A Study to Investigate the Mechanical Properties of Recycled Carbon Fibre/Glass Fibre-Reinforced Epoxy Composites Using a Novel Thermal Recycling Process. *Processes* **2020**, *8*, 954. [CrossRef]
11. Ci, Y.Z. Research on Module Creation in Equipment Modular Design. Master's Thesis, National University of Defense Technology, Changsha, China, 2004.
12. Luo, G.F. Research and Application of Key Technologies in Manufacturing-Service-Oriented Modular Design of Complex Equipment. Zhengzhou Institute of Light Industry. 2017.
13. Brunoe, T.D.; Daniel, G.; Soerensen, H.; Nielsen, K. Modular Design Methodology in Mechanical Engineering. *Chem. Eng. Equip.* **2020**, *11*, 183–184.
14. Chen, X.J.; Yu, Y.; Xie, J.B. Modular Design Technologies and Applications for Complex Equipment. *Equip. Manuf. Technol.* **2024**, *5*, 118–120+136.
15. Qi, Z.; Zhang, C.; Qiao, L.; Qin, J.; Wang, S. The Test Study on Tension-torsion Coupling Effect of ACSR in Overhead Transmission Lines. *J. Phys. Conf. Ser.* **2024**, *2731*, 012027. [CrossRef]
16. Morgan, V.T. Research on Tension Layering Characteristics of Steel-Cored Aluminum Conductors for Overhead Lines. *Electr. Wire Cable* **2015**, *4*, 30–33.
17. Yang, G.Y.; Wen, Z.M.; Gu, X.; Wu, M.Y.; You, W.R.; Xu, X. Research on Calculation Method of Strand Layer Stress in Steel-Cored Aluminum Conductors. *Electr. Wire Cable* **2023**, *3*, 40–45.
18. Zhang, L.; Huang, J.; Zhong, Y.L.; Yan, Z.T. Tension, Torsion Coupling Mechanical Properties of Steel-Cored Aluminum Conductors. *J. Southwest Jiaotong Univ.* **2021**, *56*, 889–896+904.
19. Wu, J.G.; Xu, H.H.; Liu, S.S.; Zhou, X.K. Design and Development of Tensile Numerical Simulation System for Steel-Cored Aluminum Conductors. *Electr. Power Equip. Manag.* **2020**, *11*, 166–168.
20. Yu, J.; Wu, C.; Huang, H.; Xie, D.; Qin, F.; Jiang, J.; He, G. Discussion on AC Resistance and Temperature of ACSR Based on Finite Element Model Assistance. *Energies* **2025**, *18*, 539. [CrossRef]

21. *IEC 61089*; Round Wire Concentric Lay Overhead Electrical Stranded Conductors. International Electrotechnical Commission (IEC): Geneva, Switzerland, 1991.
22. *ASTM B232/B232M*; Standard Specification for Concentric-Lay-Stranded Aluminum Conductors, Coated-Steel Reinforced (ACSR). ASTM International: West Conshohocken, PA, USA, 2023.

**Disclaimer/Publisher's Note:** The statements, opinions and data contained in all publications are solely those of the individual author(s) and contributor(s) and not of MDPI and/or the editor(s). MDPI and/or the editor(s) disclaim responsibility for any injury to people or property resulting from any ideas, methods, instructions or products referred to in the content.

machines

MDPI

*Article*

# Development of a Test Rig for Detecting Fatigue Cracks in a Plastic Component of a Medical Device via Acoustic Signal Acquisitions

**Luigi Leopardi [1], Valerio Mangeruga [1,*], Matteo Giacopini [1], Marco Di Settimi [2] and Roberto Rosi [2]**

[1] Engineering Department "Enzo Ferrari", University of Modena and Reggio Emilia, 41125 Modena, Italy; luigi.leopardi@unimore.it (L.L.); matteo.giacopini@unimore.it (M.G.)
[2] Astra Research s.r.l., 41126 Modena, Italy; marco.disettimi@astraresearch.it (M.D.S.); roberto.rosi@astraresearch.it (R.R.)
* Correspondence: valerio.mangeruga@unimore.it

**Abstract**

This work presents the design and implementation of a mechanical test bench developed for the comparative evaluation of three configurations of a mechanical biomedical device: the reference version and two optimized alternatives aimed at improving long-term reliability and functional performance. The test bench performs mechanical fatigue testing under controlled and repeatable conditions, simulating the cyclic loads typical of real-world operation. A key innovation of this system is the integration of a non-invasive acoustic acquisition module, which continuously monitors the dynamic behavior of the device during testing. The analysis of acoustic signals allows for the early detection of wear, looseness, deformation, and the onset of structural defects, providing valuable insight into the device's mechanical health without altering its configuration. This study also details the engineering design of the control system, emphasizing both hardware integration and software architecture supporting real-time signal processing. Experimental results demonstrate that acoustic analysis represents an effective non-destructive approach for evaluating the endurance and reliability of compact plastic biomedical devices. The proposed methodology contributes to more accurate service life estimation, supports product validation, and promotes continuous improvements in the safety and quality of mechanical systems used in biomedical applications.

**Keywords:** test rig; acoustic signals; fatigue life; biomedical devices; non-invasive diagnostics

## 1. Introduction

In the field of biomedical technology, there is a continuous evolution of increasingly sophisticated devices, designed to improve patients' quality of life and support healthcare personnel in therapy management. Among these, mechanical devices play a primary role, representing an essential component of everyday therapeutic practice. These include, for example, mechanical dispensers for drug administration, which may be disposable or designed for a limited number of uses. Although often small in size and seemingly simple, such devices perform critical functions within the therapeutic process, as they ensure the controlled and precise release of medication according to well-defined modes and timing.

The proper functioning of these devices is essential not only to guarantee the effectiveness of pharmacological treatment but also to safeguard patient safety. Possible malfunctions—such as mechanical blockages, irregular dosing, or structural failures—can compromise therapy

adherence and, in more severe cases, create clinical risks with potentially significant consequences, particularly for vulnerable patients or in high-risk contexts [1].

From an engineering perspective, these devices exhibit a relatively complex structure, often made of plastic materials and characterized by compact geometries and multiple moving parts. Such features make them inherently prone to mechanical wear, clearance accumulation, and material degradation, especially under repeated use. Consequently, it becomes crucial to study their behavior not only through analytical models and numerical simulations but also by means of physical experiments and fatigue tests specifically designed to replicate real operating conditions.

In this context, the assessment of long-term mechanical reliability becomes a central issue [2]. The ability to detect potential functional anomalies or hidden defects in advance, even before they manifest critically, is fundamental for realistically and safely estimating the service life of the device, while minimizing the likelihood of unexpected failures during operation.

A particularly promising approach in this field consists of integrating advanced non-invasive monitoring techniques, including the acquisition and analysis of acoustic signals generated during fatigue tests. Acoustic analysis of mechanical components is a typical approach for the early detection of failures or excessive clearances, especially in complex mechanisms or components that are difficult to instrument directly [3–5]. When properly processed, these signals can provide valuable insights into abnormal mechanical play, incipient cracks, or localized material degradation. Such techniques are especially effective for compact plastic devices, widely used in the biomedical industry due to their cost-effectiveness, light weight, and ease of manufacturing.

One of the main advantages of acoustic testing lies in its inherently non-invasive nature: the analysis is carried out without physically interfering with the internal structure of the device and without altering its functional configuration. This aspect is crucial, as it allows for the monitoring of the system actual behavior during operation, avoiding the introduction of sensors or equipment that might alter the device mechanical dynamics. As a result, a faithful and representative evaluation of the product life cycle can be obtained, supporting design, validation, and continuous improvement processes.

Ultimately, the combination of analytical precision and non-invasiveness makes acoustic testing a highly strategic tool for the development and verification of biomedical devices that are increasingly reliable, safe, and durable.

The present work describes in detail the design and construction of a mechanical test bench developed for the comparative evaluation of three different configurations of a purely mechanical biomedical device, a nominal configuration currently available on the market and two alternative optimized solutions, designed to improve long-term structural reliability and functional performance. The possibility of comparing three different components, one of which is currently commercialized and has known life data, on the same test bench allows for the validation of both the methodology and the rig [6].

This work proposes the integration of acoustic analysis technologies to identify failures on test benches for fully assembled biomedical components. Specifically, the study aims to perform analysis not on a single component or specimen [7], but on the complete device. Furthermore, by detecting damage during testing through non-invasive measurement techniques, the approach enables the use of the test architecture while minimizing intervention on the analyzed device. Minimal invasiveness on the samples helps to reduce the risk of damage due to handling, an often difficult-to-reproduce variable, and allows for the test bench to be employed with a reduced setup time, i.e., for periodic testing.

The integration of acoustic analysis technology in the field of small biomedical devices requires correlating the microphone signal with damage propagation in small thermoplastic devices, a correlation that has been scarcely investigated compared to metallic components [4].

The combination of these analytical challenges, small and inaccessible devices, short cycles, plastic fatigue, and fully assembled plastic components, has been scarcely investigated in the literature and represents a relevant research opportunity.

The test bench was conceived to perform mechanical fatigue tests under controlled and reproducible conditions, simulating the cyclic stresses typical of real device use. To support the experimental activity, an acoustic acquisition system was integrated, capable of monitoring the dynamic behavior of components in real time throughout the entire operating cycle. The analysis of sound signals generated by the device mechanical operation provides an objective, continuous, and completely non-invasive assessment of the internal condition of the components, thereby offering valuable information on wear, looseness, deformation, or the onset of defects.

This implementation enables a systematic and consistent evaluation of the three analyzed solutions, allowing for a more accurate estimation of their remaining service life and the identification of possible structural or functional criticalities, with a view toward continuous improvement aimed at enhancing product safety and overall quality.

This methodology is useful for detecting failures in fully assembled components at the end of the manufacturing line. The purpose of the output is to evaluate the service life while considering all the variables encountered during the development and manufacturing process.

Furthermore, this study highlights the engineering rationale behind the development of the control system, with particular focus on the software architecture and hardware components dedicated to the management of the acoustic acquisition system, which constitutes a fundamental part of the decision-making algorithm employed to evaluate the device mechanical endurance. Finally, the methodology for processing acoustic signals and their integration into the performance validation process is discussed, with the aim of demonstrating the effectiveness of this approach as a non-destructive analysis tool in the mechanical domain.

## 2. Specific Mechanical Issue and Investigation Methodology

### *2.1. Mechanical Issue*

The specific issue addressed in this analysis concerns a drug delivery device intended for inhalation therapy. The system, designed for individual and home use, consists of a set of micro-mechanical components integrated into a compact and user-friendly body. The main functions that the device is required to perform include the following:

- The precise dosing of the active ingredient to be administered;
- The effective mixing of the drug in solid form (typically micronized powder) with the airflow generated during patient inhalation;
- The accurate counting of remaining doses, in order to avoid incomplete administrations or overdosing;
- The generation of an acoustic signal, in the form of a “click,” to confirm to the user the correct positioning of the device for effective administration.

In this context, the component under detailed investigation is the mechanism responsible for generating the acoustic feedback—a sharp and recognizable sound produced during device actuation, which serves as confirmation to the user that the therapeutic action has been correctly performed. This sound has not only an informative function but also represents a critical element for the clinical effectiveness of the treatment, as it ensures that administration takes place under the conditions required by the usage protocol.

The emission of the acoustic signal is the direct consequence of a mechanical stress applied to an elastic component of the device. Specifically, the mechanism can be effectively modeled as a cantilever beam, fixed at one end and subjected to an imposed displacement at the other end, which is then released in an almost impulsive manner. This triggers a free oscillatory motion during which the component vibrates within the audible frequency range, generating the characteristic "click" (Figure 1). The component responsible for producing the "click," hereafter referred to as the click arm, is actuated by a kinematic system linked to the opening and closing movements of the device. The mechanism can be imagined as being driven by two cams, each with a different profile, attached to the device cover. One cam engages the click arm during opening and the other during closing. These cams approximate the behavior of the internal mechanism used by the device to excite the click arm, which itself is not subject to direct analysis.

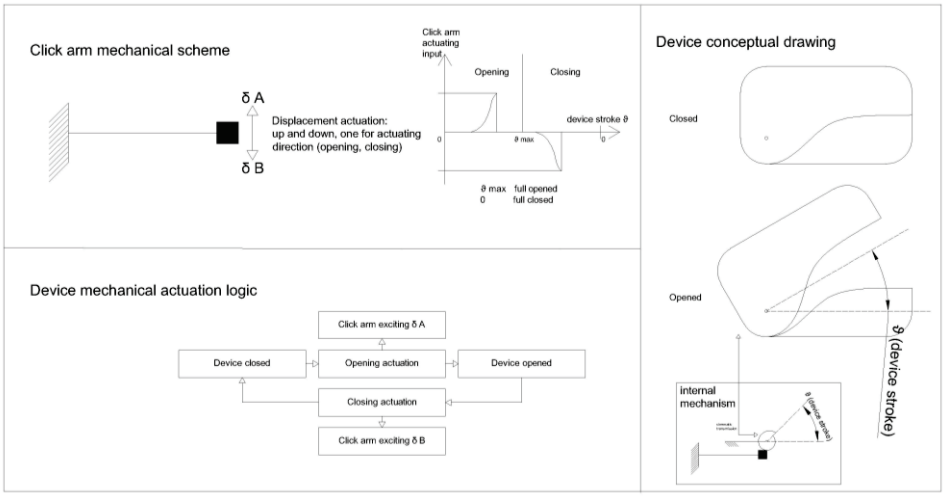



**Figure 1.** Device operation scheme.

The operating conditions of the mechanism are strongly constrained by geometric and material selection factors. The small dimensions of the device impose strict spatial limitations on the component geometry, requiring an extremely compact and optimized design. Furthermore, material choice is heavily influenced by biocompatibility requirements.

To obtain an acoustic response that is sufficiently intense and distinguishable during use, while still respecting geometric constraints, the structure operates in an elastoplastic deformation regime. Despite the relative simplicity of the mechanism, its small size prevents the adoption of a design capable of entirely avoiding material plasticization and thereby eliminating the issue of low-cycle fatigue. As a result, the total number of possible actuations is limited: it is estimated that the component can withstand only a few hundred cycles before its mechanical properties degrade beyond functional limits.

In order to increase the safety margin with respect to the required service life of the component, a geometric optimization process was undertaken. This optimization, implemented through iterative loops of redesign and Finite Element (FE) calculations, produced two improved geometries, whose details are out of scope of the present contribution. However, due to insufficient background knowledge regarding material properties, friction effects, and other factors, the analyses carried out could only provide a comparative assessment relative to the original solution. To establish an absolute evaluation of the problem, the construction of an experimental test bench was therefore deemed necessary.

*2.2. Investigation Methodology*

The small size and structural complexity of the system prevent the integration of mechanical sensors within the component, making direct monitoring of internal stresses or deformations impossible. Moreover, to ensure that the test is representative of real operating conditions, it is not feasible to adopt equivalent external actuation methods, such as applying linear or rotary actuators directly to the disassembled component. The behavior of the mechanism is strongly influenced by the fully assembled device, which provides the actual constraints and boundary conditions, including internal friction, mechanical couplings, and functional clearances.

Given these constraints, the most effective validation strategy involves performing endurance tests on the fully assembled device, actuated under conditions similar to those experienced by the end user. The activation cycle is therefore replicated by an anthropomorphic arm that simulates the operator action, ensuring consistency between test conditions and real use [8].

The monitoring of component functionality is carried out by analyzing the acoustic signal emitted during each activation cycle. Although indirect, this methodology enables non-invasive verification of the component actual functionality, detecting possible degradation over time in the form of reduced sound intensity, changes in the spectral content of the signal, or the disappearance of the "click." Such variations provide a reliable indicator of the component damage threshold being exceeded.

This approach also respects the constraints of miniaturization and does not interfere with the structural integrity of the system. Through appropriate audio acquisition and subsequent signal processing—using, for example, time- and frequency-domain analysis techniques (FFT, spectrograms, cepstrum, etc.)—it becomes possible to objectively identify the onset of functional degradation [9].

In addition to acoustic analysis, a load cell is used to measure the actuation force (opening and closing of the device). Monitoring the actuation load makes it possible to detect jamming conditions or increased friction. This is useful for stopping the test in time in the event of a component failure that does not produce a significant change in the "click," but which could continue damaging the device and make it impossible to identify the root cause. The test interruption based on load cell monitoring also allows for the validation of the complete component and the measurement of possible end-of-life conditions arising from causes external to the click arm itself.

## 3. Test Setup

The mechanical actuation of the component is performed using an anthropomorphic robotic arm. The choice of employing a robotic arm allows for natural motion, consistent with the manual operation of a portable device, while at the same time ensuring that identical movements are repeated across cycles (Figure 2).

This is an essential requirement for the test setup, which must replicate real operating conditions as closely as possible while guaranteeing repeatability between cycles.

The actuating cycle consists of device opening and closing, as illustrated in Figure 1. The movement is controlled by displacement corresponding to the full available stroke. The velocity is constant at the maximum speed allowed by the robot for each segment. Consequently, the actuating frequency is determined by the actuation speed, allowing for one full cycle to be completed every 5 s. The actuating frequency is not critical for the test parameters, as real operational actuation is much slower and occurs only a few times during a day. Therefore, the speed is only relevant for the duration of the tests.

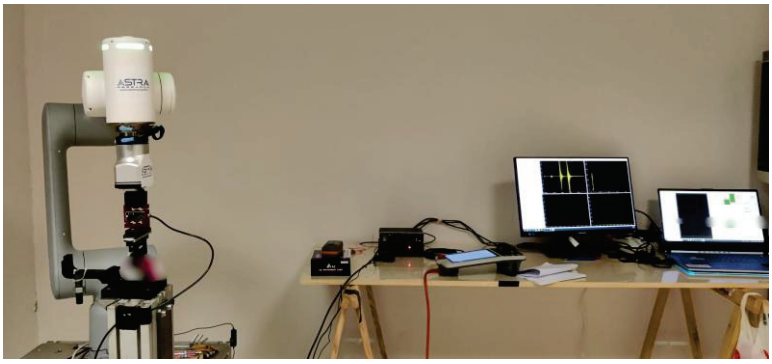


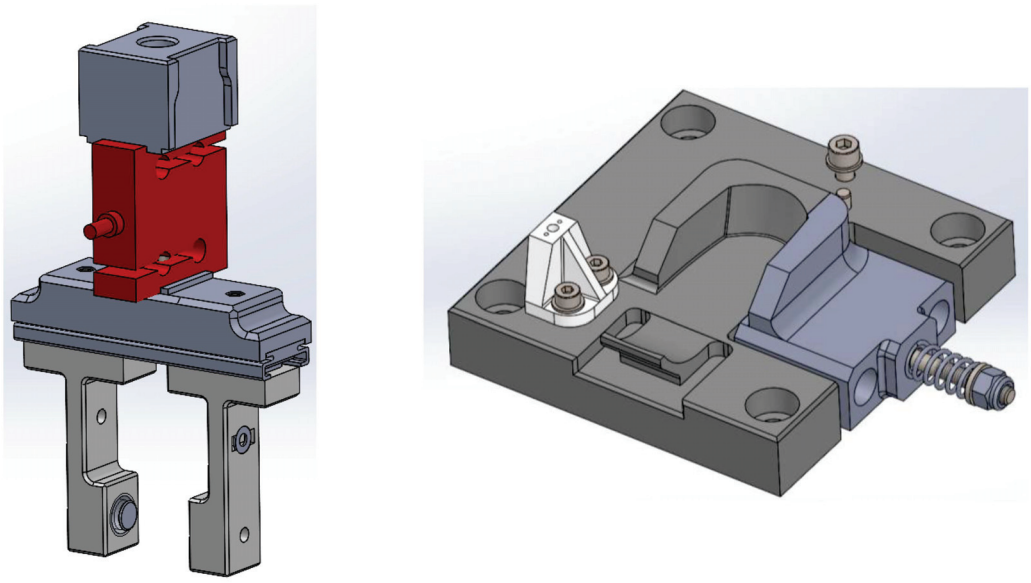
**Figure 2.** Test setup.

The gripping fixtures are manufactured by 3D printing with plastic material and are designed to meet the following requirements:

- Avoid mechanical interference (e.g., excessively high contact pressures);
- Be non-destructive (no drilling, interference fits, etc.);
- Be chemically non-aggressive (neutral adhesives or treatments in a way to do not damage the material);
- Allow the integration of a load cell for monitoring the actuation load.

The adopted solution was to design friction-based grippers with controlled load application.

The lower gripper (Figure 3a) accurately reproduces the shape of the component. The component itself is composed of two shells that can slide relative to each other, thereby generating load at the interface with the component and securing the device in place. The load is elastically applied via a helical spring. The entire lower gripper assembly is fixed to the base.



(**a**) (**b**)

**Figure 3.** (**a**) Uppergripping (**b**) Lower gripping.

The upper gripper (Figure 3b) also applies contact load to ensure sufficient friction for actuation. In addition, adhesive pads are used to reduce the stiffness of the applied load, improve the distribution of the contact area, and provide a minimal adhesive force. The adhesives employed are certified as chemically non-interfering with the thermoplastics used in the device.

The kinematic structure of the upper gripper consists of two floating arms relative to the robot gripping point. This floating configuration ensures automatic centering without the risk of inducing parasitic loads. Between the arm guide and the robot gripper, a load cell is installed. The load cell provides output data regarding the actuation torque.

The trajectory of the robotic arm is programmed to ensure that the axis of the gripper always remains tangent to the device opening path. By maintaining tangency between the gripper position and the circular opening trajectory, radial loads are avoided, and the actuation torque can be extracted directly and reliably from the load cell.

## 4. Analysis Setup and Robot Interface

The functional analysis is carried out through the acquisition of three analog signals (Figure 4):

- Microphone signals
  - An environmental microphone.
  - A capsule microphone positioned close to the device.
- Signal from the load cell

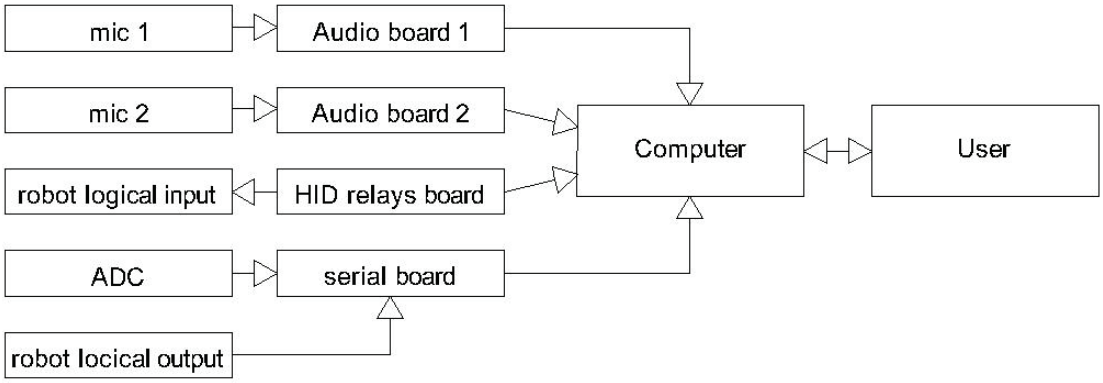



**Figure 4.** Hardware diagram.

### *4.1. Acquisition of Microphone Signals*

The environmental microphone was included solely to provide an ambient reference track for use during post-processing. The rationale behind this choice is that, unlike the local capsule microphone, the environmental microphone captures the device signal in a highly attenuated form while strongly amplifying environmental disturbances. For this role, a capacitive cardioid-pattern microphone was selected. It is positioned at a distance from the device, with its direction of minimum sensitivity oriented toward the device itself. This placement is intended to minimize the detection of the device "click" signal.

In contrast, the capsule microphone positioned close to the device is specifically intended to maximize the capture of the device signal while attenuating external noise. This capsule has predominantly directional characteristics and is oriented directly toward the component under test, at just a few millimeters of distance. A foam windscreen was placed over the capsule to eliminate potential air flow noise. However, the controlled laboratory environment in which the tests were conducted made additional precautions unnecessary. In fact, even in the early tests, the recorded signal proved to be remarkably clean [10,11].

In this case, the use of an appropriate frequency filter is sufficient to cancel background noise. Indeed, the combination of placing the microphone close to the system relative to the noise intensity, together with adequate gain settings, ensures that the noise has minimal influence on the frequency spectrum of interest. The data collected from the environmental microphone are useful for future studies aimed at evaluating the possibility

of improving a noise-canceling model by combining signals from both the environmental and local microphones. Implementing a noise-canceling algorithm would further expand the applicability of this test rig.

The two microphones are acquired through separate audio interfaces, while the load cell signal is acquired via an analog-to-digital converter (ADC). The environmental microphone requires +48 V phantom power, supplied directly by the acquisition interface. The capsule microphone also requires phantom power, but at a significantly reduced level of approximately 4 V. Therefore, a suitable voltage reducer was introduced.

Both supply voltages are derived from their respective audio interfaces. This ensures that the ADCs share the same voltage reference as that which powers the microphones, thereby eliminating the risk of amplitude drift caused by supply voltage variations. If an external circuit had been used, small fluctuations in supply voltage—likely to differ between the ADC and the power supply unit (assuming two separate devices)—could have introduced unpredictable amplitude errors. The issue is resolved by maintaining proportionality between the microphone supply voltage and the reference voltage of the acquisition board [12].

The solution required the inclusion of a component to step down the supply voltage for the capacitive capsule microphone, since high-performance commercial audio interfaces typically provide only +48 V phantom power.

Both audio interfaces used are capable of 24-bit, 192 kHz acquisition. However, after initial testing, it was determined that the problem under investigation could be adequately addressed using 16-bit, 44 kHz sampling. This was advantageous in terms of data storage requirements. It was estimated that the full test campaign on 89 components, with 40 min trials, generated approximately 1.8 TB of data. The data are stored as binary vectors in HDF-format data frames, without any lossy compression algorithm. For this reason, storage requirements are not comparable to typical audio files such as WAV, where compression or reduced resolution is often applied.

### *4.2. Load Cell Acquisition*

The load cell is used both to monitor the evolution of the device resistant load and to prevent forcing the device into closure in the event of damage leading to mechanical blockage. The chosen sensor is a conventional S-type load cell with a full scale of 2 kg. Electrically, the cell is configured as a full-bridge type and is supplied with a calibration certificate, which allows for its use without the need for additional calibration. The load cell is an AEP transducer with a sensitivity of 2 mV/V and an uncertainty of 0.002%.

The analog-to-digital conversion is performed using the Texas Instruments ADS1220, a 24-bit Sigma-Delta ADC [13,14]. For this application, it is configured in single differential channel mode with a 5V reference voltage. Communication with the PC is handled via an Arduino Mega 2560, which communicates with the ADC through SPI and is responsible for

- Setting the ADS1220 registers;
- Reading and packaging data from the ADC;
- Reading the robot status contact.

The analog signal is acquired at 24-bit resolution and 330 samples per second. The Arduino communicates with a Python 3.12 software, running on the setup computer, via a serial port, transmitting hexadecimal strings. Each packet contains the robot contact status, the value acquired by the ADC, and the timestamp associated with the value. The ADC provides a data-ready (DRDY) pin, which ensures that the buffer is not overwritten until the value is read. This guarantees synchronization with the circuit clock, but it is not sufficient to ensure the exact temporal position of the samples. Relying solely on the Time Sample field recorded in the register to reconstruct the time series could lead to two problems:

- Propagation of a time error, caused by even small discrepancies in the actual sample time;
- Loss of traceability of a missed acquisition, e.g., due to a full buffer.

To mitigate this issue, the Arduino is configured with an interrupt driven by the DRDY pin, helping to compensate for potential systematic errors in the temporal alignment of the samples.

Two additional digital signals—test start and emergency contact—are managed via an external HID relay board. The choice to use a separate relay board rather than integrating these functions into the Arduino + ADC circuit was motivated by two reasons: ensuring an additional technology option for future applications and guaranteeing access to the emergency contact even if the Arduino + ADC system were to lock up. In this regard, the use of an HID device is advantageous due to its versatility, ease of implementation, and fast deployment. Numerous libraries are available depending on the intended application.

All I/O signals are managed by Python programs running concurrently on the same computer. These programs are responsible for

- Ensuring correct timing of signals;
- Executing the required operations;
- Detecting the presence or absence of failure conditions;
- Managing the test sequence (cycle counting, robot start/stop, etc.).

The software logic is described in detail in the following section.

## 5. Software Logic

The software can be divided into three main interfaces:

- Cycle manager;
- Audio signal analyzer;
- Serial interface signal analyzer (load cell and robot contact).

The last two points are invoked by the user through the cycle manager.

In the software diagram (Figure 5), hollow arrows represent user commands, while solid arrows indicate the flow of information exchanged between the different software blocks.

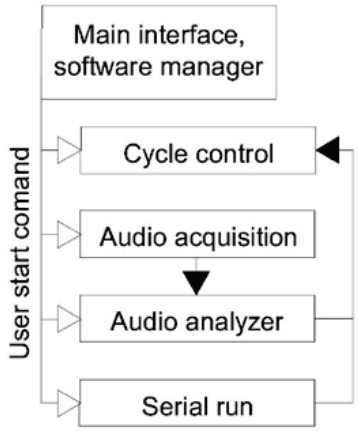



**Figure 5.** Global software architecture.

The Cycle Control block outputs directly to the Main Interface. The main interface contains both the commands for starting and stopping the other applications and the commands for managing the test cycle.

The audio acquisition system does not directly generate an output visible to the user; therefore, a semaphore was added to the main interface to confirm its activation. The

acquisition tool produces packets addressed to the audio analyzer, which are then used to generate the reference outputs.

### *5.1. Cycle Manager*

The cycle management interface is the first program launched at startup. It functions both as the main user interface and as the cycle manager (Figure 6). The areas in red indicate that the corresponding tools are inactive; they turn green when the tools are started.

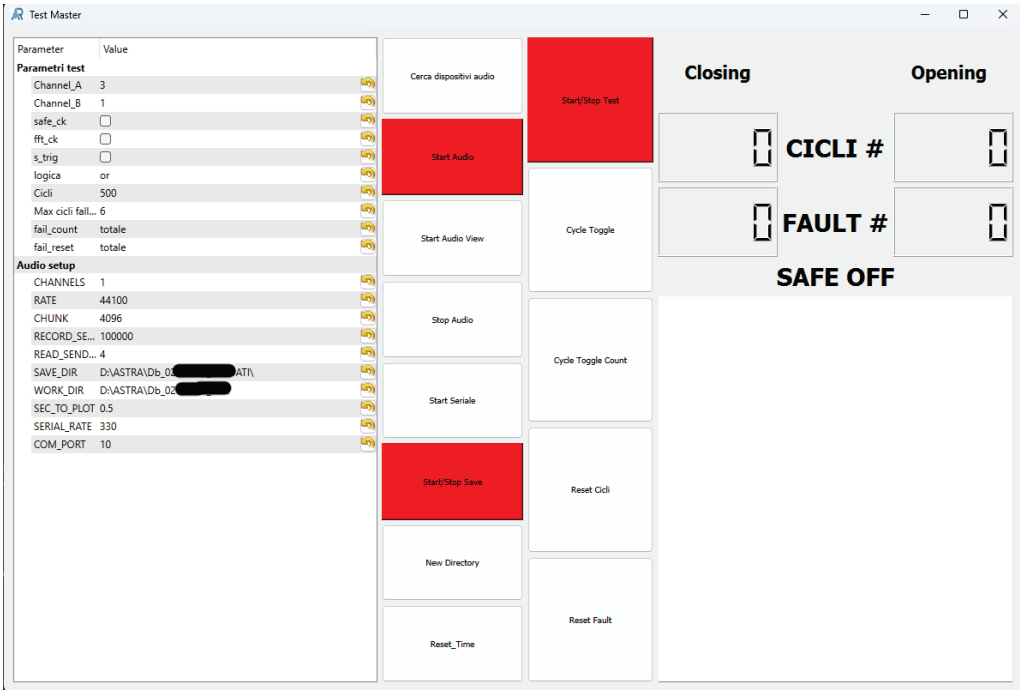



**Figure 6.** Cycle management tool screenshot.

Within this program, the following tasks are performed:

- Input of test parameters;
- Communication with the robot;
- Management of test start, stop, and safe shutdown;
- Logging of test execution.

The user interface shown in the diagram (Figure 7) represents the main interface, which controls the startup of the other applications as well as the cycle parameters. From this interface it is possible to configure the pre-launch settings of the various software submodules (such as serial ports, sampling frequencies, etc. Once all the necessary systems have been initialized, the user can configure the cycle and start the test.

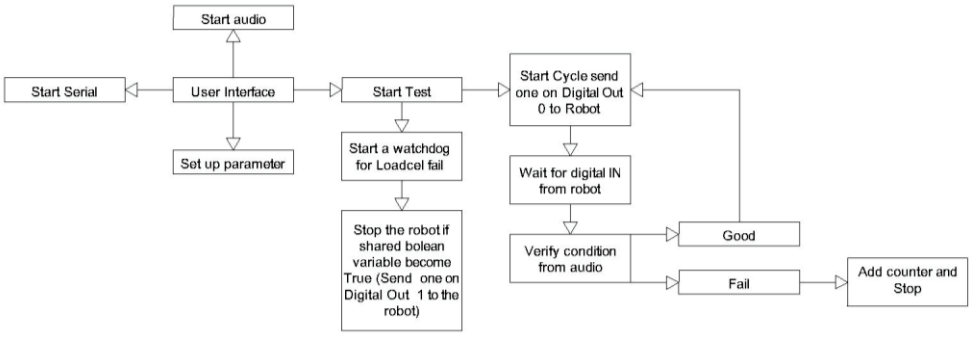



**Figure 7.** Cycle manager schematic.

The cycle configuration has been designed to be as general as possible. Among the required parameters for test automation, the most important are

- Cycle limit;
- Failure logic.

The upper cycle limit defines the maximum number of cycles, beyond which the test loses significance regardless of whether a failure has occurred. Cycles are categorized into opening and closing phases. Ideally, in cyclic actuation, the mechanism should return to its starting position at the end of each cycle. However, in cases where intermediate positions exist, it may be useful to split the cycles into sub-cycles.

The failure logic requires several parameters to be configured:

- Failure detection strategy;
- Tolerance time (in cycles) before stopping;
- Reset strategy if the tolerance time is not exceeded.

The failure detection strategy defines which features are monitored to declare a component as failed. In this work, amplitude and frequency checks are performed. The user can choose whether to monitor one, both, or apply logical combinations (OR/AND) between them [15].

The failure tolerance time, expressed in cycles, sets the number of consecutive failures required before declaring a definitive failure. This avoids stopping the test due to spurious measurement errors or transient information loss, while keeping the margin of error very small and limited to a few cycles. This tolerance can be disabled by setting it to zero. It is important to note that this mechanism does not override safety checks: once a safety condition is triggered, the test stops immediately regardless of tolerance settings.

The reset strategy defines how the system exits the failure tolerance window. Since each cycle can be split into two sub-cycles, i.e., opening and closing, the user can specify whether the reset condition should be evaluated on a single sub-cycle or on the entire cycle. This tolerance ensures that the test does not stop when an isolated error is detected. Because this tolerance is known and very small, it does not affect the test results.

At the end of the test, the tool generates a log file, where each executed sub-cycle is recorded as a row.

Each log entry includes the following:

- Values analyzed by the dedicated tools;
- Failure status (ON or OFF);
- Cycle number;
- Actuation time;
- Execution timestamp.

### *5.2. Audio Acquisition and Analyzer*

The user interface for the audio analyzer comprised a detection-parameter setting area and a visualization of time-domain signals and frequency-domain computations (Figure 8).

The main challenge in this part of the system is ensuring that all audio packets are preserved (i.e., preventing the loss of temporal segments) while maintaining a sufficiently low latency to allow for real-time usability.

To address this issue, the system extensively relies on the queue principle (Figure 9).

The queues are of the FIFO type (First-In-First-Out), allowing for processes to operate independently so that a slowdown in one stage does not block the previous one. This approach prioritizes data integrity (no packet loss) at the expense of a slightly less strict real-time performance. In other words, the system guarantees that the entire timeline

of interest is processed, with latency between acquisition and output depending on the available computational power [16,17].

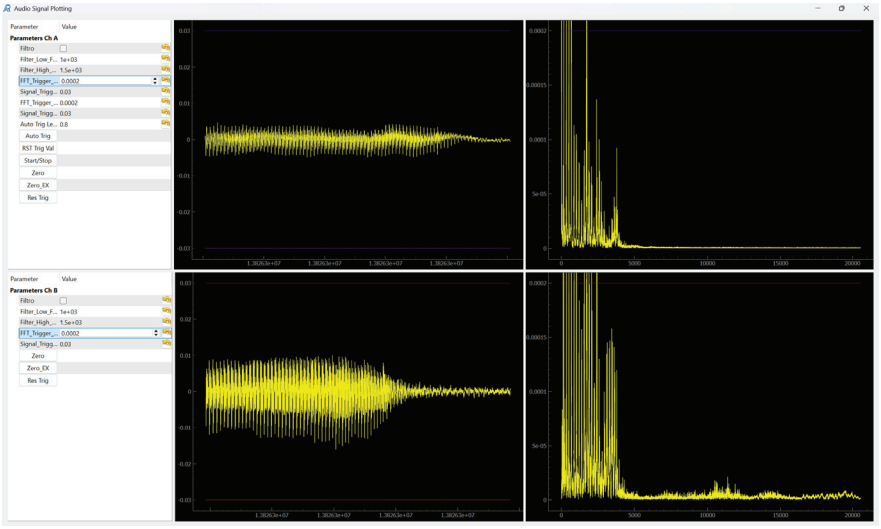


**Figure 8.** Audio analysis tool screenshot.

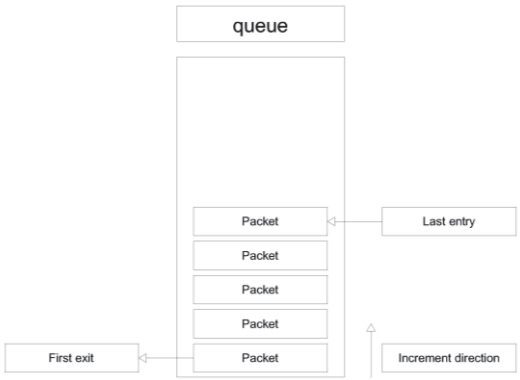



**Figure 9.** Queue logic flowchart.

The following functions are executed for each channel involved in the test (Figure 10).

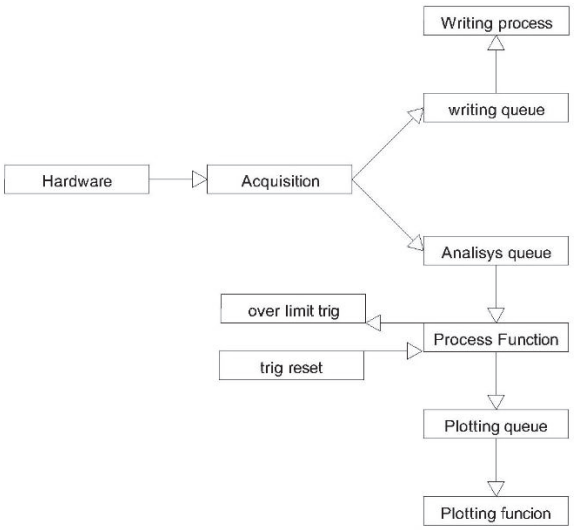



**Figure 10.** Audio processing logic diagram.

A timestamp is assigned to every acquired audio packet. Since each packet contains a defined number of samples and a fixed sampling frequency, the corresponding time vector can be reconstructed. Tests were conducted to check for reconstruction errors by comparing the expected acquisition period with the time delta between the last sample of one packet and the first sample of the next one. These tests, performed across different sampling frequencies with random input signals of varying amplitude, showed errors only within numerical precision limits. This means that the hardware system is adequate for the required operating conditions.

In the Writing Process, acquired RAW data are written directly to the disk without conditioning. Data are grouped into fixed-length blocks, and upon completion of each block, the function writes a Data Frame into an HDF (h5) file.

This process generates multiple files during the test, each with a fixed number of samples. At the end of each test, all files are merged into one using an appropriate tool. This ensures that any occurrences during the test do not compromise the data already written in the previous files. In the processing sequence, the signal is analyzed both in the time domain and in the frequency domain. The objective is to determine whether a minimum amplitude threshold is exceeded, thereby validating whether the component has operated correctly.

For each packet, the processing pipeline consists of

- Band-pass filtering;
- FFT computation;
- Threshold comparison.

Filtering is performed using two consecutive 10th-order Butterworth filters (low-pass and high-pass) to isolate the band of interest.

The FFT is executed with redundancy factor 4 (see Figure 11).

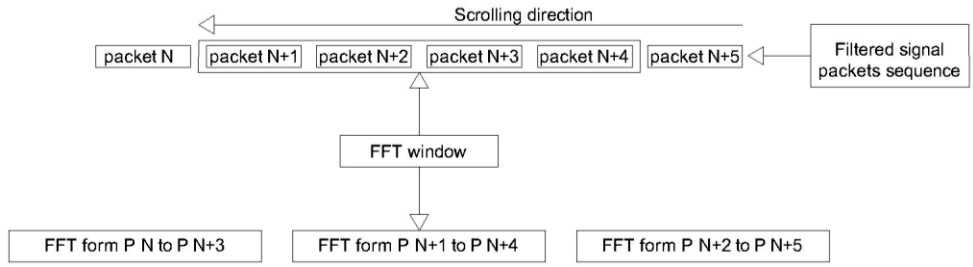



**Figure 11.** FFT processing logic diagram.

Each time a new packet is available, an FFT is computed including the current packet and the previous three. Given that each packet spans a duration T,

- AcqFilt(0, 4T) $\rightarrow$ FFT(0);
- AcqFilt(T, 4T + T) $\rightarrow$ FFT(1);
- AcqFilt(2T, 4T + 2T) $\rightarrow$ FFT(2);
- ...

Here, AcqFilt(t) is the time-domain filtered acquisition vector, and FFT(n) is the matrix of transforms (dimensions: m = 2T, n = processed packets—3) [18–21].

This method ensures that at least one transform fully contains the signal of interest. Since successive transforms overlap in time, the amplitude evaluation remains stable. For this reason, windowing functions are not used, as they would introduce uncertainty depending on whether the signal of interest falls within the same window segment, potentially causing amplitude errors. The windowing algorithm used in this case does not

combine the FFTs with each other; it is only applied to ensure that the click signal is fully captured within a single FFT window.

Once the sequence of FFTs is obtained, both the time-domain and frequency-domain results are compared against predefined thresholds. When the thresholds are exceeded, two shared Boolean variables ("success") are triggered: one corresponding to the time-domain check, the other to the frequency-domain check.

With this configuration, the average lag from the acoustic occurrence to the triggering event is approximately 400 ms. However, this value is strongly influenced by the window size and the hardware capabilities. In particular, the window size directly affects the time lag, as it is necessary to wait for the acquisition to complete before performing the analysis. At the same time, the minimum window size is constrained by the duration of the acoustic event.

After verifying these "success" variables, the cycle controller resets them to zero and instructs the robot to proceed with the next cycle [22].

### *5.3. Serial Port Analyser*

The serial port analyzer performs the following tasks:

- Reading the load cell signal;
- Plotting it as a time-domain graph;
- Comparing it against predefined threshold values (specifically, protection limits);
- Reading the status of digital inputs.

The program receives packets from the serial interface and distinguishes whether they contain status information or a time-series segment from the load cell (see Figure 12) [23–25].

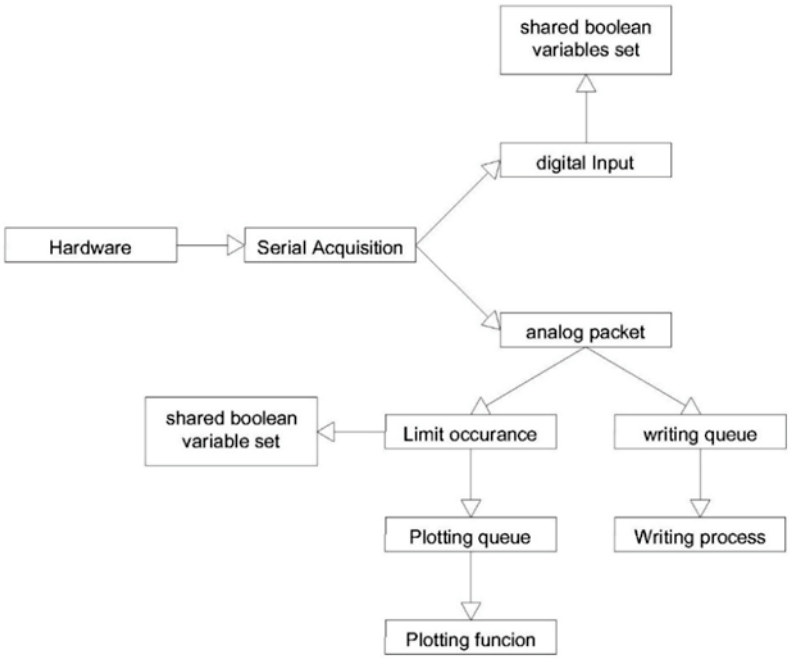



**Figure 12.** Serial acquisition logic diagram.

- In the case of Boolean status signals, the analyzer simply updates the corresponding shared variables.
- If the packets contain load cell data, the software processes them, plots the signal, and stores it.

This analysis implements a safety circuit based on load limits. When the signal exceeds the threshold, the shared variable "safe" is set to 1. As is standard in safety logic, the reset of the "safe" state can only be performed manually via the user interface.

The system operates in a manner very similar to the audio analyzer. Similarly to audio systems, the data are written to disk in fixed-length packets. However, since the load cell is used exclusively for protection purposes, no frequency-domain analysis is required in this case.

## 6. Results

The proposed setup allowed for all system "clicks" to be detected and enabled evaluation of the actual lifetime of all tested samples. Specifically, the results provide two key pieces of information:

- Decay of the natural frequency as cracks propagate;
- Useful life of the samples during the test.

When presenting the following results, we would like to note that sensible values have been normalized with respect to a reference limit value for industrial confidentiality reasons [26].

Figure 13 shows a typical output in the time domain. In particular, it displays the recordings from the proximity microphone corresponding to a generic cycle, including both opening and closing phases. From the signal, the peak values identified by the red markers can be easily extracted. In the graph, the horizontal red line represents the signal threshold.

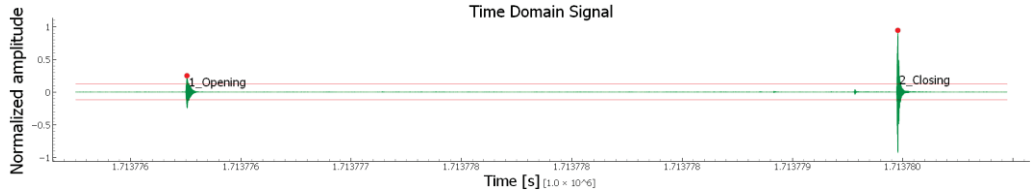
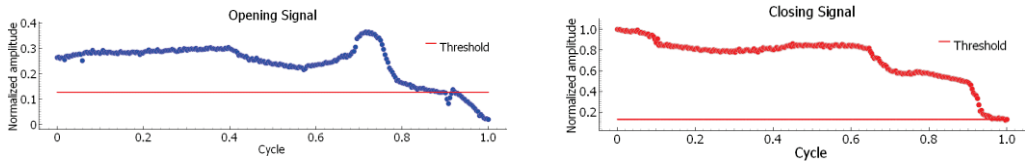



**Figure 13.** Time-based signal example.

The maximum recorded for each cycle can then be plotted as a function of the opening and closing sub-cycles, as shown in Figure 14.




(**a**) (**b**)

**Figure 14.** Amplitude peaks, in the time domain, plotted over cycles: opening sub-cycle in blue (**a**); closing sub-cycle in red (**b**).

By observing the figure, a decay in amplitude is immediately noticeable—particularly for the closing signal—as the number of cycles increases. This trend highlights the onset of the fracture in the "click arm" under investigation [27,28]. To increase the reliability and confidence of the results, in addition to the time-domain Mini One—Cooper R50–53 (2001–2006) Rivestimento del sottoporta delle minigonne lateralianalysis, a frequency-domain analysis was also performed using the FFT of the signal, as described in detail in Section 2.1. In particular, Figure 15 shows the trend of the maximum amplitude in the frequency domain as a function of the opening and closing sub-cycles, while Figure 16 displays the corresponding frequency, also as a function of the sub-cycles.

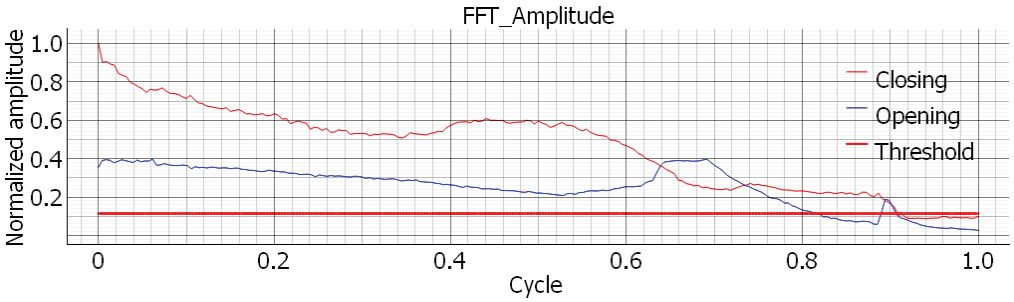



**Figure 15.** Peak amplitude over cycles, in red closing cycles in blue opening cycles.

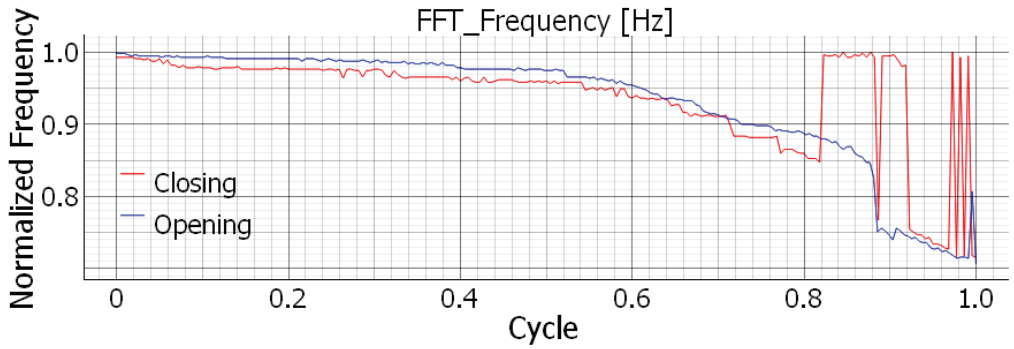



**Figure 16.** FFT frequency of peaks over cycles, in red closing cycles in blue opening cycles.

In all the diagrams, a general decrease can be observed both in the amplitude of the peaks and in the corresponding frequency. This decay is observed in all components and across all tests, showing the same behavior. Qualitatively, this result is consistent with the behavior of a generic clamped beam, where the propagation of a crack near the clamped end leads to an overall reduction in bending stiffness and, consequently, in both the first natural frequency and the oscillation amplitude when excited by an imposed end displacement, see Figure 1.

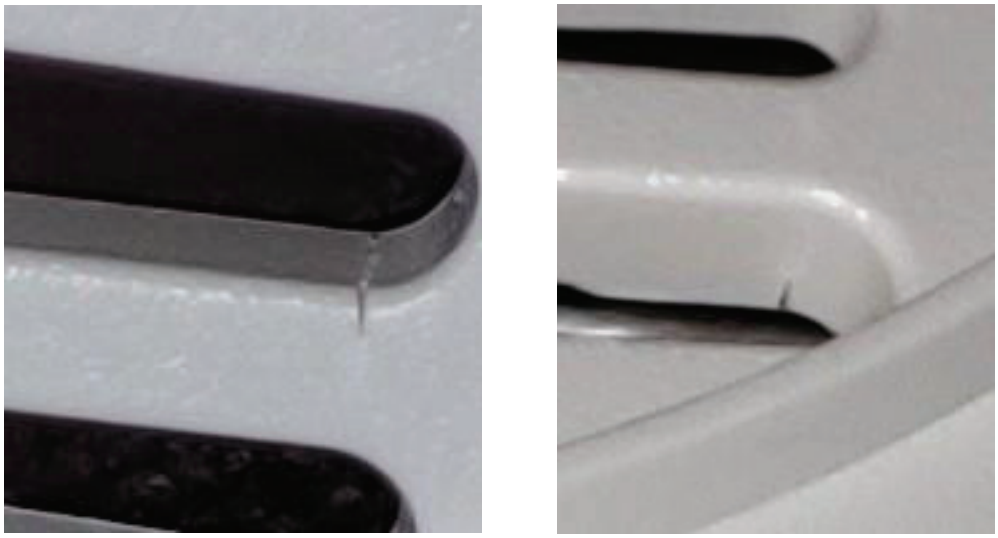
The decrease in amplitude and frequency was also confirmed by visual inspection of the components. Unfortunately, the "click arm" is not accessible without disassembling the device, and the limited number of specimens does not allow for multiple analyses at progressive cycle stops to study the continuous propagation. However, it was possible to stop a few tests when an initial decay became perceptible, and Figure 17 shows the initial crack propagation. This behavior is consistent with the already described behavior of a clamped beam.

In order to identify the service life of the component, it appears evident that an appropriate lower threshold can be defined for the amplitudes as a function of the cycles, both in the time and frequency domains, as well as for the corresponding frequencies as a function of the cycles.

In this case, amplitude monitoring is used to control the test, since the main function of the component is to emit perceptible acoustic feedback. Provided that the signal remains within the audible frequency range, functionality is confirmed if the amplitude remains above a predefined limit.

Moreover, by comparing Figures 15 and 16, the amplitude signal appears more stable, particularly in the final decay region. In fact, in the frequency plot, near the end of the test, the closing curve exhibits some spikes or unusually high values that do not conform to the expected decay. This can be explained considering the kinematics of the mechanism: during closing, higher-frequency peaks, normally filtered out, can interfere with the decay period. Indeed, as the component begins to fail, the decay of both frequency and amplitude is not

uniform across the spectrum. Some cycles, at crack initiation, may feature higher-frequency peaks with amplitudes comparable to the characteristic response, causing temporary instability in the plot.



(**a**) (**b**)

**Figure 17.** Two examples of the start of crack propagation: specimen 1 (**a**), specimen 2 (**b**).

In terms of amplitude, the perceptible acoustic threshold was defined subjectively according to usage requirements and, in consultation with the manufacturer, was set to ensure the device would not fall below a level where damage would become imperceptible. To determine this operational limit, several samples were taken near failure and evaluated subjectively by the client.

Once the limit thresholds are defined, for each tested sample, the service life can be identified as the intersection between the amplitude–cycle curves and their corresponding thresholds, both in the time and frequency domains.

Figure 18 shows the experimentally derived service life for the 21 tested samples across the three types, i.e., the original (Reference) and the two optimized solutions obtained from numerical simulations (Type A and Type B). To reduce test variability and maximize sample homogeneity, all specimens were produced from the same molding batch.

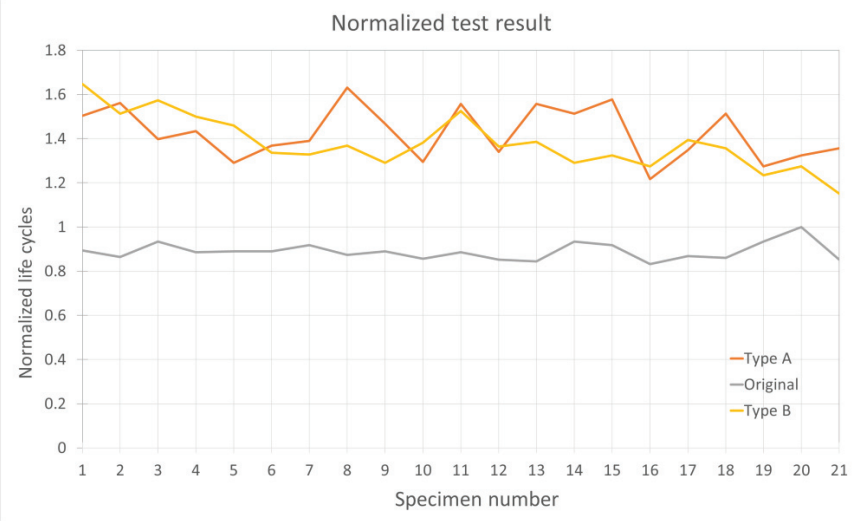



**Figure 18.** Normalized test life for each specimen.

The service life was normalized with respect to the maximum value obtained for the reference configuration. Good stability and consistency can be observed among the results belonging to the same type, thus validating the measurement system and the repeatability of the tests.

The results indicate that the two optimized designs demonstrate approximately 50% improved performance. This outcome also validates the calculation methodology, although the detailed method is beyond the scope of this discussion. Overall, the results not only confirm that the product-specific objectives are met but also validate the investigation methodology, demonstrating that the test bench functions as intended.

## 7. Conclusions and Future Developments

This work presents the design and implementation of a mechanical test bench for evaluating three configurations of a biomedical device. A real-time acoustic acquisition system enabled non-invasive monitoring under cyclic loading, reproducing operational stresses.

The methodology described in this work is designed for seamless integration into the production line. Its ultimate goal was to provide a system capable of testing samples during manufacturing. This was useful for identifying any issues that occur during component production, whether related to materials or assembly, and allows for the affected lot to be removed.

The results demonstrate that acoustic monitoring reliably detects early signs of failure and allows for the estimation of service life by correlating amplitude trends with operating cycles. This approach provides an objective measure of structural performance and durability, validating the test bench as a robust platform for fatigue testing of compact mechanical devices.

The system combination of hardware and software components ensures repeatability and accuracy, while its modular design offers potential for adaptation to other devices. Future improvements include the development of a single interface board to increase versatility, the implementation of wireless signal acquisition for moving components, and a generalized software interface to manage various cycle protocols. Integration with robots or other industrial devices could further enhance automation.

From a data analysis perspective, the availability of time- and frequency-domain signals allows for energy analyses, noise reduction, and the application of AI algorithms for pattern recognition or predictive maintenance. These enhancements would expand the test bench capabilities and provide deeper insights into device behavior under cyclic stress.

**Author Contributions:** Conceptualization, L.L. and M.D.S.; methodology, L.L.; software, L.L.; validation, L.L.; data curation, L.L.; writing—original draft preparation, L.L.; writing—review and editing, M.G. and V.M.; supervision, M.G. and R.R.; project administration, R.R.; funding acquisition, R.R. All authors have read and agreed to the published version of the manuscript.

**Funding:** This research received no external funding.

**Data Availability Statement:** The raw data supporting the conclusions of this article will be made available by the authors on request.

**Conflicts of Interest:** The authors Luigi Leopardi, Valerio Mangeruga and Matteo Giacopini were engaged by the company Astra Research s.r.l. The remaining authors declare that the research was conducted in the absence of any commercial or financial relationships that could be construed as a potential conflict of interest.

## References


1. Zamzam, A.H.; Abdul Wahab, A.K.; Azizan, M.M.; Satapathy, S.C.; Lai, K.W.; Hasikin, K. A Systematic Review of Medical Equipment Reliability Assessment in Improving the Quality of Healthcare Services. *Front. Public Health* **2021**, *9*, 753951. [CrossRef]
2. Nithyanandan, P.; Hoag, S.W.; Dalby, R.N. The Analysis And Prediction of Functional Robustness of Inhaler Devices. *J. Aerosol Med.* **2007**, *20*, 19–37. [CrossRef]
3. Shi, S.; Wu, G.; Chen, H.; Zhang, S. Acoustic Emission Monitoring of Fatigue Crack Growth in Hadfield Steel. *Sensors* **2023**, *23*, 6561. [CrossRef]
4. Xiang, D. Acoustic Emission Detection of Early Stages of Cracks in Rotating Gearbox Components. *AIP Conf. Proc.* **2017**, *1806*, 070010.
5. Ciaburro, G.; Padmanabhan, S.; Maleh, Y.; Puyana-Romero, V. Fan Fault Diagnosis Using Acoustic Emission and Deep Learning Methods. *Informatics* **2023**, *10*, 24. [CrossRef]
6. Antonaci, P.; Bocca, P.; Masera, D. Fatigue Crack Propagation Monitoring by Acoustic Emission Signal Analysis. *Eng. Fract. Mech.* **2012**, *81*, 26–32. [CrossRef]
7. Krummenacker, J.; Hausmann, J. Determination of Fatigue Damage Initiation in Short Fiber-Reinforced Thermoplastic through Acoustic Emission Analysis. *J. Compos. Sci.* **2021**, *5*, 221. [CrossRef]
8. Wiegandt, F.C.; Froriep, U.P.; Doll, T.; Dietzel, A.; Pohlmann, G. Novel Test Bench for Inhaler Characterization Including Real-Time Determination of Output, Output Rate, and Liquid Water Content of Delivered Aerosols. *J. Aerosol Med. Pulm. Drug Deliv.* **2021**, *34*, 32–41. [CrossRef]
9. Jacob, E.; William, K.; Yani, S.; Ramachandran, R.A.; Walkosz, J.; Didem, O.; Louis, G.M.; Mathew, M.T. Acoustic Emission-Based Diagnostic Tool for Temporomandibular Joint Implant Fixation Screw Loosening. *J. Mech. Behav. Biomed. Mater.* **2025**, *171*, 107137. [CrossRef] [PubMed]
10. Tan, K.; Zhang, X.; Wang, D. Deep Learning Based Real-Time Speech Enhancement for Dual-Microphone Mobile Phones. *IEEE/ACM Trans. Audio Speech Lang. Process* **2021**, *29*, 1853–1863. [CrossRef]
11. Hartbower, C.E.; Morais, C.F.; Reuter, W.G.; Crimmins, P.P. Acoustic Emission from Low-Cycle High-Stress-Intensity Fatigue. *Eng. Fract. Mech.* **1973**, *5*, 765–789. [CrossRef]
12. Reverter, F.; Gasulla, M.; Pallas-Areny, R. Analysis of Power-Supply Interference Effects on Direct Sensor-to-Microcontroller Interfaces. *IEEE Trans. Instrum. Meas.* **2007**, *56*, 171–177. [CrossRef]
13. Wang, Y.; Fang, Y.; Liu, H.; Su, X.; Chen, Z.; Li, S.; He, N. A Highly Integrated and Diminutive Fluorescence Detector for Point-of-Care Testing: Dual Negative Feedback Light-Emitting Diode (LED) Drive and Photoelectric Processing Circuits Design and Implementation. *Biosensors* **2022**, *12*, 764. [CrossRef]
14. Khan, S.; Won, J.; Shin, J.; Park, J.; Park, J.-W.; Kim, S.-E.; Jang, Y.; Kim, D.J. SSVM: An Ultra-Low-Power Strain Sensing and Visualization Module for Long-Term Structural Health Monitoring. *Sensors* **2021**, *21*, 2211. [CrossRef]
15. Venkatasubramanian, V.; Rengaswamy, R.; Yin, K.; Kavuri, S.N. A Review of Process Fault Detection and Diagnosis. *Comput. Chem. Eng.* **2003**, *27*, 293–311. [CrossRef]
16. Müller, M. An Educational Guide through the FMP Notebooks for Teaching and Learning Fundamentals of Music Processing. *Signals* **2021**, *2*, 245–285. [CrossRef]
17. Siebert, J.; Groß, J.; Schroth, C. A Systematic Review of Packages for Time Series Analysis. *Eng. Proc.* **2021**, *5*, 22. [CrossRef]
18. Lo, P.-C.; Lee, Y.-Y. Real-Time Implementation of the Moving FFT Algorithm. *Signal Process.* **1999**, *79*, 251–259. [CrossRef]
19. Vasilakis, C.; Tsagkaropoulos, A.; Koutoulas, I.; Reisis, D. Improving the Fast Fourier Transform for Space and Edge Computing Applications with an Efficient In-Place Method. *Software* **2025**, *4*, 11. [CrossRef]
20. Wu, C.; Low, M. FFT-Based Simultaneous Calculations of Very Long Signal Multi-Resolution Spectra for Ultra-Wideband Digital Radio Frequency Receiver and Other Digital Sensor Applications. *Sensors* **2024**, *24*, 1207. [CrossRef] [PubMed]
21. Henry, M. An Ultra-Precise Fast Fourier Transform. *Measurement* **2023**, *220*, 113372. [CrossRef]
22. Wu, L.; Yao, B.; Peng, Z.; Guan, Y. An Adaptive Threshold Algorithm for Sensor Fault Based on the Grey Theory. *Adv. Mech. Eng.* **2017**, *9*, 168781401769319. [CrossRef]
23. Zhang, Y.; Yuan, Q.; Shui, T.; Hu, G.; Chen, X.; Shi, Y. Development of a Load Monitoring Sensor for the Wire Tightener. *Electronics* **2025**, *14*, 3716. [CrossRef]
24. Hubbard, B.R.; Pearce, J.M. Open-Source Digitally Replicable Lab-Grade Scales. *Instruments* **2020**, *4*, 18. [CrossRef]
25. Carboni, M.; Bernasconi, A. Acoustic Emission Based Monitoring of Fatigue Damage in CFRP-CFRP Adhesive Bonded Joints. In *European Workshop on Structural Health Monitoring*; Rizzo, P., Milazzo, A., Eds.; Springer International Publishing: Cham, Switzerland, 2021; pp. 605–615.
26. Deschanel, S.; Ben Rhouma, W.; Weiss, J. Acoustic Emission Multiplets as Early Warnings of Fatigue Failure in Metallic Materials. *Sci. Rep.* **2017**, *7*, 13680. [CrossRef] [PubMed]

27. Chai, M.; Lai, C.; Xu, W.; Duan, Q.; Zhang, Z.; Song, Y. Characterization of Fatigue Crack Growth Based on Acoustic Emission Multi-Parameter Analysis. *Materials* **2022**, *15*, 6665. [CrossRef] [PubMed]
28. Thiele, M.; Pirskawetz, S. Analysis of Damage Evolution in Concrete under Fatigue Loading by Acoustic Emission and Ultrasonic Testing. *Materials* **2022**, *15*, 341. [CrossRef]

**Disclaimer/Publisher's Note:** The statements, opinions and data contained in all publications are solely those of the individual author(s) and contributor(s) and not of MDPI and/or the editor(s). MDPI and/or the editor(s) disclaim responsibility for any injury to people or property resulting from any ideas, methods, instructions or products referred to in the content.

MDPI AG
Grosspeteranlage 5
4052 Basel
Switzerland
Tel.: +41 61 683 77 34

*Machines* Editorial Office
E-mail: machines@mdpi.com
www.mdpi.com/journal/machines




Disclaimer/Publisher's Note: The title and front matter of this reprint are at the discretion of the Guest Editors. The publisher is not responsible for their content or any associated concerns. The statements, opinions and data contained in all individual articles are solely those of the individual Editors and contributors and not of MDPI. MDPI disclaims responsibility for any injury to people or property resulting from any ideas, methods, instructions or products referred to in the content.





Academic Open
Access Publishing

mdpi.com

ISBN 978-3-7258-8432-2